

Understanding Effect and Diagnosis of Internal Leakage in Hydrostatic Actuation Systems

by

Amit Thakur

A thesis submitted to the Faculty of Graduate Studies of
The University of Manitoba
in partial fulfillment of the requirements of the degree of

MASTER OF SCIENCE

Department of Mechanical and Manufacturing Engineering
University of Manitoba
Winnipeg, Manitoba, Canada

Abstract

This research presents implementation of the Wavelet transform for detecting internal leakages occurring within an Electro-Hydrostatic Actuation (EHA) system. Simulation studies are carried out in order to investigate the feasibility of a particular approach and to determine the level of accuracy that can be expected in the experimental system. The effect of friction, orifices and the dynamics of motor/pump are considered during the simulation study. Experimental analysis based on Wavelet transform is conducted for detecting internal leakage. The original pressure signals at either side of the cylinder are decomposed using Wavelet transform to detect internal leakage which is clearly identified.

Results obtained through the use of Wavelet transform prove that this method is fast and easily-implementable for leakage detection in EHA on the basis of the pressure data obtained. Internal leakages as low as 0.0042 lit/min are shown to be detectable 85% of the time using a structured input signal.

Dedicated to all my mentors of my life because it is their blessings and teachings which has made me stand today at this point of my life and will always be the reason of my success.

**Guru Brahma Guru Vishnu
Guru Devo Maheshwara
Guru Sakshat Param Brahma
Tasmai Shri Gurave Namah**

Acknowledgments

My appreciation first goes to my supervisor, Dr. Nariman Sepehri, for his fabulous direction which has brought about a unique academic life at University of Manitoba for me. I appreciated his guidance, encouragement and helpful discussions. The work presented here would certainly not have been accomplished without his influence and support. From my supervisor, I have learned a great deal about problem solving and presentation of the results of my research work. I would also like to thank the other members of my dissertation committee: Dr. Subramaniam Balakrishnan and Dr. W.K. Fung.

My gratitude extends to the members of the research group of my professor, especially Dr. Amin Yazdanpanah and Mr. Yaser Maddahi who provided me with an appropriate atmosphere to perform this research.

I ultimately would like to pay my gratitude to my parents and mentors. Without the inspiration that they provided this work would not have been possible. This dissertation belongs more to them than to me.

Contents

1. Introduction.....	1
1.1. Preliminary Remarks	1
1.2. General description about EHA and fault detection	5
1.3 Objective of this research	8
1.4. Thesis outline.....	9
2.1 Description of EHA	10
2.1. Fluid Power.....	10
2.2. Pump Controlled EHA.....	12
2.3. EHA system design.....	13
2.4. Experimental test rig.....	19
2.5. Operational process of EHA.....	26
2.6.Summary	27
3. Actuator Internal Leakage and Detection	28
3.1. Internal Leakage	28
3.2. Leakage Detection	29
3.2.1. Fourier Series	30
3.2.2. Wavelet Transform	32
3.2.2.1 Continuous Wavelet Transform.....	34
3.2.2.2. Discrete Wavelet Transform.....	35
3.2.2.3. Properties of Wavelet Transform.....	35
3.2.2.4. Advantages of Wavelet Transform	36
3.3. Summary.....	37
4. Verification of EHA model using Simulation and Experimental Studies	39
4.1. Modeling of EHA	40

4.1.1.	Motor/Pump System	40
4.1.2.	Orifices System.....	42
4.1.3.	Hydraulic Cylinder.....	43
4.1.4.	Friction.....	45
4.2	Simulation and Experimental Results	49
4.2.1.	System without orifice (Throttling valve)	49
4.2.2.	System with orifice (Throttling valve)	59
4.3.	Effect of variable orifice.....	85
4.4.	Summary.....	89
5.	Identification of Internal Leakage using Wavelet Transform.....	91
5.1.	Fault Detection.....	91
5.2.	Large Leak	93
5.3.	Medium Leak	105
5.4.	Small Leak	115
5.5.	Extra-Small leak.....	124
5.6.	Evaluation of fault detection.....	142
5.7.	Summary.....	146
6.	Conclusions and Future Work	148
6.1.	Contribution of this thesis.....	148
6.2.	Future Work.....	150
	Appendix A: Details of the fittings applied in EHA	152
	Appendix B: Steps to run the experimental test rig (EHA).....	153
	Appendix C: Data sheet of RMS values of detail coefficients ($d_1, d_2, d_3, d_4, d_3d_4$) obtained on pressure chamber P_A and P_B of the actuator	154
	References.....	158

List of Tables

Table 2.1.: Details of Servo Motor parameters obtained from manufacturer (Bearing Engineers)	22
Table 4.1: Specifications of EHA system obtained from real-world parameters, MATLAB, manufacturer of motor, pump and mechanical fittings respectively.....	48
Table 4.2: Details of tests conducted without orifice effect.	49
Table 4.3: Details of tests conducted with variable orifice effect.....	60
Table 5.1: Comparison of success rate for fault detection on both sides of actuator. ..	146

List of Figures

Figure 2.1: Block 1 represents combination of motor and pump.	14
Figure 2.2: Blocks 1, 2, 3 and 4 represent the combination of motor and pump, relief valve, accumulator and shut-off valves respectively.....	14
Figure 2.3: Blocks 1, 2, 3, 4 and 5 represent the combination of motor and pump, relief valve, accumulator, shut-off valves and filters on both sides of cylinder respectively.	15
Figure 2.4: Blocks 1, 2, 3, 4, 5, 6 and 7 represent the combination of motor and pump, relief valve, accumulator, shut-off valves, filters, pilot operated valves and orifices with one-way free flow and other way controlled flow on both sides of cylinder respectively.	17
Figure 2.5: Simplified schematic EHA test rig used for modeling and simulation.	19
Figure 2.6: Experimental test rig.	20
Figure 2.7: Servo Motor.....	21
Figure 2.8: Performance graph of servo motor obtained from manufacturer (Bearing Engineers).	23
Figure 2.9: SST-6000-RCX servo drive.	23
Figure 2.10: Fixed displacement pump.....	25
Figure 2.11: Quanser Data Acquisition Board.....	26
Figure 3.1: Internal leakage in the cylinder.	29
Figure 3.2: Signal $x(t)$ and its FFT.	32
Figure 3.3: Daubechies mother wavelet (db8).....	33
Figure 3.4: Time, frequency, STFT and wavelet view of signal analysis.	34
Figure 4.1: Simplified schematic of EHA test rig.....	41
Figure 4.2: a) Coulomb friction model, b) Static friction model, c) Stick-Slip friction model and d) Stribeck curve.....	46
Figure 4.3: Stribeck curve in friction vs. velocity.	47
Figure 4.4: (a) Input voltage as $3\sin(4t)$, (b) angular velocity of motor and (c) displacement of piston obtained without orifice.	52
Figure 4.5: Pressures in chambers A (a), and B (b) of cylinder.....	53

Simulated and experimental input voltage (a) as $5\sin(2t)$, (b) angular velocity of motor and (c) displacement of piston without orifice conditions.....	55
Figure 4.7: Pressures in chambers A (a), and B (b) of cylinder.....	56
Figure 4.8: Simulated and experimental input voltage given as $7\sin(4t)$ in (a), (b) angular velocity of motor and (c) displacement of piston without orifice conditions.	58
Figure 4.9: Pressures in chambers A (a), and B (b) of cylinder.....	59
Figure 4.10: Pressures at inlet/outlet A (a) and B (b) of pump.....	62
Figure 4.11: Pressures in chamber A (a), and B (b) of cylinder.	63
Figure 4.12: Flow through orifices (Q_A and Q_B).....	64
Figure 4.13: Effect on simulated pressures P_1 and P_A due to 25% closed orifices.....	64
Figure 4.14: Effect on simulated pressures P_2 and P_B due to 25% closed orifices.	65
Figure 4.15: Effect on experimental pressures P_1 and P_A due to 25% closed orifices....	66
Figure 4.16: Effect on experimental pressures P_2 and P_B due to 25% closed orifices....	66
Figure 4.17: Pressures at inlet/outlet A (a) and B (b) of pump.....	67
Figure 4.18: Pressures in chamber A (a), and B (b) of cylinder.	68
Figure 4.19: Pressures at inlet/outlet A (a) and B (b) of pump.....	70
Figure 4.20: Pressure in chamber A (a), and B (b) of cylinder.....	71
Figure 4.21: Pressure at inlet/outlet A (a) and B (b) of pump.	72
Figure 4.22: Pressures in chamber A (a), and B (b) of cylinder.	73
Figure 4.23: Pressure at inlet/outlet A (a) and B (b) of pump.	74
Figure 4.24: Pressures in chamber A (a) and B (b) of cylinder.	75
Figure 4.25: Pressures at inlet/outlet A (a) and B (b) of pump.	76
Figure 4.26: Pressure in chamber A (a), and B (b) of cylinder.....	78
Figure 4.27: Pressure at inlet/outlet A (a) and B (b) of pump.	79
Figure 4.28: Pressure in chamber A (a), and B (b) of cylinder.	80
Figure 4.29: Pressure at inlet/outlet A (a) and B (b) of pump.	81

Figure 4.30: Pressure in chamber A (a), and B (b) of cylinder.....	82
Figure 4.31: Pressure at inlet/outlet A (a) and B (b) of pump.	83
Figure 4.32: Pressure in chamber A (a), and B (b) of cylinder.....	84
Figure 4.33: Pressure signal at the inlet of the pump.....	85
Figure 4.34: Pressure signal at the outlet of the pump.....	86
Figure 4.35: Pressure at chamber A of the cylinder.....	86
Figure 4.36: Pressure at chamber B of the cylinder.....	87
Figure 4.37: Pressure at the inlet of the pump.	87
Figure 4.38: Pressure at the outlet of the pump.	88
Figure 4.39: Pressure in chamber A of the cylinder	88
Figure 4.40: Pressure in chamber B of the cylinder.....	89
Figure 5.1: Experimental input voltage of $3\sin(4t)$, angular velocity of motor and displacement of the piston.....	93
Figure 5.2: Close-up view from 50 th to 70 th seconds to show the behaviour of Fig. 5.1.	94
Figure 5.3: Large level of internal leakage shown with the pressures as P_A and P_B at both sides of the cylinder	95
Figure 5.4: Close-up view from 50 th to 70 th seconds to show the behaviour of Fig. 5.3	95
Figure 5.5: Four-level detail wavelet coefficients of P_A pressure signal shown in Fig. 5.3.	96
Figure 5.6: Close-up view from 50 th to 70 th seconds to show the behaviour of Fig. 5.5.	96
Figure 5.7: RMS values of wavelet coefficient, d_3 , d_4 and d_3d_4 as shown in Fig. 5.5	97
Figure 5.8: Four-level detail wavelet coefficients of P_B pressure signal shown in Fig. 5.3.	98
Figure 5.9: Close-up view from 50 th to 70 th seconds to show the behaviour of Fig. 5.8.	98
Figure 5.10: RMS values of wavelet coefficient, d_3 , d_4 and d_3d_4 as shown in Fig. 5.8. .	99
Figure 5.11: Experimental input voltage of $5\sin(2t)$, angular velocity of motor and displacement of the piston.	99

Figure 5.12: Close-up view from 80th to 100th seconds to show the behaviour of Fig. 5.11. 100

Figure 5.13: Large level of internal leakage shown with the pressures as P_A and P_B at both sides of the cylinder 101

Figure 5.14: Close-up view from 80th to 100th seconds to show the behaviour of Fig. 5.13 101

Figure 5.15: Four-level detail wavelet coefficients of P_A pressure signal shown in Fig. 5.13. 102

Figure 5.16: Close-up view from 80th to 100th seconds to show the behaviour of Fig. 5.15. 102

Figure 5.17: RMS values of wavelet coefficient, d₃, d₄ and d₃d₄ as shown in Fig. 5.15 103

Figure 5.18: Four-level detail wavelet coefficients of P_B pressure signal shown in Fig. 5.13. 104

Figure 5.19: Close-up view from 80th to 100th seconds to show the behaviour of Fig. 5.18. 104

Figure 5.20: RMS values of wavelet coefficient, d₃, d₄ and d₃d₄ as shown in Fig. 5.18. 105

Figure 5.21: Experimental input voltage of 3sin (4t), angular velocity of motor and displacement of the piston. 106

Figure 5.22: Close-up view from 80th to 100th seconds to show the behaviour of Fig. 5.21. 106

Figure 5.23: Medium level of internal leakage shown with the pressures as P_A and P_B at both sides of the cylinder 107

Figure 5.24: Close-up view from 80th to 100th seconds to show the behaviour of Fig. 5.23 107

Figure 5.25: Four-level detail wavelet coefficients of P_A pressure signal shown in Fig. 5.23. 108

Figure 5.26: Close-up view from 80th to 100th seconds to show the behaviour of Fig. 5.25. 108

Figure 5.27: RMS values of wavelet coefficient, d₃, d₄ and d₃d₄ as shown in Fig. 5.25 109

Figure 5.28: Four-level detail wavelet coefficients of P_B pressure signal shown in Fig. 5.23. 109

Figure 5.29: Close-up view from 80th to 100th seconds to show the behaviour of Fig. 5.28. 110

Figure 5.30: RMS values of wavelet coefficient, d₃, d₄ and d₃d₄ as shown in Fig. 5.28. 110

Figure 5.31: Experimental input voltage of 8sin (1t), angular velocity of motor and displacement of the piston. 111

Figure 5.32: Medium level of internal leakage shown with the pressures as P_A and P_B at both sides of the cylinder.	111
Figure 5.33: Close-up view from 80 th to 100 th seconds to show the behaviour of Fig. 5.32	112
Figure 5.34: Four-level detail wavelet coefficients of P_A pressure signal shown in Fig. 5.32.	112
Figure 5.35: Close-up view from 80 th to 100 th seconds to show the behaviour of Fig. 5.34.	113
Figure 5.36: RMS values of wavelet coefficient, d_3 , d_4 and d_3d_4 as shown in Fig. 5.34	113
Figure 5.37: Four-level detail wavelet coefficients of P_B pressure signal shown in Fig. 5.32.	114
Figure 5.38: Close-up view from 80 th to 100 th seconds to show the behaviour of Fig. 5.37.	114
Figure 5.39: RMS values of wavelet coefficient, d_3 , d_4 and d_3d_4 as shown in Fig. 5.37.	115
Figure 5.40: Small level of internal leakage shown with the pressures as P_A and P_B at both sides of the cylinder	116
Figure 5.41: Close-up view from 80 th to 100 th seconds to show the behaviour of Fig. 5.40	116
Figure 5.42: Four-level detail wavelet coefficients of P_A pressure signal shown in Fig. 5.40.	117
Figure 5.43: Close-up view from 80 th to 100 th seconds to show the behaviour of Fig. 5.42.	117
Figure 5.44: RMS values of wavelet coefficient, d_3 , d_4 and d_3d_4 as shown in Fig. 5.42	118
Figure 5.45: Four-level detail wavelet coefficients of P_B pressure signal shown in Fig. 5.40.	118
Figure 5.46: Close-up view from 80 th to 100 th seconds to show the behaviour of Fig. 5.45.	119
Figure 5.47: RMS values of wavelet coefficient, d_3 , d_4 and d_3d_4 as shown in Fig. 5.45.	119
Figure 5.48: Small level of internal leakage shown with the pressures as P_A and P_B at both sides of the cylinder	120
Figure 5.49: Close-up view from 80 th to 100 th seconds to show the behaviour of Fig. 5.48	120
Figure 5.50: Four-level detail wavelet coefficients of P_A pressure signal shown in Fig. 5.48.	121
Figure 5.51: Close-up view from 80 th to 100 th seconds to show the behaviour of Fig. 5.50.	121
Figure 5.52: RMS values of wavelet coefficient, d_3 , d_4 and d_3d_4 as shown in Fig. 5.50	122

Figure 5.53: Four-level detail wavelet coefficients of P_B pressure signal shown in Fig. 5.48.	122
Figure 5.54: Close-up view from 80 th to 100 th seconds to show the behaviour of Fig. 5.53.	123
Figure 5.55: RMS values of wavelet coefficient, d_3 , d_4 and d_3d_4 as shown in Fig. 5.53.	123
Figure 5.56: Extra-Small level of internal leakage shown with the pressures as P_A and P_B at both sides of the cylinder	125
Figure 5.57: Close-up view from 80 th to 100 th seconds to show the behaviour of Fig. 5.56	125
Figure 5.58: Four-level detail wavelet coefficients of P_A pressure signal shown in Fig. 5.56.	126
Figure 5.59: Close-up view from 80 th to 100 th seconds to show the behaviour of Fig. 5.58.	126
Figure 5.60: RMS values of wavelet coefficient, d_3 , d_4 and d_3d_4 as shown in Fig. 5.58	127
Figure 5.61: Four-level detail wavelet coefficients of P_B pressure signal shown in Fig. 5.56.	127
Figure 5.62: Close-up view from 80 th to 100 th seconds to show the behaviour of Fig. 5.61.	128
Figure 5.63: RMS values of wavelet coefficient, d_3 , d_4 and d_3d_4 as shown in Fig. 5.61.	128
Figure 5.64: Experimental input voltage of $3\sin(4t)$, angular velocity of motor and displacement of the piston.	129
Figure 5.65: Close-up view from 80 th to 100 th seconds to show the behaviour of Fig. 5.64.	129
Figure 5.66: Extra-Small level of internal leakage shown with the pressures as P_A and P_B at both sides of the cylinder	130
Figure 5.67: Close-up view from 80 th to 100 th seconds to show the behaviour of Fig. 5.66	130
Figure 5.68: Four-level detail wavelet coefficients of P_A pressure signal shown in Fig. 5.66.	131
Figure 5.69: Close-up view from 80 th to 100 th seconds to show the behaviour of Fig. 5.68.	131
Figure 5.70: RMS values of wavelet coefficient, d_3 , d_4 and d_3d_4 as shown in Fig. 5.68	132
Figure 5.71: Four-level detail wavelet coefficients of P_B pressure signal shown in Fig. 5.66.	132
Figure 5.72: Close-up view from 80 th to 100 th seconds to show the behaviour of Fig. 5.71.	133
Figure 5.73: RMS values of wavelet coefficient, d_3 , d_4 and d_3d_4 as shown in Fig. 5.71.	133

Figure 5.74: Extra-small level of internal leakage shown with the pressures as P_A and P_B at both sides of the cylinder	134
Figure 5.75: Close-up view from 80 th to 100 th seconds to show the behaviour of Fig. 5.74	134
Figure 5.76: Four-level detail wavelet coefficients of P_A pressure signal shown in Fig. 5.74.	135
Figure 5.77: Close-up view from 80 th to 100 th seconds to show the behaviour of Fig. 5.76.	135
Figure 5.78: RMS values of wavelet coefficient, d_3 , d_4 and d_3d_4 as shown in Fig. 5.76	136
Figure 5.79: Four-level detail wavelet coefficients of P_B pressure signal shown in Fig. 5.74.	136
Figure 5.80: Close-up view from 80 th to 100 th seconds to show the behaviour of Fig. 5.79.	137
Figure 5.81: RMS values of wavelet coefficient, d_3 , d_4 and d_3d_4 as shown in Fig. 5.79.	137
Figure 5.82: Extra-Small level of internal leakage shown with the pressures as P_A and P_B at both sides of the cylinder	138
Figure 5.83: Close-up view from 80 th to 100 th seconds to show the behaviour of Fig. 5.82	138
Figure 5.84: Four-level detail wavelet coefficients of P_A pressure signal shown in Fig. 5.82.	139
Figure 5.85: Close-up view from 80 th to 100 th seconds to show the behaviour of Fig. 5.84.	139
Figure 5.86: RMS values of wavelet coefficient, d_3 , d_4 and d_3d_4 as shown in Fig. 5.84	140
Figure 5.87: Four-level detail wavelet coefficients of P_B pressure signal shown in Fig. 5.82.	140
Figure 5.88: Close-up view from 80 th to 100 th seconds to show the behaviour of Fig. 5.87.	141
Figure 5.89: RMS values of wavelet coefficient, d_3 , d_4 and d_3d_4 as shown in Fig. 5.87.	141
Figure 5.90: Difference in non-leaking and leaking RMS values of d_3 on pressure chamber P_A with respect to mean values of leak.	142
Figure 5.91: Difference in non-leaking and leaking RMS values of d_4 on pressure chamber P_A with respect to mean values of leak.	143
Figure 5.92: Difference in non-leaking and leaking RMS values of d_3d_4 on pressure chamber P_A with respect to mean values of leak	143
Figure 5.93: Difference in non-leaking and leaking RMS values of d_3 on pressure chamber P_B with respect to mean values of leak.	144

Figure 5.94: Difference in non-leaking and leaking RMS values of d_4 on pressure chamber P_B with respect to mean values of leak. 145

Figure 5.95: Difference in non-leaking and leaking RMS values of d_3d_4 on pressure chamber P_B with respect to mean values of leak. 145

CHAPTER

1

INTRODUCTION

1.1 Preliminary Remarks

An actuator is a device that creates mechanical motion by converting various forms of energy into linear or rotary mechanical energy. Common examples of actuators in our day to day lives include electric motors, pneumatic cylinders or hydraulic actuators. Hydraulic actuators have a broad range of airborne, mobile and stationary applications, and are frequently used in aerospace engineering (e.g. flight surface actuation), in off-highway equipment such as in backhoes and loaders, in the manufacturing industry, and also in robotics. In general, hydraulic systems are able to generate a greater output force than their electric or pneumatic counterparts, and this is primarily due to their high operating pressure and the working fluid's relative lack of compressibility. Some unique features of hydraulic systems include a wide operating range (in terms of force/torque, speed and direction), high force to mass ratio (actuators/motors develop

relatively large force/torque for comparatively small devices) and the lubricating properties of the fluid itself (Merrit, 1967).

This study will investigate fault detection in a hydrostatic system, otherwise referred to as an Electro-Hydraulic Actuator (EHA). An EHA system consists of a variable speed AC motor, a fixed displacement pump, an accumulator, connecting tubes, an actuator, and sensors to measure pressure and displacement of the actuator. The potential applications of EHAs are mainly in the fields of robotics and aerospace engineering (Habibi, 2000). In a typical EHA system, the electric motor drives the pump which creates the required amount of flow that is needed to move the actuator piston. Situating the electric motor and the actuator close to one another (i.e. having the power supply and actuation module in a lumped unit configuration), results in greater hydraulic stiffness (producing faster response), a reduction in the volume of oil required (which reduces the risk of fire) and a reduction in the length of tubes or hoses (thereby lowering the risk of leakage). This configuration is extremely appealing for flight surface actuation systems because the EHA can be positioned at the wing itself which eliminates the need for a centralized fluid power system requiring long tubes and hoses: “The new Lockheed Martin F-35 Joint Strike Fighter’s flight controls used Electro Hydrostatic Actuation (EHA) technology for the first time in a production aircraft. The technology provided several benefits. The actuators are smaller and weigh less; performance is more efficient and the F-35 is less vulnerable to enemy fire” (Heney, 2002).

The force to mass ratio of the actuation system is directly related to the bulk and overall mass of a manipulator as heavy actuation units will require heavier links. In robots with high degrees of freedom, the EHA can be configured as a single lumped unit (supply and actuation module forming an integral part, which results in a stiff system) near the base. However, it is also

possible to use a different configuration wherein the supply module is near the robot's base and is connected to the actuation module which is further away than in the previous scenario. Whereas these configurations can be supportive for manipulating links from the base in order to minimize weight at the actuation point. Hydraulic stiffness is reduced by using longer, more flexible hoses for connecting the supply module to the actuation system (Habibi, 2000).

Viscosity is an important property of the fluid and is essential for the purpose of lubrication. Viscous friction in the actuator arises because force is required to shear the fluid. This force, referred to as viscous friction, is proportional to the area in contact, the velocity of the piston, and is inversely proportional to the film thickness (Merrit, 1967). In hydraulic systems, low viscosity will increase leakage in the system whereas a large viscosity value will decrease efficiency. Due to leakage, the seals in the actuator will start to experience wear with deterioration of the oil resulting in reduced lubricating properties. When EHAs are used for flight surface actuation, friction should be limited to the actuator's viscous friction, but external stick-slip friction may actually dominate. Therefore, quantifying the total friction force is important because, in addition to giving information about the seal in the actuator and the oil condition, it can also reveal potential problems in the movable flight surfaces. Such problems are reflected in the load-pressure measurements of the EHA; if an unusual damping coefficient is measured or estimated using load-pressure measurements, it may be indicative of problems with the movable joints of the flight surfaces. Performance of stroke is the most important factors in the operation of EHAs which is defined as the maximum amount of extension of a linear actuator. The most important performance characteristic of an EHA system is its accuracy.

Selection of leakage levels for fault detection technique is very important for the EHA because certain failures can result in system breakdown and increased expense. Failures of EHA systems

in safety-critical applications, such as in flight surface actuation in aircraft, can be catastrophic and may result in the loss of lives. Early fault detection, predicated on the monitoring of gradual decline in system performance, is highly useful in assessing the need for preventative maintenance which increases safety and reduces unproductive downtime. As a consequence, Fault Detection and Isolation (FDI) techniques for hydraulic systems have been growing over the past decade. Faults in hydraulic systems may range from component failure and fluid contamination, to pipe leakage and material wear (Skormin and Apone, 1995; Zhou, 2002; Zavarehi et al., 1999; Khan, 2002; Zhang and Jiang, 2002).

When the pressure drops, efficiency decreases as well and, in the worst case scenario, may cause the actuator to freeze. This leads to a change in the pump's characteristics, such as motor efficiency and total inertia (Yu, 1997). Wear of the actuator cylinder and the seals also causes changes in the friction characteristic which can significantly affect the dynamic performance of an actuator. As Lischinsky, (1999) has shown, friction can increase the total driving force by as much as 30%.

One of the greatest concerns regarding fluid power systems is the leakage of hydraulic fluid. Leakage is divided into two categories: internal leakage, which occurs when fluid leaks into another chamber of the cylinder, and external leakage, which occurs when the fluid leaks out of the hydraulic circulation. Internal leakage is caused by the wear of the piston seal that closes the gap between the piston and the cylinder wall, and external leakage is caused when the seal separating the actuator rod and the cylinder wears out. External leakage appears as the result of a failure in the hydraulic supply line or in the connection between the valve and actuator chambers. In general, leakages influence both the system's responsiveness and its overall efficiency. While

external leakage can be easily inspected visually, internal leakage cannot be detected until the actuator seal is completely damaged.

1.2 General description about EHAs and fault detection¹

Actuators has the ability to be coupled with many different devices including, but not limited to, piezoelectric, electromagnetic linear motors, shape memory alloys, lead-screw or ball-screw drives, and friction-based ultrasonic piezoelectric, multistage, and hydrostatic actuators. For example, a coarse positioning stage such as an electromagnetic linear motor can be combined in a series with a fine positioning stage driven by a piezoelectric actuator. Unfortunately, this solution is very complex and tends to be quite costly because its hybrid nature is dependent upon the simultaneous control of multiple actuators and sensors. Alternately, electromechanical actuators such as electric-motor-driven lead-screws are becoming more popular because they have lower energy requirements and are much quieter than hydraulic and pneumatic actuators. Despite these advantages, electromechanical actuators cannot be used when spark generation is a concern, their power-to-weight ratios are significantly lower than hydraulic actuators, and the control strategies such as PI (Proportional-Integral) control or PID (Proportional-Integral-Derivative) control are required for them to achieve a high level of accuracy which can be very complex.

In EHA the flow returning from the actuator is fed directly into the inlet of the pump rather than into a reservoir. Central to the design of this system is a unique, symmetric, single rod actuator and the use of inner-loop velocity feedback around the motor, which eliminates dead zones in the motor/pump subsystem.

¹The main portion of this Section was adopted from Ph.D. theses by Goharrizi (2011).

As a result of these design elements, the researchers found that the EHA showed great potential with respect to high-accuracy, high-load positioning (Sampson, 2005). As a result of these findings, the EHA has become the focus of this research project.

In an experimental setup, the pump operates at the same pressure, disregarding the typically minor pressure drop that occurs due to the piping structure and the setup of the pump and the actuator. Because the pump delivers only the required amount of fluid at the required load pressure, the overall efficiency of an Electro-Hydrostatic system can be higher than a traditional hydraulic system. The first issue with traditional hydraulic systems is that the fluid reservoir adds significant volume and weight to the entire setup as it is recommended that the volume of the reservoir be 2-3 times the flow rate in the system. Second, the performance of a system using a traditional single or double-rod linear actuator depends on the direction of motion. This is due to the disparity of space on each side of the actuator piston, which causes rod velocity and output force to vary according to the direction of travel for a fixed-flow input and pressure difference.

The main benefit of using an EHA is defined as the absence of a bulky fluid reservoir and expensive servo valve. Instead, the flow of hydraulic fluid to the actuator is controlled by the rotation of the electric motor, which drives the fixed displacement pump directly. The gear pump has a fixed displacement, which is defined as volume of fluid pumped per rotation of the pump. Therefore, the flow rate of the fluid is directly proportional to the speed of the pump as well as the speed of electric motor. Since the active pressure areas on each side of the actuator's rod are equal, there will be equal amounts of fluid entering and leaving the symmetrical actuator. This allows the output of the pump to be directly connected to one chamber of the actuator while the input is connected to another chamber. In addition, a small accumulator maintains a minimum system pressure to prevent cavitations in the cylinder, and makes up for fluid loss caused by

external leakage. The final result is a proportional actuator rod velocity which is created by the controlled rotational speed of the electric motor. The direction of motion of the rod can be controlled by changing the rotational direction of the electric motor.

Signal processing helps to deal with the analysis of signals, whether discrete or continuous. The signal processing technique used in this study is called as Wavelet Transform (WT) which decomposes a signal into components of mother wavelets (Daubechies, 1992). Fourier transform decomposes a signal into constituent sine waves of different amplitudes and frequencies, whereas Wavelet transform decomposes a signal into both scaled and shifted versions of a mother wavelet with the information of time for the signal. Wavelet transform is reflected to be the most well-liked technique for fault detection due to its ability to possess both time and frequency properties. Wavelet transform completely depends on the choice of the mother wavelet for any analysis. Daubechies wavelets are compactly supported with external phase and highest number of vanishing moments for a given support width. Daubechies mother wavelet (db8) was found, through a series of tests, to be a good choice for internal leakage detection. Hence, from the point of implementation, it is a good choice. Mother wavelet, db8 is chosen to maintain acceptable overlapping between two adjacent frequency bands while keeping the computational time manageable. This leads to a prior subjective assumption regarding the characteristics of the investigated phenomenon (Loutridis, 2004). Consequently, only signal features that correlate well with the shape of the wavelet function have a chance to lead to high value coefficients. All other features will be masked or completely ignored (Loutridis, 2004). The overlap occurs in between the frequency bands which are associated with the wavelet signals but can be reduced by using a higher order of mother wavelet. Discrete Wavelet transform is extremely simple to apply, and the patterns that arise from the use of this transform are clear and

reliable which makes it a robust tool for the diagnosis faults (Antonino-Davin et al., 2009). Moreover, the method is very easy to implement and the computational requirement are negligible (Antonino-Davin et. al., 2009). A wavelet-based method for detection of sensor faults was developed by Zhang and Yan (2001). Wavelet transform for online hydraulic pump health diagnosis was employed by Gao et. al. (2003) wherein pulsation pressure signals were used to isolate faults contributing to pump malfunctions by examining wavelet coefficients. Cusido et al. (2008) applied two different methods based on Short-Time Fourier Transform (STFT) and wavelet decomposition to investigate fault detection in induction machines. They concluded that wavelet analysis is more effective than STFT in detecting faults associated with induction machines. Additionally, WT was shown to be more sensitive and robust in detecting faults associated with hydraulic pumps than had been demonstrated by the FFT approach (Gao et. al., 2005).

1.3 Objective of this Research

The proposed objectives of this research are to:

- a) Construct a close to real-world experimental test rig for setting up the EHA system to acquire experimental data.
- b) Develop a simple yet accurate mathematical model that is able to describe an EHA system usable for simulation studies.
- c) Establish a method that is capable of detecting small-level internal leakages that would not be identifiable using any of the previously proposed methods. Small leakages are extremely

interesting and fascinating for early detection of fault and to be analysed using Wavelet transform.

1.4 Thesis Outline

Chapter 2 outlines the basics of fluid power, which is used to conduct the research on EHA. This chapter also includes a discussion about the pump-controlled EHA and the operational process of the EHA experimental test rig along with a brief description of each of the components used as specified by the design.

Chapter 3 details the actuator's internal leakage and fault detection technique using Wavelet transform. Wavelet transform is explained along with its applications and its approach towards the research related to EHA.

Chapter 4 presents the mathematical modeling of the EHA through detailed equations for the motor/pump, orifices, friction and hydraulic cylinder. This chapter further discusses the validity of simulated and experimental results in the presence and absence of orifices installed in the experimental test rig with variable input conditions.

Chapter 5 explains the method applied for the purpose of identifying internal leakages using Wavelet transform on experimental pressures signals. In addition, this method provides the detail coefficients required to estimate the time of leakage for the entire data sample. The system performs the testing of large to extra-small levels of leakage under sine wave input with variable amplitudes and frequencies.

Chapter 6 presents the conclusions of my research and considers possibilities for future work in this field.

CHAPTER

2

DESCRIPTION OF ELECTRO- HYDROSTATIC ACTUATION SYSTEM (EHA)

2.1 Fluid Power

Fluid power is energy that is transmitted and controlled with the help of pressurized fluid. The term fluid power applies to both hydraulics and pneumatics. The term hydraulics is defined as that branch of engineering that deals with fluids as a transmitting medium for energy. The use of hydraulics goes far back in the history of man's effort to harness nature, but it was not until the first few decades of the twentieth century that the use of hydraulic power became commonplace. Thanks to the development of sophisticated electronics, electrohydraulic actuation systems have become widely employed in high-power-demand applications such as aerospace engineering and in heavy-duty industrial equipment. Hydraulics uses pressurized liquids such as, oil or water while pneumatics deals with compressed air or neutral gases. Fluid power can be easily combined with other technologies through the use of sensors, actuators, and microprocessors.

Fluid power works on Pascal's law which states that, "pressure exerted by a confined fluid acts undiminished equally in all directions."

Fluid power systems can be employed to transport, excavate and lift materials as well as to control or power mobile equipment. The use of mobile power fluid is most common in industries such as construction, agriculture, aviation, and the military. Some of the applications of fluid power include backhoes, graders, tractors, truck brakes and suspension systems, spreaders, highway maintenance vehicles, metalworking equipment, controllers, automated manipulators, material handling, and assembly equipment. Fluid power is used for both commercial and military aircraft, spacecraft/aircraft and related support equipment used in landing gear, brakes, flight controls, motor controls and cargo loading equipment.

The basic components of a typical fluid power system are:

- i. Hydraulic pump which converts mechanical power to fluid power.
- ii. Cylinder or motor which converts fluid power to linear or rotary mechanical power.
- iii. Filters, regulators and lubricators help in conditioning of the fluid.
- iv. Manifolds, hose, tube, fittings, and couplings are used to allow the flow of fluid.
- v. Sealing devices help in containing the fluid.
- vi. Instruments such as pressure switches, gauges, flow meters, sensors and transducers which are used to monitor the performance of a fluid power system.

A few of the advantages of fluid power are:

- i. Linear or rotary force is easily adjustable from a fraction of an ounce to several hundred tons of output.

- ii. It is easy to start or stop, accelerate or decelerate, reverse or position huge forces with great accuracy. Analog (infinitely variable) and digital (on/off) control are possible.
- iii. A single hydraulic pump can provide power and control for numerous machines or machine functions when combined with fluid power.
- iv. Unlike electric motors, hydraulic motors can produce large amounts of torque while operating at low speeds. Some hydraulic motors can even maintain torque at zero speed without overheating. Fluid power has the unique attribute of constant torque.
- v. The fluid power industry has established design and performance standards for hydraulic and pneumatic products through the National Fluid Power Association (NFPA) and the International Organization for Standardization (ISO).

2.2 Pump-controlled EHA

Electro-Hydraulic Actuation systems (EHA) use a combination of fluid power, electricity, electronic controls and mechanical engineering. Electrical energy works as an input for the system with the help of fluid power to make mechanical actuation system move in one axis with variable speed in open-loop (analog-velocity) and closed-loop (position control) mode. Electro Hydrostatic Actuation systems can be designed and installed with various components such as valves, orifices, shuttle valves, etc. A pump-controlled EHA is equipped with valve. The flow of hydraulic oil into the cylinder is made possible with the help of an electric motor that is connected to a pump. Without the presence of valves, the displacement of the piston and control of the pressure in the cylinder would not be possible.

2.3 EHA system design

The experimental EHA test rig is designed and constructed according to the schematic representation shown in Fig. 2.1. The test rig has been constructed and interfaced with a computer with the goal of better understanding and detecting the effects of pressures at inlet/outlet of pump, at either ends of the hydraulic actuator, as well as to gauge the performance of the Electro Hydrostatic Actuation system itself.

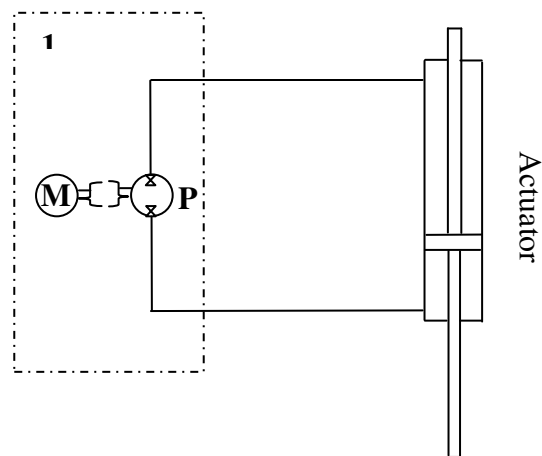


Fig. 2.1 Block 1 represents combination of motor and pump.

Figure 2.1 represents a very basic EHA system equipped with an electric motor coupled with a fixed displacement pump which is connected to the hydraulic actuator. The piston in the cylinder is actuated by the flow of oil from the motor/pump.

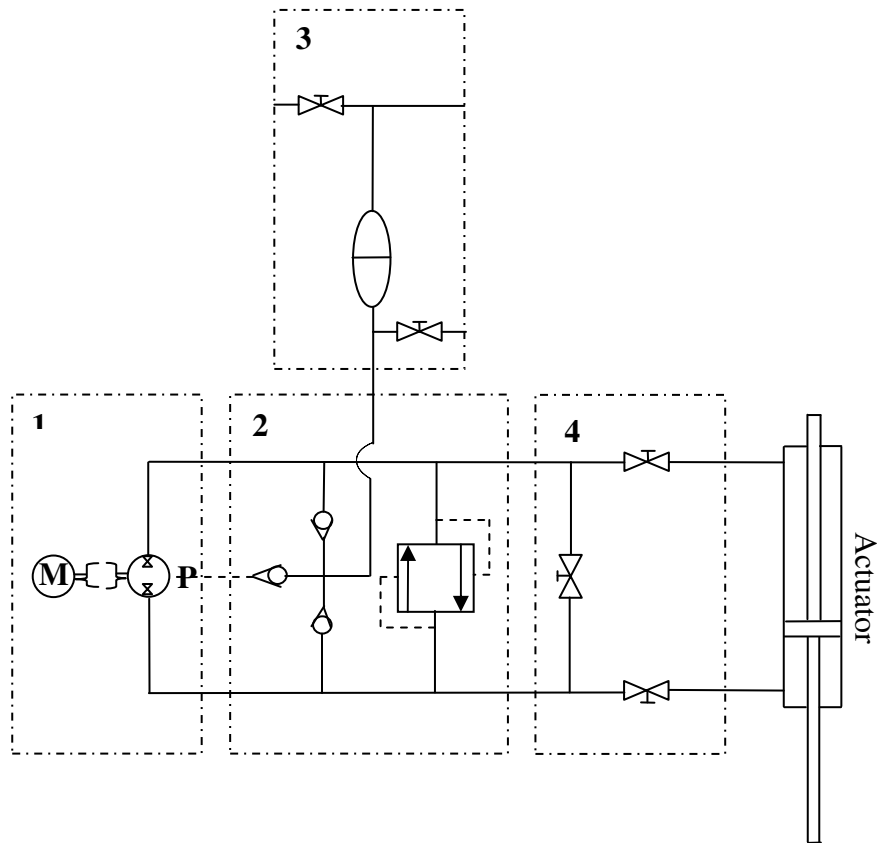


Fig. 2.2 Blocks 1, 2, 3 and 4 represent the combination of motor and pump, relief valve, accumulator and shut-off valves respectively.

Figure 2.2 shows how to move from a basic level of EHA to an intermediate level by adding block numbers 2, 3 and 4. Block 2 is fitted with check valves which allow one-sided flow to both lines and to the fluid accumulator in block 3 with a relief valve installed in connection with both lines in the second block. The provision of three shut-off valves in the 4th block is intended to stop the flow of the hydraulic oil in both lines and let the flow of oil be circulated within blocks 1 to 4. However, the opening of the shut-off valves allows for the oil to flow towards the hydraulic cylinder while using one closed shut-off valve to stop the flow from being circulated within the first four blocks.

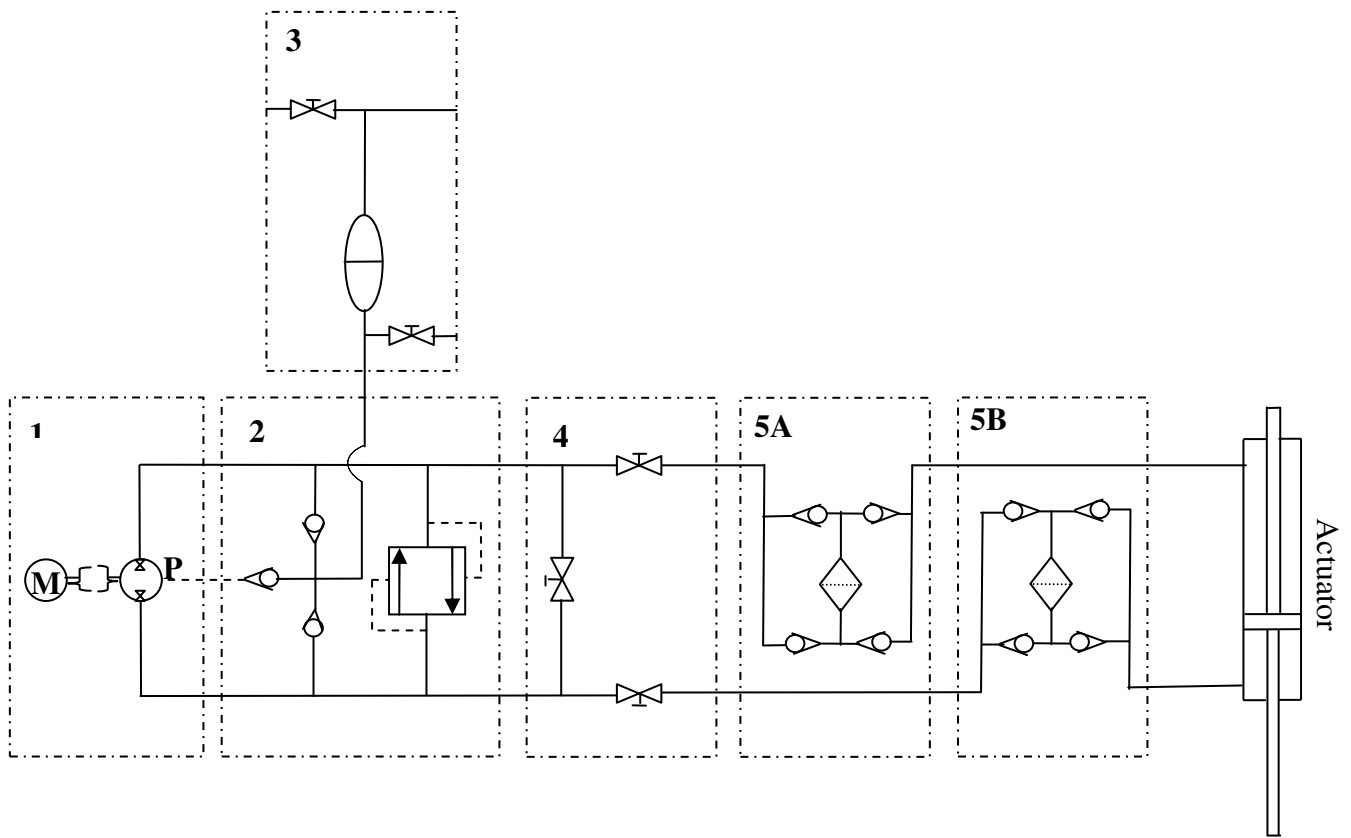


Fig. 2.3 Blocks 1, 2, 3, 4 and 5 represent the combination of motor and pump, relief valve, accumulator, shut-off valves and filters on both sides of cylinder respectively.

Installation of filters (as shown in Fig. 2.3) on both sides of the lines which are equipped with check valves allows the flow of oil to enter and exit the filters and to be circulated throughout the rest of the system. Filters help to remove dirt and impurities from the fluid which not only aids in maintaining a high level of performance and efficiency but also creates the actuation effect from the hydraulic cylinder.

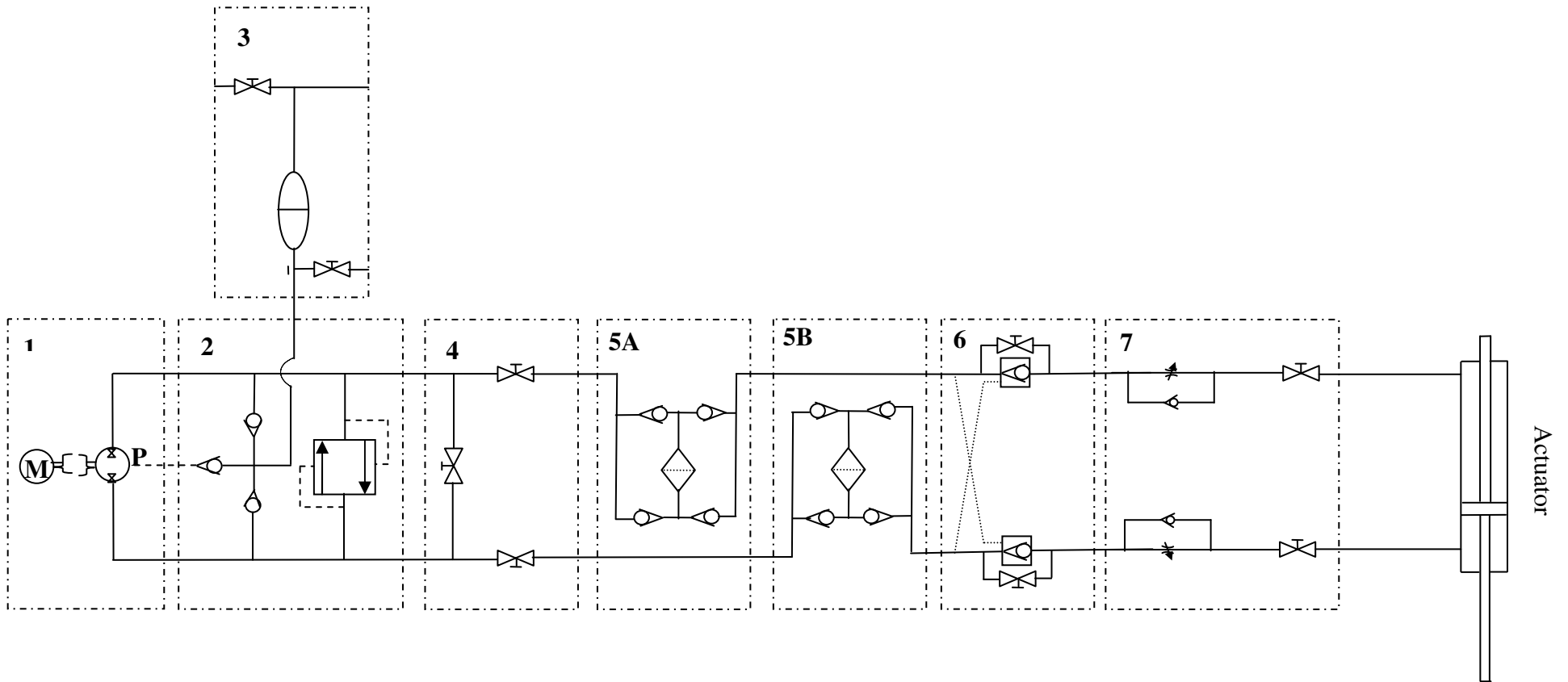


Fig. 2.4 Blocks 1, 2, 3, 4, 5, 6 and 7 represent the combination of motor and pump, relief valve, accumulator, shut-off valves, filters, pilot operated valves and orifices with one-way free flow and other way controlled flow on both sides of cylinder respectively.

Detailed explanation of the EHA system as shown in Fig. 2.4 shows the presence of an electric motor coupled with a bent-axis fixed displacement pump connecting with check valves allowing the flow to the system through lines and hoses which can be seen in block 2 of the diagram. The third block in the design consists of a small hydraulic oil accumulator. Furthermore, the fourth block and the second block are connected by pipes and hoses and are equipped with shut-off valves designed to allow the flow of fluid to the entire system, letting it circulate through to the fourth block. Filters are provided and used in blocks 5A and 5B to eliminate dirt and impurities in the fluid on both sides of the system. This EHA system is also equipped with the provision of shuttle valves in block six; however, this block is not used to study the behaviour and performance of the experimental test rig. Finally, two orifices are installed on both sides of the lines in the seventh block which are closely studied and analyzed to observe the presence and effect of one-way free flow and one-way controlled flow orifices. This can be easily done by manually operating the needle valve and managing the flow from the orifices. All of the blocks are further connected to a cylinder in order to achieve the actuation effect of the piston with pipe lines, hoses and mechanical fittings. These are explained individually in Appendix A. Figure 2.5 represents a simplified version of the design shown in Fig. 2.4 and reflects all the important factors for the modeling and performance of the EHA.

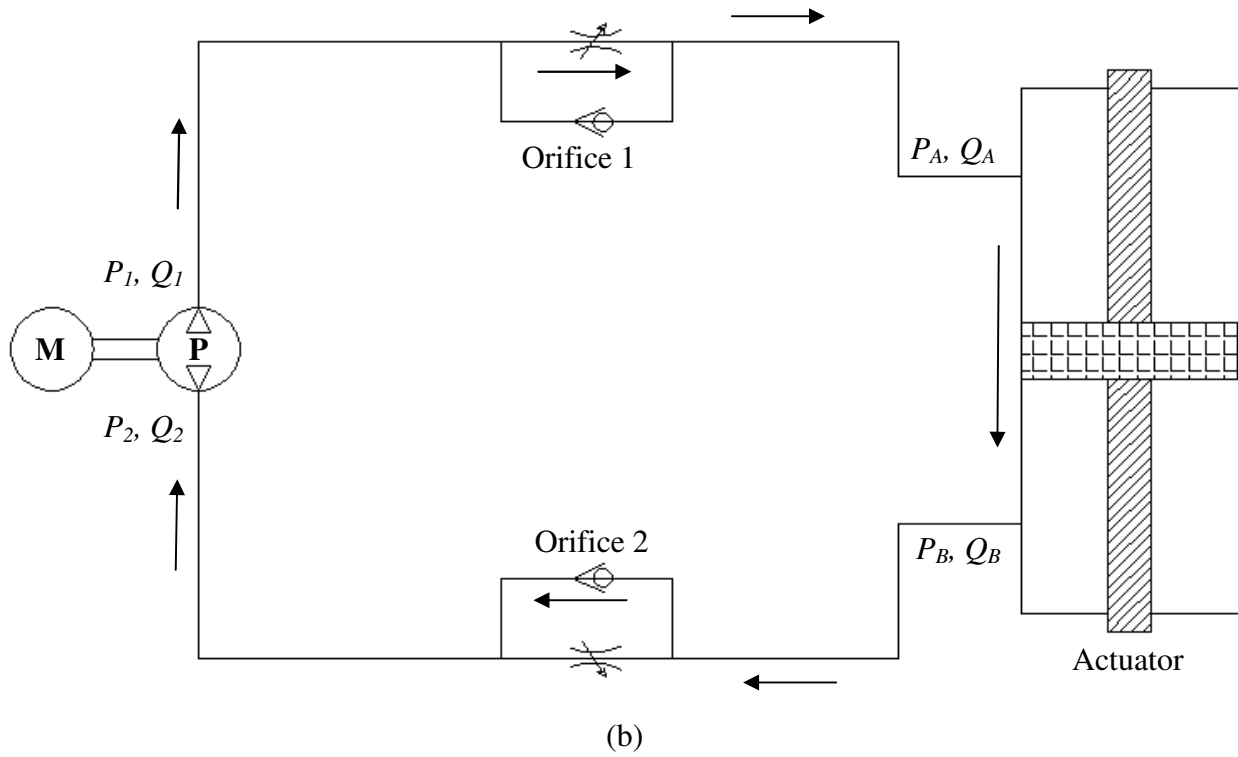
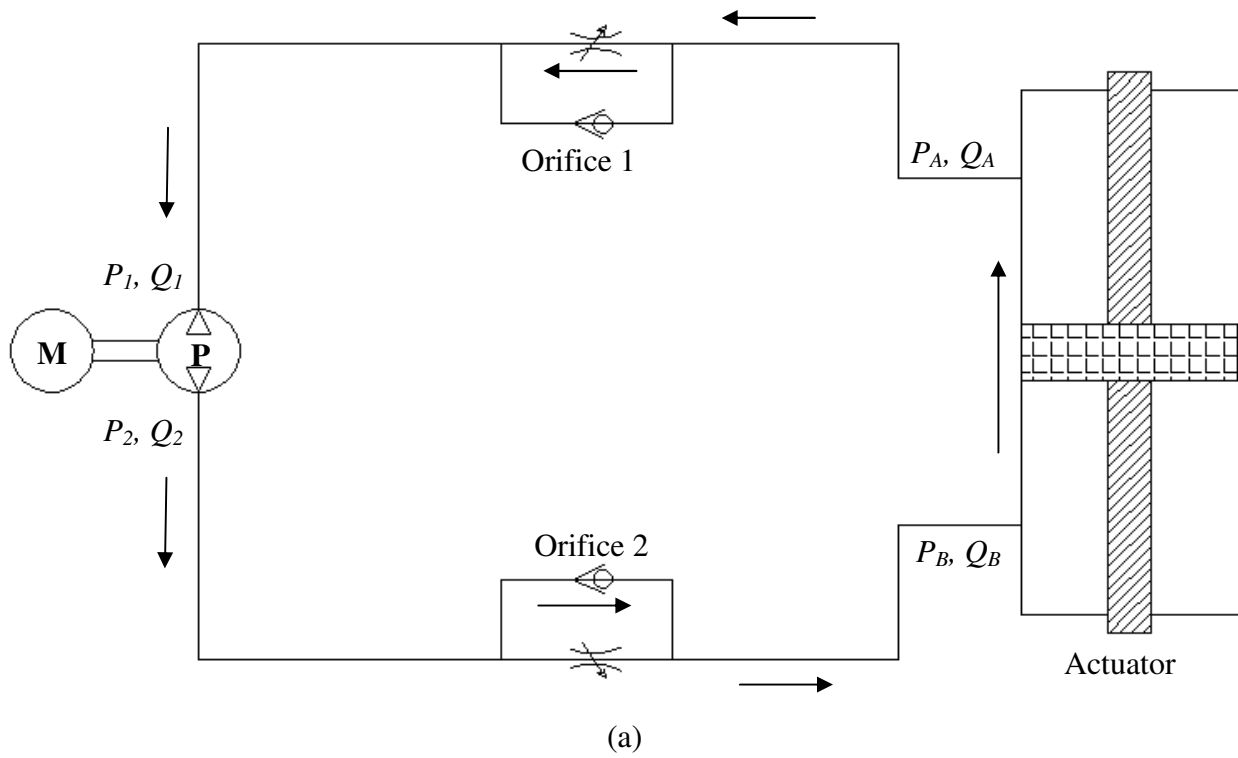


Fig. 2.5 Simplified schematic EHA test rig used for modeling and simulation and the difference between (a) and (b) is the direction of the flow of hydraulic oil.

2.4 Experimental test rig

The experimental test rig used for performing all the tests is shown below in Fig. 2.6, and is made up of components such as an electric motor, a pump, a servo drive, sensors (pressure and position) and a data acquisition board.

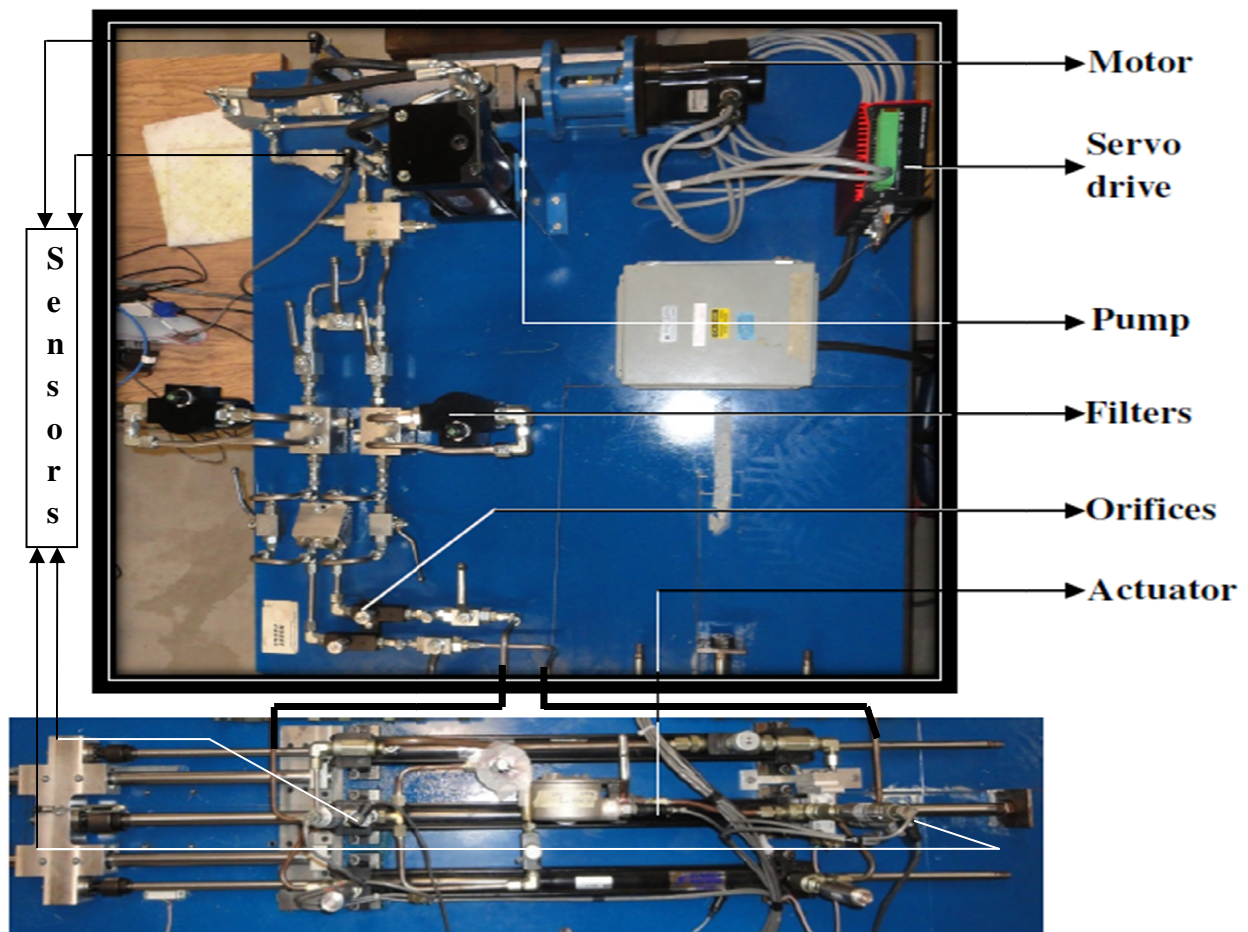


Fig. 2.6 Experimental test rig

a) **Servo Motor:** This test rig has M-4650 motor which is a brushless, permanent magnet rotary servo motor (Fig. 2.7). The motor combines rugged design, high power density, industrial reliability and excellent value. The M-4650 has a sealed, high bandwidth, precision encoder

to ensure reliable operation and is connected to an SSt-6000 RCX servo drive. The M-4650 servo motor receives the signal from the servo drive in terms of amplified voltage. The stators are mechanically locked and chemically bonded to eliminate slippage. This motor needs at least 220V AC to operate.



Fig. 2.7 Servo Motor

Figure 2.8 and Table 2.1 depict the performance and parameter information of this servo motor respectively.

Table 2.1 Details of Servo Motor parameters obtained from manufacturer (Bearing Engineers).

Motor Parameters	
Ambient Temp (°C)	25.0
Winding Resistance @ Ambient (Ω)	0.730
Inductance (mH)	3.550
Drive Input Voltage (V)	260.0
Phase to phase peak Kt (oz-in/A)	98.615
Rotor Inertia (oz-in-s ²)	0.102
Static Friction (oz-in)	12.800
Dynamic Friction (oz-in/kRPM)	2.400
RMS Torque Limit (oz-in)	1128.830
Ke (Vpeak/kRPM)	72.975
Electrical Time Const. (mS)	4.863
Mechanical Time Const. (mS)	1.088
Max Winding Temp (°C)	135
Thermal Resistance (°C/W)	1.150
Resistance @ Tmax (Ω)	1.043
0 Ω Damping (oz-in/kRPM)	9858.11
“Black Watts” Limit (W)	10.000
Motor Constant (oz-in/W)	115.420
Nominal Peak Power (W)	4184.2
Worst Case Peak Power (W)	3138.2
RMS Output Power (W)	1536.2
Drive Peak Current (A)	23.0
Drive Cont. Current (A)	9.0
Motor Max. Cont. Current (A)	9.00

b) **SSt-6000RCX Servo Drive:** The SSt-6000-RCX servo drive is a 3rd generation vector torque control drive that helps in obtaining high level accuracy in Original Equipment Manufacturer (OEM) production environments (Fig. 2.8 and 2.9). The drive is equipped with operational features that were added to eliminate sensors such as to encode position of the motor quadcounts and simplify control harness wirings. Electrical and operational features were added to help OEMs meet compliance agency requirements, including electrical safety, RF compatibility and machine safety. The connectors were specifically selected for their

compatibility with a wide variety of mating connectors. Rapid configuration and built-in troubleshooting tools are included to help simplify and speed up the development, production and field services of the servo drive.

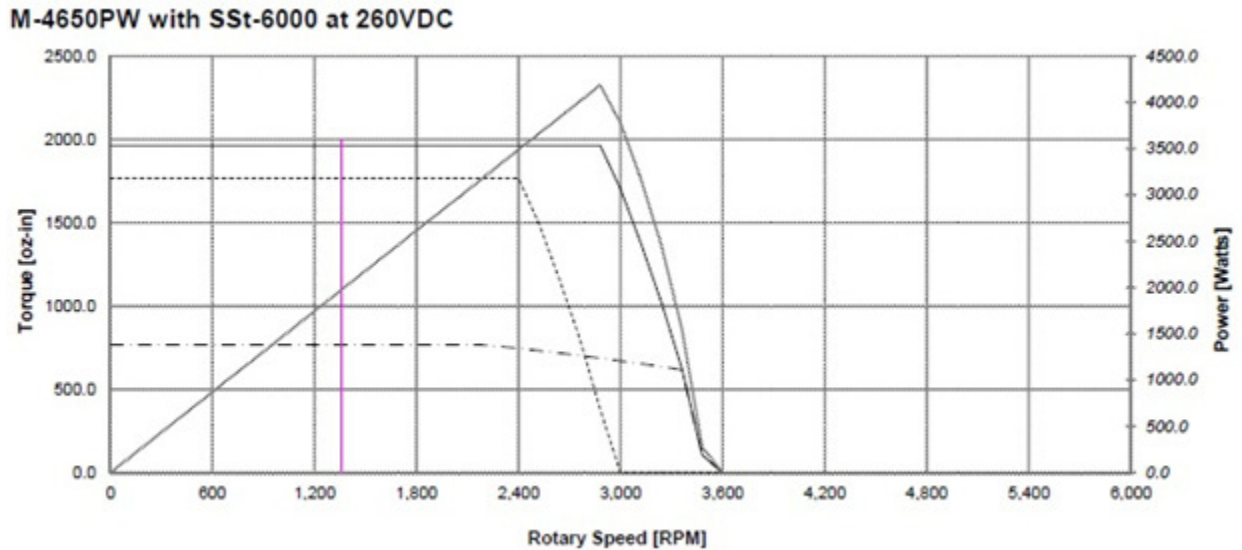


Fig. 2.8 Performance graph of servo motor obtained from manufacturer (Bearing Engineers).



Fig. 2.9 SSt-6000-RCX servo drive.

The controller port of the SSt-6000 RCX drive is a high level digital feedback output which simplifies the control software requirements. The wire running to the controller port is equipped with two sections of cables, which have analog and encoder plugs at the each end

which run to the analog output and encoder port in the Q8 Quanser DAQ board respectively. The analog output port connected to the Quanser DAQ board is responsible for sending the voltage commanded using the C++ or MATLAB Simulink program, which further commands the motor connected to drive to rotate clockwise or anti-clockwise depending on the negative or positive voltage as well as its range. The encoder port describes the position of the motor rotation in terms of 20,000 quadcounts per revolution of the rotor. The provision of a safety plug in the servo drives which functions in the brake output and ARM input.

- c) **Fixed Displacement Pump:** The fixed displacement hydraulic pump, (F11-005-HU-CV-K-000-000-0) depicted in Fig. 2.10, has the capability to rotate in clockwise and counter-clockwise direction depending on the input voltage. Further, the motor is coupled with the pump by a flexible Oldham coupler which causes them to rotate together. This pump is designed and manufactured for use in open-loop or closed loop circuits in industrial applications. The pump can rotate in either direction and is equipped with inlet and outlet holes which let the flow of the oil move back and forth depending on whether the rotor is moving in a clockwise or counter-clockwise direction. The pump can achieve a maximum speed of 4000 RPM, which is the same as the motor to which it is connected. This pump has fixed displacement of $4.9\text{cm}^3/\text{rev}$. and a maximum limit of pressure rated at 5000 psi. The oil tank (i.e. accumulator) used in this test rig is also connected to the pump in order to provide oil to the entire system with the help of pressure generated from the pump.

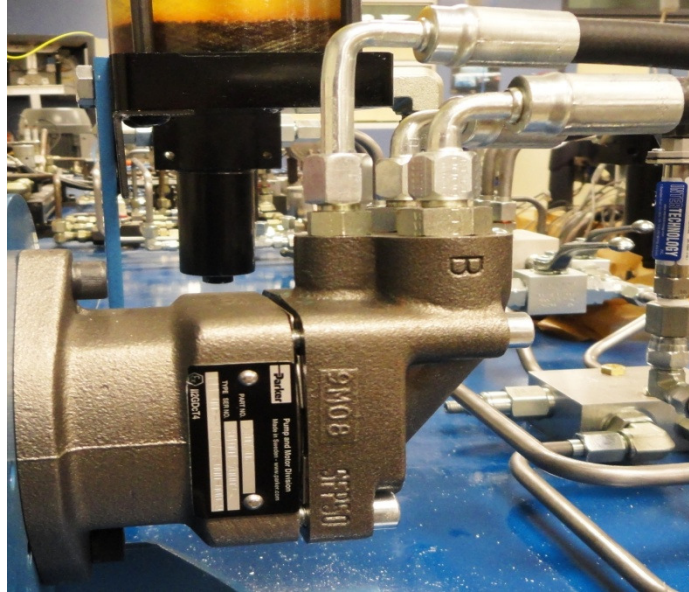


Fig. 2.10 Fixed displacement pump.

d) Sensors: This experimental test rig has five sensors consisting of one position sensor and four pressure sensors. The position sensor is situated to encode the movement of the actuation piston which is 60 cm long. The position sensor is a rotary type sensor which monitors the movement of the piston rod and transmits the information to the Q8 board which is connected to the PC. Furthermore, with the help of WinCon software, it can store, track and observe the piston's position. The pressure sensors are installed at four different locations: two are connected to the inlet and outlet of the pump flow, and the other two are installed on each side of the cylinder to measure pressure changes. The maximum limit of each pressure sensor is 3000 psi.

e) Quanser Data Acquisition board (DAQ): This Quanser Q8 board (Fig. 2.11) serves as the interface between the computer and the servo drive which is connected to the motor. The Q8 DAQ is an extremely versatile and powerful tool for measuring and controlling an extensive

range of input and output signals. This device allows for the flexibility to connect up to eight I/O analog ports, eight encoders and thirty two digital I/O ports within one terminal board. The Q8 board is extremely useful in obtaining complex measurements of data from any control system. One of the major benefits to using the Q8 board is that even when many are linked together, it is still easy to synchronize input/output.

The specifications of the Quanser Q8 terminal board are explained below for control systems and the measurement of complex systems:

- i. High resolution - 14-bit inputs.
- ii. High speed sampling up to 350 kHz.
- iii. Simultaneous sampling of A/D, digital and encoder inputs.
- iv. Extensive I/O: 8 each of A/D, D/A, encoders & 32 digital I/O on the same board.
- v. Integrated with MATLAB/Simulink via Quanser's WinCon and SLX solutions.
- vi. Pulse Width Modulation (PWM) outputs on-board.
- vii. Easy synchronization of multiple Q8 boards.

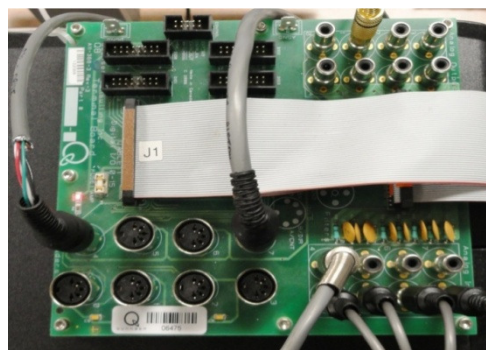


Fig. 2.11 Quanser Data Acquisition Board

In this setup, this board is integrated with MATLAB's toolbox (i.e. Simulink via Quanser's WinCon), which helps build the blocks of Simulink that send the signal in terms of voltage to the SSt-6000-RCX servo drive.

2.5 Operational process of EHA

The Electro Hydrostatic Actuation system illustrated in Fig. 2.6 is an integration of mechanical and electrical engineering in that it uses a mechanical test rig and an electric motor with a digital AC servo drive (operating at 220-240 V AC), with an EMI filter installed in between to reduce the effect of noise by keeping distance of less than 6" of wire.

The SSt-6000-RCX servo drive is a 3rd generation vector torque control drive which helps in obtaining high level accuracy in position control when used with smaller motors. The SSt-6000-RCX is connected to the Data Acquisition Board and computer through a diagnostic port with two output wires. The first wire goes to the computer in the form of an RS-232 plug and the other is connected to the oscilloscope to observe the responses. The controller port of the SSt-6000-RCX drive is a high level digital feedback output which simplifies all control software requirements. This wire also has two sections of cables which have analog and encoder plugs at the other end of the wire which respectively go in the encoder output and encoder port in the DAQ board. The analog output port connected to the Quanser DAQ board is responsible for transmitting the voltage signal from the C++ or MATLAB Simulink program to the motor, commanding it to rotate clockwise or counter-clockwise depending on the negative or positive voltage and its range. The encoder port records the motor's rotation at a rate of 20,000 quad counts per revolution.

The motor is connected to the servo drive by encoder plugs located at the end of motor. Further, the motor is coupled with the pump by a flexible Oldham coupler which synchronizes up the rotation of the pump and motor. The pump has inlet and outlet holes which allow the oil move back and forth depending on which direction the piston is moving.

The oil tank in this test rig is also connected to the pump in order to provide the oil supply for the entire system with the help of pressure generated from the pump. In between the line connections, filters are installed on both sides with the throttling valves i.e. orifices to control the pressure of flow of oil; followed by the cylinder. Check valves are provided at every step to divert or stop the flow if necessary. The mechanical test rig is controlled by the pump. The pump is connected to the servo motor and drive which are in turn interfaced with the Quanser DAQ board. On the board, input/output analog ports and encoder ports are used which help in receiving and sending signals in terms of voltage from the computer to the test rig. Four pressure sensors and one encoder are connected to the input analog ports and encoder port respectively.

2.6 Summary

The descriptive study of fluid power and its applications presented in this chapter explains its use in hydraulic actuation systems and Electro-Hydrostatic Actuation (EHA) systems. Furthermore, the EHA design used in this research has been presented in step-by-step detail and an elaborative study has been conducted on each component of the EHA and their applications within the experimental EHA system. The operational process of the test rig has been explained in section 2.5 in order to make clear the mechanical set up and the way in which each component affects its operation.

CHAPTER

3

ACTUATOR INTERNAL LEAKAGE DETECTION

3.1 Internal Leakage

A drop in hydraulics performance is often the primary sign of an issue with a hydraulic system, and these problems usually occur as a result of longer life time or erratic and diminished slow functioning of the hydraulic systems. Flow in the EHA system helps to determine the actuation speed and reduction in the velocity factors indicates a loss in flow. Lack of flow in a hydraulic system can be caused by external or internal leakage. External leakage, such as a burst hose, is usually obvious and therefore easy to find. Internal leakage can occur in the pump, valves, or actuators and it is considerably more difficult to detect and isolate (Fig. 3.1).

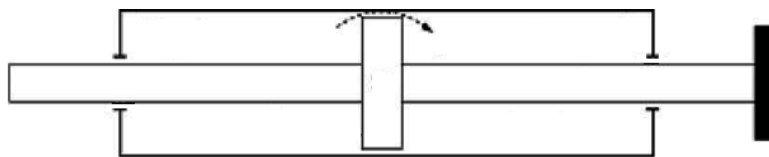


Fig. 3.1 Internal leakage in the cylinder

This EHA test rig has been equipped with a flow-meter to detect and observe the level of internal leakage. The internal leak is caused with the help of a needle-valve which has been installed in between the ends of the actuator. Internal leakage is typically created by small orifices or pathways that permit hydraulic fluid to flow from a high pressure chamber to a low pressure chamber. These intentional internal leaks do not allow the fluid to exit the hydraulic circuit so there is no visual indication of leak.

3.2 Leakage Detection¹

Excessive internal leakage can arise due to flaws in system design, incorrect component selection, and excessive wearing of a component during routine operation. Diminishing system performance, decreased reliability, and increased operating temperatures are the first detectable signs of excessive internal leakage. In hydraulic cylinders, cylinder rod drift or creep and the cylinder's inability to hold position would be attributed to increased leakage. Excessive leakage occurs as the result of lubricant bypassing a piston seal either through a worn seal or a worn cylinder barrel. In most cases, detection of unplanned internal leakage is reliant on specific tools used to examine the location and quantity of the leak. After collecting the data related to internal leakage at different levels, the pressure signals are analyzed by using Discrete Wavelet Transform method (DWT).

¹The main portion of this Section was adopted from Ph.D. theses by Goharrizi (2011).

3.2.1 Fourier series

Fourier series decomposes any periodic function or periodic signal ranging from infinity to the sum of a set of simple oscillating functions. Fourier analysis is the branch of Fourier series which breaks down a signal into constituent sine wave of different frequencies and phases. The mathematical technique used for transforming any signal from time-based to frequency-based is called Fourier analysis. It can be classified in two parts: Continuous Fourier Transform (CFT) or Discrete Fourier Transform (DFT). The Fourier transform of a continuous time signal, $x(t)$ is defined as:

$$X(\omega) = \int_{-\infty}^{+\infty} e^{-j\omega t} x(t) dt \quad (3.1)$$

$X(\omega)$ is a complex decomposition of the original signal $x(t)$ into constituent exponential functions at each frequency ω .

On the other hand, DFT helps in converting a sampled time representation of a signal into a sampled frequency representation. The DFT shows a relationship between frequency and amplitude of a signal. The DFT is given as follows:

$$X[n] = \sum_{k=0}^{N-1} x[k] e^{-2\pi i n k / N} \quad n = 0, 1, \dots, N - 1 \quad (3.2)$$

where $x[k]$ is the original signal and N is the length of the sampled original signal.

The Fast Fourier Transform (FFT) algorithm can be used for efficient calculation of the DFT (Proakis and Manolakis, 2007). A Fourier analysis example has been shown which consists of two cosine components of 100 Hz and 30 Hz (Gao, 2008) and they are extremely useful for the analysis of periodic, time-invariant or stationary phenomena.

$$x(t) = \cos(2\pi \times 100t) + 0.5 \times \sin(2\pi \times 30t) \quad (3.3)$$

The original signal along with its FFT is shown in Fig. 3.2. This figure shows that the FFT of the original signal reveals its two dominant frequency components. The most prevalent frequency components of a signal can be observed. The major drawback of the Fourier analysis is that the time information of a signal is lost when it is transformed to the frequency domain (The Mathworks, 2005). By observing the Fourier transform of a signal, it is impossible to see when a particular event happened because of the lack of time-based information. This deficiency of the Fourier analysis can be solved to some extent by windowing the signal, which is technique wherein small sections are analysed at a time. This leads to an analysis technique known as the Short-Time Fourier Transform (STFT). The problem with the STFT is that the size of the time-window is the same for all frequencies, but this can be circumvented through the use of wavelet analysis (Goharrizi, 2011).

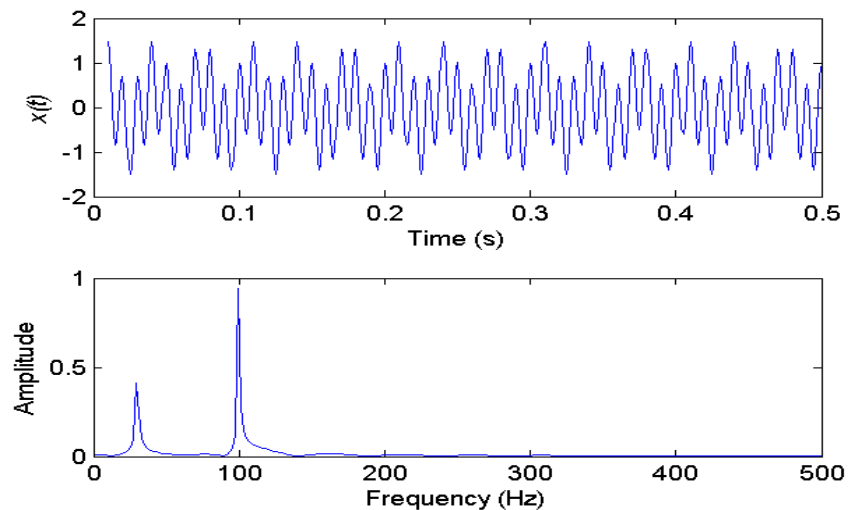


Fig. 3.2 Signal $x(t)$ and its FFT (Goharrizi, 2011).

3.2.2 Wavelet Transform (Goharrizi, 2011)

A wavelet is an oscillatory waveform of effectively limited duration with an average value of zero (Burrus, 1998). The energy of a wavelet is concentrated in time to be suitable for the analysis of transient, nonstationary or time-varying phenomena. Wavelets still have the characteristics of an oscillating wave but they also have the ability to be analysed in terms of time and frequency through the use of simple mathematics (Burrus et al., 1998). As per section 3.2.1, Fourier analysis breaks down a signal into sine waves of different frequencies, whereas wavelet analysis breaks down a signal into shifted and scaled versions of the original (or mother) wavelet (The Mathworks, 2005).

Daubechies has made an enormous contribution in the field of wavelet analysis, and wavelets are among the most popular in use. The description of Daubechies family wavelet is expressed in the form, dbN (N represents the order and db is the surname of the wavelet). It starts from db1 and goes to db10 which are considered the mother wavelets for the analysis of the signal and in this research for all the analysis, db8 is selected related to internal leakage applications. As a result, Daubechies' wavelets can be implemented efficiently via the Fast Wavelet Transform (FWT). Fig. 3.3 depicts basis functions for wavelet transform (db8 mother wavelet).

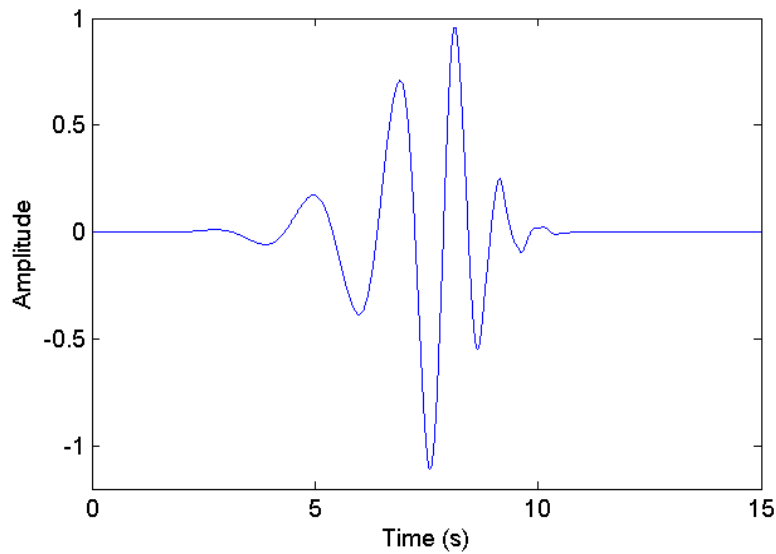


Fig. 3.3 Daubechies mother wavelet (db8) (Goharrizi, 2011).

The choice of wavelet depends on the nature of the particular application. For smooth signals, a wavelet that is itself smooth is needed. In contrast, signals that contain discontinuities are better analyzed using wavelets with good spatial localization to accurately map rapid changes in the signal (Thomas A. Ridsdill-Smith, 2000). There are other useful properties that the wavelets can possess. In order to have a sparse representation of a signal using wavelet analysis, the selection of the function helps in resembling the features of the signal under investigation (Daubechies, 1992).

Wavelet analysis allows for long time intervals when low-frequency information is required, and shorter intervals when high-frequency information is needed (The Mathworks, 2005). Figure 3.4 depicts the time domain, frequency-domain, STFT and wavelet views of signal analysis. The windowing method is very useful in wavelet analysis aimed at defining variable-sized regions.

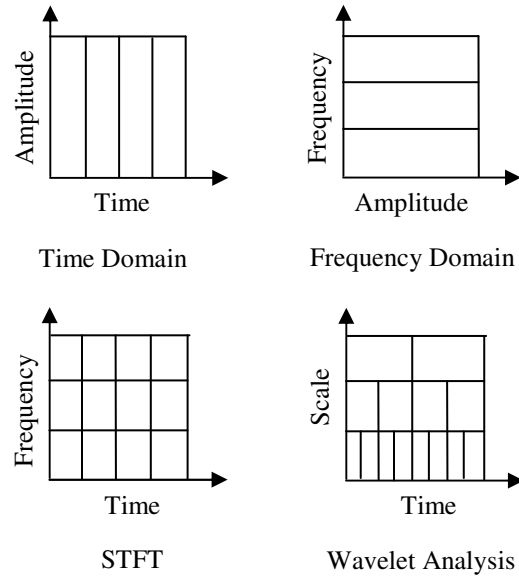


Fig. 3.4: Time, frequency, STFT and wavelet view of signal analysis (Goharrizi, 2011).

Keeping the analysis low scale produces compressed wavelets with higher frequencies and rapidly changing details whereas high scale analysis generates stretched wavelets with lower frequencies and changes that are slower with coarse features.

3.2.2.1 Continuous Wavelet Transform

The Continuous Wavelet Transform (CWT) is defined as the sum over all time of the signal multiplied by the scaled and shifted versions of the wavelet function ψ . The CWT of a signal $x(t)$ is defined as:

$$CWT(a, b) = \int_{-\infty}^{+\infty} x(t)\psi_{a,b}^*(t)dt \quad (3.4)$$

With an inverse transform:

$$x(t) = \int_{-\infty}^{+\infty} \int_{-\infty}^{+\infty} CWT(a, b)\psi_{a,b}^*(t)dadb \quad (3.5)$$

where

$$\psi_{a,b}(t) = |a|^{-1/2} \psi\left(\frac{t-b}{a}\right) \quad (3.6)$$

$\psi(t)$ is the mother wavelet. The asterisk in Eq. (3.5) denotes a complex conjugate, and $a, b \in R, a \neq 0$ (R is the set of all real numbers) are the scaling and shifting parameters, respectively. $|a|^{-1/2}$ is the normalization factor of $\psi_{a,b}(t)$ so that if $\psi(t)$ has a unit length, then its scaled version $\psi_{a,b}(t)$ also has a unit length.

The basic functions are localized in frequency for both Fourier and wavelet transforms. The most important difference between these transforms is that wavelet functions are localized in time and Fourier basis functions are always active. This localization feature, along with a wavelet's localization of frequency, makes wavelet analysis suitable for different applications such as data compression and detecting features in signals (Burrus, 1998).

3.2.2.2 Discrete Wavelet Transform

The DWT analyzes the signal at different frequency bands with different resolutions by decomposing the signal into approximate coefficients and detail coefficients. DWT employs two sets of functions, scaling functions and wavelet functions, which are associated with low pass and high pass filters, respectively. The decomposition of the signal into different frequency bands is simply obtained by successive high pass and low pass filtering of the time domain signal (Goharrizi, 2011).

3.2.2.3 Properties of wavelet transform

A number of issues are important in designing wavelet functions. This section explains these issues and their effects.

- i. **Linearity:** The WT is linear which means that the transform of the sum of two signals equals the sum of their transforms.
- ii. **Smoothness:** Smoothness of wavelet functions is very important. If the wavelets have discontinuities or strong singularities, then coefficient quantization errors will cause these discontinuities and singularities to appear in analyzed signals. These effects are highly objectionable, particularly in smooth regions of signals (Zafarifar, 2002).
- iii. **Approximation accuracy:** Accuracy of approximation is another important design criterion. Wavelet analysis allows constructing smooth, compactly supported bases that can exactly reproduce any polynomial up to a given degree.
- iv. **Compact support:** Compactly supported scaling function and wavelet function lead to Finite Impulse Response (FIR) filters.

3.2.2.4 Advantages of wavelet transform

Wavelet transform has several advantages (Burrus et al., 1998 and Zafarifar, 2002):

- i. The size of wavelet coefficients drop off rapidly with large classes of signals. This property makes wavelets effective in signal and image compression, denoising and detection. Donoho (1993) has shown that wavelets are nearly optimal for a wide class of signals for compression, denoising and detection.
- ii. A more accurate local description and separation of signature characteristics can be obtained by wavelet analysis. As opposed to a Fourier coefficient which cannot represent temporary events, a wavelet coefficient represents a component that is itself local and easier to interpret.

- iii. Suitable mother wavelets can be used depending on particular applications.
- iv. Wavelets are smooth.
- v. Discrete Wavelet transform and its inverse can be calculated with fast and efficient algorithms.
- vi. Wavelets are based on multi-resolution signal analysis. Wavelet decomposition allows for the analysis of a signal at different scales, which results in superior objective and subjective performance.

3.3 Summary

This chapter has outlined fundamental notions of actuator internal leakage and its detection process through the use of Wavelet transform. Wavelet transform is useful in detecting leakage because it provides the ability to process the signal with respect to time, whereas Fourier series can only do so with respect to frequency. In addition, this chapter has provided a detailed explanation about pressure signal processing using Wavelet transform for detecting leakages in EHA systems. Due to leakage in the system, pressure at both ends of the cylinder drops significantly.

CHAPTER

4

MODELING, SIMULATION AND VALIDATION OF ELECTRO- HYDROSTATIC ACTUATOR

Modeling of any physical system is always necessary to express and analyze its performance under real environmental conditions. In actual situations, all the constraints work in a completely dynamic scenario along with the relationship between the input and output. In constructing mathematical models, researchers always try to understand the characteristics of the system as close as to the actual environmental conditions as possible. Mathematical equations help to recognize and get close to the experimental set-up by using real data and inputs so that the output should be able to provide the desired position, velocity, and rotation of the motor, as well as flow from the pump and pressure measurements at all the monitored locations.

Mathematical modeling can be done using two approaches: firstly, modeling can be achieved with the help of fundamental principles and important physical processes which take place in the

experimental set-up, and equations are explained to describe the actual electro-hydraulic actuation system. In this approach the parameters used in the equations are assumed with the help of experiment. The second approach, also known as the black-box approach, states that actual inputs and outputs are observed and a model is fitted based on observations without considering the internal mechanism involved. Many research efforts have been focussed on considering the dynamic characteristics of electro-hydraulic actuation systems with the use of derivations and equations within mathematical models. With the advancement of measuring instruments and computer technology, the complicated dynamic behaviours can be observed and studied much more accurately.

4.1 Modeling of EHA

Figure 4.1 shows the schematic for the experimental Electro Hydrostatic Actuation test rig which is mathematically modeled in this chapter. Electro Hydrostatic Actuation (EHA) system is a well known term which acts, depending on the conversion of mechanical energy, using power from electricity in combination with hydraulics or pneumatics. This test rig involves the integration of hydraulics and electric actuation which is referred to as Hydrostatic Actuation and is controlled with the help of pump. The experimental test rig consists of FPVM (Fixed Pump Variable Motor) which rotates in a clockwise or counter-clockwise motion depending on the input voltage. The direction of the rotation of the motor depends on the negative or positive value of the voltage range sent to DAQ board from ± 10 V. The flow of the fluid is dependant on the fixed displacement of the pump which pushes the fluid to both sides of the cylinder. This test rig is equipped with one double rod cylinder, and there are two orifices installed on the way from the

fluid from pump to the piston. The orifices allow one sided free flow towards the cylinder on both sides, and controlled flow on the reverse side when fluid is returning towards the pump.

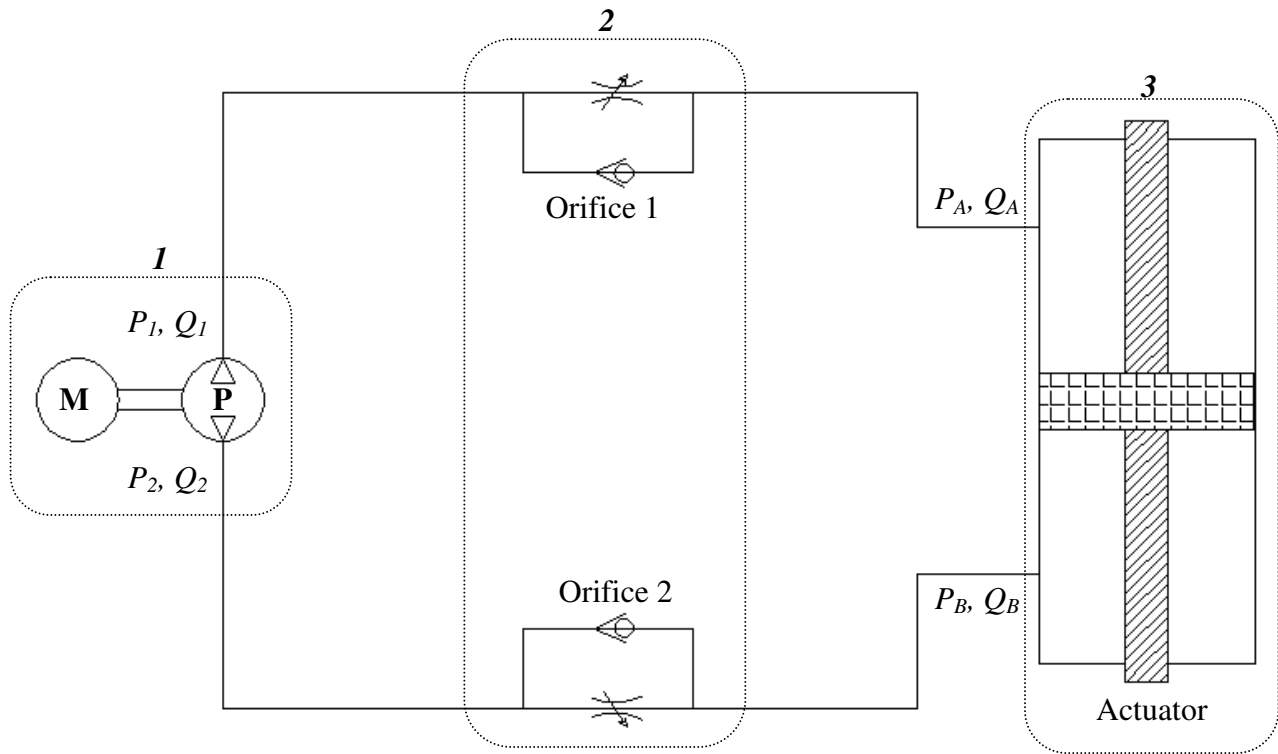


Fig. 4.1 Simplified schematic of EHA test rig

In the following sections, the symbolic modeling of motor/pump, orifice, cylinder and friction are presented.

4.1.1 Motor/Pump system

The test rig is completely stable with the effect of PI (Proportional-Integral) control in motor which closes the loop around the rotation of the motor. The SSt-6000RCX drive connected with the motor plays a significant role as the controller of the motor. The drive allows the operator to set the maximum limit of rotations and provides the advantage of applying further gains to control the motor speed with the restriction applied in terms of the maximum allowed rotations.

The rotations in this variable motor are observed with the help of encoder counts that are connected to the SSt-6000-RCX drive. The SSt-6000-RCX drive shows the encoder counts in terms of quad counts in the software which controls the motor and allows the user to make changes to the characteristics of the motor and servo drive through the use of computer. The relation between quad counts and revolution states that 1 revolution of the rotor is equal to 20,000 quad counts. The input for the motor is received with the help of the servo drive in terms of the voltage transmitted from the Simulink application of MATLAB. This voltage also causes the motor to rotate in the clockwise or counter-clockwise direction. The rotation of the motor allows the flow of fluid from the pump with fixed displacement, q_b .

The following mathematical equations represent the flow from the pump with respect to fixed displacement (Eqn.4.1) , and the rotation of the motor with respect to the load pressure on the motor shaft which acts as load torque(Eqn. 4.5 and 4.6). The equations are represented in the differential state space format with respect to time. The equations are numerically solved using RangE-Kutta method in visual studio C++ 2008 with a step size of 0.0001.

$$Q_1 = \frac{q_b}{2\pi} \omega ; Q_1 = Q_2 \quad (4.1)$$

$$I = I + h(\omega_d - \omega); \textit{Proportional and integral control equation for closed loop motor} \quad (4.2)$$

$$V = k_p(\omega_d - \omega) + K_i I \quad (4.3)$$

$$\frac{di}{dt} = \frac{V}{L_c} - \frac{R_c}{L_c} i - \frac{C_e}{L_c} \omega \quad (4.4)$$

$$\frac{d\omega}{dt} = \frac{C_m}{J_M} i - \frac{B_M}{J_M} \omega - \frac{q_b P_f}{2\pi J_M} \quad (4.5)$$

$$P_f = P_1 - P_2 \quad (4.6)$$

When hydraulic fluid runs into the pump it is mentioned as Q_1 regardless of direction. q_b represents the fixed displacement of fluid from the pump while the rotation of the motor is shown by ω . The current produced by the operation of the electric motor is expressed with respect to time in differential expression as $\frac{di}{dt}$. Similarly, $\frac{d\omega}{dt}$ reflects the rotation of the electric motor. V is the input voltage for the electric motor which further commands the EHA system to respond. Resistance and inductance of the motor is shown as R_C and L_C respectively. C_e is denoted as back electromotive force while C_m is electromagnetism torque constant. The sum of the damping coefficient and the moment of inertia of the motor and pump is expressed as B_M and J_M respectively. P_f defines the load pressure on the motor shaft.

4.1.2 Orifices system

This experimental Electro Hydrostatic Actuation system is equipped with two orifices. Each orifice allows for free flow in one direction and variable controlled flow in the opposite direction. The flow from the orifice has a huge impact on the pressure drop at the location P_A, P_B . The area of a cross-section of the orifice is less than the area of the line which allows for the flow of hydraulic fluid. This orifice feature is modeled with the help of the equations presented below by retaining all non-linear behaviors of the orifice in the equations.

$$A_{line} = \frac{\pi}{4} (d_{line})^2 \quad (4.7)$$

$$A_{ori} = kA_{line}; k \text{ varies depending on the ratio of opening area for orifice} \quad (4.8)$$

$$Q_A = C_{dori} \sqrt{\frac{2}{\rho}} A_{line} \sqrt{(P_1 - P_A)} ; (P_1 > P_A) \quad (4.9)$$

$$Q_A = -C_{dori} \sqrt{\frac{2}{\rho}} A_{ori} \sqrt{(P_A - P_1)} ; (P_1 \leq P_A) \quad (4.10)$$

$$Q_B = C_{dori} \sqrt{\frac{2}{\rho}} A_{line} \sqrt{(P_B - P_2)} ; (P_B > P_2) \quad (4.11)$$

$$Q_B = -C_{dori} \sqrt{\frac{2}{\rho}} A_{ori} \sqrt{(P_2 - P_B)} ; (P_B \leq P_2) \quad (4.12)$$

In these equations of orifices, d_{line} is used to show diameter of the line from which fluid is flowing, and A_{line} expresses the area of the same line with A_{ori} as the area of the orifice. Q_a and Q_b denotes flow of fluid from the orifice in both directions of the test rig with C_{dori} expressing the drag coefficient of the orifice, and ρ is used to denote fluid density. P_1 and P_2 is for pressure at the inlet and outlet point of the pump while P_A and P_B express the pressure at both ends of the cylinder.

4.1.3 Hydraulic Cylinder

The Double-Acting Hydraulic Cylinder converts hydraulic energy into mechanical energy in the form of translational motion. The energy through hydraulic chambers (identified as A and B) helps in transforming hydraulic energy into mechanical energy while the chamber accounts for the fluid compressibility in the cylinder chamber. Hydraulic fluid pumped under pressure into one of the two cylinder chambers forces the piston to move and exert force on the cylinder rod. Double-acting cylinders transfer force and motion in both directions. Movement of the rod is limited by the mechanical translational hard stop block in such a way that the rod can travel only between cylinder caps.

Equations defining the displacement, velocity and acceleration of the rod along with the dynamic calculation of pressures at the inlet and outlet of the pump and both sides of the cylinders are well monitored with the help of state space equations. The pressure equations described below use the calculation of the flow Q_1, Q_A and Q_B which comes from the pump and both orifices respectively.

$$\frac{dx}{dt} = v \quad (4.13)$$

$$\frac{dv}{dt} = a \quad (4.14)$$

$$a = \frac{1}{M_{eq}} (P_A A_A - P_B A_B - F_f - F_l) \quad (4.15)$$

$$\frac{dP_1}{dt} = \frac{K_{oil}}{V_1} (Q_1 - Q_A) \quad (4.16)$$

$$\frac{dP_2}{dt} = \frac{K_{oil}}{V_2} (Q_B - Q_1) \quad (4.17)$$

$$\frac{dP_A}{dt} = \frac{K_{oil}}{V_A} (Q_A - A_A v) \quad (4.18)$$

$$\frac{dP_B}{dt} = \frac{K_{oil}}{V_B} (-Q_B + A_B v) \quad (4.19)$$

where, $\frac{dx}{dt}$, represents the velocity of the cylinder rod and x is the displacement of the rod with maximum displacement of 60 cm. $\frac{dv}{dt}$ stands for the acceleration of the rod which further includes the total mass of the system M_{eq} . The pressure calculations of both chambers (noted as P_A, P_B) are directly related to their areas A_A, A_B . The dynamic friction calculation is defined in the section below as F_f . The volume of the both sides of the cylinder are represented as V_1, V_2, V_A and V_B . The load at the actuator is shown as F_l , however it is kept as zero in this analysis.

4.1.4 Friction

The presence of friction is normal for points of contact in all mechanical systems, e.g., bearings, transmissions, hydraulic and pneumatic cylinders, valves, brakes, and wheels. da Vinci stated the two basic laws of friction, the first of which being that the area in contact has no effect on friction and the second stating that if the load of an object is doubled, its friction will also be doubled. The basic pattern of coulomb friction (static friction with stick-slip friction model) is shown in Fig. 4.2 reflects the Stribeck curve and friction regimes of stick-slip motion (He, 2010).

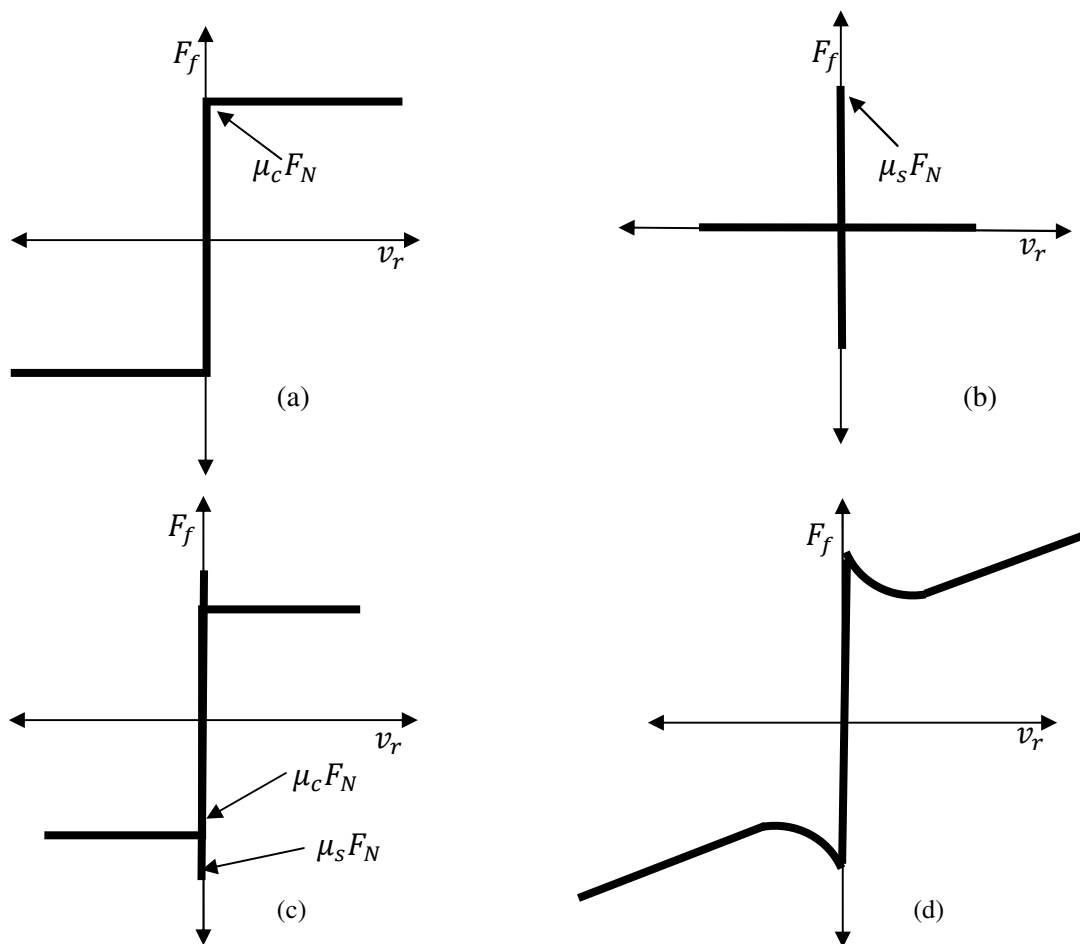


Fig. 4.2 a) Coulomb friction model, b) Static friction model, c) Stick-Slip friction model and d) Stribeck curve

This test rig is modeled with entirely dynamic frictional equations which have the characteristics of coulomb, viscous and stick-slip frictions. Friction force is modeled as a function of relative velocity and pressure and is assumed to be the sum of coulomb, viscous and Stribeck components. Coulomb friction force consists of the preload force caused by seal squeeze during assembly and is proportional to the pressure. The combination of Coulomb and Stribeck friction forces at zero velocity is often referred to as breakaway friction force.

$$F_C = F_{pr} + F_{cfr}(P_A - P_B) \quad (4.20)$$

$$F_f = F_C (1 + (K_{brk} - 1) (e^{-C_c |v|})) \text{sign}(v) + F_v v \quad ; \quad (|v| > v_{th}) \quad (4.21)$$

$$F_f = \frac{F_C(1 + (K_{brk} - 1) (e^{-C_c |v|}) + F_v v_{th}}{v_{th}} v \quad ; \quad (|v| \leq v_{th}) \quad (4.22)$$

The preload force F_{pr} is caused by seal squeeze during assembly. The Coulomb friction coefficient, F_{cfr} defines the proportionality between the Coulomb friction force and the pressure in cylinder chambers. The friction force F_f , which increases over the Coulomb friction F_C , when multiplied by the breakaway friction coefficient K_{brk} , which is referred to as breakaway friction force. Transition approximation coefficient C_c (obtained from MATLAB) is used for the approximation of the transition between breakaway and Coulomb frictions. The product of viscous friction coefficient F_v and v_r (the velocity of the piston), are added to Coulomb friction and Stribeck friction. To avoid discontinuity at ($v = 0$), a small region ($|v| \leq v_{th}$) where v_{th} is threshold velocity is introduced around zero velocity where friction force is assumed to be linearly proportional to velocity.

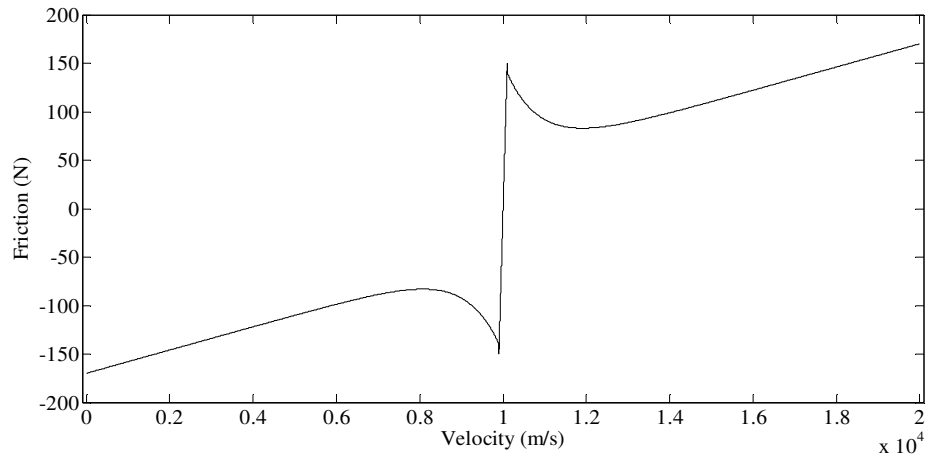


Fig. 4.3 Stribeck curve in friction vs. velocity.

Table 4.1: Specifications of EHA system obtained from real-world parameters, MATLAB, manufacturer of motor, pump and mechanical fittings respectively.

Parameter	Symbol	Value
Pre load force at piston	F_{pr}	25 N
Combined mass of piston and rod	M_{eq}	12.3 Kg
Viscous damping coefficient	F_v	300 Ns/m
Actuator stroke	L	0.6 m
Piston area	A_A, A_B	633 mm ²
Volume of fluid in either side of actuator	V	234 cm ³
Coulomb friction coefficient	F_{cfr}	1.0×10 ⁻⁶
Transition coefficient	C_c	10
Breakaway friction force increase coefficient	K_{brk}	3
Velocity threshold	v_{th}	0.01m/s
Displacement of the pump	q_b	4.9×10 ⁻⁶ m ³ /rev
Fluid bulk modulus	β	689 MPa
Resistance of motor	R_c	0.73 Ω
Inductance of motor	L_c	3.55×10 ⁻³ henry
Back electromotive force constant	C_e	0.6963 V/(rad/s)
Sum of moment of inertia of motor and pump	J_M	0.000874 Kg m ²
Electromagnetism torque constant	C_m	0.6963 Nm/A
Sum of damping coefficient of motor and pump	B_M	4.855×10 ⁻⁴ Nm/(rad/s)
Fluid Density	ρ	847 Kg/m ³
Drag coefficient of orifice	C_d	0.92
Diameter of line	d_{line}	7 mm

4.2 Simulation and Experimental results

The EHA system has gone through the simulation tests on the basis of the mathematical equations shown above. The experimental tests are performed on the sine wave input with different amplitudes and frequencies. The system is evaluated with and without the effect of orifice conditions. Furthermore, the experiments are dependant on the scale of closed orifices which are explained in the following sub-sections of this chapter.

4.2.1 System without orifice (Throttling valve)

In this scenario, the motor/pump is directly connected to the hydraulic actuator. The orifice is fully open and tested with three different inputs in sine wave with variable amplitude and frequency to ensure the consistent performance of the EHA. Table 4.2 explains about the tests conducted in the category of system without orifice.

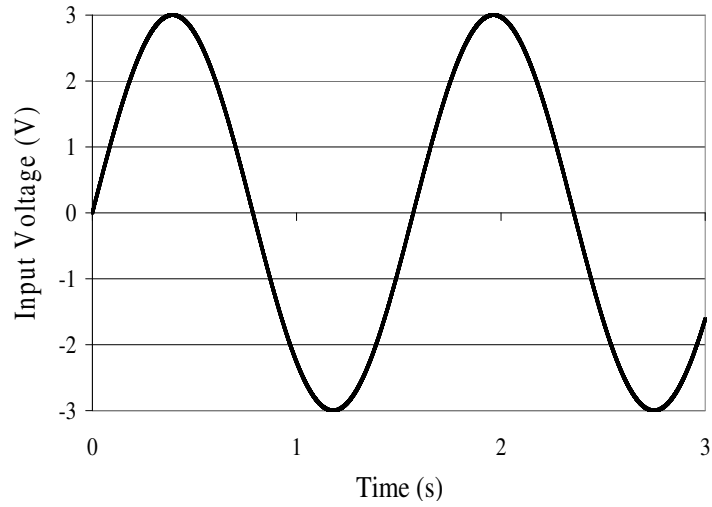
Table 4.2 Details of tests conducted without orifice effect

Test #	Input	Category
a)	$3\sin(4t)$	No orifice
b)	$5\sin(2t)$	No orifice
c)	$7\sin(4t)$	No orifice

a) In this case, the study is conducted by comparing experimental and simulation results, and the EHA is provided with a sine wave input of amplitude 3 volts and frequency 4 rad/s. The servo

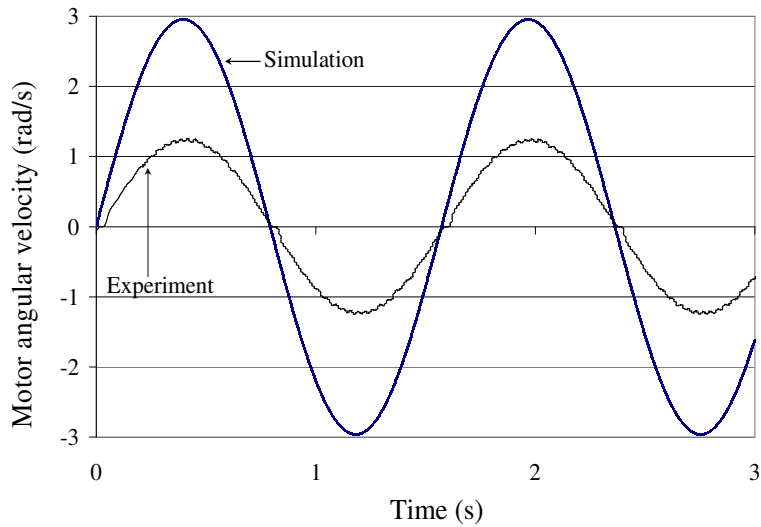
drive connected to the experimental test rig is equipped with built-in control systems and, further, in all the experiments the motor is working under closed loop conditions with a proportional gain of 50,000 and integral gain of 100 to close the loop around the motor. Similarly the loop is closed around the mathematical equations of motor as shown in section 4.1.1.

As shown in Fig. 4.4(a), input voltage as $3\sin(4t)$ given to the experimental test rig helps in obtaining the angular velocity of the motor (as shown in Fig. 4.4 (b)) in which simulation and experimental results follow the exact same pattern of sine wave output. The results perfectly track each other qualitatively, however lag in quantity. The lag in the experimental angular velocity when compared to the simulation results is due to the relative complexity of the experimental setup over the simplified modeled system which is due to the internal control system available in servo drive. Similarly, Fig. 4.4(c) adequately reflects displacement of the piston on the basis of qualitative tracking. However, the experimental result has almost 30% error to follow the simulated result due to environmental factors such as friction which is not possible to model exactly and due to smaller value of amplitude. Also, the displacement of the piston is obtained in an open loop, so the error can easily be removed by the use of a controller. The pressure signals are monitored and simulated at both ends of the cylinder which is shown in Figs. 4.5(a) and (b) respectively. The pressure signals also have good quality of tracking towards each other, but when the sine wave changes its direction from negative to positive, some noise at the peaks can be observed due to noise in the sensors and lack of a closed loop controller.



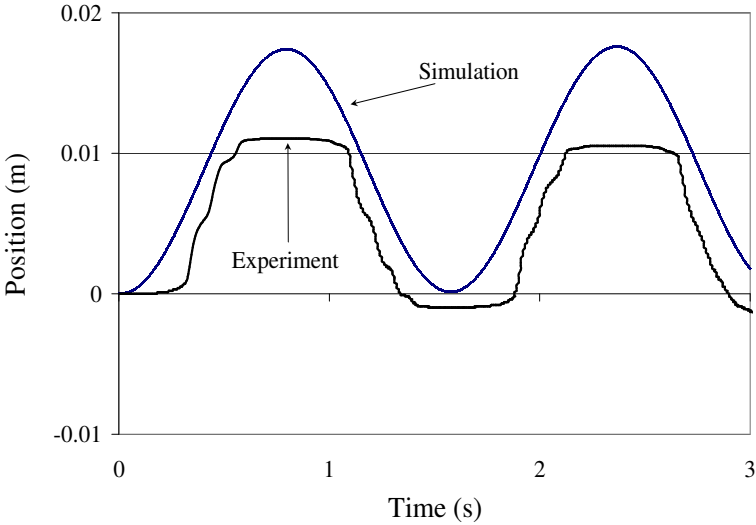
(a)

The performance of the system (shown in Figs. 4.4 and 4.5) is under the control of an open loop system around the displacement of piston and closed loop around the motor. The motor/pump is directly connected to the cylinder with the hydraulic fluid flowing into the lines depending upon speed of the motor and the fixed displacement of the pump.



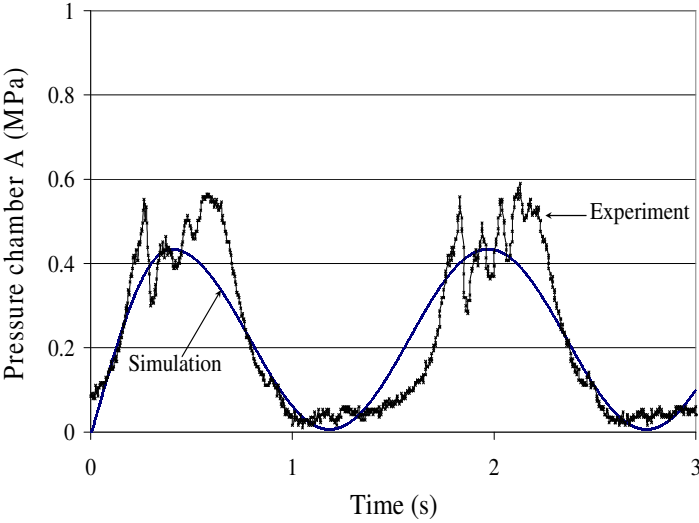
(b)

The lag in the experimental and simulation plots in Fig. 4.4 (c) is due to the smaller value of amplitude. The drift in experimental displacement of the piston is due to the effect of friction.

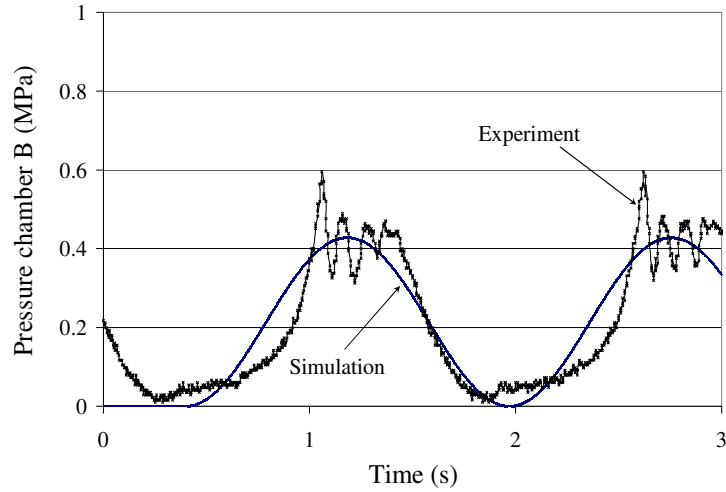


(c)

Fig. 4.4 (a) Input voltage as $3\sin(4t)$, (b) angular velocity of motor and (c) displacement of piston obtained without orifice.



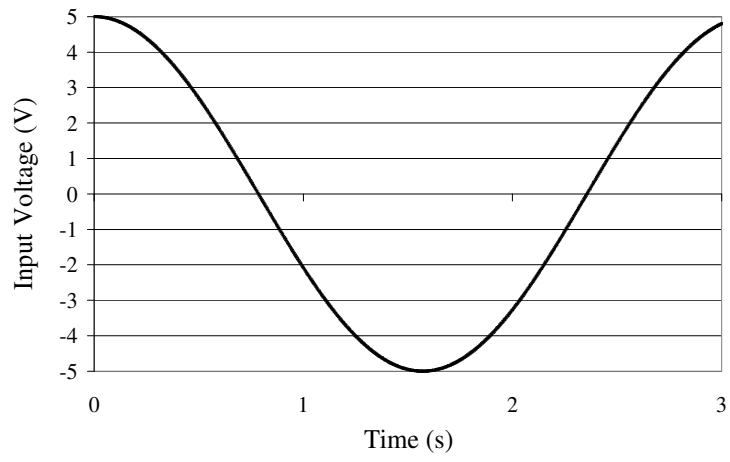
(a)



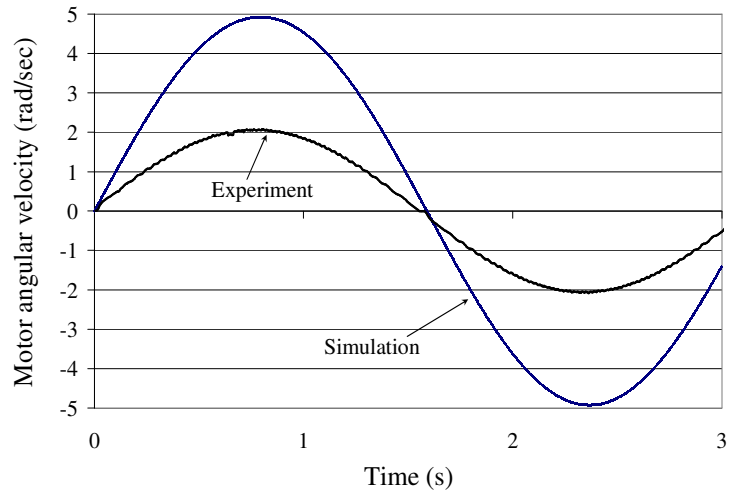
(b)

Fig. 4.5 Pressures in chambers A (a), and B (b) of cylinder.

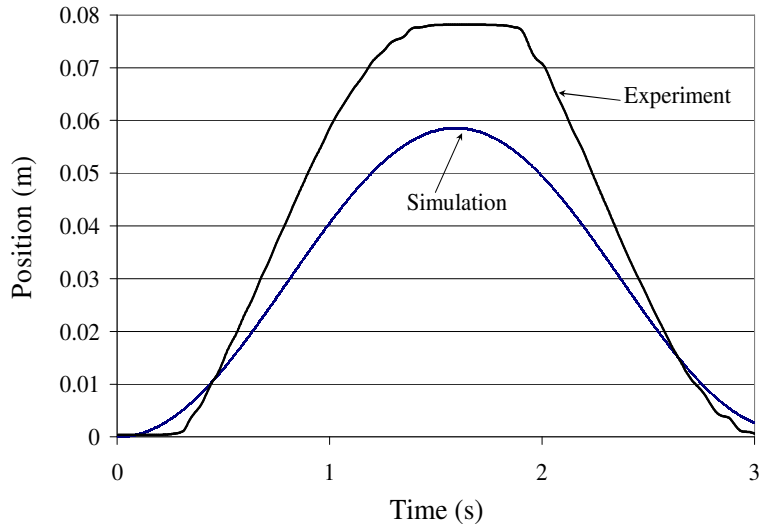
b) In this case, input voltage in terms of sine wave with amplitude of 5 volts and frequency of 2 rad/s to the test rig is shown in Fig. 4.6(a). Figure 4.6 (b) shows how the simulation and experimental angular velocity of motor results follow each other qualitatively. Figure 4.6(c) shows the displacement of the piston in which the experimental position is followed by the simulated position qualitatively, although there is almost 20% quantitative difference in the peaks of both results.



(a)



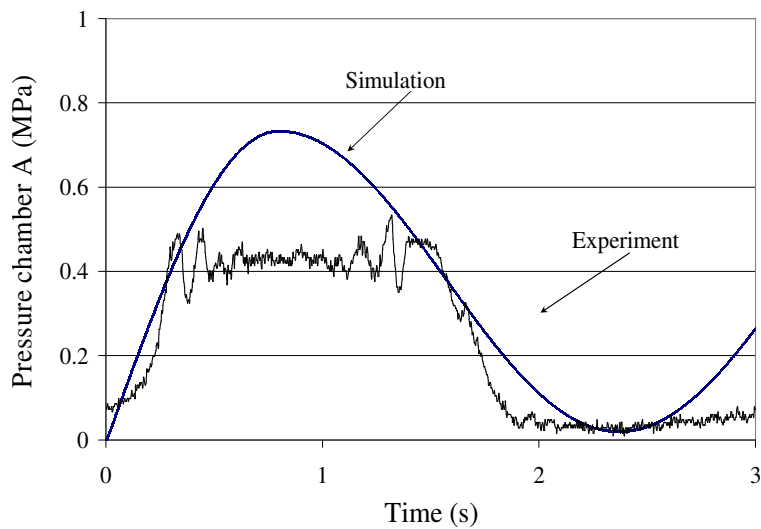
(b)



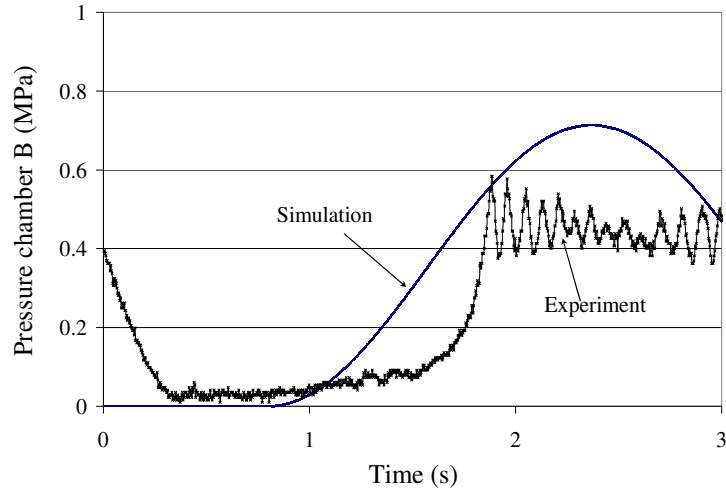
(c)

Fig. 4.6 Simulated and experimental input voltage (a) as $5\sin(2t)$, (b) angular velocity of motor and (c) displacement of piston without orifice conditions.

The pressure signals at both ends of the cylinder are shown in Figs. 4.7 (a) and (b) in which experimental results are followed by the simulated output of pressure. In this case, the system operates in the open loop condition which generates noise at the peaks of sine wave input.



(a)



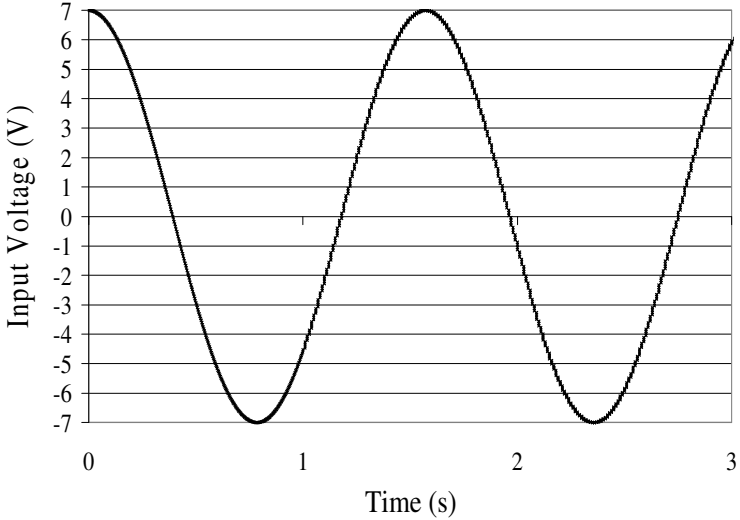
(b)

Fig. 4.7 Pressures in chamber A (a), and B (b) of cylinder.

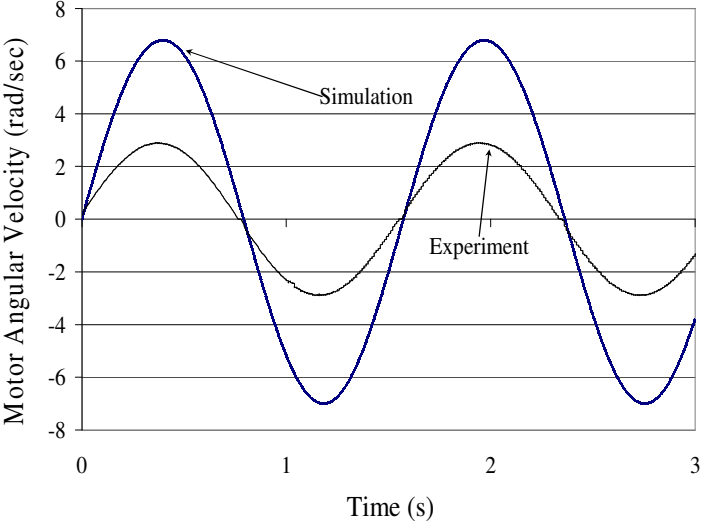
c) This experiment is intended to justify the simplest model of the system acting in an open loop condition with the combination of the motor and pump directly in contact with the cylinder. The test is conducted with a sine wave of 7 volts amplitude and a 4 rad/s frequency. The results of the experimental and simulated angular velocity of the motor with the same control gains in the SSt-6000-RCX servo drive connected to the variable rotation motor and the proportional gain of 1.2 and integral gain of 0.1 in the software simulation are qualitatively identical.

The input voltage and the angular velocity of the motor are shown in Figs. 4.8 (a) and (b). The displacement of the piston in Fig. 4.8 (c), which is attained from experimental and simulated data, is tracked in terms of the pattern followed by the signals although it certainly has around 15% difference with respect to the base line of the axis in the signal from experiment and simulation.

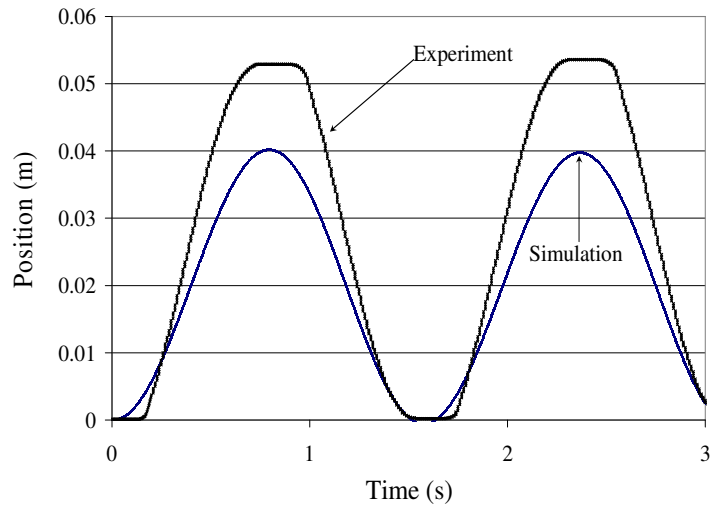
Similarly, the difference in the pressure signal shown in Figs. 4.9 (a) and (b), as per the experimental and simulated data, is significant in terms of the peaks of the sine wave, whereas the behaviour and the outline of the signal are exactly similar to each other.



(a)

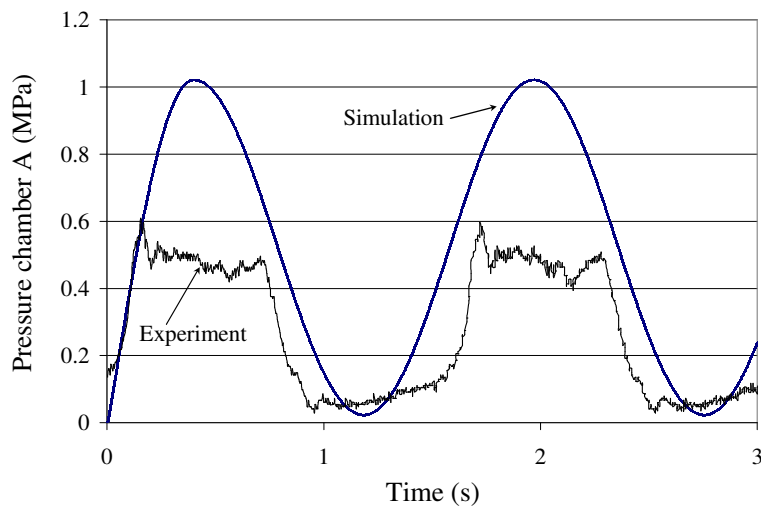


(b)

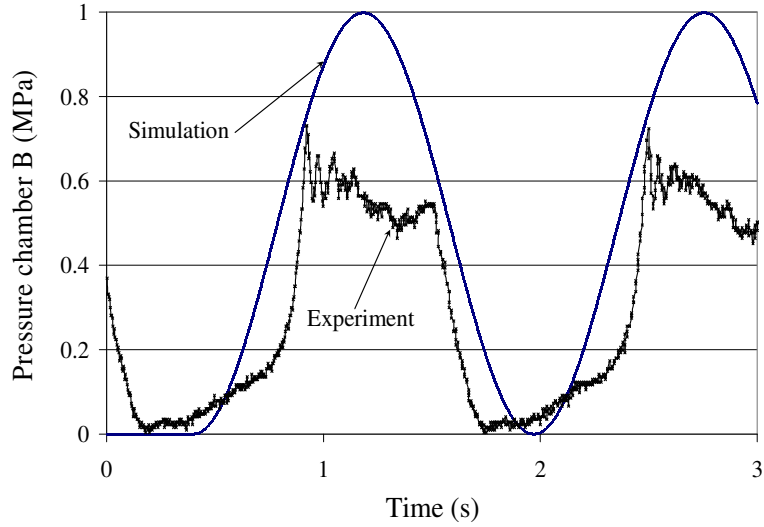


(c)

Fig. 4.8 Simulated and experimental input voltage given as $7\sin(4t)$ in (a), (b) angular velocity of motor and (c) displacement of piston without orifice conditions.



(a)



(b)

Fig. 4.9 Pressures in chamber A (a), and B (b) of cylinder.

4.2.2 System with orifice (Throttling valve)

Now that analysis of three different inputs for a simplified case of an Electro Hydrostatic test rig system has been conducted, tests are performed on the next level. The inclusion of the orifice in the experimental test rig generates the throttling effect in the system. In order to observe the behaviour of the orifice, the software simulation is also modeled with equations related to the orifice so that the effect on the results of the experimental and simulated data can be seen clearly.

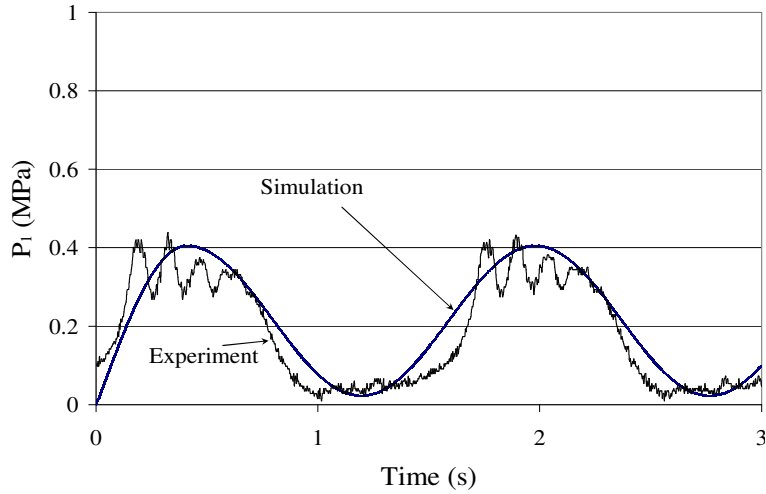
The effect of the orifice is monitored by 3 different categories under the different input conditions as mentioned in Table 4.3.

Table 4.3 Details of tests conducted with variable orifice effect

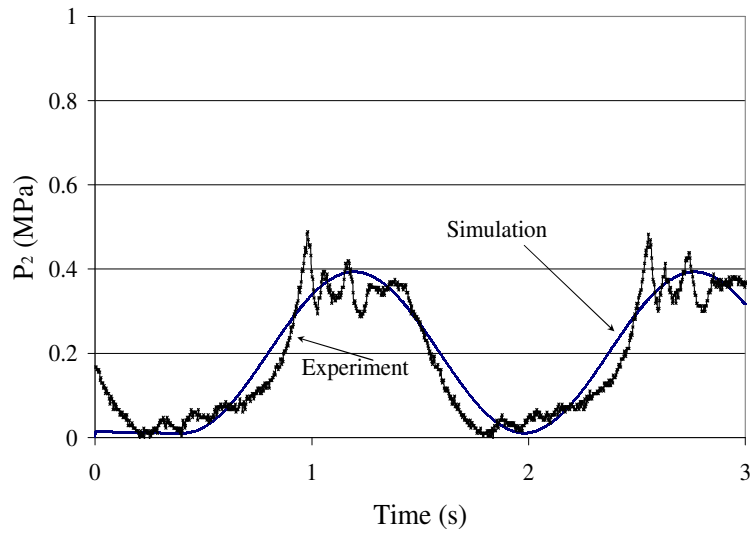
Test #	Input	Category
a)	$3\sin(4t)$	25% closed orifice
b)	$5\sin(2t)$	25% closed orifice
c)	$7\sin(4t)$	25% closed orifice
d)	$3\sin(4t)$	50% closed orifice
e)	$5\sin(2t)$	50% closed orifice
f)	$7\sin(4t)$	50% closed orifice
g)	$3\sin(4t)$	75% closed orifice
h)	$5\sin(2t)$	75% closed orifice
i)	$7\sin(4t)$	75% closed orifice

a) This case is tested under the sine wave input of amplitude 3 volts with 4 rad/s frequency with 25% closed orifice which creates a throttling effect in the flow of hydraulic oil. The diameter of the orifice measures roughly 3.75 mm out of 5 mm (i.e. diameter of the line) and works under same open loop around the displacement of the piston and closed loop around the motor with identical gains as has been explained in the no orifice case described above.

Due to the involvement of the orifice in the test rig, there are four pressure sensors to be monitored in all the cases. Two of these pressure sensors are analyzed at the inlet/outlet of the pump, and the other two pressure sensors are installed at both ends of the cylinder. As per the graphs shown in Figs. 4.10 (a) and (b), pressure at the inlet/outlet of the pump goes up to the level of 0.4 MPa and follows the path of the simulated results for the same pressure locations. The noise at the peaks of the sine wave patterns in the experimental results is due to the lack of a closed loop controller.



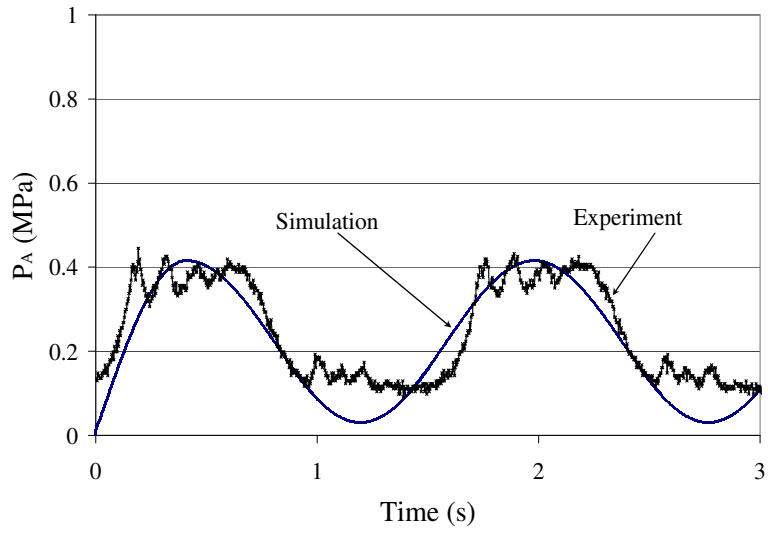
(a)



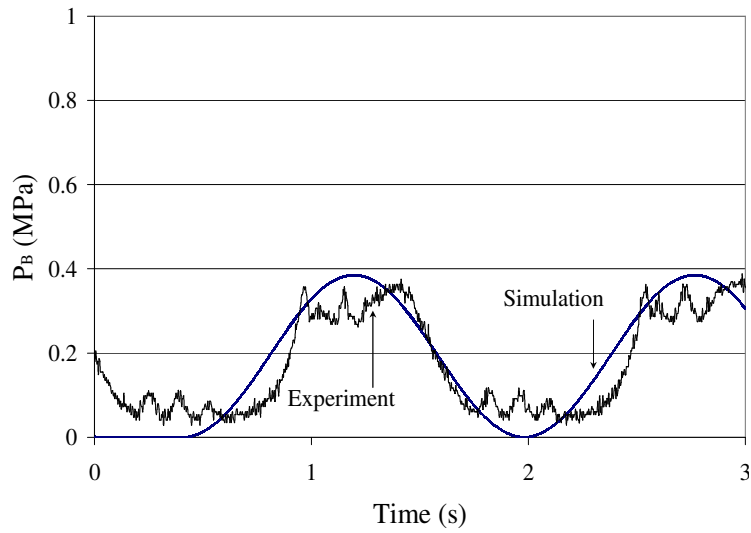
(b)

Fig. 4.10 Pressures at inlet/outlet A (a) and B (b) of pump.

Similarly, Figs. 4.11 (a) and (b) show that the experimental and simulated results follow each other, reaching a maximum of 0.4 MPa with noise at the peaks that is easily detected by the sensors. Given this, the conclusion says that the presence of an orifice with a small closing does not create any difference in the pressure signals obtained at the pump and cylinder ends.



(a)



(b)

Fig. 4.11 Pressures in chamber A (a), and B (b) of cylinder.

The effect of flow (Q_A and Q_B) through orifices (in this case 25% closed) allows for one-way free flow on one side and controlled flow on the other as is shown in Fig. 4.12. The behaviour of flow on both sides is similar.

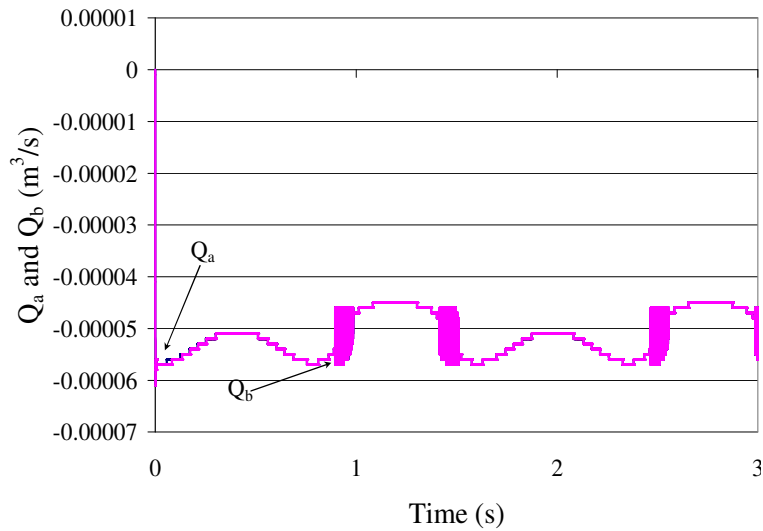


Fig. 4.12 Flow through orifices (Q_A and Q_B).

In Figs. 4.13 and 4.14, the effect in mathematical modeling of 25% closed orifices can be seen in terms of the differences in the level of peaks of P_1 , P_A and P_2 , P_B . The change in the area of the orifice in relation to the area of the line creates a significant impact in the peaks of all pressure signals. The pressure at location P_1 is less than location P_A because of the presence of the orifice and, inversely, location P_2 is greater than location P_B .

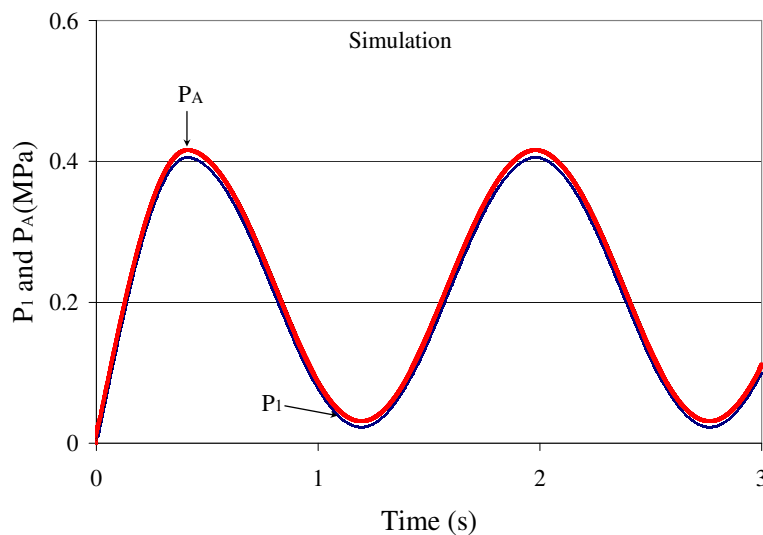


Fig. 4.13 Effect on simulated pressures P_1 and P_A due to 25% closed orifices.

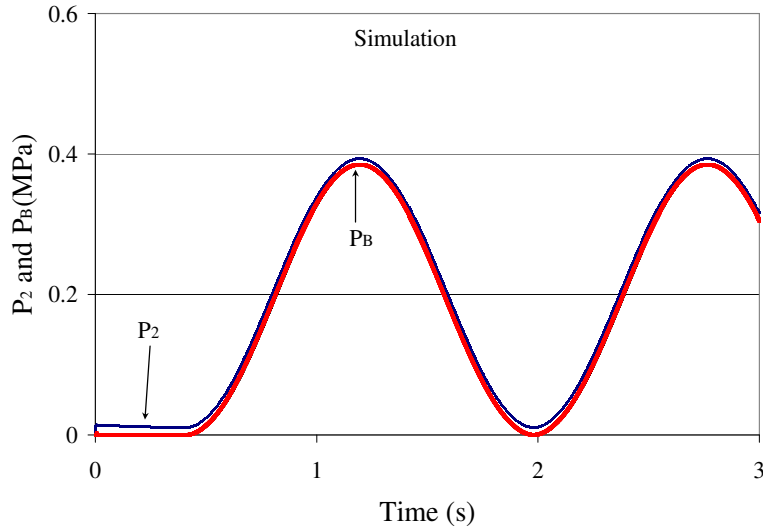


Fig. 4.14 Effect on simulated pressures P_2 and P_B due to 25% closed orifices.

The effect of 25% closed orifices on the test rig can be seen in terms of difference in the level of peaks of P_1 , P_A and P_2 , P_B in Figs. 4.15 and 4.16. P_1 , P_2 , P_A and P_B are located at the inlet/outlet of the pump and the two chambers of the cylinder according to Fig. 4.1. The comparison between P_1 and P_A is conducted due to one side of the system having a common orifice in between which allows flow Q_a to effect the range of pressures of P_1 and P_A . Similarly, P_2 and P_B are compared on the basis of a common orifice that allows flow Q_B to affect the pressures.

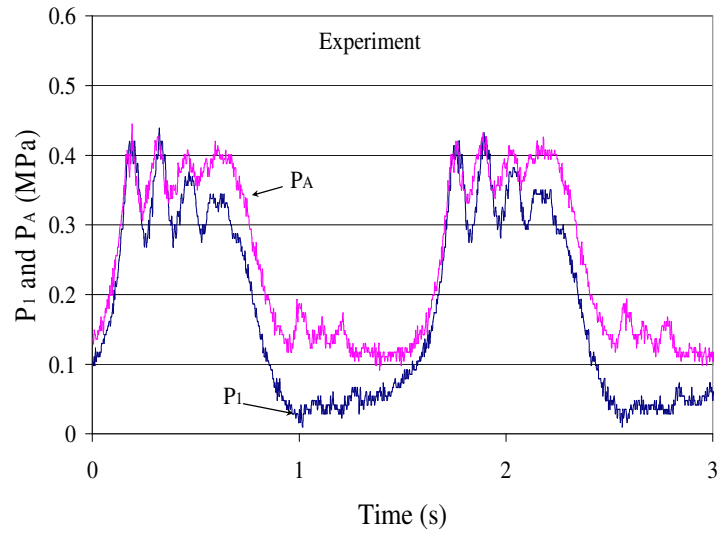


Fig. 4.15 Effect on experimental pressures P_1 and P_A due to 25% closed orifices.

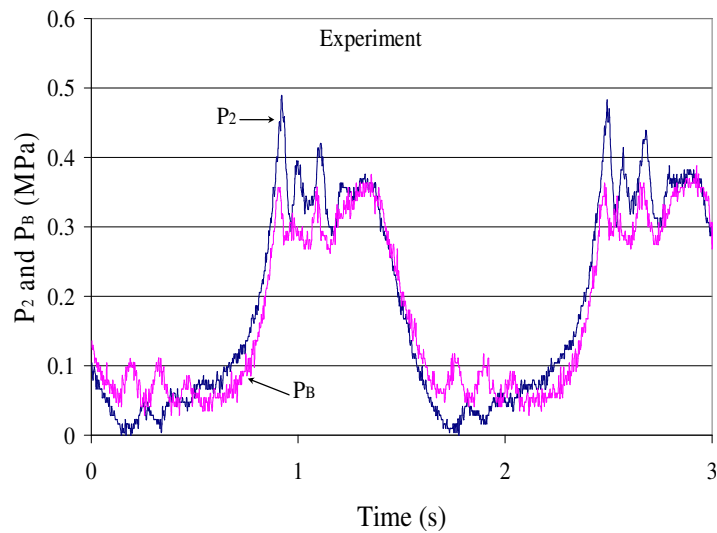
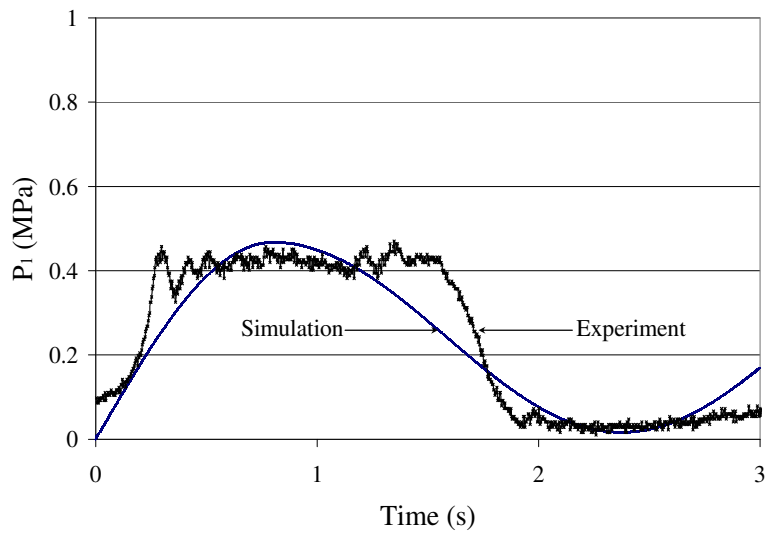


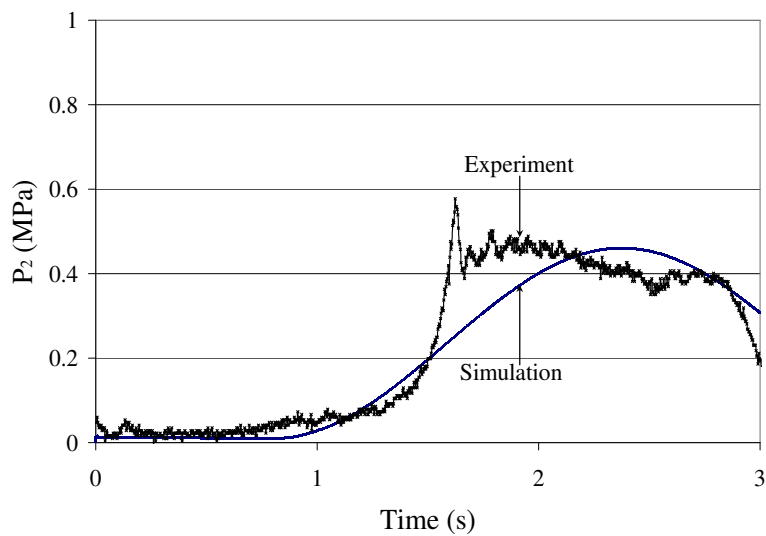
Fig. 4.16 Effect on experimental pressures P_2 and P_B due to 25% closed orifices.

b) The second experiment using an orifice that is 75% open and 25% closed uses an amplitude of 5 volts and a 2 rad/s frequency in the form of sine wave input. The performance of the system mainly depends on the pressure generated at all the points under observation, though the target is to match the pressures at the pump location and at cylinder site, which becomes the key reason

for the difference between experimental and simulation input results. The primary objective in the following experiments is to match with the pressure signal and its range. Figures 4.17 (a) and (b) represent the pressure points at the inlet/outlet of the pump and, as can be seen, the experimental and simulation results track the pattern of the signal and range of the peaks quite well.



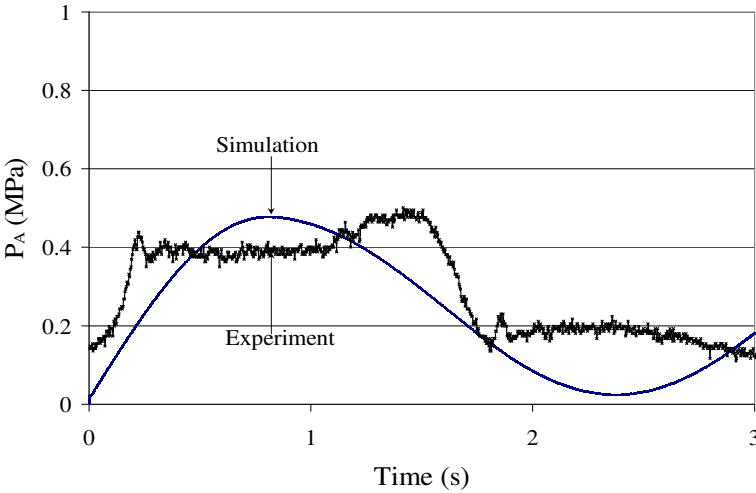
(a)



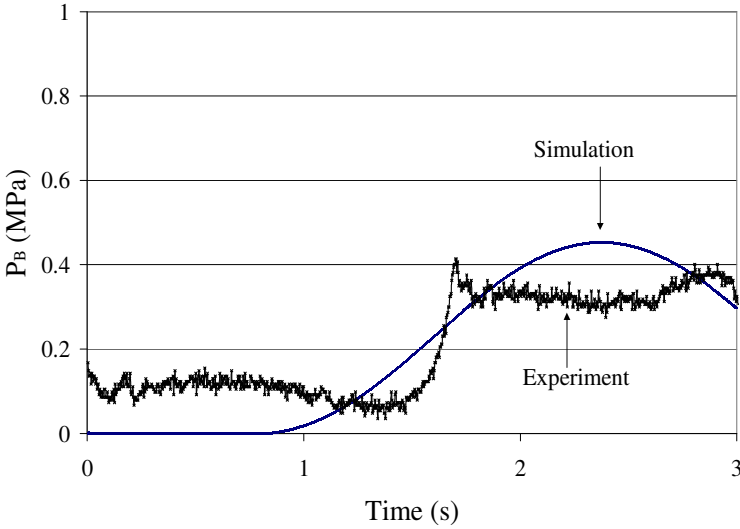
(b)

Fig. 4.17 Pressures at inlet/outlet A (a) and B (b) of pump.

Figures 4.18 (a) and (b) clearly show the effect of the orifice on the pressure results of the simulation and experimental test rig at both cylinder ends. The experimental data tracks the path of the simulation result fairly well whereas the throttling effect creates the back pressure effect of the higher & lower peaks affecting quantitative tracking of data.



(a)



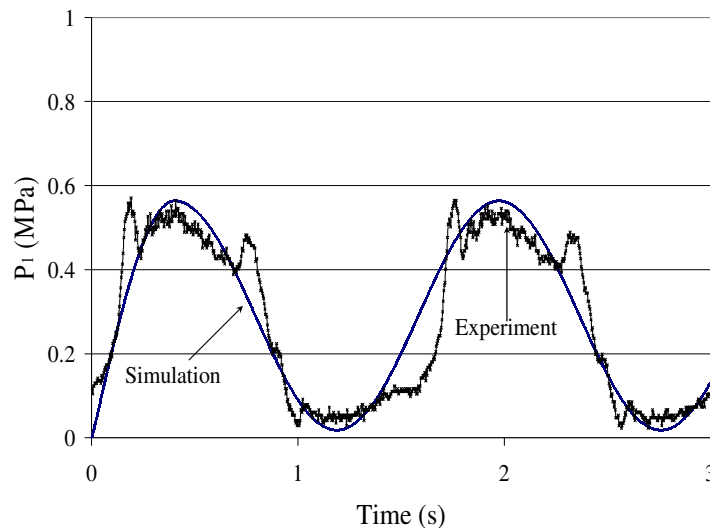
(b)

Fig.4.18 Pressures in chamber A (a), and B (b) of cylinder.

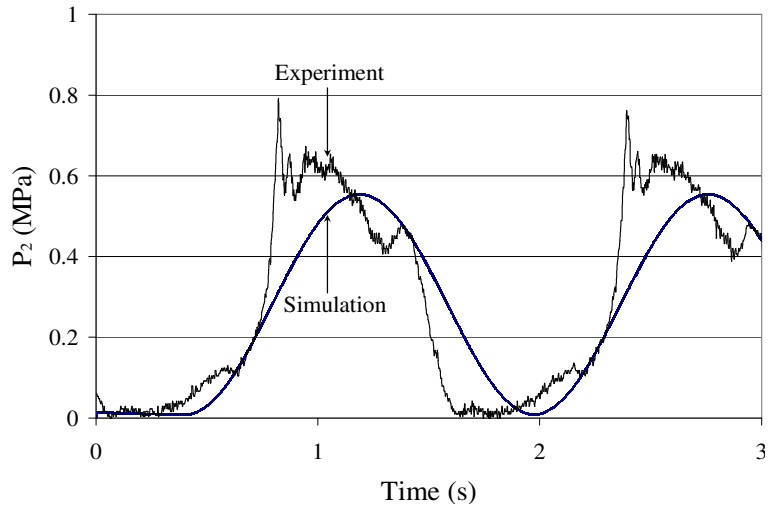
c) This test is the last experiment in the category of 25% closed orifice with an amplitude of 7 volts and a 4 rad/s frequency in sine wave input to the software simulation and experimental test rig. The pressure at the inlet/outlet of the pump graphs in Figs. 4.19 (a) and (b) nicely tracks the pattern of the sine wave and the exact range of the peaks. However, there is noise at the peaks of the signal which is due to the open loop system and the lack of a controller.

Figures 4.20 (a) and (b) represent the pressure at the cylinder ends with the presence of a 25% closed orifice installed in the pathway from the pump to the cylinder. The graphs show the qualitative tracking of the signal but are not able to match the exact range of the peaks because of the throttling and back pressure acting on the cylinder side which is the major reason for the humps at the peaks with noise in the experimental signals.

The simulation data in Figs. 4.19 and 4.20 gives the ideal required pressure output at pump and cylinder site respectively.

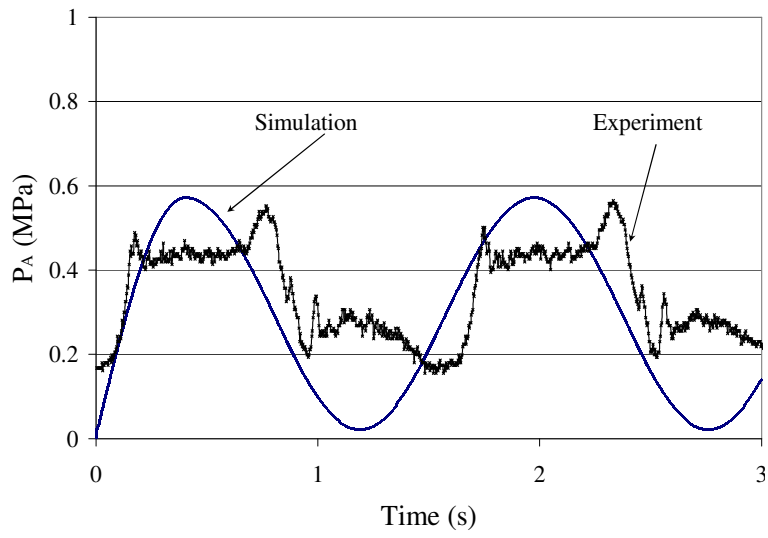


(a)

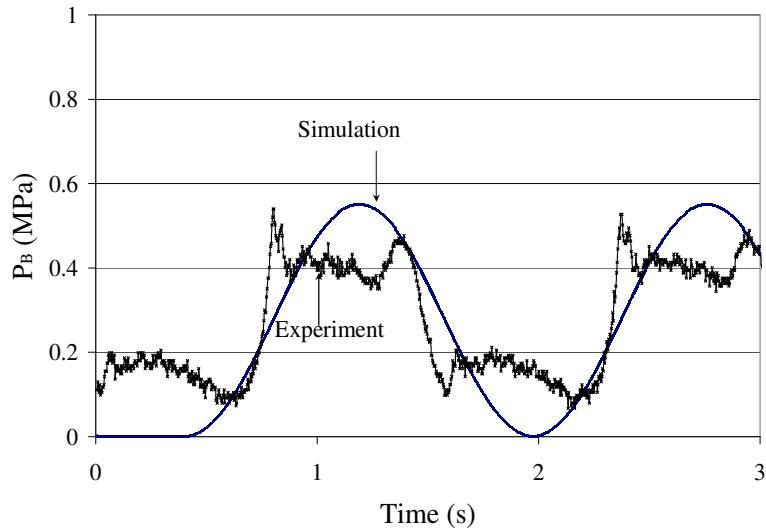


(b)

Fig. 4.19 Pressures at inlet/outlet A (a) and B (b) of pump



(a)



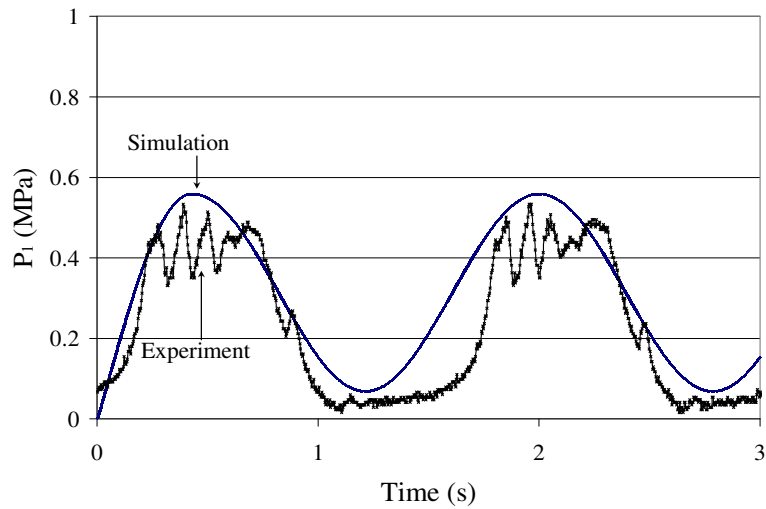
(b)

Fig. 4.20 Pressure in chamber A (a), and B (b) of cylinder.

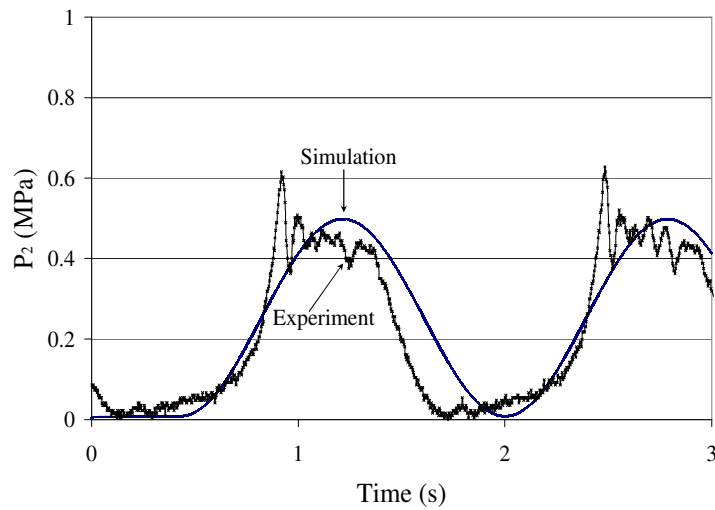
As 25% closed orifice is examined in the examples above, further, the following cases belongs to 50% closed orifice which results in making the rest 50% as open orifice.

d) This experiment is conducted repeating the input and conditions of the previous tests with only a change in the area of the orifices placed in between the pump and the cylinder. The area of the orifices is reduced to 50% with the help of controllable valve. The input in this experiment is 3 volts amplitude and a 4 rad/s frequency on a sine wave with a closed loop around the motor.

The difference between the experimental and simulated pressure is the lack of an appropriate controller. The objective in these tests is to attain qualitative tracking that is close to the environmental setup in an open loop system.



(a)

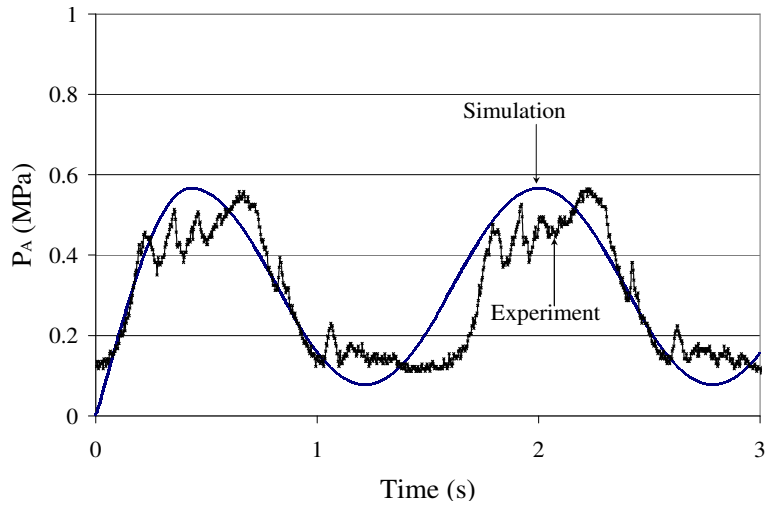


(b)

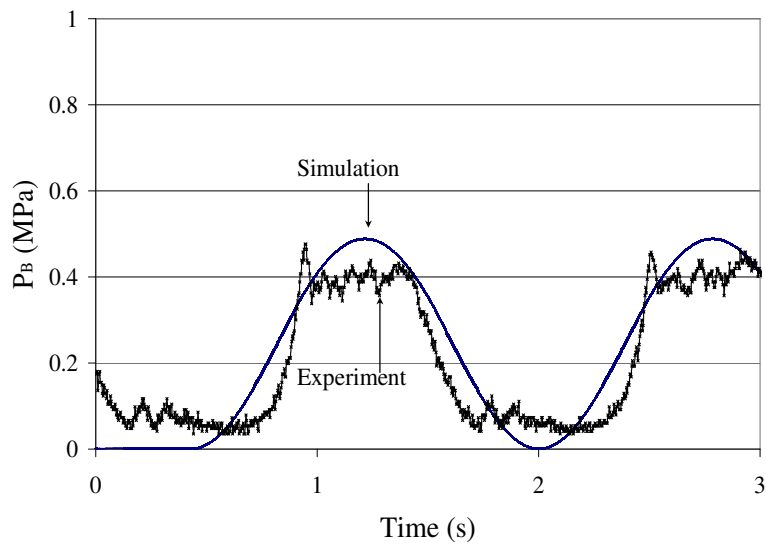
Fig. 4.21 Pressure at inlet/outlet A (a) and B (b) of pump.

The pressure signals in Figs. 4.21 (a) and (b) explain the simulation and experimental results at pump with good tracking and satisfactory capability to match up with range of the peaks in the noise-avoidable condition.

Similarly, Fig. 4.22 represents the pressure at chambers A and B of the cylinder with good tracking and nice matching of the range of the peaks of pressure.



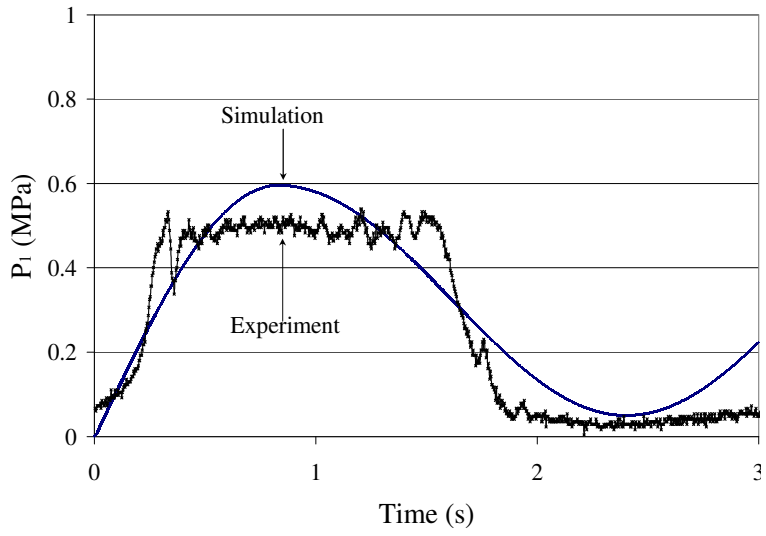
(a)



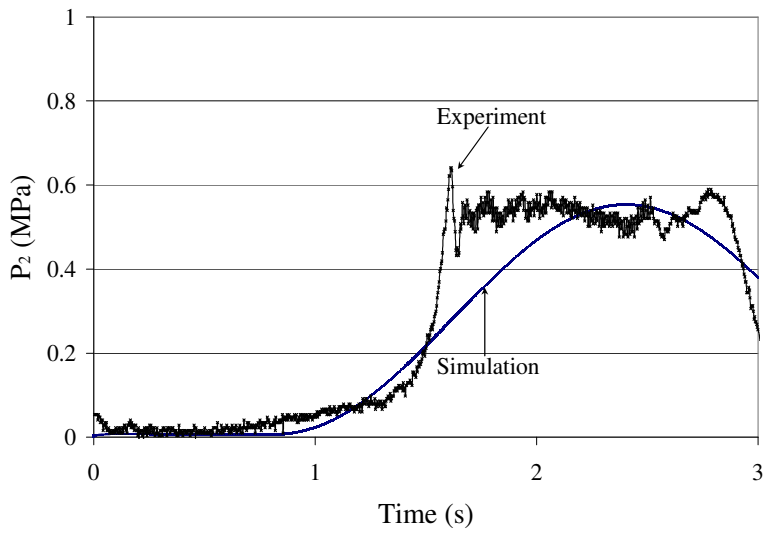
(b)

Fig. 4.22 Pressures in chamber A (a), and B (b) of cylinder.

e) The second experiment with a half closed orifice area will use an input of 5 volts amplitude and a 2 rad/s frequency given to a sine wave. The pressure results at the inlet/outlet of the pump shown in Figs. 4.23 (a) and (b) show the tracking of the simulation and experimental patterns with an error of range of approximately 5% at the peaks.

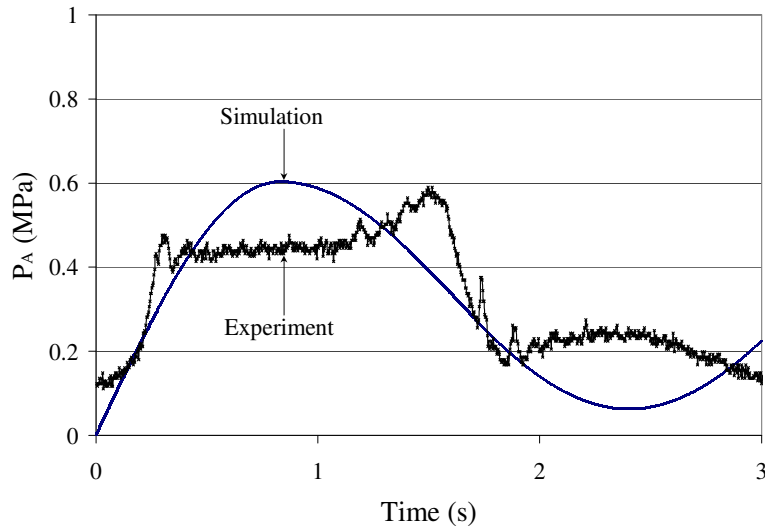


(a)

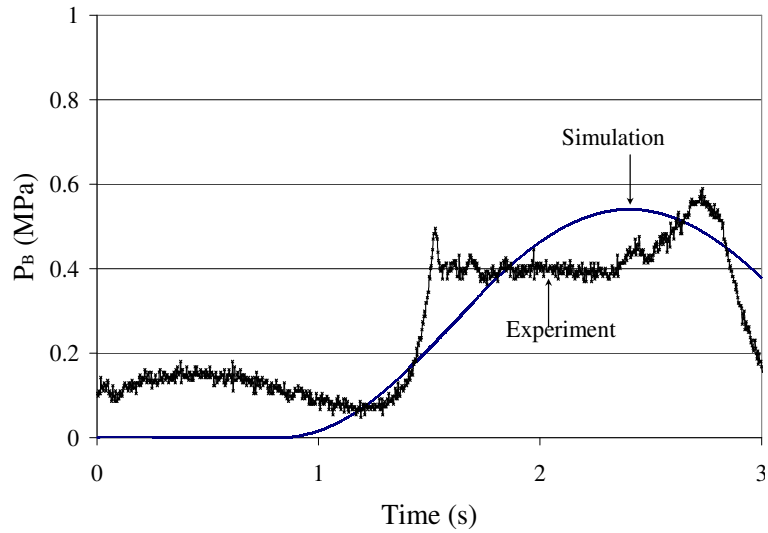


(b)

Fig. 4.23 Pressure at inlet/outlet A (a) and B (b) of pump.



(a)

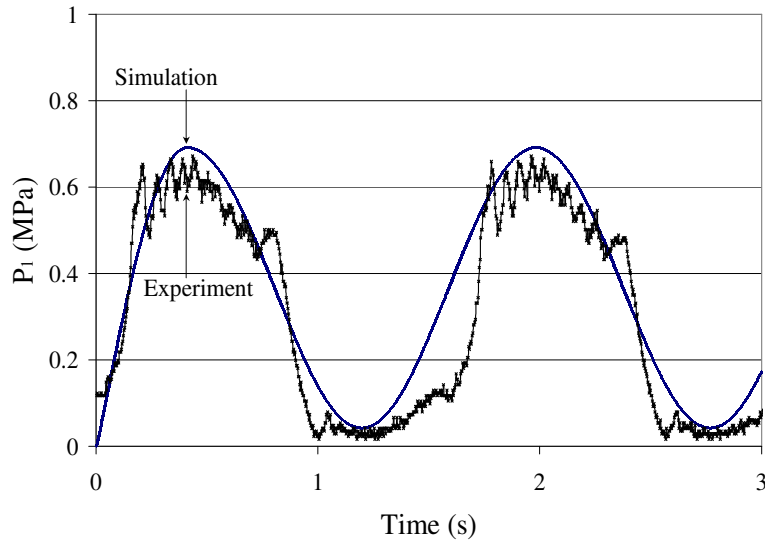


(b)

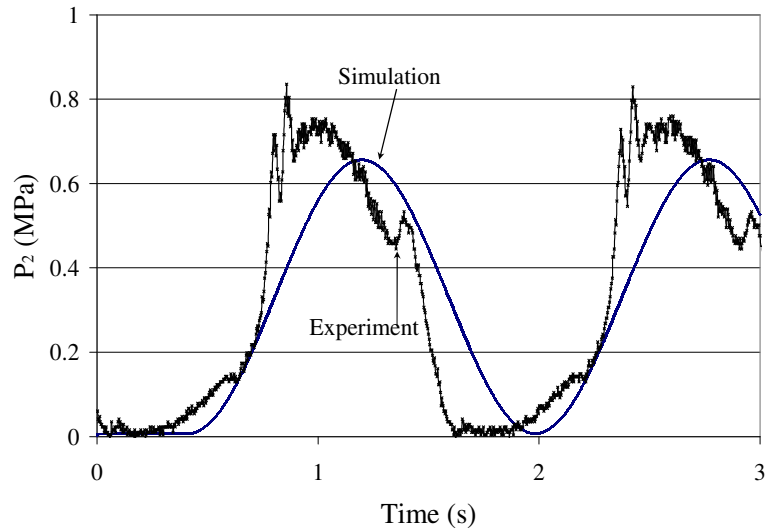
Fig. 4.24 Pressures in chamber A (a) and B (b) of cylinder.

Fig. 4.24 (a) and (b) represent the pressure measurements at both ends of the cylinder. The pressure demonstrate consistent trajectory, but they fail to match the amplitude of the peaks witnessed in the simulation. This effect is caused by the tightening of the orifice which in turn causes increased back pressure in the signals.

f) The third test in the category of 50% reduced orifice area will be done to analyze the last input with 7 volts amplitude and a 4 rad/s frequency in sine wave input in both the experimental and software based simulation of the Electro Hydrostatic Actuation system.



(a)

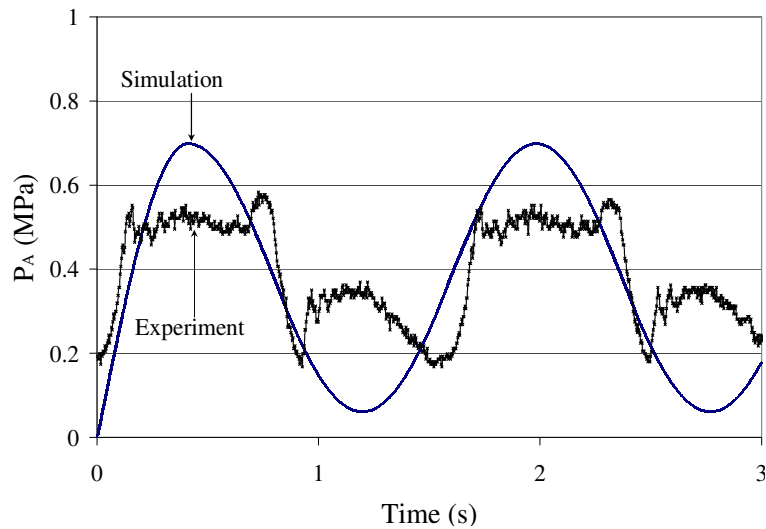


(b)

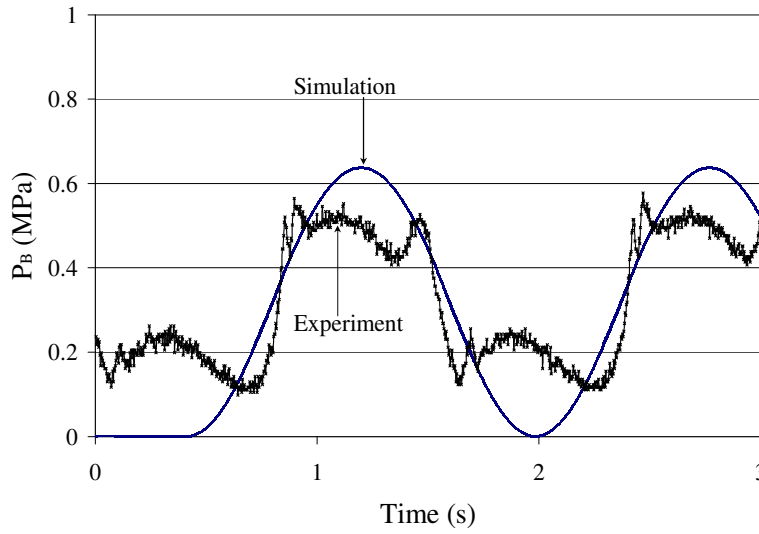
Fig. 4.25 Pressures at inlet/outlet A (a) and B (b) of pump.

The range of the pressure signals increases with the increase of the amplitude in the input which can readily be seen in Figs. 4.25 and 4.26 at the pump and cylinder respectively. The increase in the height of the peak due to back pressure acting on the cylinder from the presence of a tighter orifice can be seen in Fig. 4.26. It has very good tracking of the path followed with a suitable match in the range although there is some delay in the tracking of the path of the pressure signal.

As mentioned above, Figs. 4.26 (a) and (b) present the pressure signal output from both cylinder chambers. The increase in the size of the small humps in the experimental data proves the behaviour of the orifice at higher amplitude which results in the prominent effect of back pressure and a reduced capability to match with the range of the achievable pressure as shown by the simulation results.



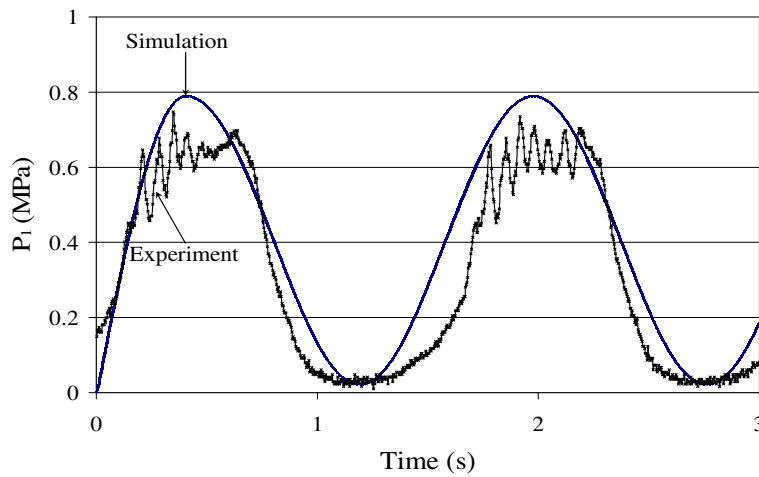
(a)



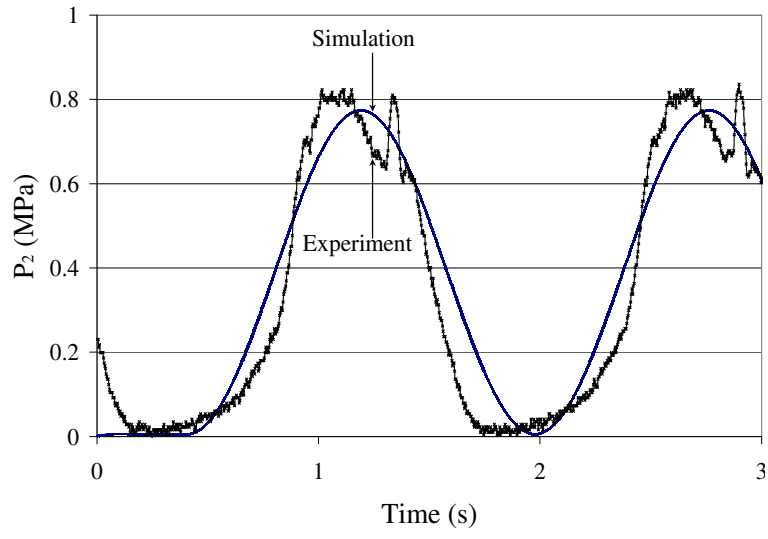
(b)

Fig. 4.26 Pressure in chamber A (a), and B (b) of cylinder.

g) The final category of experimentation uses orifices closed to 75% of their area which allows only 25% area for flow of the fluid. This experiment has 3 volts of amplitude with a 4 rad/s of frequency as input. The pressure signals at the inlet/outlet of the pump are analyzed in Figs. 4.27 (a) and (b) which proves that the experimental test rig's data has good path tracking and adequate ability to match up with the range of the simulation results.



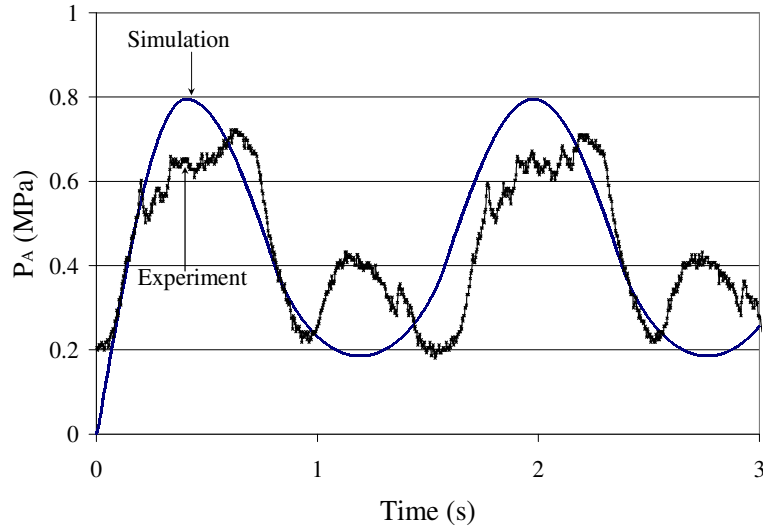
(a)



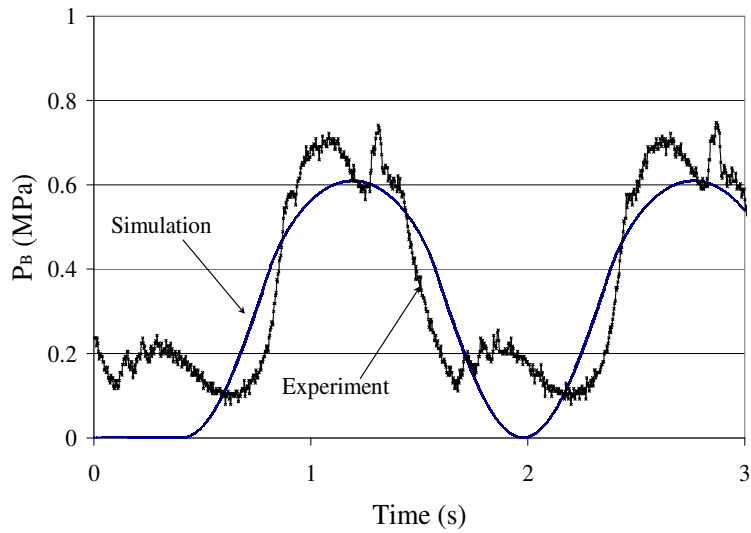
(b)

Fig. 4.27 Pressure at inlet/outlet A (a) and B (b) of pump.

Figures 4.28 (a) and (b) represent the pressure output from both chambers of the cylinder respectively. The reason for the error in path tracking and smaller peaks is because of the reduced area of the orifice which results in the increase of back pressure and more throttling effect.



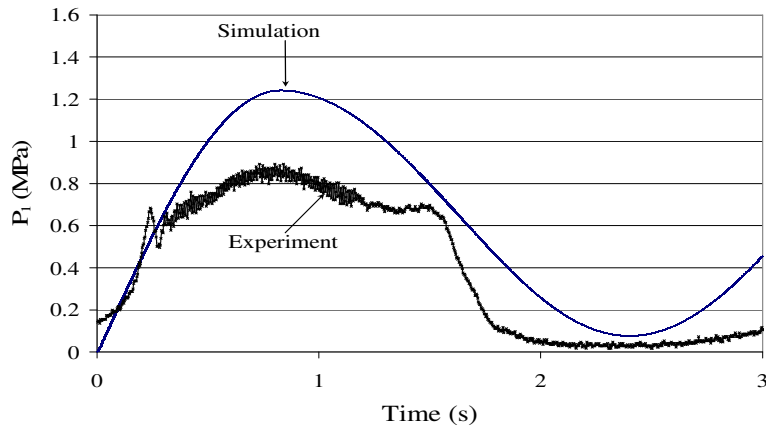
(a)



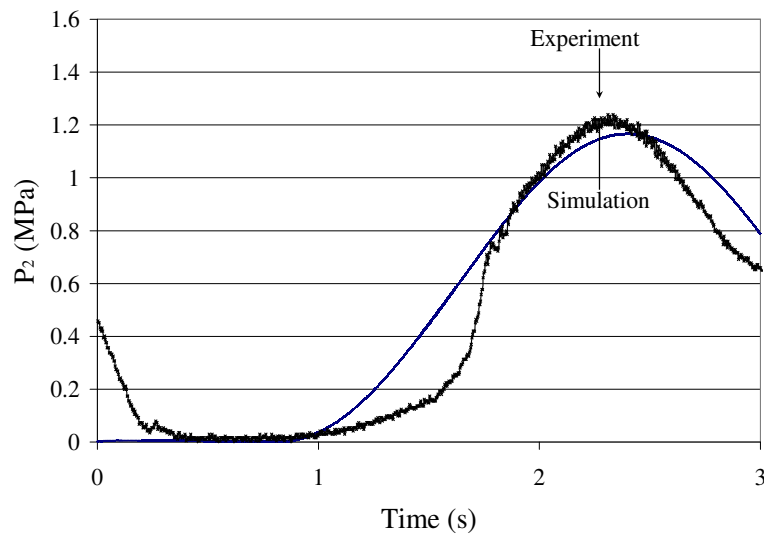
(b)

Fig. 4.28 Pressure in chamber A (a), and B (b) of cylinder.

h) The second experiment with an orifice opened to 25% of its area is performed with an input of 5 volts and a 2 rad/s input in a sine wave. Figure 4.29 (a) shows a poor ability to match with the range of the pressure with good tracking of the pattern while Fig. 4.29 (b) is capable of good path traceability within the same range of experimental and simulation results.



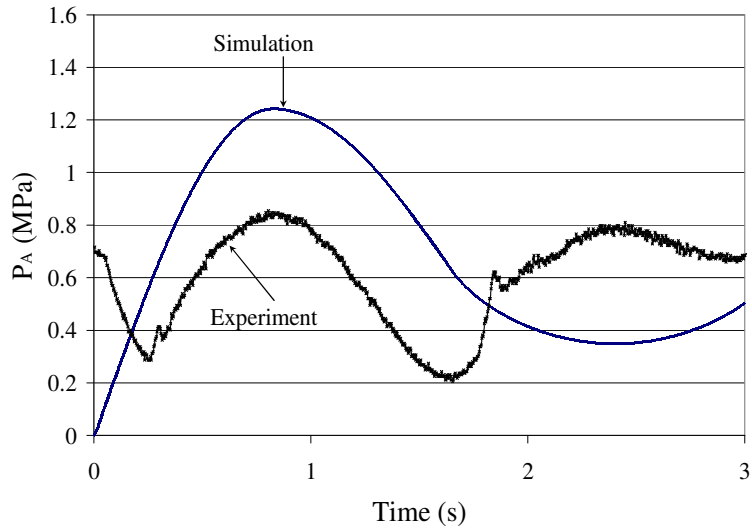
(a)



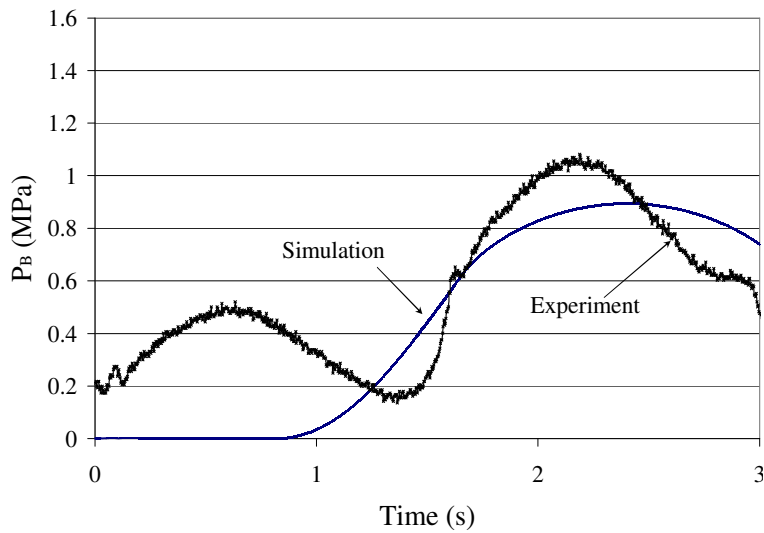
(b)

Fig. 4.29 Pressure at inlet/outlet A (a) and B (b) of pump.

Figures 4.30 (a) and (b) reflect the pressure generated in both chambers of the cylinder. They are both able to show the qualitative response, however the difference in the range of the signals and the increasing size of the humps is strong evidence of back pressure and throttling behaviour that originates due to the presence of the orifices and the lack of a control system to remove noise from the signal, which also serves to reduce the difference in the range.



(a)

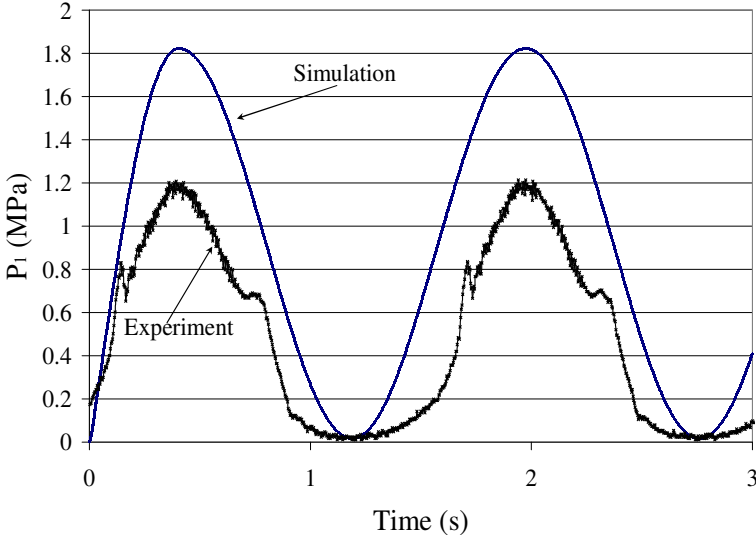


(b)

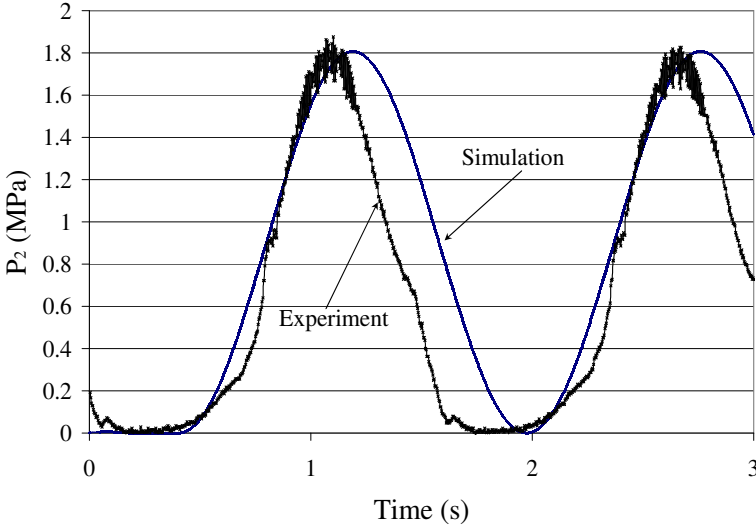
Fig. 4.30 Pressure in chamber A (a), and B (b) of cylinder.

i) The final experiment aims to observe the behaviour of an orifice at 75% controlled flow with the presence of 7 volts amplitude and a 4 rad/s frequency in the form of sine wave input in both the Electro Hydrostatic Actuation system and software simulation. Figure 4.31 (a) has the ability to track the path of the pressure within the presence of noise in the sensors with huge differences

in the range of pressure whereas Fig. 4.31 (b) has comparatively good tracking ability and a much smaller difference in the range of pressure.



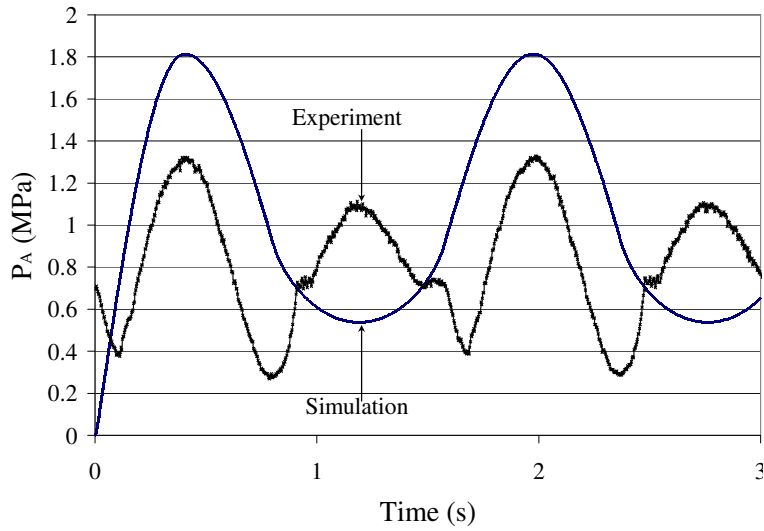
(a)



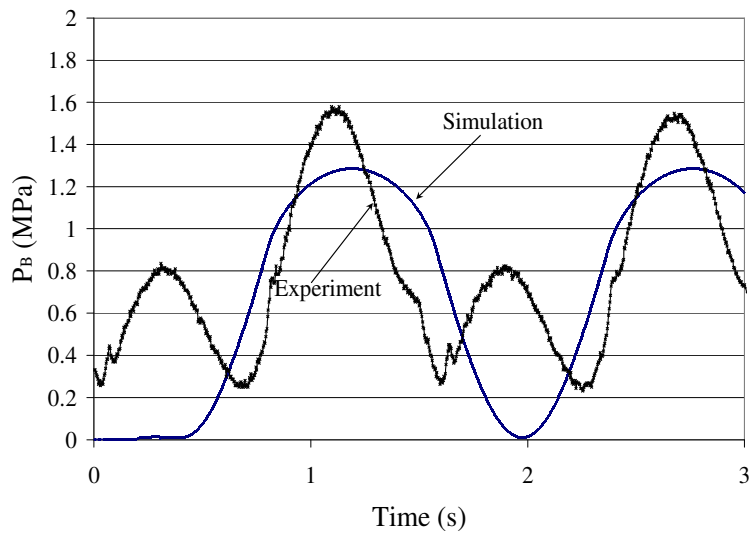
(b)

Fig. 4.31 Pressure at inlet/outlet A (a) and B (b) of pump.

Figure 4.31 represents the pressure output at the pump locations of the experimental test rig and software simulation. Figures 4.32 (a) and (b) illustrate the differences in behaviour of the pressure signals which is indicated by larger humps in the experimental results. This reflects poor tracking.



(a)



(b)

Fig.4.32 Pressure in chamber A (a), and B (b) of cylinder.

4.3 Effect of variable orifice

This section explains and describes the effects and consequences of orifices with the help of pressure signals. The performance of orifices can be easily shown by comparing a 25% opened orifice with a 50% opening and a 50% opened orifice with 75% opened orifice. Furthermore, to validate the results, the same strategy is used to compare the experimental test rig data with the variable area of the orifice.

a) Comparison of simulation results

This section compares, the pressure signal data collected at the inlet/outlet of the pump and the data taken from both ends of the cylinder. Firstly, the comparison is conducted at the inlet of the pump between 25%, 50% and 75% closed cross-sectional area of orifices. The rise in range of pressure can be seen in Figs. 4.33 to 4.36. The range of pressure has a significant difference which is observed at both ends of the cylinders as well in the comparison of the 25%, 50% and 75% closed orifices.

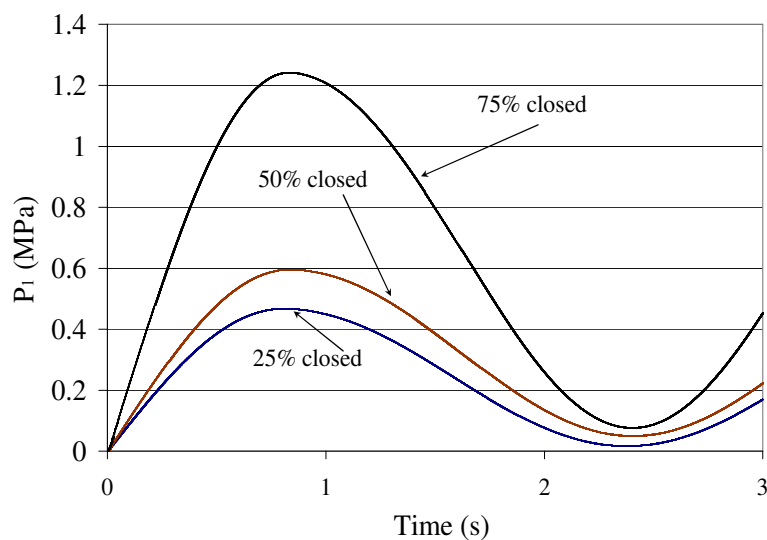


Fig. 4.33 Pressure signal at the inlet of the pump.

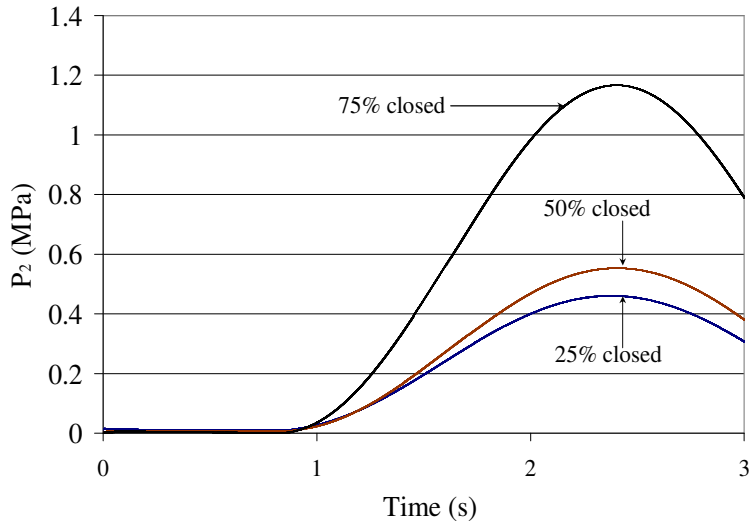


Fig. 4.34 Pressure signal at the outlet of the pump.

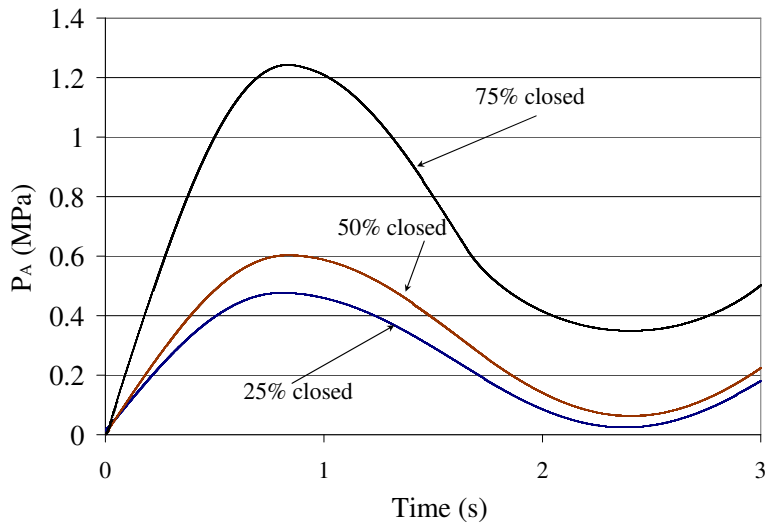


Fig. 4.35 Pressure at chamber A of the cylinder.

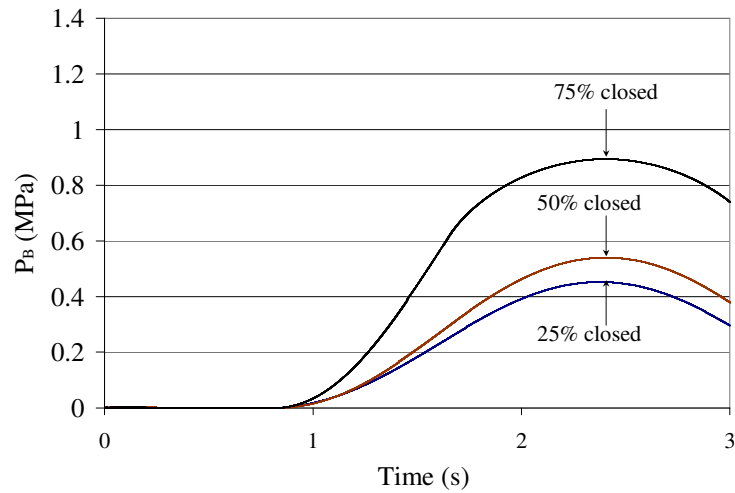


Fig. 4.36 Pressure at chamber B of the cylinder.

b) Comparison of experimental results

With the tests complete, it remains to compare pressure signals obtained at the same sine wave input of $5\sin(2t)$ in 25%, 50% and 75% closed level orifices. The comparison between 25%, 50% and 75% closed orifices shows that by tightening the orifice, the range of pressure signals always increases. Figures 4.37, 4.38, 4.39, 4.40 show the pressures at the inlet/outlet of the pump and at both ends of the cylinder at 25%, 50% and 75% closed orifice.

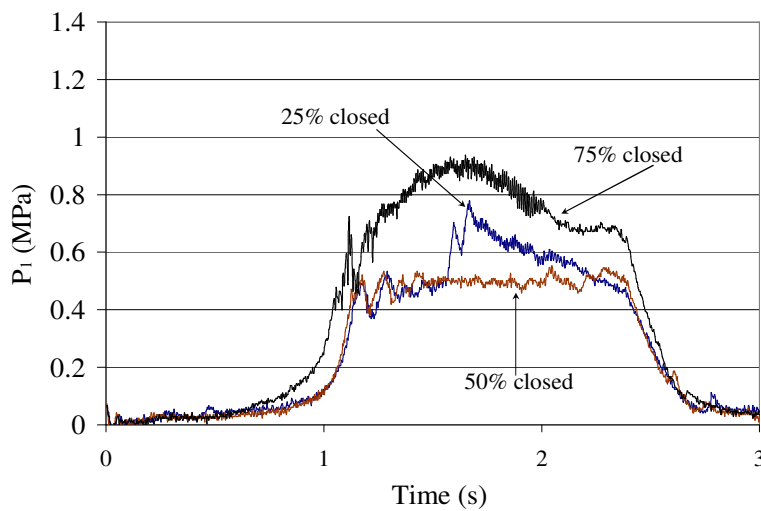


Fig. 4.37 Pressure at the inlet of the pump.

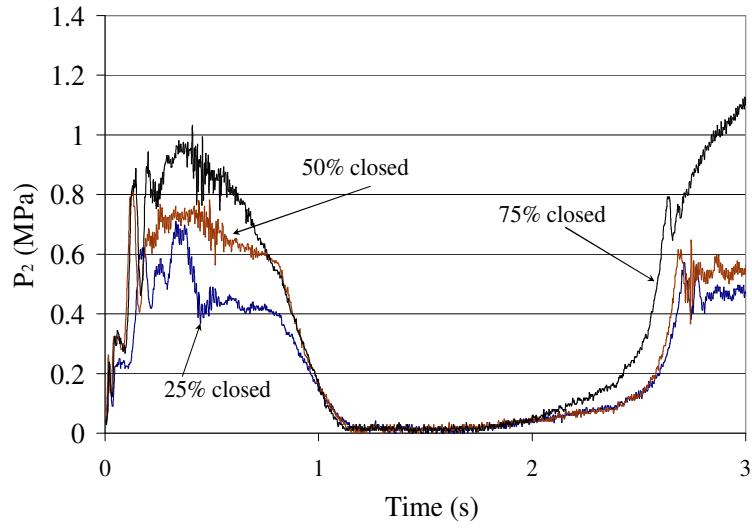


Fig. 4.38 Pressure at the outlet of the pump

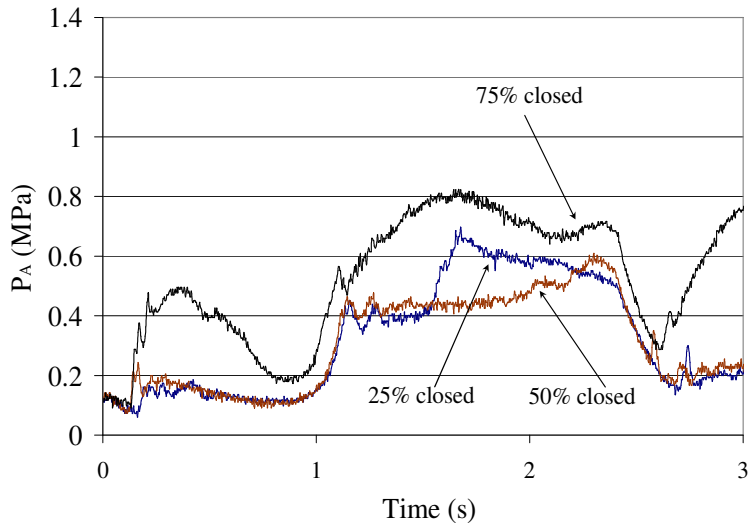


Fig. 4.39 Pressure in chamber A of the cylinder.

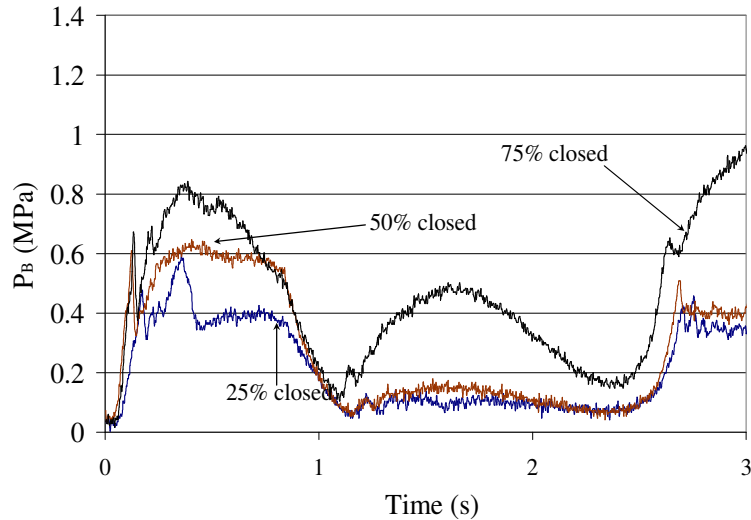


Fig. 4.40 Pressure in chamber B of the cylinder.

The rise in the range of the pressure signals due the tightened orifice is proved and easily seen in all the figures of section 4.3.

4.4 Summary

In this chapter, the detailed mathematical modeling of the EHA and its components are described. The EHA system is then described using the simplified model of an experimental test rig. Moreover, the equations for the motor, pump, orifices, friction and hydraulic actuator are all shown in detail, and, the specifications used for performing the simulation tests are expressed. The behaviour of the experimental test rig (EHA) confirms the validity of the mathematical equations used for modeling a closed loop system around the motor and an open loop across the actuator.

The simulation results are validated by the experimental results which provided good qualitative tracking of the angular velocity of motor, the displacement of the piston and pressure signals. The results shown in the case of orifices explaining its presence or absence with variable opening

area of orifices allowed one-way free flow and controlled flow on the other side. The introduction of orifices into the EHA system contributed in the creation of the throttling affect in data obtained by simulation and experiment scenarios. This resulted in the drifting of the piston position as well. The tighter orifice created high levels of throttling effect which caused back pressure from the cylinder and more drift in the displacement of the actuator.

CHAPTER

5

IDENTIFICATION OF INTERNAL LEAKAGE USING WAVELET TRANSFORM

5.1 Fault Detection

The detection of internal leakage faults through the use of the Wavelet transform method is done by analyzing the pressure data obtained from both ends of the cylinder. This analysis is done with the assistance of MATLAB programming. The size of the leak is adjusted from the level of a large leak to that of an extra-small leak as the target of this experiment is to identify the Wavelet Analysis' ability to detect extra-small leaks. The Electro Hydrostatic Actuation system is tested with one cylinder which is connected to the VMFP (Variable Displacement Motor and Fixed Displacement Pump). The cylinder used in the test rig is a double rod cylinder and its back and forth motion can be varied depending on the desired action. There is a chance for the occurrence of internal leakage at the piston inside the cylinder as shown in Fig. 3.1. One possible reason for leakage could be the excessive wear of the piston and seals inside the cylinder which

can cause sluggish movement or settling under load. Piston leakage can also be caused by the wearing down of the piston seals, rings, or from scoring on the cylinder walls. The latter may be caused by dirt and grit in the oil. Internal leakage can be one of the major reason to effect cylinder performance and the efficiency of any hydraulic system.

The experiments outlined below are focused on using Discrete Wavelet Transform (DWT) to detect faults that arise due to internal leakage in both chambers. The analysis of DWT on the pressure signals of both chambers of cylinder are done in MATLAB. The application of Discrete Wavelet Transform (DWT) for internal leakage detection is described below in all the experiments. Four detail coefficients of wavelets are obtained from the pressure signals of both chambers (i.e. P_A and P_B) under normal as well as faulty operating conditions due to internal leakage. Daubechies' wavelet (Daubechies, 1992) has been selected as the mother wavelet over many other choices (e.g., Coiflets, Meyer wavelet, Gaussian wavelet, Mexican hat wavelet and Morlet wavelet). From the viewpoint of implementation, Daubechies' wavelet is a good choice for this application because it provides a high order mother wavelet which better avoids overlap between adjacent frequency bands (Cusido et al., 2008). It is for this reason that the order eight has been chosen for these experiments.

The experiments conducted below are categorized based on the level of leakage created at the cylinder. Ultimately, the aim is to detect the smallest leak possible. The categorizations of the experiments conducted are as follows:

- i. Large leak (0.0150 lit/min)
- ii. Medium leak (0.0100 lit/min)
- iii. Small leak (0.0075lit/min)
- iv. Extra-small leak (0.0042 lit/min)

Tests are done on large, medium and small leaks to show that the DWT method is able to diagnose the fault with the help of changes in the signal. However, the main focus of this experimental study is to detect leakages on an extra-small scale.

5.2 Large Leak

In this case, two tests are performed under different input conditions with variable amplitude and frequency to make sure that the wavelet is able to detect changes in the pressure signals at the leakage points.

a) In this scenario, the Electro Hydrostatic Actuation system is triggered with an input of a sine wave having amplitude of 3 volts and a frequency of 4 rad/s. The wavelet analysis is performed on pressure signals at both ends of the cylinder which is obtained by using an input of $3\sin(4t)$.

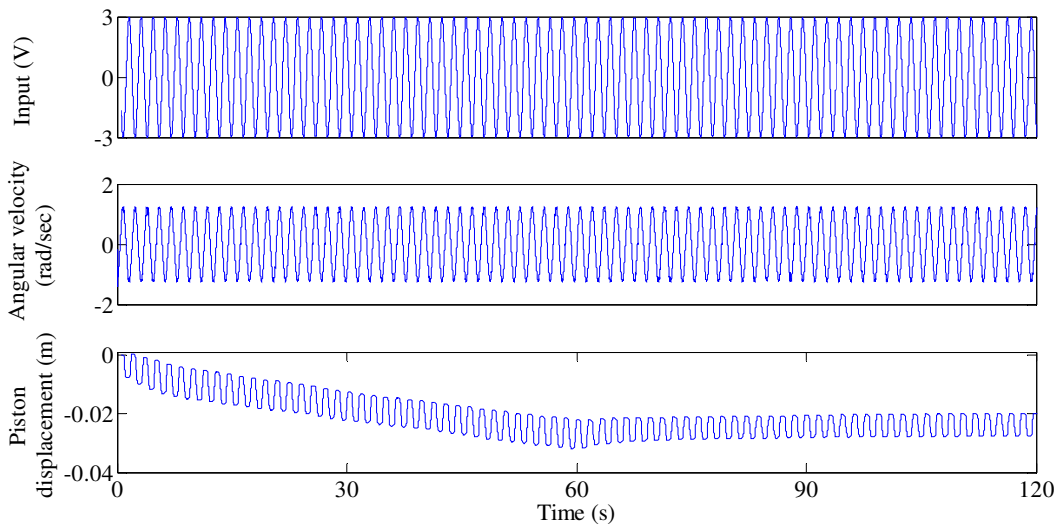


Fig. 5.1 Experimental input voltage of $3\sin(4t)$, angular velocity of motor and displacement of the piston.

The duration of the experiment was 120 seconds wherein the first 60 seconds were conducted without leakage and the final 60 seconds were carried out under conditions of large level internal leakage. Figure 5.1 represents the input signal given to the EHA test rig along with the angular velocity of the motor. As the motor is equipped with internal closed loop which helps in maintaining angular velocity without any change even after the leak is introduced. The displacement of the piston, which is also shown in Fig. 5.1, is shown for the entire 120 seconds. The drifting of the displacement of the piston occurs because of the higher level of friction and presence of orifices in the test rig. However, when leakage is introduced at the 60th second, the piston stops drifting as a result. Figure 5.2 shows the enlarged version of Fig. 5.1 from 50th to 70th second in order to provide a close-up view of how the signals behave.

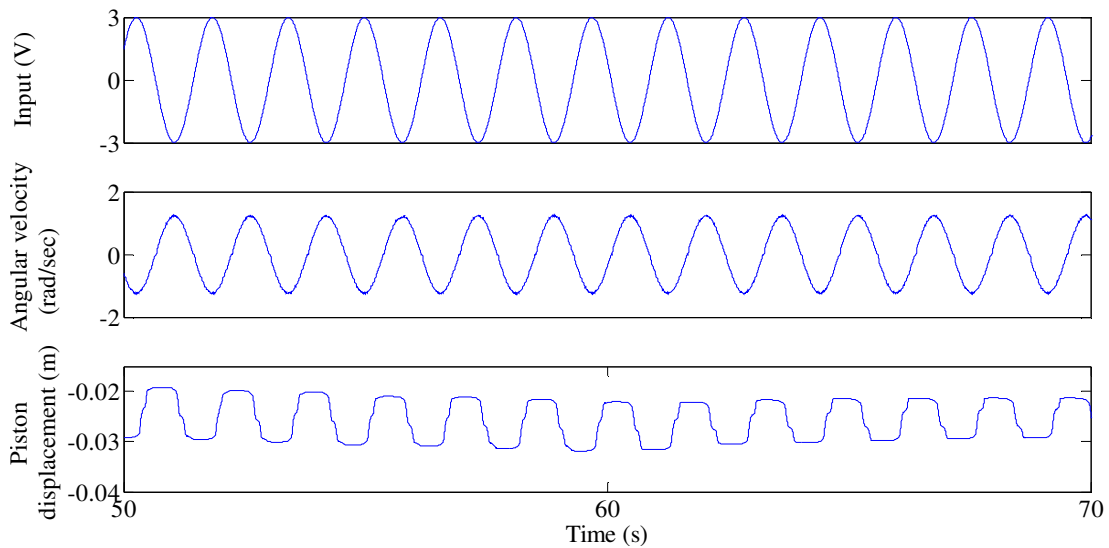


Fig. 5.2 Close-up view from 50th to 70th seconds to show the behaviour of Fig. 5.1.

The level of internal leakage created through the use of a needle valve at the 60 second mark is shown in Fig. 5.3. The pressure signals on both sides of the cylinder (P_A and P_B) are also depicted in Fig. 5.3 and it will be these signals that will be analyzed through Wavelet transform.

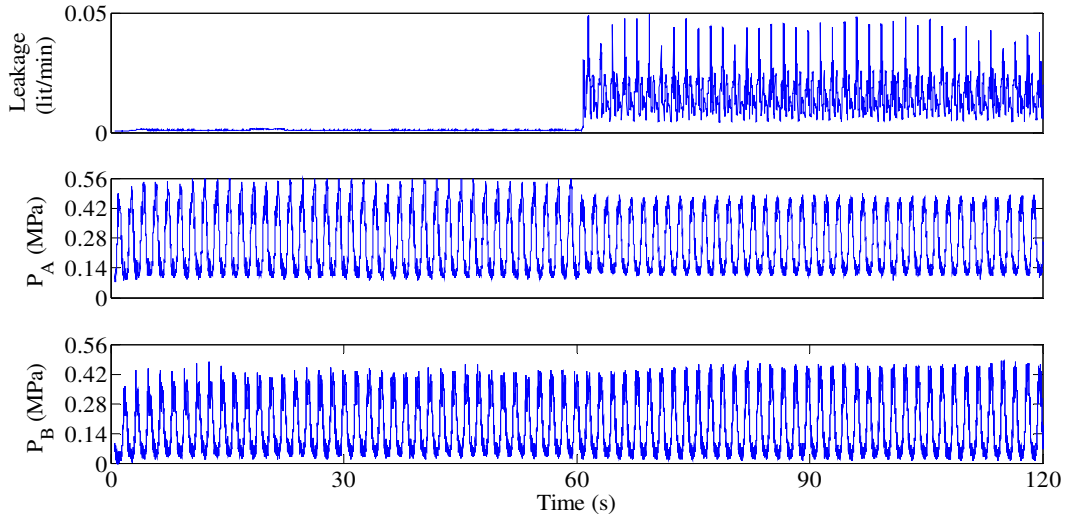


Fig. 5.3 Large level of internal leakage shown with the pressures as P_A and P_B at both sides of the cylinder.

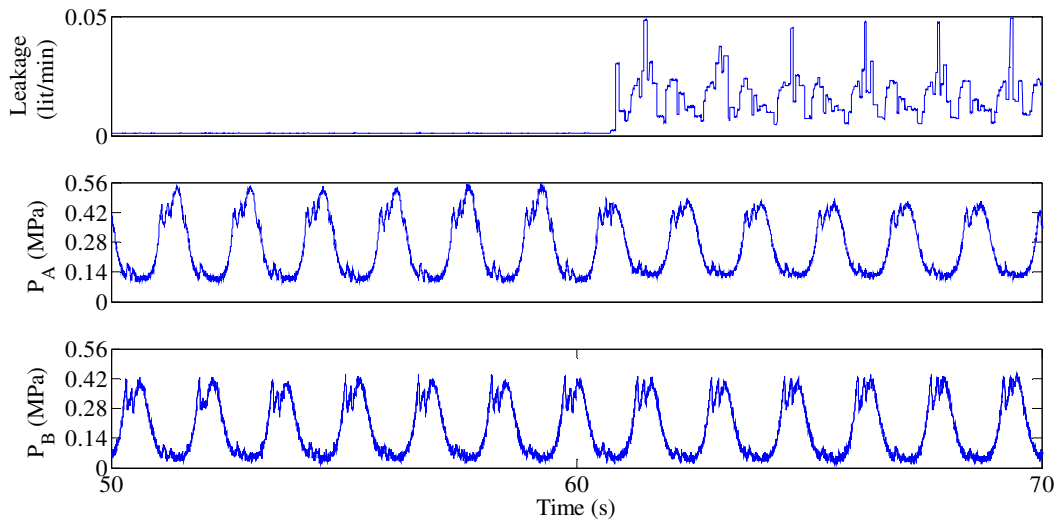


Fig. 5.4 Close-up view from 50th to 70th seconds to show the behaviour of Fig. 5.3.

The use of Wavelet transform on pressure signal P_A (Fig. 5.3) shows significant changes in graphs d_3 and d_4 . These changes are visible in Fig. 5.5 which represents four detail coefficients obtained by using mother wavelet db8 in running wavelet analysis on pressure signal P_A . The multiplication of detail coefficients d_3 and d_4 is called as amplified coefficient named as d_3d_4 which proves the change in the signal and this can be clearly observed in Fig. 5.5.

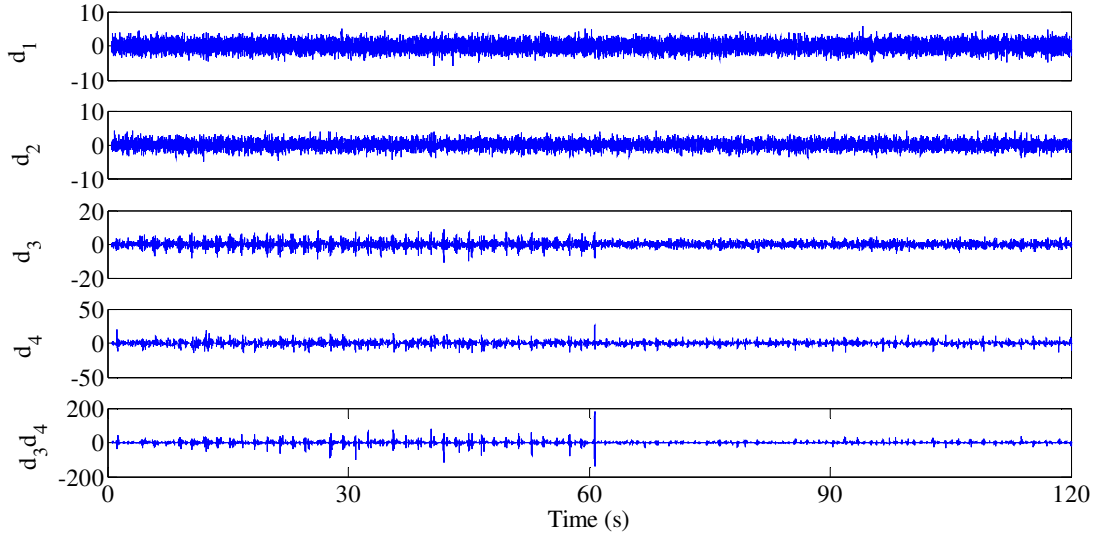


Fig. 5.5 Four-level detail wavelet coefficients of P_A pressure signal shown in Fig. 5.3.

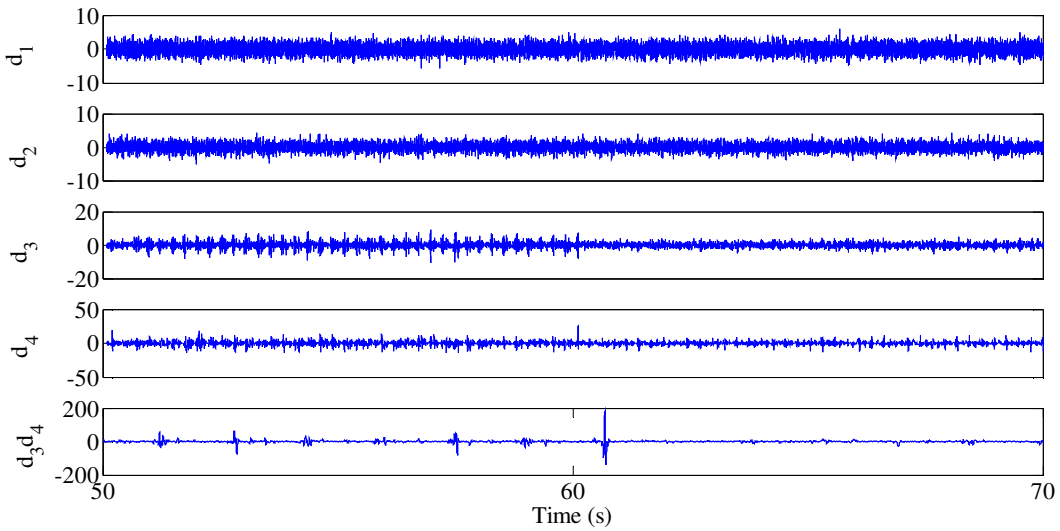


Fig. 5.6 Close-up view from 50th to 70th seconds to show the behaviour of Fig. 5.5.

To prove the sensitivity of the leakage detection technique using wavelet transforms, RMS of the detail coefficients d_3 , d_4 and d_{3d_4} is also shown in Fig. 5.7 for the pressure signal P_A at side one of the chamber. These RMS curves are plotted using a MATLAB program by windowing the pressure signal with a step size of 500 and window size of 1000 which helps in obtaining the difference in the non-leaking and leaking data shown in all the RMS plot shown in this section.

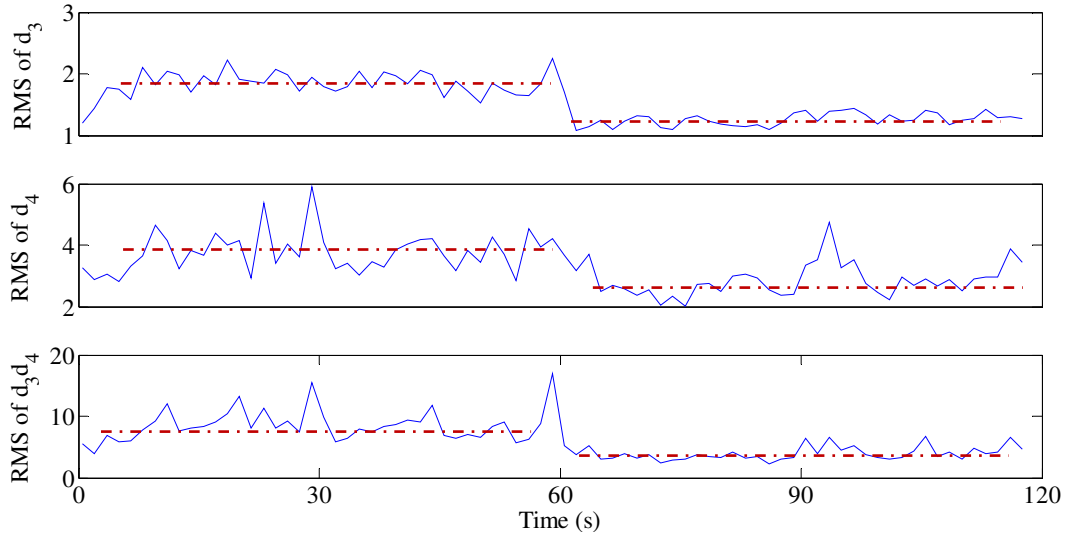


Fig. 5.7 RMS values of wavelet coefficient, d_3 , d_4 and d_3d_4 as shown in Fig. 5.5.

Similarly, in Fig. 5.8, d_4 , which is the 4th detail coefficient, also shows variation in the peaks after the first 60 seconds. Fig. 5.9, depicts the introduction of leakage during the operation of the test rig between the 50th and 70th seconds. The amplification of d_3 and d_4 as d_3d_4 also shows the change in the signal, proving the detection of internal leakage with a mean value of 0.0087 lit/min.

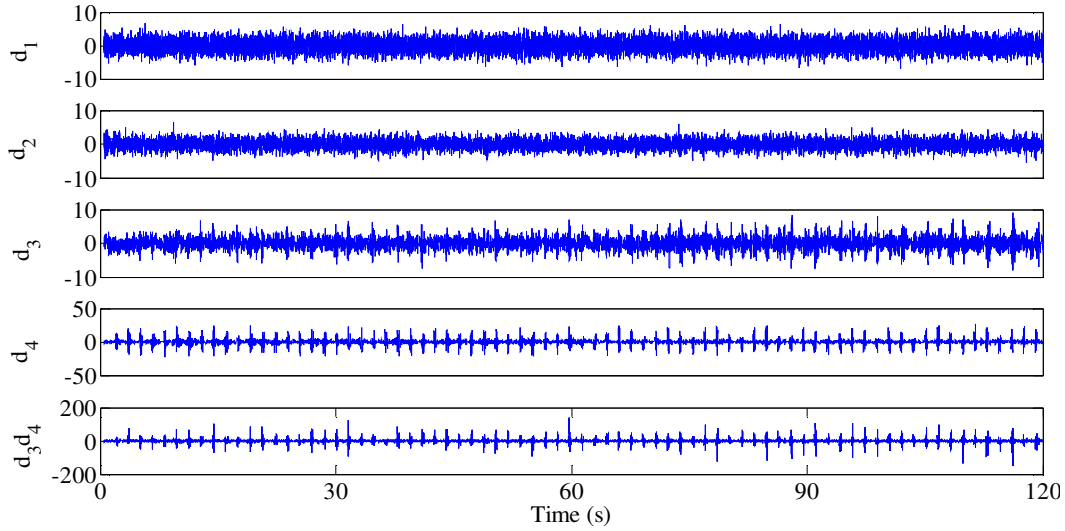


Fig. 5.8 Four-level detail wavelet coefficients of P_B pressure signal shown in Fig. 5.3.

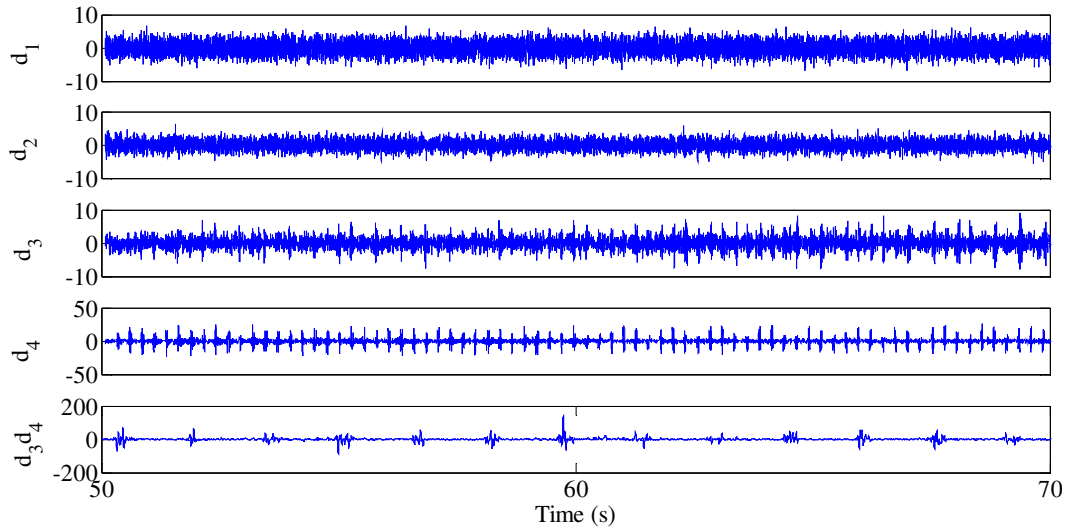


Fig. 5.9 Close-up view from 50th to 70th seconds to show the behaviour of Fig. 5.8.

The RMS values of detail coefficients d_3 , d_4 and d_3d_4 is also shown in Fig. 5.10 for the pressure signal P_A at the other side of the chamber P_B to prove the sensitivity of the leakage detection technique using wavelet transforms. The peak of the RMS values of d_3d_4 after the 60th second show the changes from the first 60 seconds which assures the effect of fault detection.

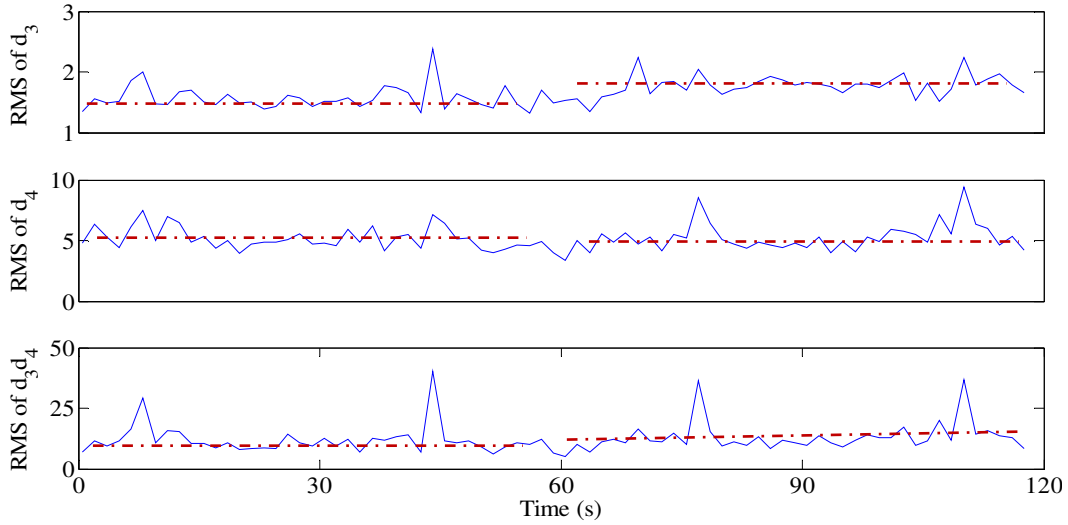


Fig. 5.10 RMS values of wavelet coefficient, d_3 , d_4 and d_3d_4 as shown in Fig. 5.8.

b) As another example of large leak case, sine waves with an amplitude of 5 volts and a frequency of 2 rad/s (*i.e.* $5\sin(2t)$) are introduced to the experimental test rig for performing fault detection. Figures 5.11 and 5.12 reflect the input to the test rig with the obtained angular velocity and displacement of piston. From this point onwards, all the tests were conducted for 180 seconds with first 90 seconds as non-leaking data and second 90 seconds as leaking data.

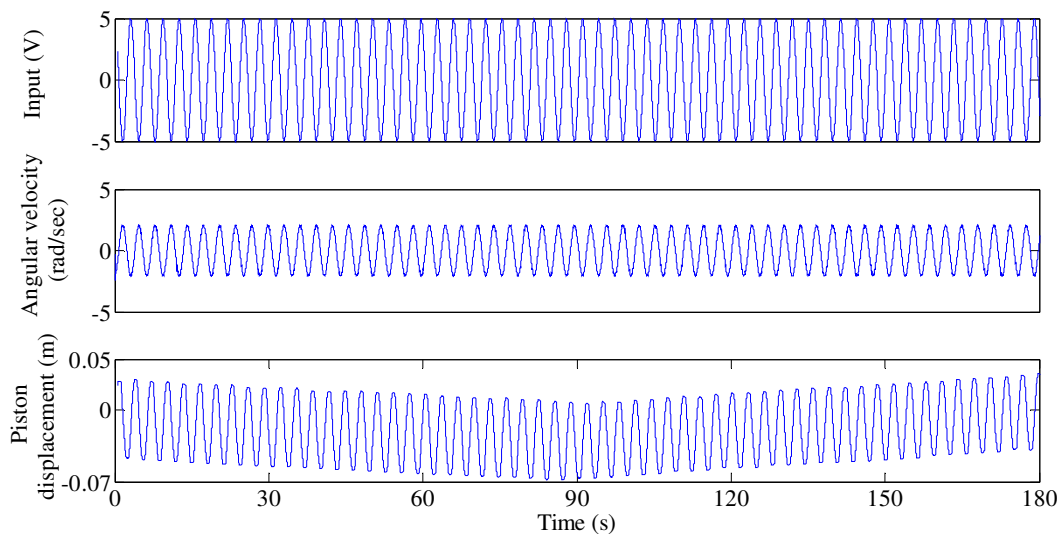


Fig. 5.11 Experimental input of $5\sin(2t)$ with angular velocity of motor and displacement of the piston.

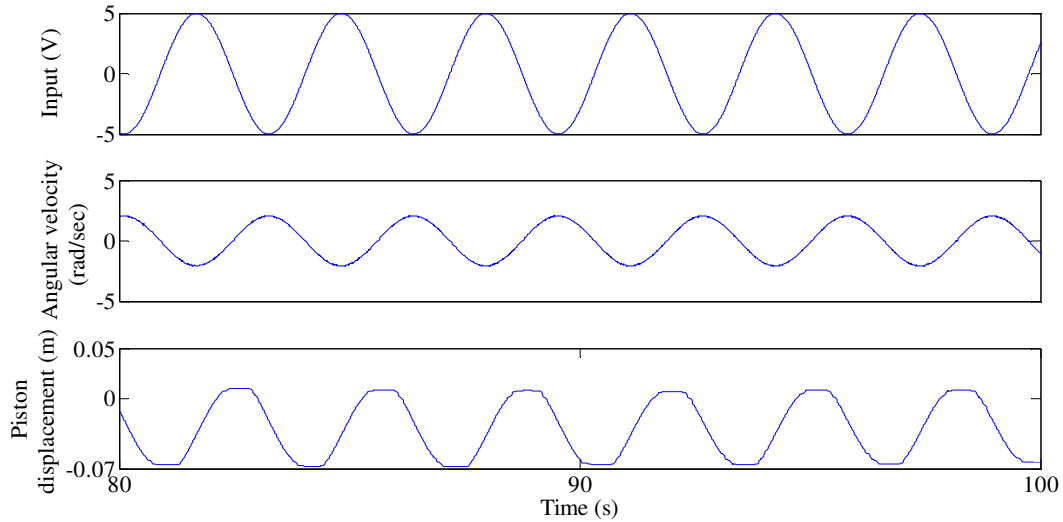


Fig. 5.12 Close-up view from 80th to 100th seconds to show the behaviour of Fig. 5.11.

Pressure signals created in both chambers of the cylinder (labelled P_A and P_B respectively) are shown in Figs. 5.13 and 5.14 with close-up view of the previous Fig. 5.13 for the purpose of obtaining an insight into the pressure signals. Internal leakage plotting provides information about the flow of fluid passing through the piston, which acts as fault created in the test rig for performing the wavelet analysis.

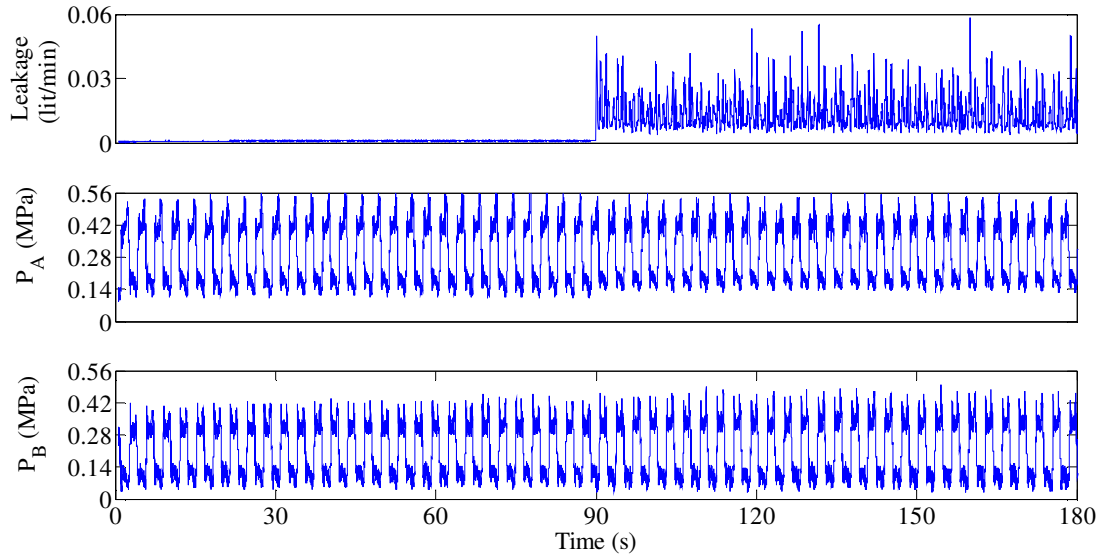


Fig. 5.13 Large level of internal leakage shown with the pressures as P_A and P_B at both sides of the cylinder.

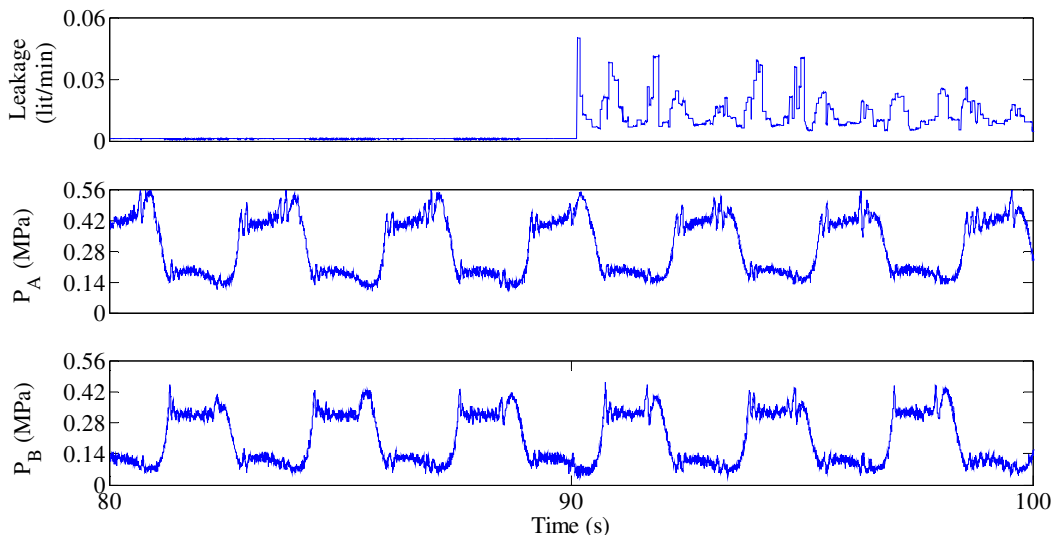


Fig. 5.14 Close-up view from 80th to 100th seconds to show the behaviour of Fig. 5.13.

In Fig. 5.15, the results of the wavelet analysis on pressure signal P_A can readily be observed in the 3rd and 4th detail coefficients (labelled d_3 and d_4) using a mother wavelet of db8. Similarly, in Fig. 5.16, the close-up view of detail coefficients from the 80th to 100th seconds proves the changes happening in the peaks of d_3 and d_4 along with the amplified d_3d_4 signal which is a

multiplication of d_3 and d_4 . Hence, the data during the leak time shows that wavelets are able to perform fault detection.

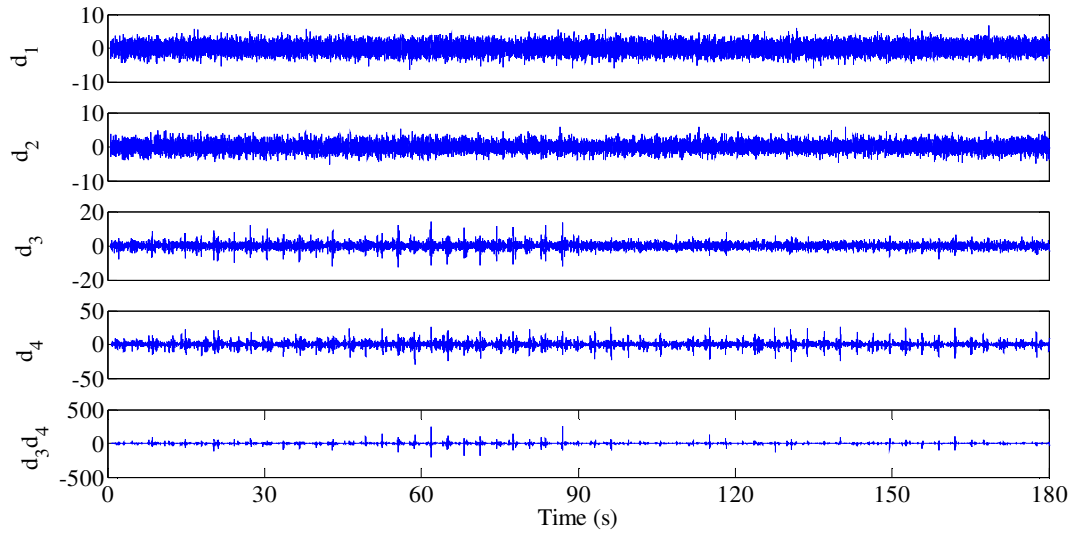


Fig. 5.15 Four-level detail wavelet coefficients of P_A pressure signal shown in Fig. 5.13.

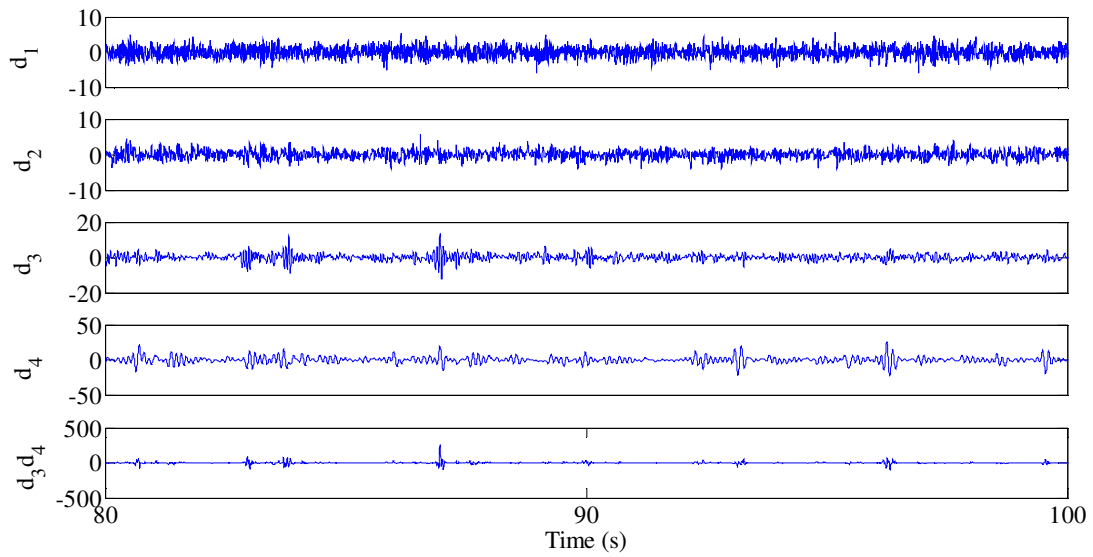


Fig. 5.16 Close-up view from 80th to 100th seconds to show the behaviour of Fig. 5.15.

The RMS curves of d_3 , d_4 and d_3d_4 also show the changes in the signals after 90 seconds of non-leaking data. The curves of the RMS shift down a little in all three plots of Fig. 5.17 during the second half of the total duration of 180 seconds, thus proving the diagnosis of a fault.

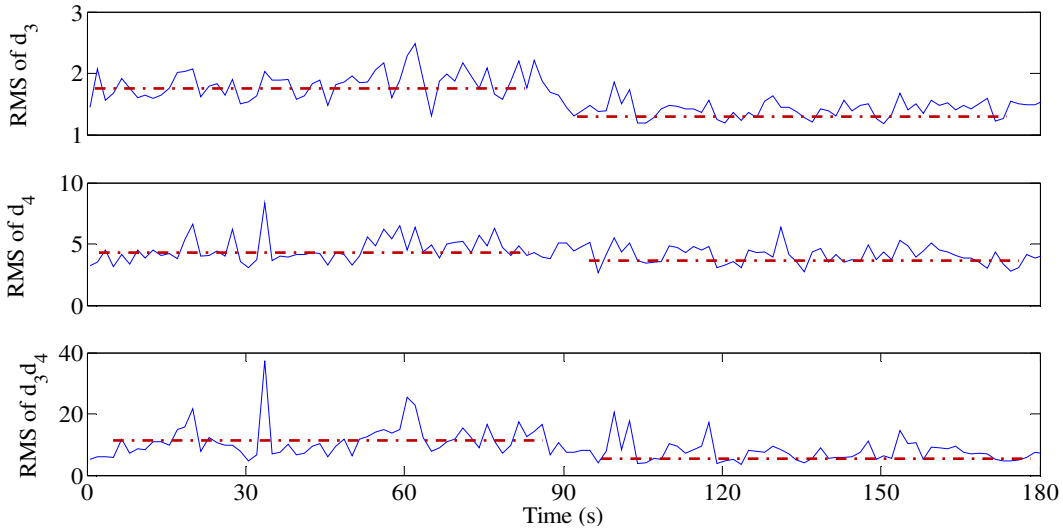


Fig. 5.17 RMS values of wavelet coefficient, d_3 , d_4 and d_3d_4 as shown in Fig. 5.15.

Wavelet transform is again used to detect leakage on the other side of the cylinder which is derived from pressure data P_B . In Fig. 5.18, the 3rd and 4th detail coefficients (labelled d_3 and d_4) show changes in the data after the first 90 seconds, although this change is not very significant. To check the effectiveness of d_3 and d_4 , amplified d_3d_4 plays a vital role in confirming the changes in signals. The close-up view of detail coefficients from the 80th to 100th second is shown in Fig. 5.19 to illustrate the difference between the final 10 seconds of the non-leaking signal and the first 10 seconds of leaking data.

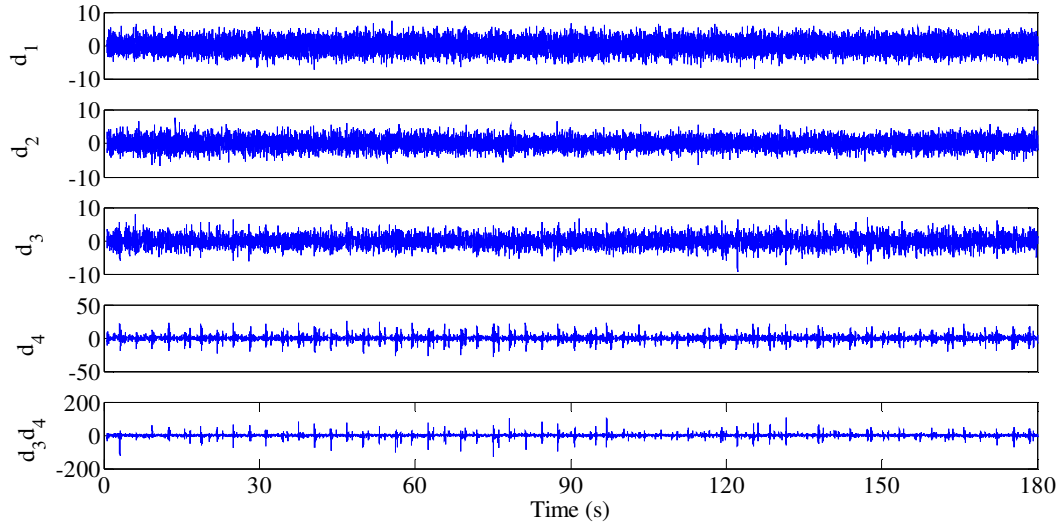


Fig. 5.18 Four-level detail wavelet coefficients of P_B pressure signal shown in Fig. 5.13.

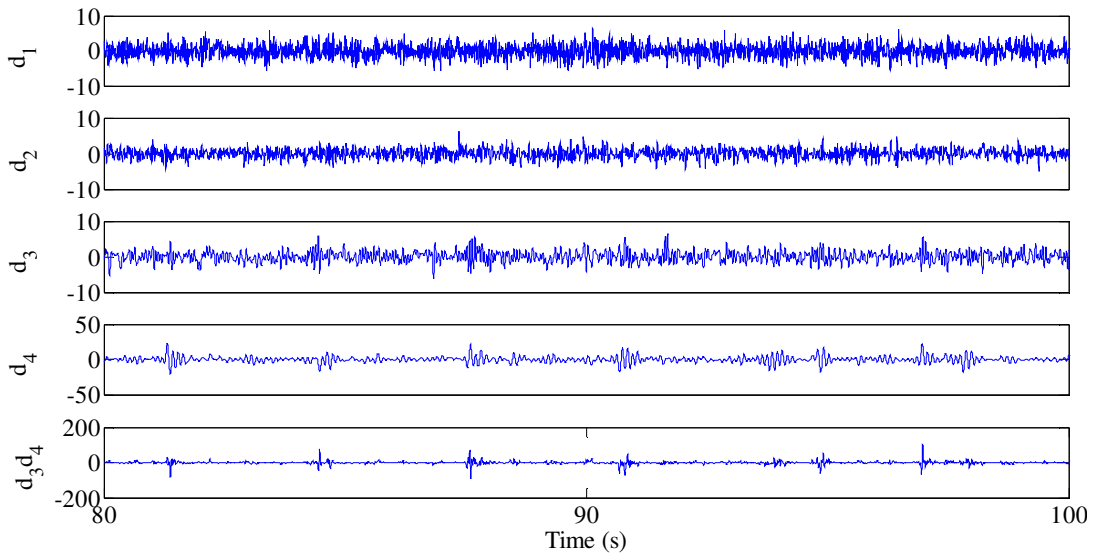


Fig. 5.19 Close-up view from 80th to 100th seconds to show the behaviour of Fig. 5.18.

Furthermore, the RMS values are calculated to prove the difference in the signals as shown in Fig. 5.20. These RMS values are obtained by the detail coefficients of the pressure signal P_B , which is obtained from the other side of the cylinder.

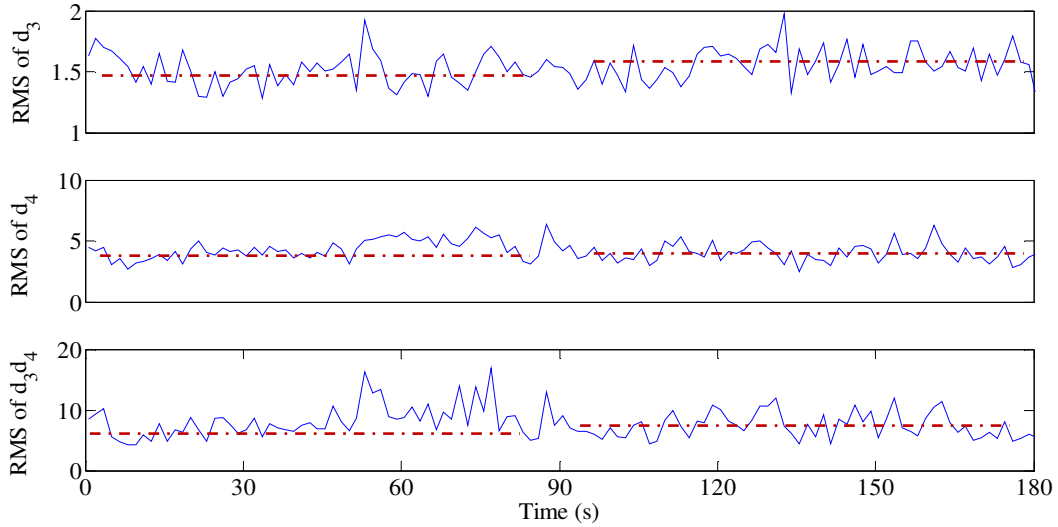


Fig. 5.20 RMS values of wavelet coefficient, d_3 , d_4 and d_3d_4 as shown in Fig. 5.18.

5.3 Medium Leak

In this case, the leak has been reduced to half of the level used in the large leak category discussed in section 5.2. The logic of reducing the leak is to check the capability of db8 mother wavelet analysis in smaller level leaks. As in the previous cases, there are two tests performed with $3\sin(4t)$ and a higher amplitude of 8 volts and considerably smaller frequency of 1 rad/s ($8\sin(1t)$) input conditions.

- a) Sine wave input with amplitude of 3 volts and a frequency of 4 rad/s is used in the experiment of medium-small internal leakage. Figures 5.21 and 5.22 (close-up of Fig. 5.21) shows the input signal, angular motor velocity, and displacement of the piston obtained by sine wave input. The pressures signals recorded in both chambers of the cylinder are shown in Fig. 5.23 along with the internal leakage plot with a close-up view in Fig. 5.24. The experiment was conducted for 180 seconds in which first 90 seconds was carried out with no

leakage and the next 90 seconds with leakage. The changes in the sine wave of the pressures in Fig. 5.23 after 90 seconds are fairly visible which reflects the presence of faults from that time.

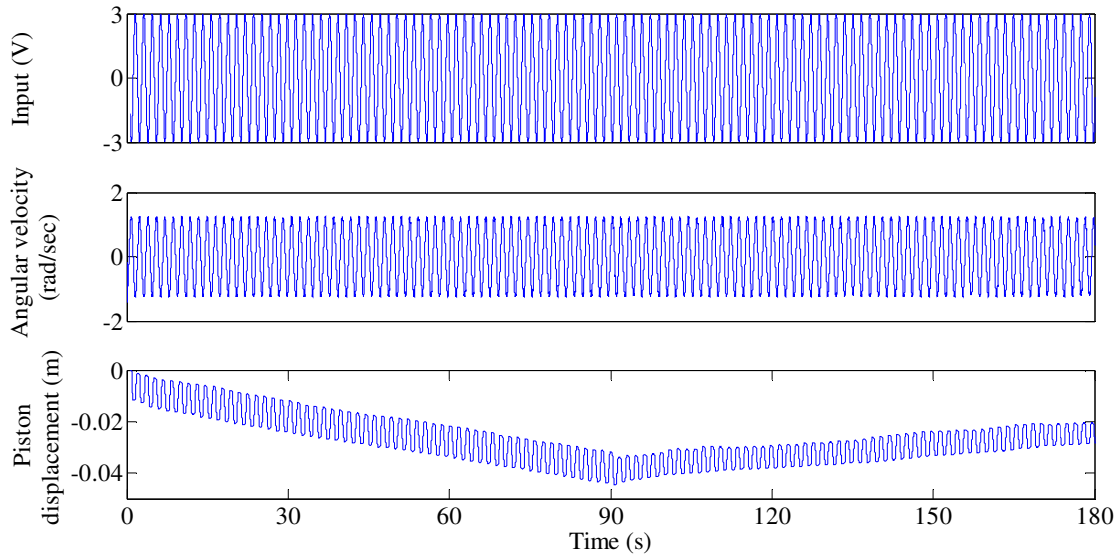


Fig. 5.21 Experimental input of $3\sin(4t)$ with angular velocity of motor and displacement of the piston.

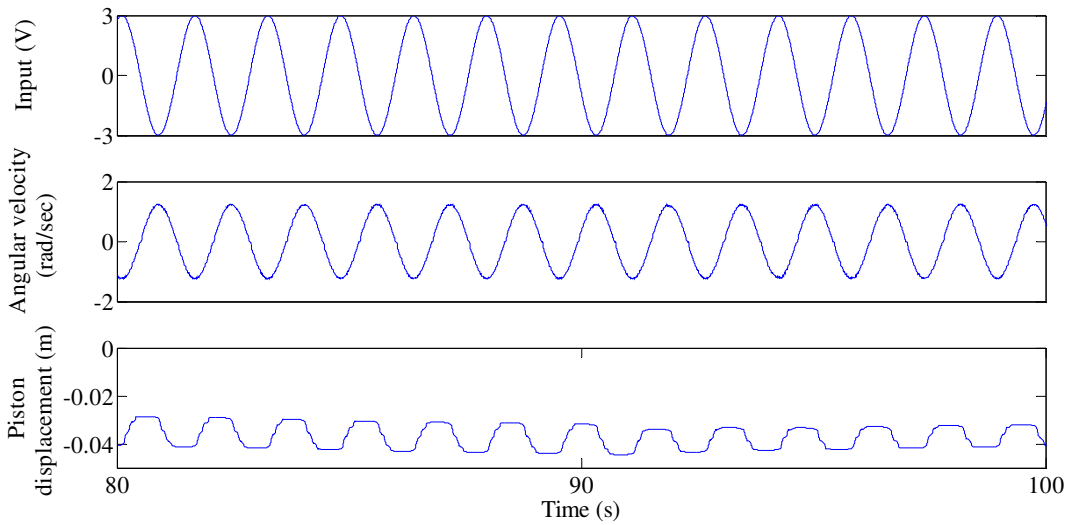


Fig. 5.22 Close-up view from 80th to 100th seconds to show the behaviour of Fig. 5.21.

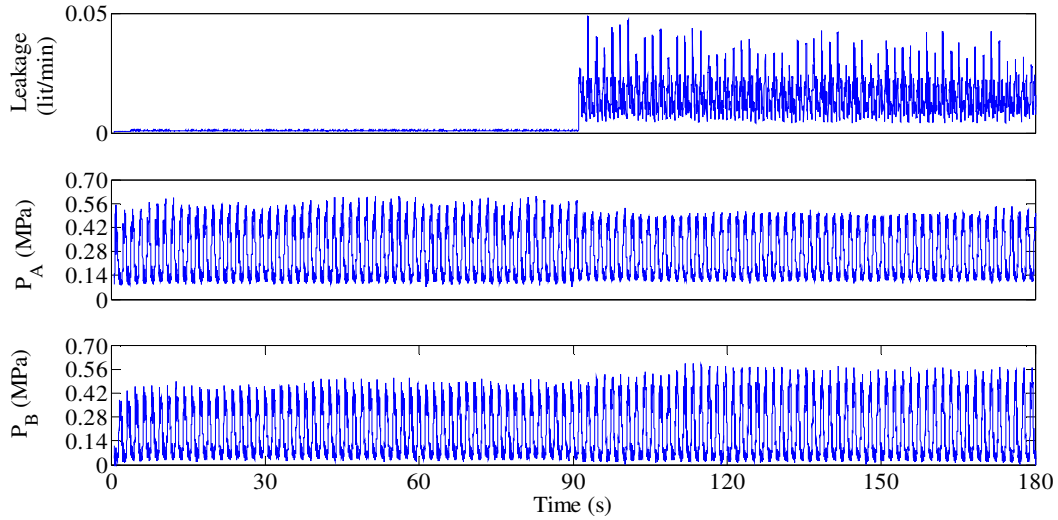


Fig. 5.23 Medium level of internal leakage shown with the pressures as P_A and P_B at both sides of the cylinder.

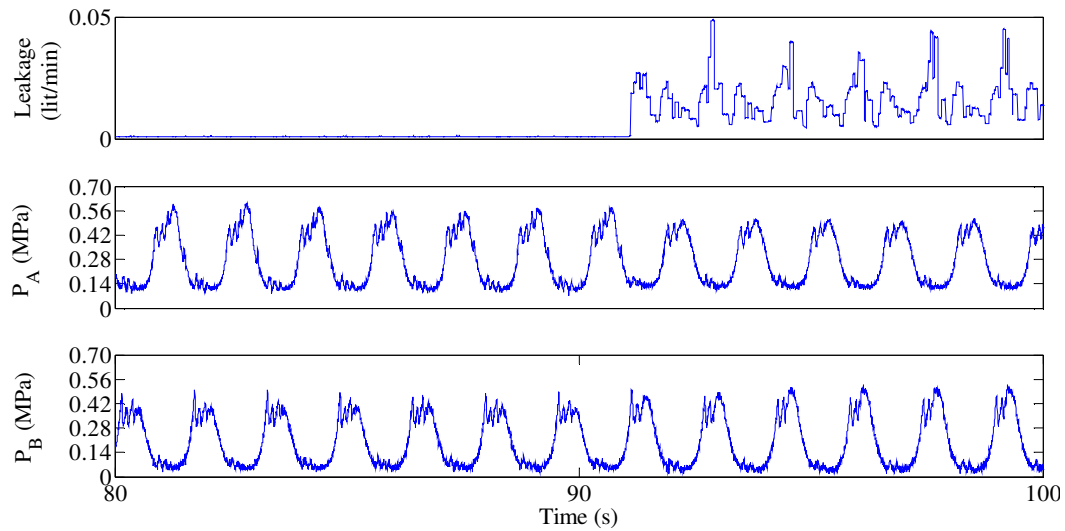


Fig. 5.24 Close-up view from 80th to 100th seconds to show the behaviour of Fig. 5.23.

Figures 5.25 and 5.28 are obtained as a result of performing wavelet analysis on P_A and P_B . In Fig. 5.23, the 3rd and 4th detail coefficients (d_3 and d_4) along with d_3d_4 show the change in the signal peaks which reflects the fault detected. Figures 5.26 and 5.29 depict the close-up view of the detail coefficients.

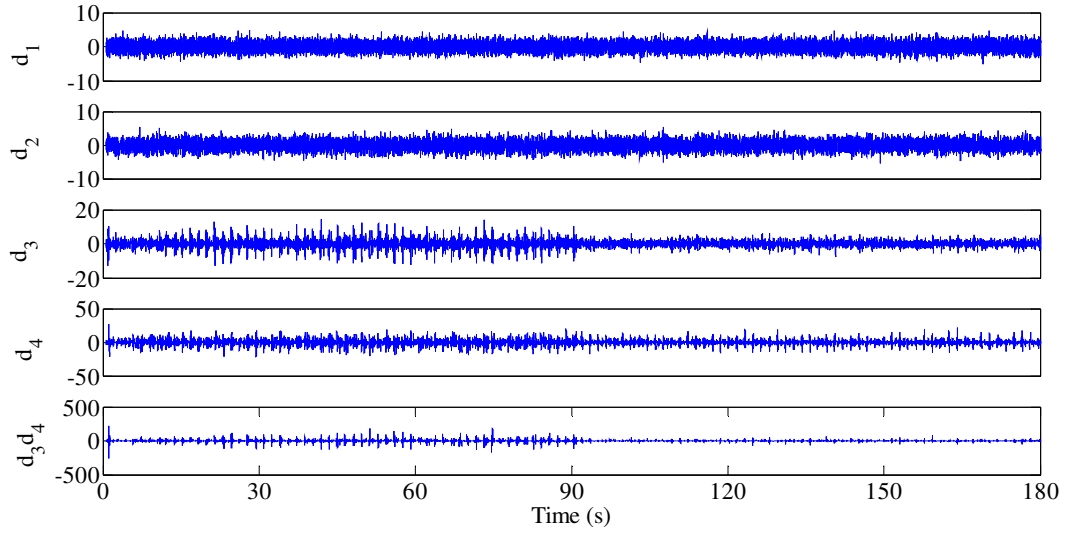


Fig. 5.25 Four-level detail wavelet coefficients of P_A pressure signal shown in Fig. 5.23.

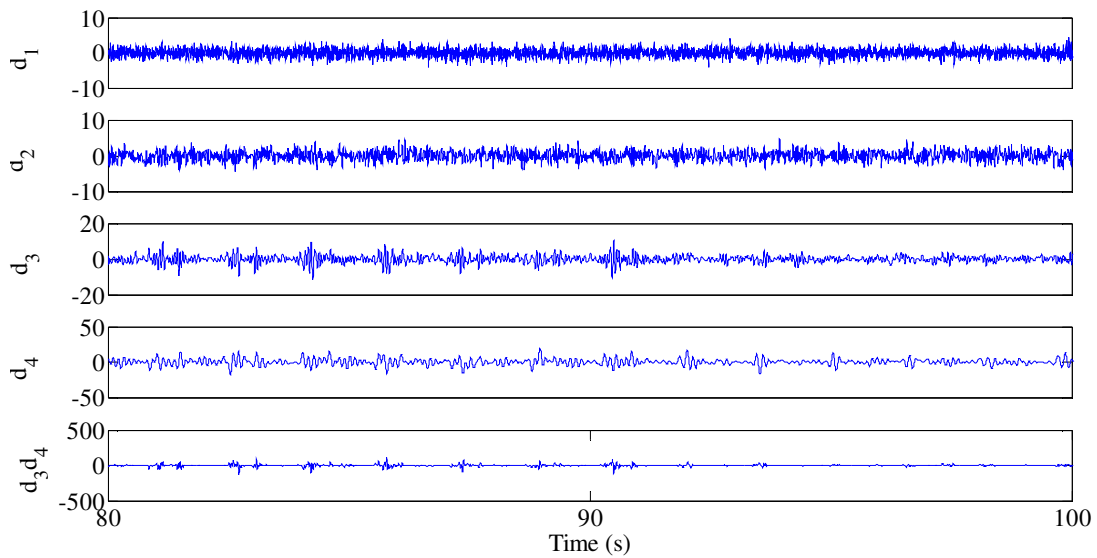


Fig. 5.26 Close-up view from 80th to 100th seconds to show the behaviour of Fig. 5.25.

The changes in the RMS values of the detail coefficients illustrate the drop in the curves after the presence of leakage which is shown in Fig. 5.27.

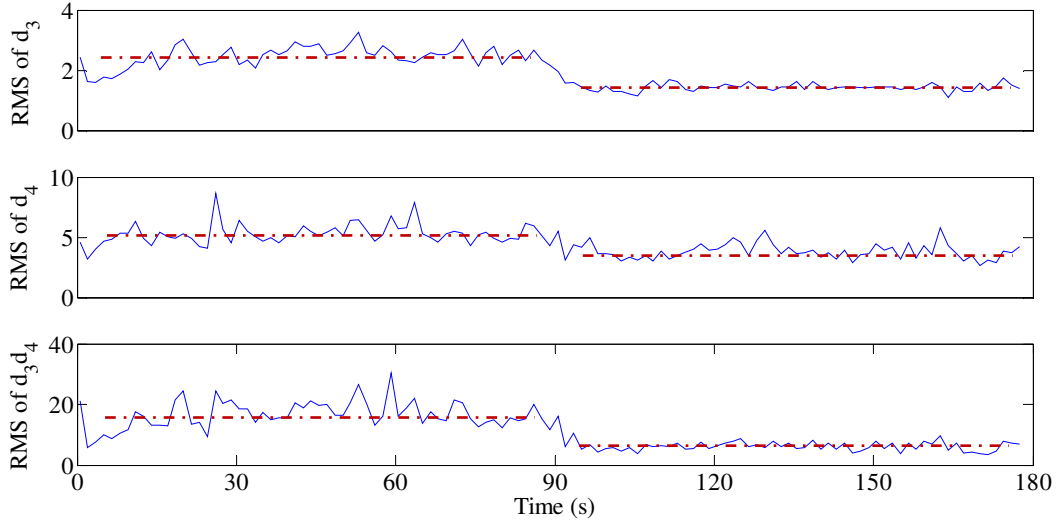


Fig. 5.27 RMS values of wavelet coefficient, d_3 , d_4 and d_3d_4 as shown in Fig. 5.25.

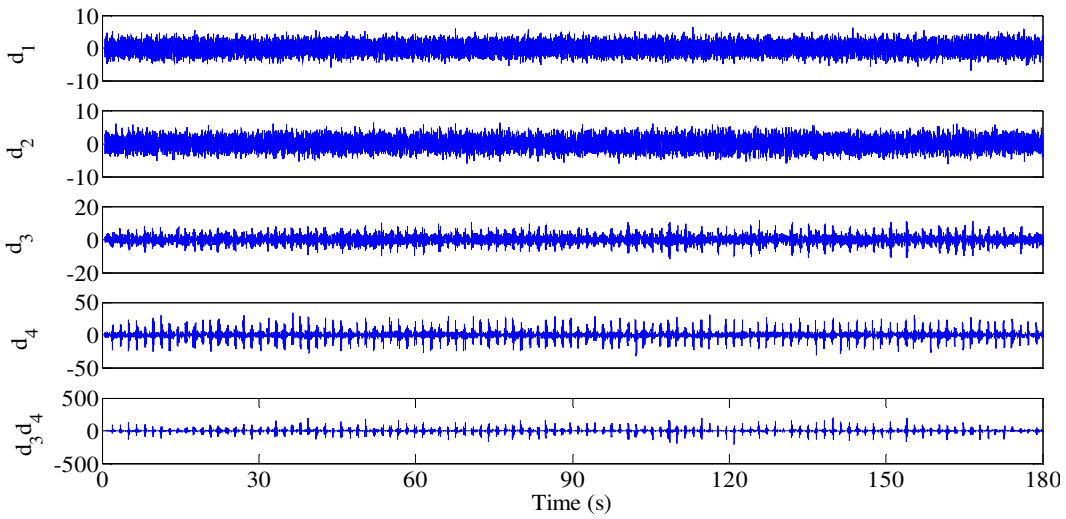


Fig. 5.28 Four-level detail wavelet coefficients of P_B pressure signal shown in Fig. 5.23.

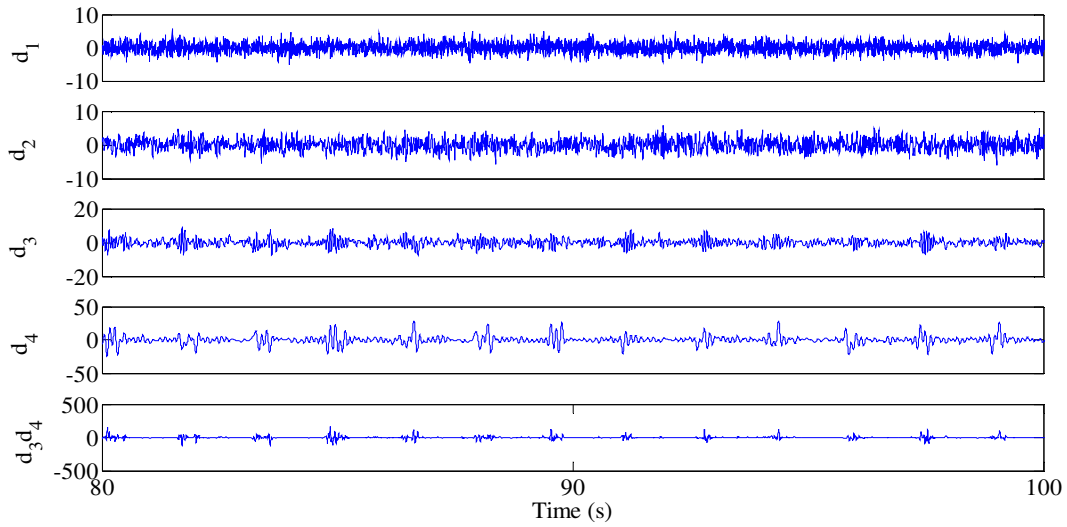


Fig. 5.29 Close-up view from 80th to 100th seconds to show the behaviour of Fig. 5.28.

The changes in the RMS values of detail coefficients obtained by using wavelet transform on the pressure signal P_B is shown in Fig. 5.30 which demonstrates significant changes in the RMS curves after non-leaking data of 90 seconds.

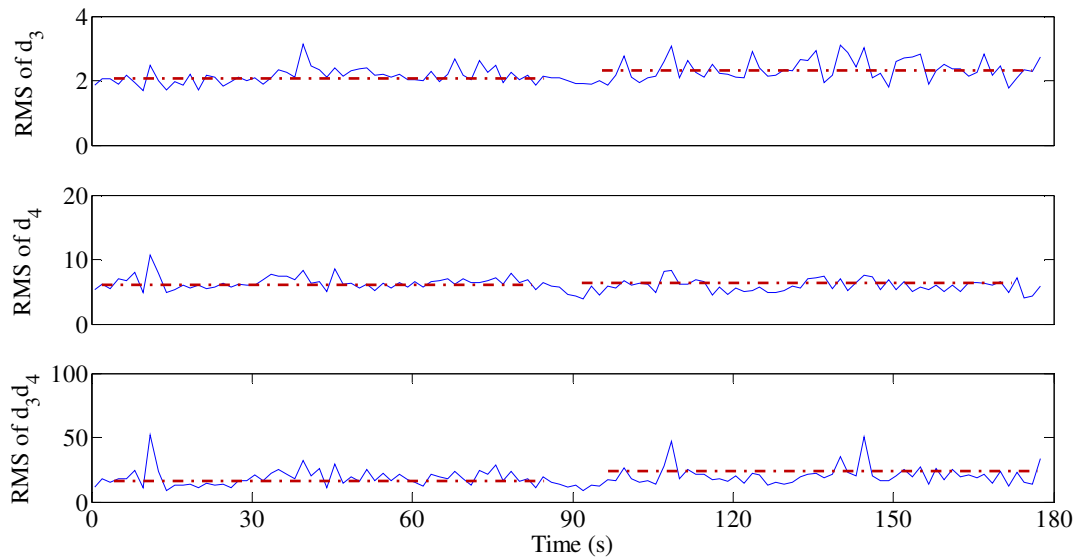


Fig. 5.30 RMS values of wavelet coefficient, d_3 , d_4 and d_3d_4 as shown in Fig. 5.28.

b) The second test in the medium leak category uses higher amplitude (8 volts) and a smaller frequency (1 rad/s) of sine wave. The objective of this test is to study the ability of Wavelet transform to diagnose internal leakage. Figure 5.31 represents the input signal and angular motor velocity with piston displacement obtained by providing an input of $8\sin(1t)$.

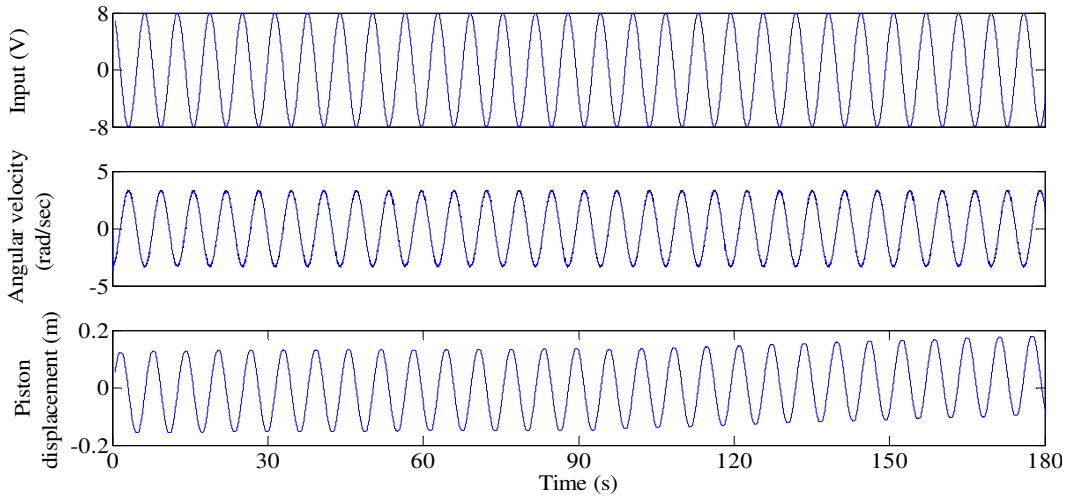


Fig. 5.31 Experimental input of $8\sin(1t)$ with angular velocity of motor and displacement of the piston.

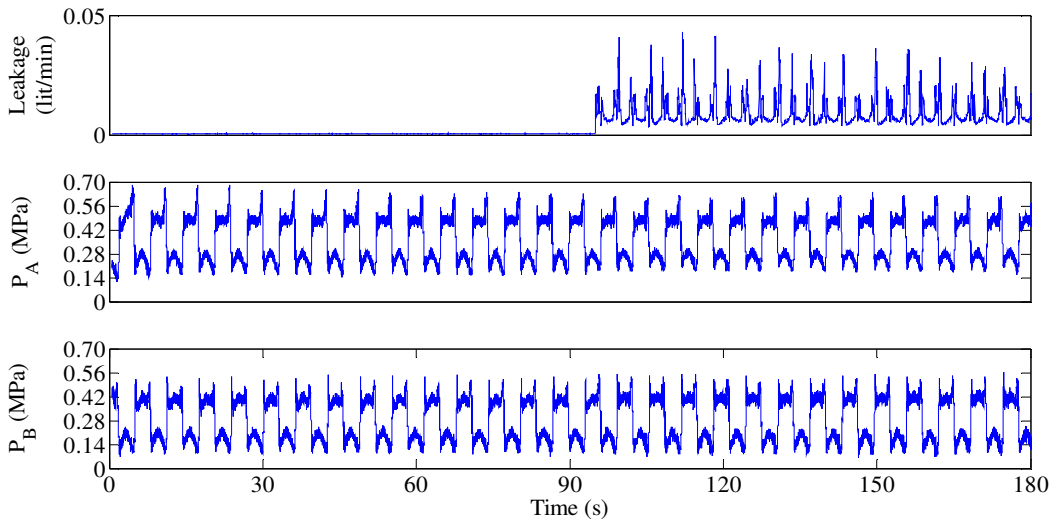


Fig. 5.32 Medium level of internal leakage shown with the pressures as P_A and P_B at both sides of the cylinder.

Pressure signals in both chambers of the cylinder are shown in Fig. 5.32 with a close-up view in Fig. 5.33 which is also equipped with the internal leakage plot showing the level of flow in terms of lit/min from the needle valve used to create the leak.

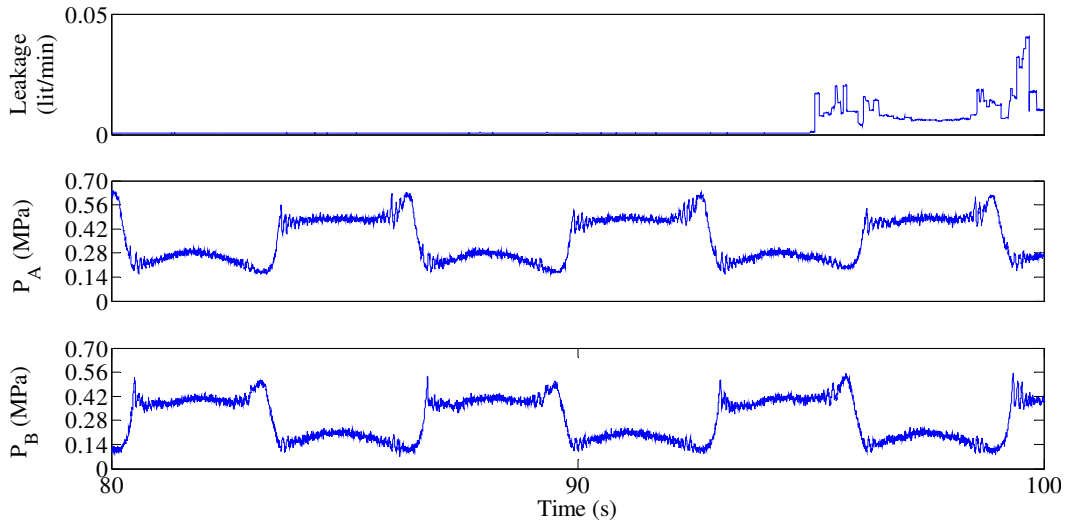


Fig. 5.33 Close-up view from 80th to 100th seconds to show the behaviour of Fig. 5.32.

The wavelet analysis on pressure signals P_A and P_B is shown in Figs. 5.34 and 5.37. The change in the peaks of the signal in d_3 , d_4 and d_3d_4 reflects the detection of fault.

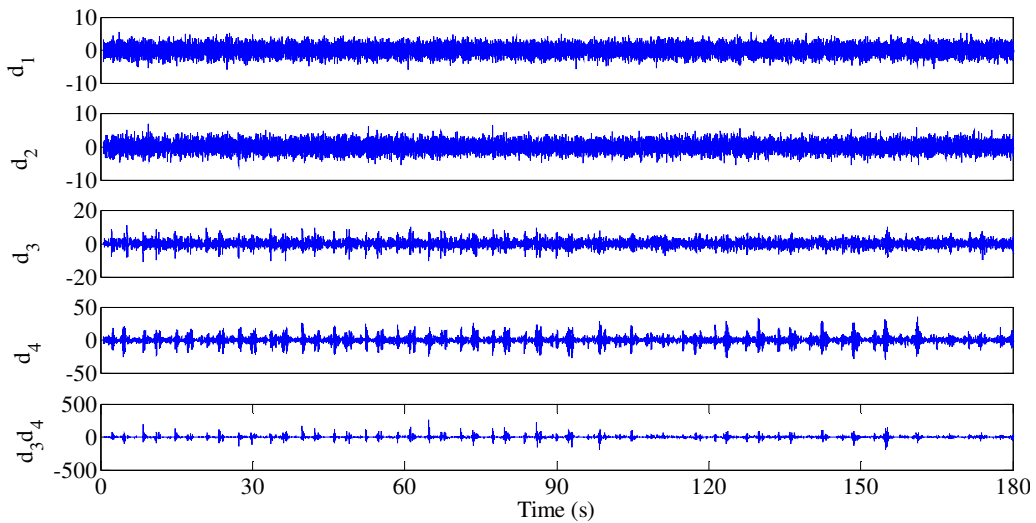


Fig. 5.34 Four-level detail wavelet coefficients of P_A pressure signal shown in Fig. 5.32.

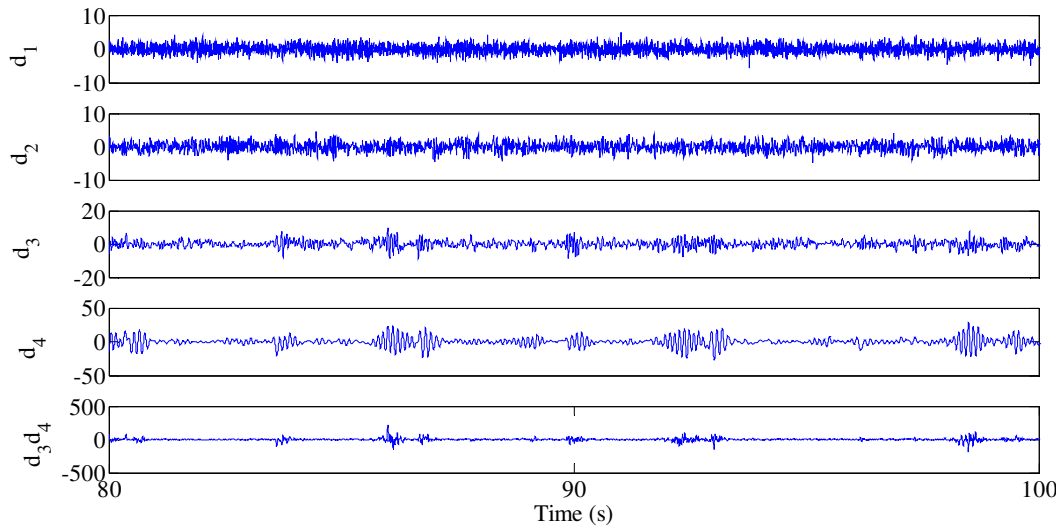


Fig. 5.35 Close-up view from 80th to 100th seconds to show the behaviour of Fig. 5.34.

The changes in the RMS value curves of d_3 and d_3d_4 that were obtained by using wavelet transform on pressure signal P_A prove that wavelet analysis is efficiently able to detect the fault created in the test rig as shown in Fig. 5.36.

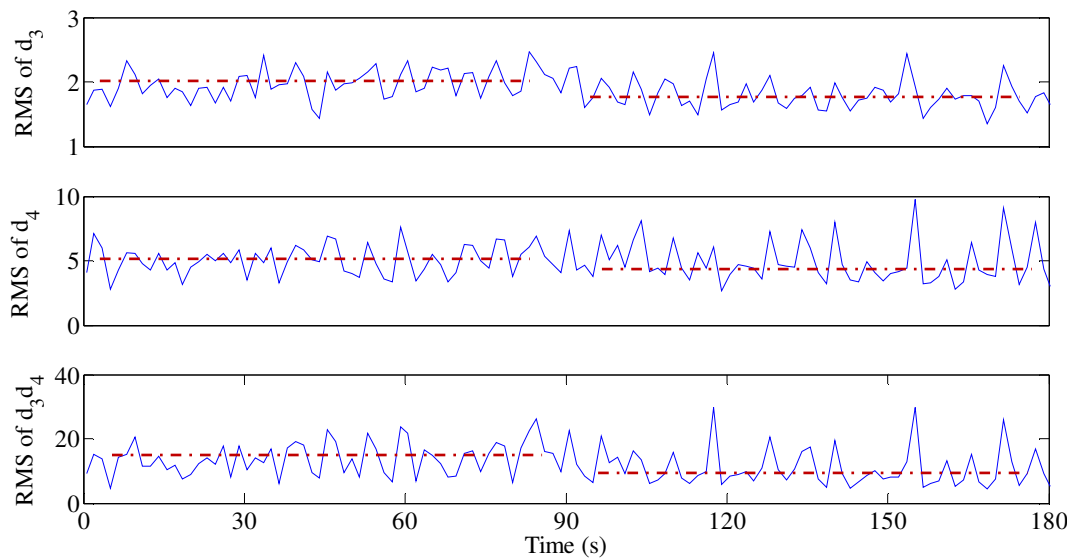


Fig. 5.36 RMS values of wavelet coefficient, d_3 , d_4 and d_3d_4 as shown in Fig. 5.34.

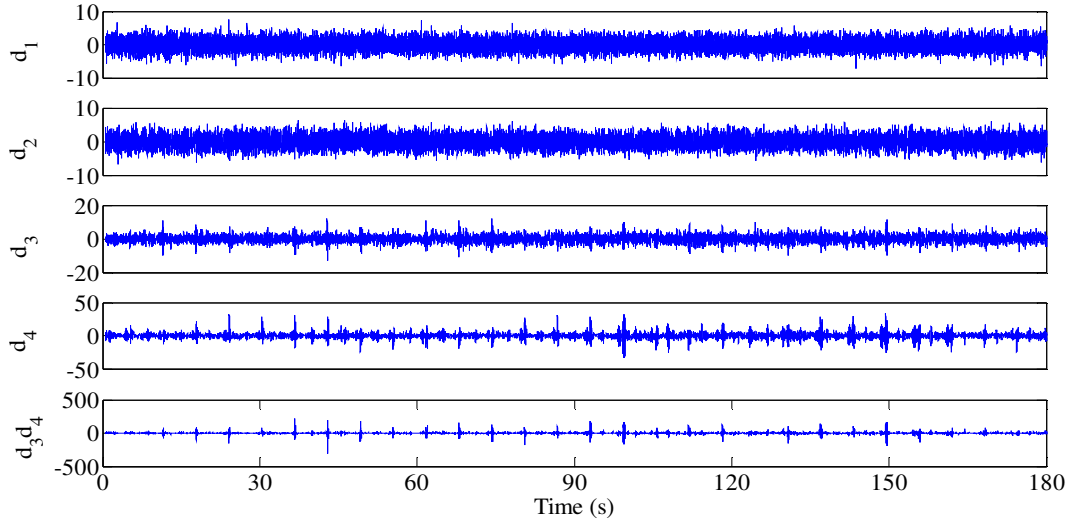


Fig. 5.37 Four-level detail wavelet coefficients of P_B pressure signal shown in Fig. 5.32.

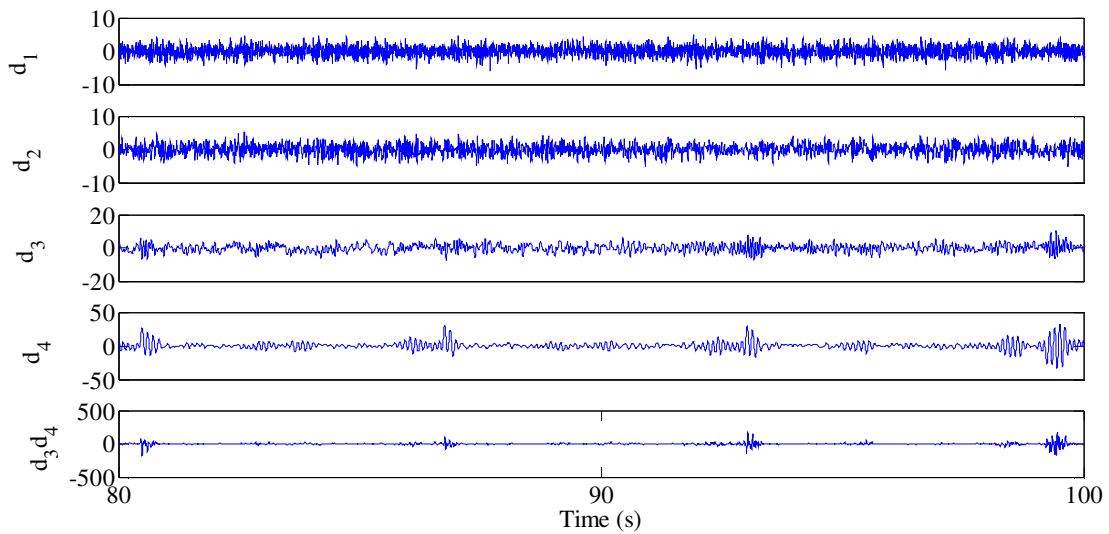


Fig. 5.38 Close-up view from 80th to 100th seconds to show the behaviour of Fig. 5.37.

According to Fig. 5.39, the RMS curves of d_4 and d_3d_4 detail the coefficients obtained from pressure signal P_B which show prominent changes in the values, further demonstrating the sensitivity of this diagnostic and detection methodology.

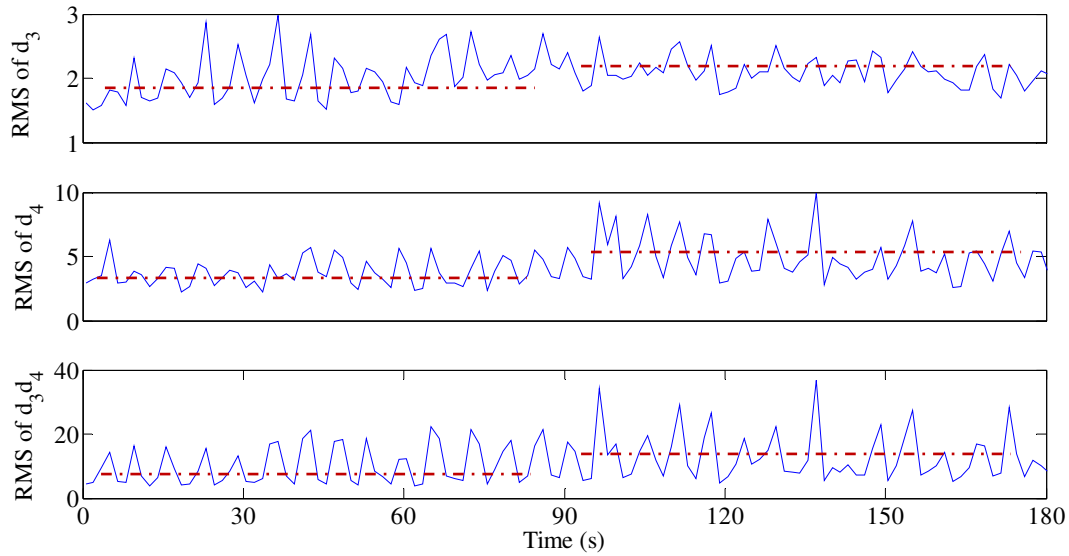


Fig. 5.39 RMS values of wavelet coefficient, d_3 , d_4 and d_3d_4 as shown in Fig. 5.37.

5.4 Small Leak

As with the test outlined in the previous section, the leak for this test has again been reduced to half of the level of the fault in section 5.3. The aim of reducing the leak is to determine the effectiveness of wavelet analysis in detecting smaller level of leaks. In this category, the same inputs are used as above, with the only difference being the reduced level of internal leakage.

a) This experiment uses small amplitude of 3 volts and a frequency of 4 rad/s as an input for sine waves in an attempt to detect a small-level internal leak. Figures 5.40 and 5.41 show the pressure signals P_A and P_B obtained at both ends of the cylinder (now with a reduced level of internal leakage) along with a close-up view that has been provided to allow for a better understanding of how these pressure signals behave.

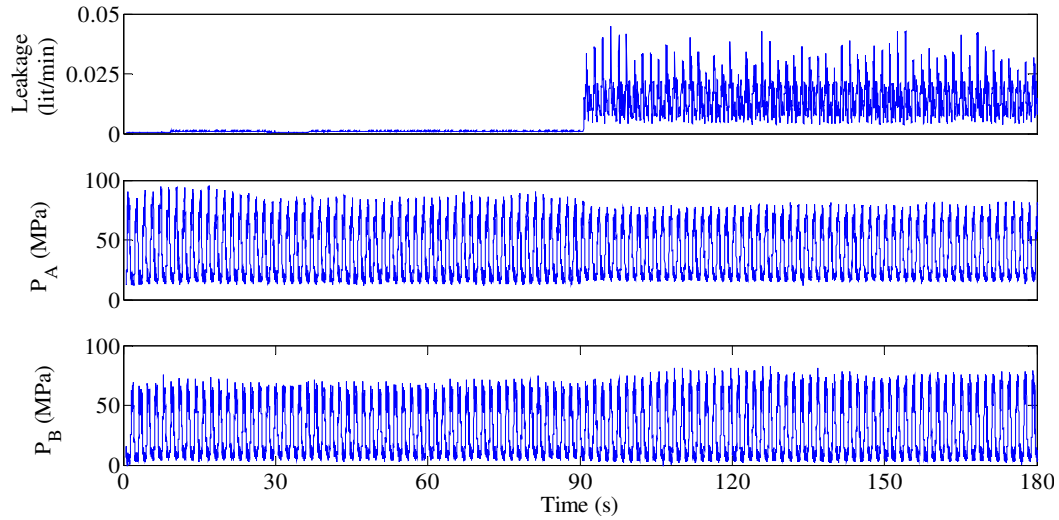


Fig. 5.40 Small level of internal leakage shown with the pressures as P_A and P_B at both sides of the cylinder.

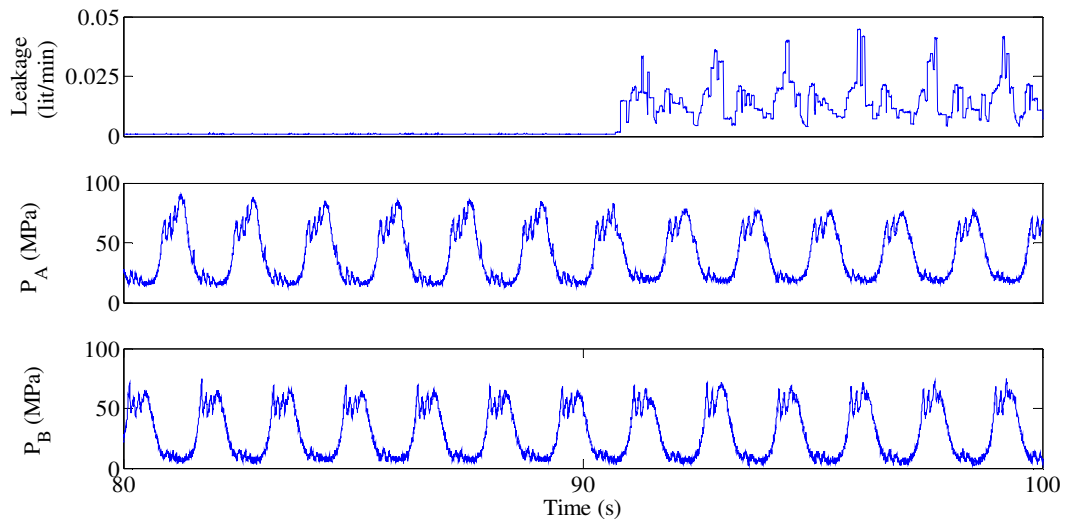


Fig. 5.41 Close-up view from 80th to 100th seconds to show the behaviour of Fig. 5.40.

Figures 5.42 and 5.45 reflect the detail coefficients obtained on the pressures of both cylinders. The 3rd and 4th level detail coefficients (d_3 and d_4) of Figs. 5.42 and 5.45 represent the differences in signal from non-leaking data and leaking data. The multiplication of d_3 and d_4

coefficients acts as the amplification of signals (labelled d_{3d_4}), and shows the significant effect of leakage during fault.

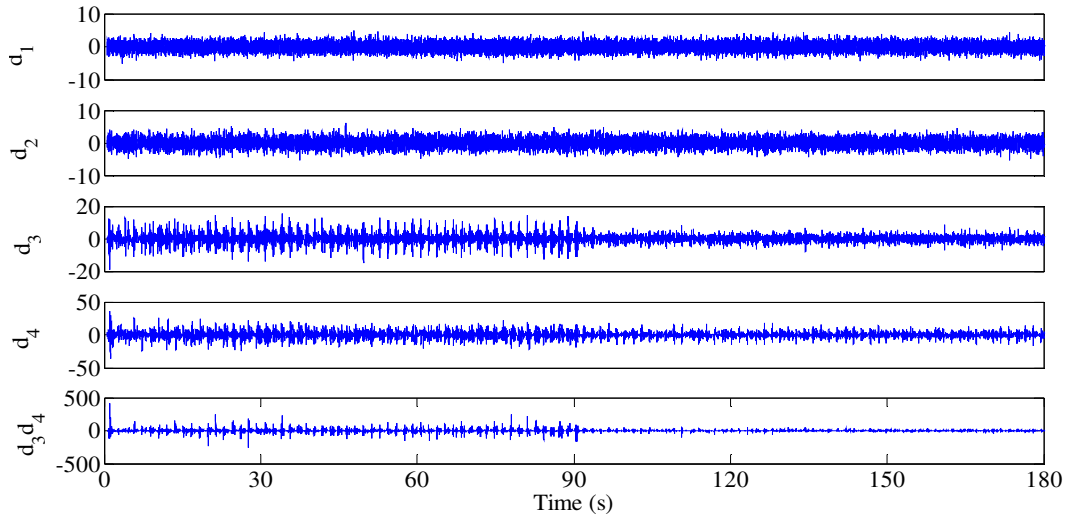


Fig. 5.42 Four-level detail wavelet coefficients of P_A pressure signal shown in Fig. 5.40.

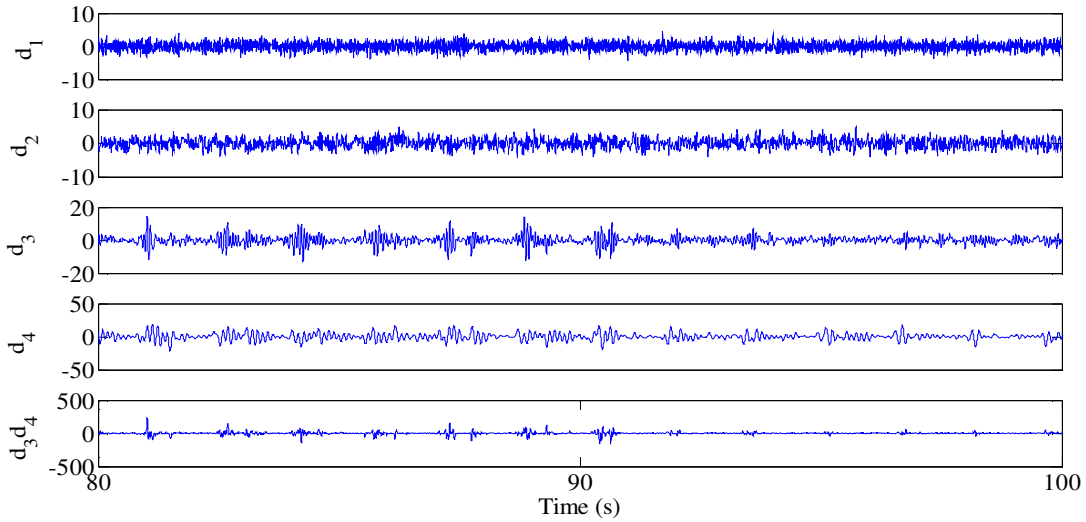


Fig. 5.43 Close-up view from 80th to 100th seconds to show the behaviour of Fig. 5.42.

The RMS curves of d_3 , d_4 and d_{3d_4} of pressure signal P_A show consistent changes in their values during leaking data in comparison to the non-leaking data which is indicated in Fig. 5.44.

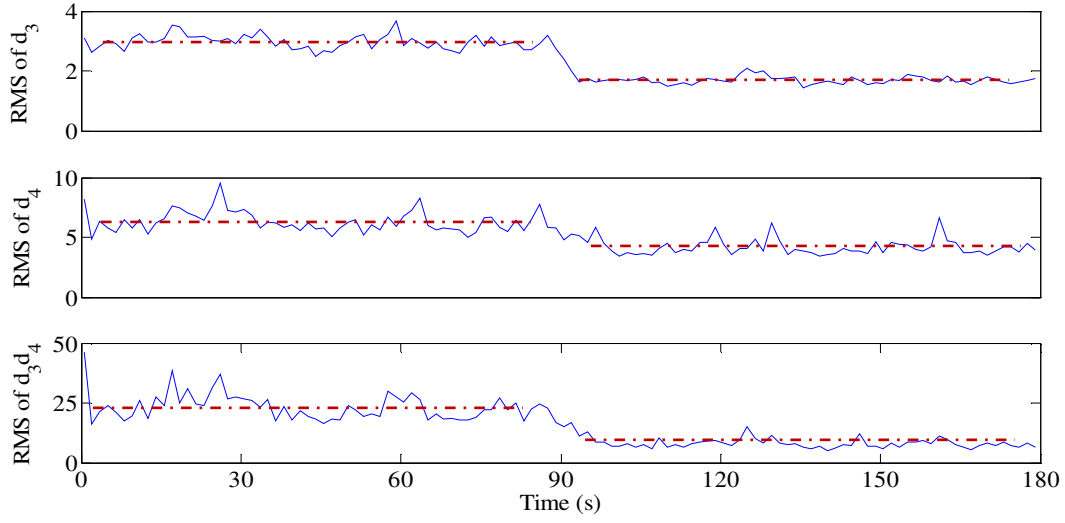


Fig. 5.44 RMS values of wavelet coefficient, d_3 , d_4 and d_3d_4 as shown in Fig. 5.42.

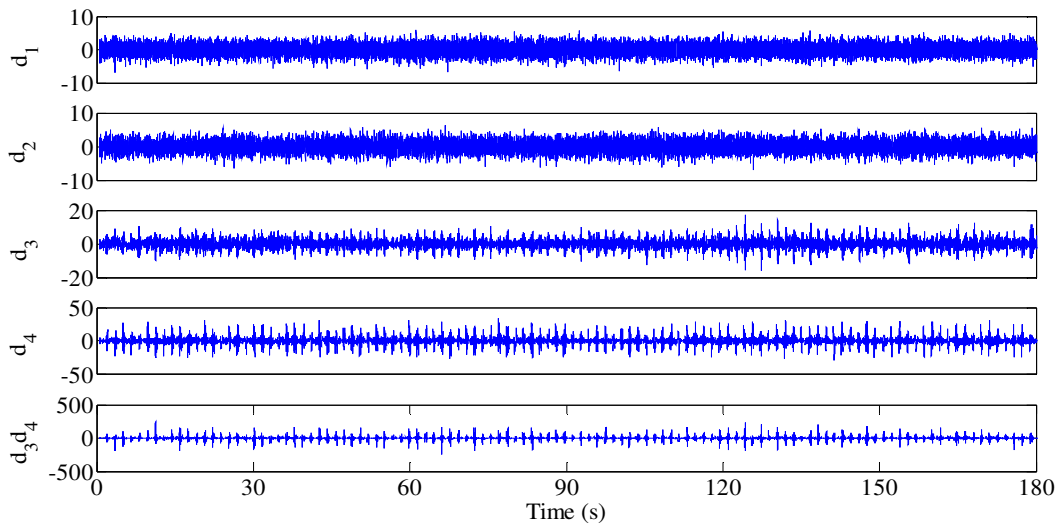


Fig. 5.45 Four-level detail wavelet coefficients of P_B pressure signal shown in Fig. 5.40.

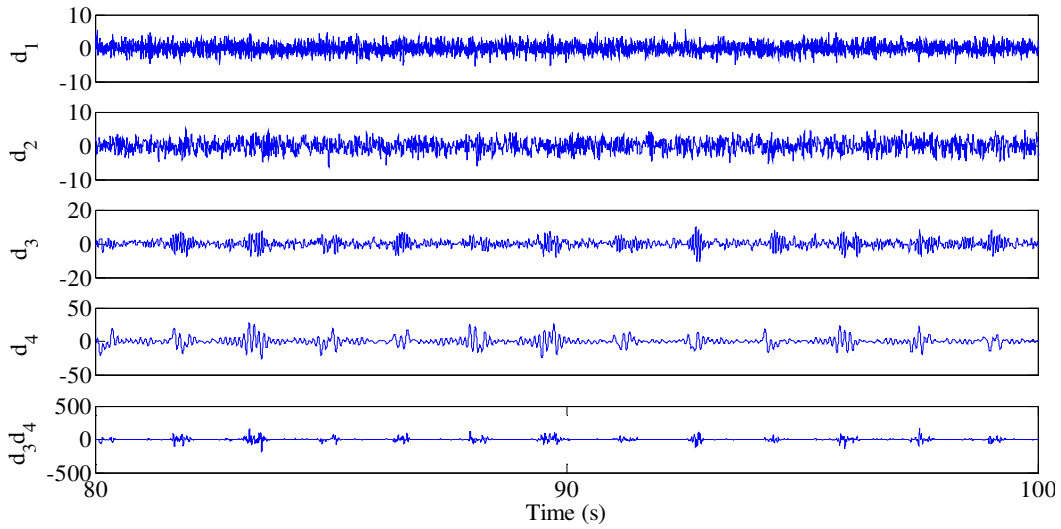


Fig. 5.46 Close-up view from 80th to 100th seconds to show the behaviour of Fig. 5.45.

The RMS curves of d_3 , d_4 and d_3d_4 of pressure signal P_B show reliable changes in values during leaking data compared to non-leaking data, and this is moderately visible in Fig. 5.47.

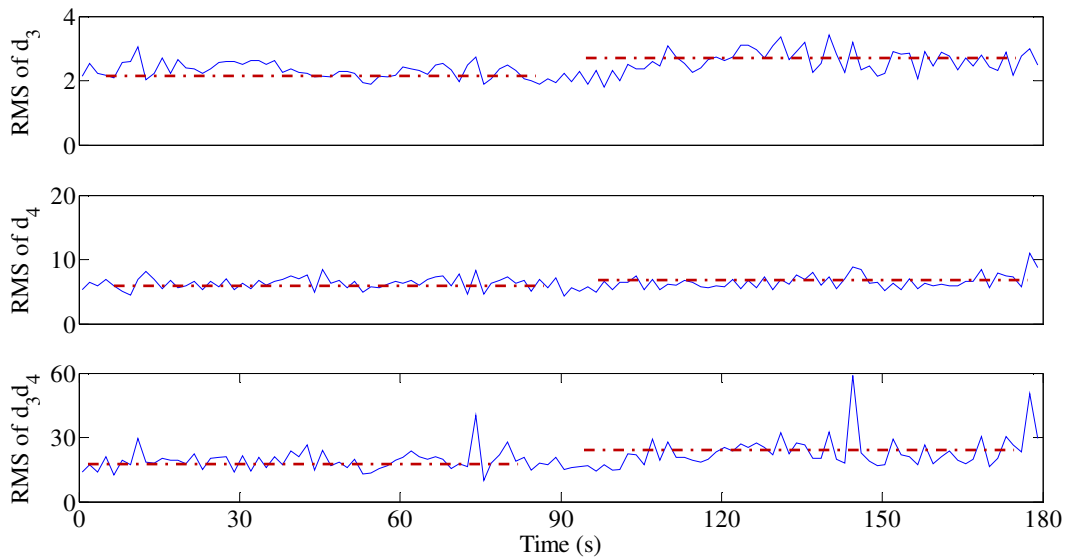


Fig. 5.47 RMS values of wavelet coefficient, d_3 , d_4 and d_3d_4 as shown in Fig. 5.45.

b) The second test for detecting a small level leak uses a sine wave having an amplitude of 8 volts and a frequency of 1 rad/s. Figures 5.48 and 5.49 show the pressure signals P_A and P_B obtained at both ends of the cylinder with the reduced level of the internal leakage along with a close-up view from 80th to 100th seconds of the pressure signals and internal leakage.

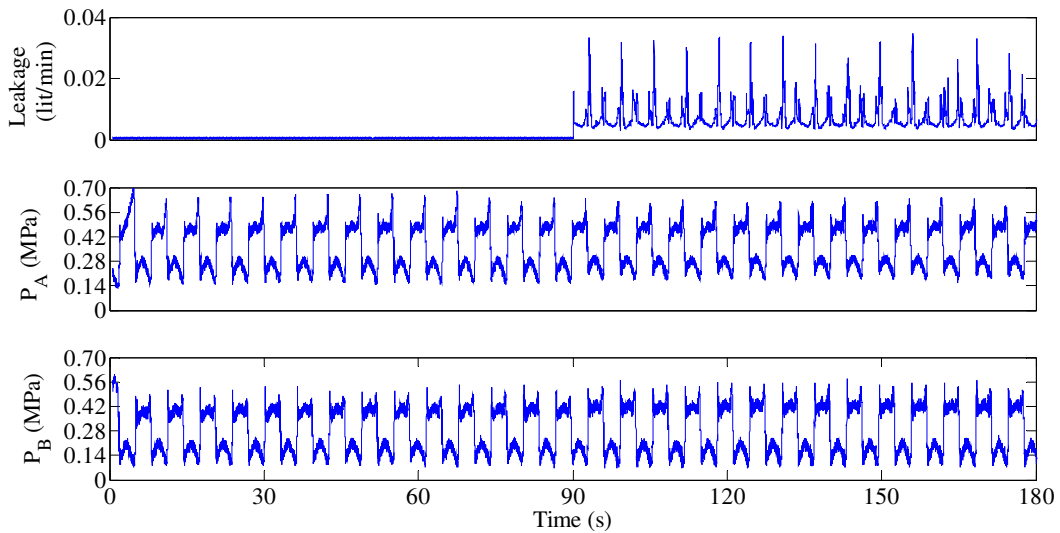


Fig. 5.48 Small level of internal leakage shown with the pressures as P_A and P_B at both sides of the cylinder.

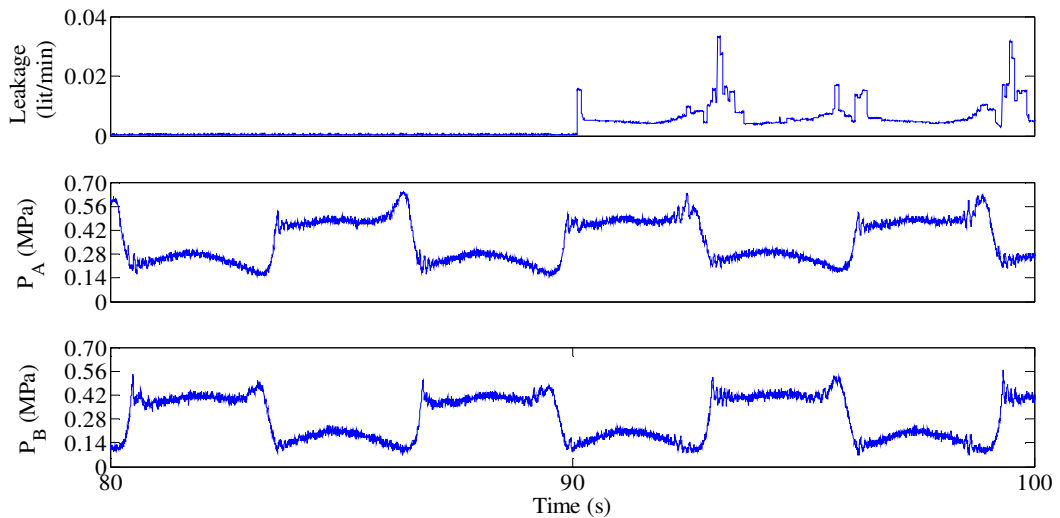


Fig. 5.49 Close-up view from 80th to 100th seconds to show the behaviour of Fig. 5.48.

Figures 5.50 and 5.53 reflect the detail coefficients obtained from the pressures of both cylinders. Amplified detail coefficient d_3d_4 (Figs. 5.50 and 5.53) shows the difference in signal between leaking data and non-leaking data. The multiplication of d_3 and d_4 coefficients acts as an amplification (labelled d_3d_4) which shows the significant effect of leakage during fault.

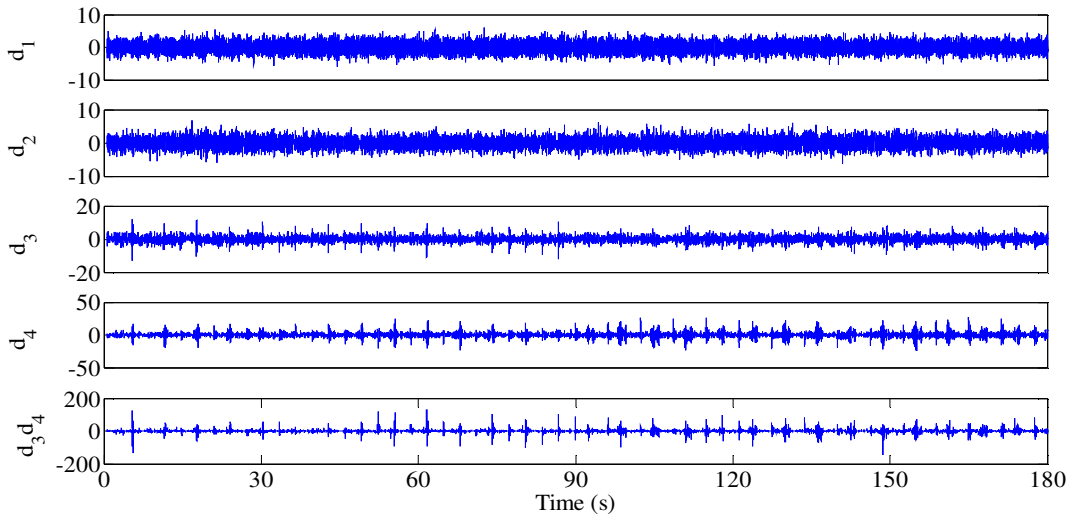


Fig. 5.50 Four-level detail wavelet coefficients of P_A pressure signal shown in Fig. 5.48.

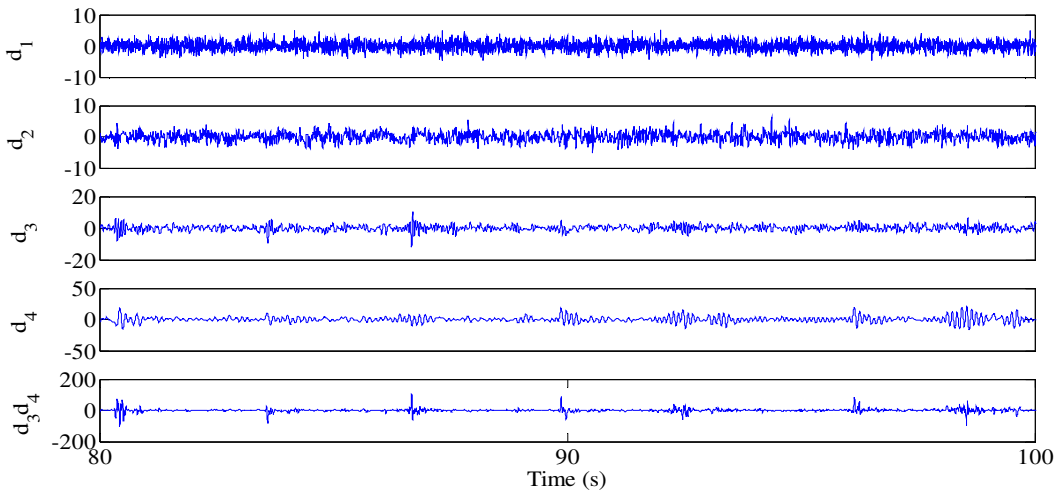


Fig. 5.51 Close-up view from 80th to 100th seconds to show the behaviour of Fig. 5.50.

The RMS curves of d_3 , d_4 and d_3d_4 of pressure signal P_A shows steady changes in the values during leaking data when compared to that of non-leaking data, and this is observable in Fig. 5.52.

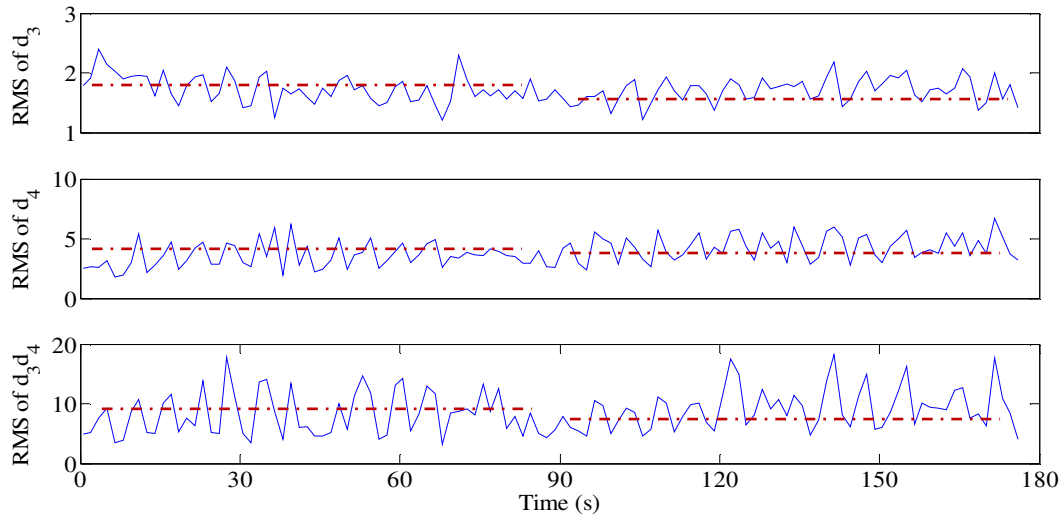


Fig. 5.52 RMS values of wavelet coefficient, d_3 , d_4 and d_3d_4 as shown in Fig. 5.50.

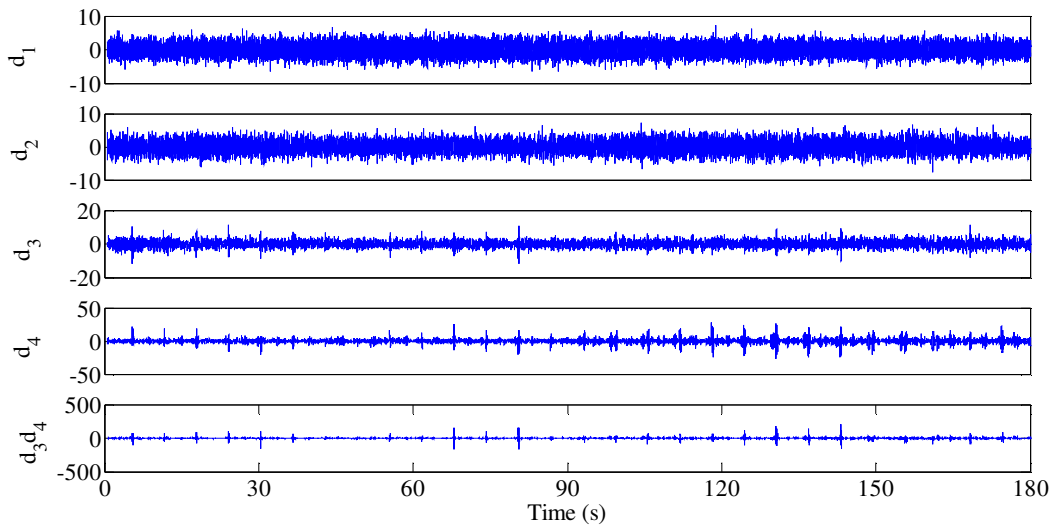


Fig. 5.53 Four-level detail wavelet coefficients of P_B pressure signal shown in Fig. 5.48.

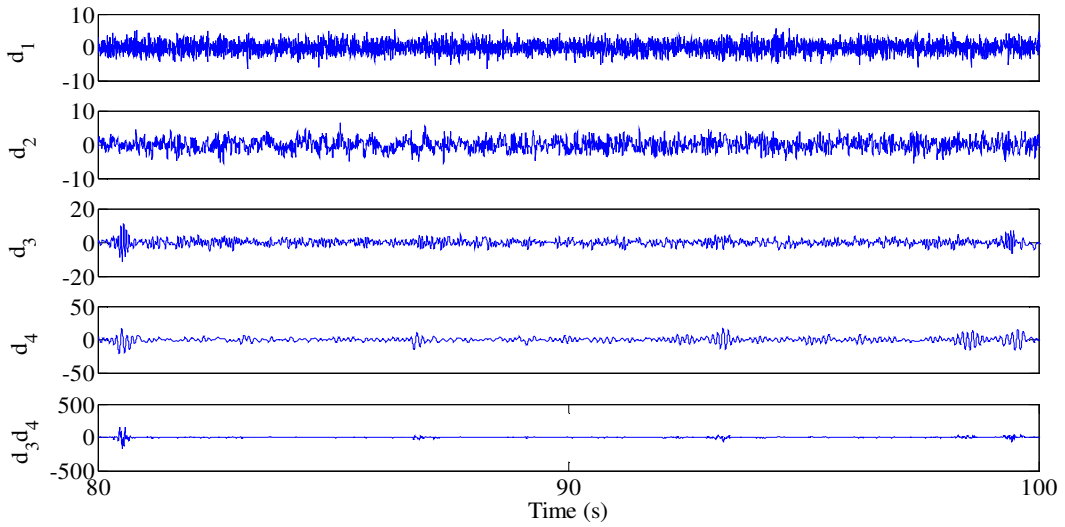


Fig. 5.54 Close-up view from 80th to 100th seconds to show the behaviour of Fig. 5.53.

The RMS curves of d_3 , d_4 and d_3d_4 of pressure signal P_B is consistent in expressing the changes in the values during leaking data when compared to non-leaking data which is comparatively visible in Fig. 5.55.

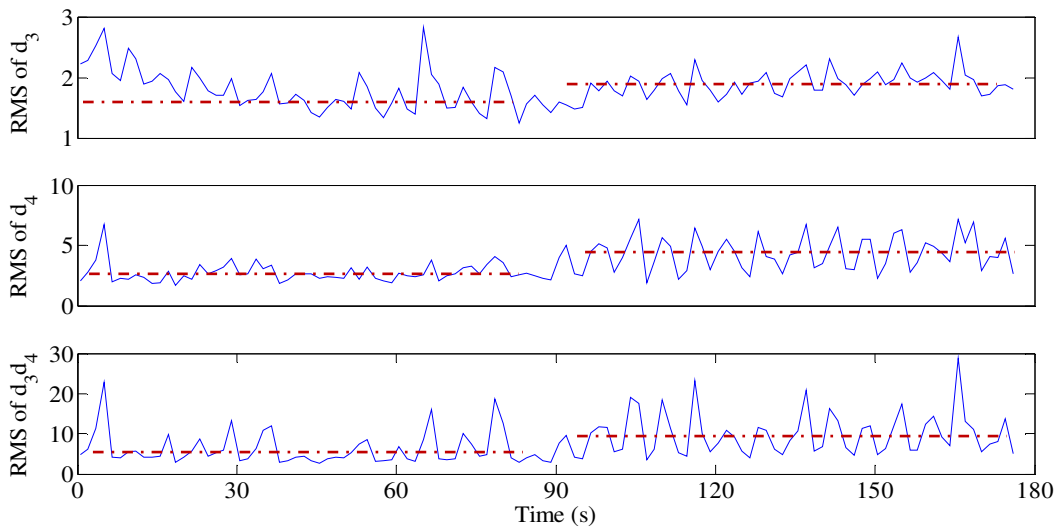


Fig. 5.55 RMS values of wavelet coefficient, d_3 , d_4 and d_3d_4 as shown in Fig. 5.53.

5.5 Extra-Small Leak

For this test, the leak is reduced to 1/16 the level of the large leak used in section 5.2. Here the system is tested using an extra-small level fault as the last trial for wavelet transform analysis. Since the leakage is so small, its effect on the Electro-Hydrostatic Actuation system is very subtle and, because of this, more tests must be done using the wavelet method to ensure that the results are reliable. Therefore, in order to determine the ability and efficiency of Wavelet transform, and the performance of db8 as a mother wavelet, four experiments are shown below using extra-small leakage conditions in which there will be no leakage for the first 90 seconds, and a small leak will be introduced for the final 90 seconds. The tests are conducted on $3\sin(4t)$, $7\sin(4t)$, $5\sin(2t)$ and $8\sin(1t)$ input conditions which have variable amplitude and frequency.

- a) For this test, small amplitude of 3 volts and a frequency of 4 rad/s are used as a sine wave input. The pressures recorded in chambers A and B of the cylinder are shown in Fig. 5.56 and Fig.5.57 provides a close-up view along with the level of internal leakage.

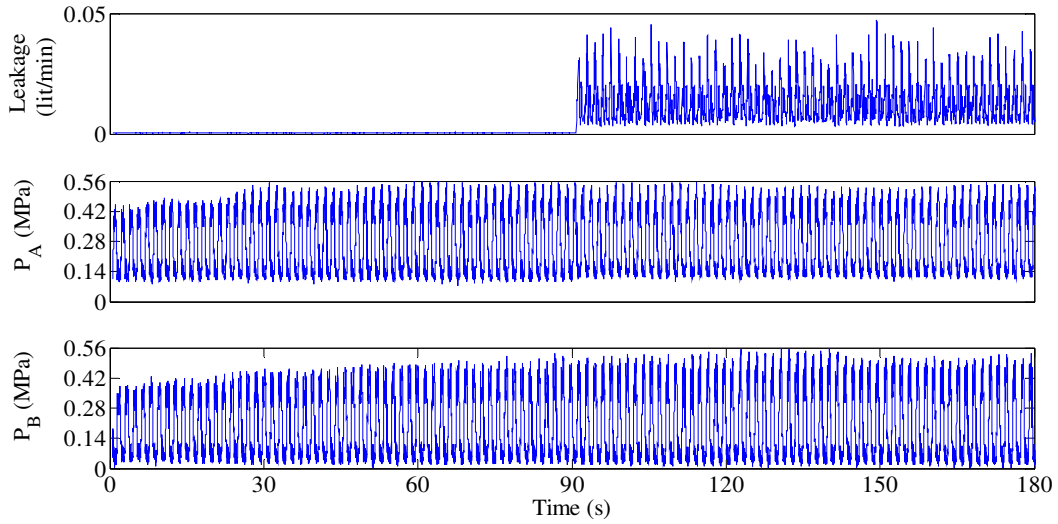


Fig. 5.56 Extra-small level of internal leakage shown with the pressures as P_A and P_B at both sides of the cylinder.

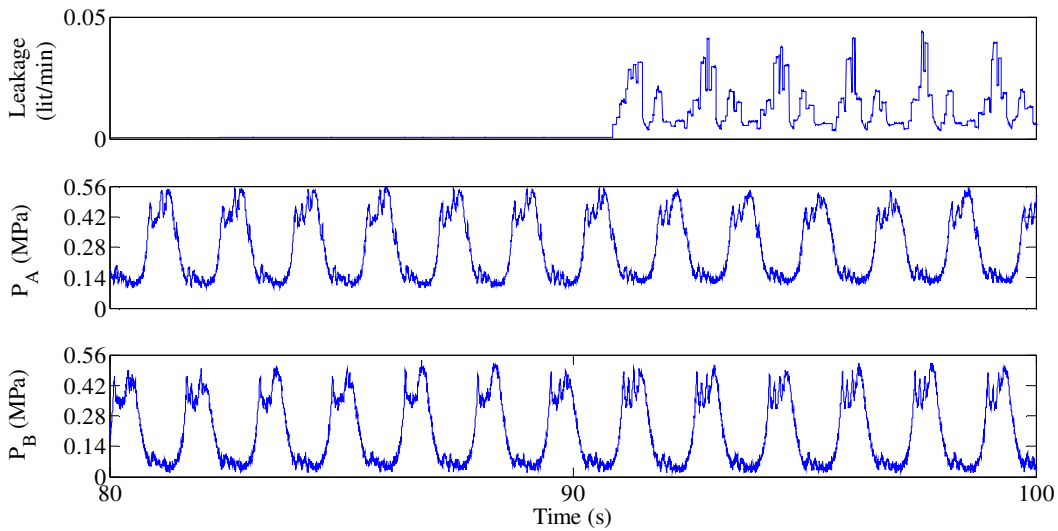


Fig. 5.57 Close-up view from 80th to 100th seconds to show the behaviour of Fig. 5.56.

In Figs. 5.58 and 5.61, the 3rd and 4th level of detail coefficient (d_3 and d_4) along with their amplification (d_3d_4) signify the leak which is represented by the change in the plotted data. The close-up view of the 80th to 100th seconds of detail coefficients of P_A and P_B also helped in

observing the behaviour of the wavelet transform during leakages which can be seen in Figs. 5.59 and 5.62.

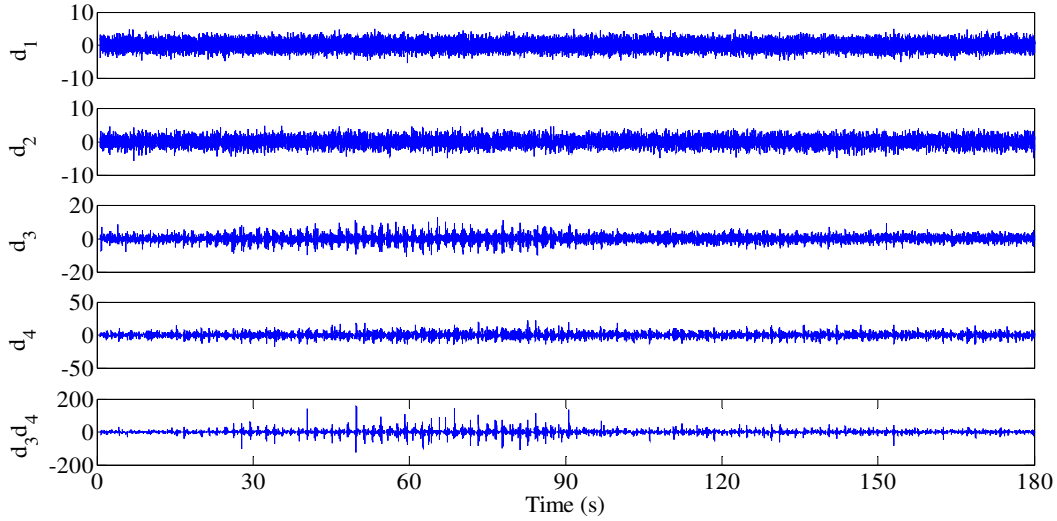


Fig. 5.58 Four-level detail wavelet coefficients of P_A pressure signal shown in Fig. 5.56.

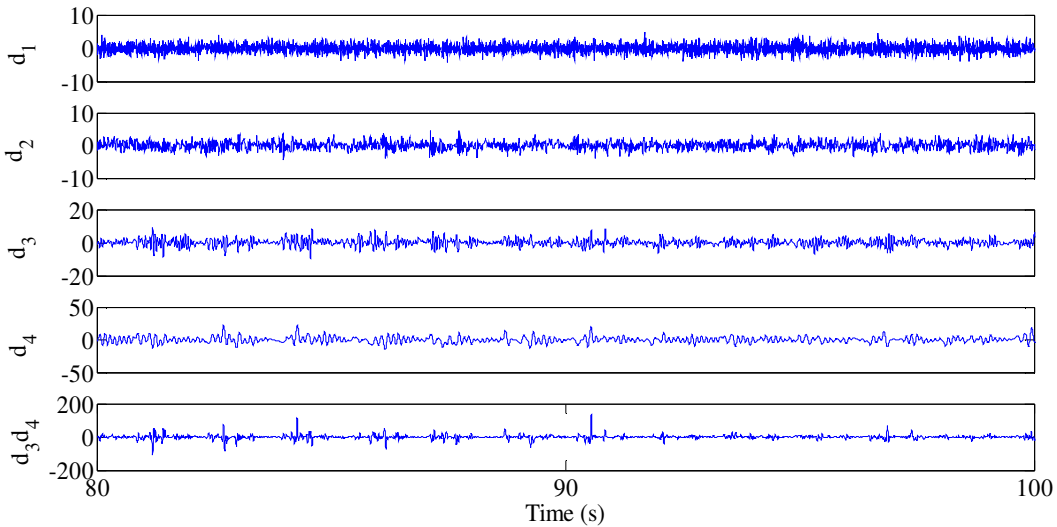


Fig. 5.59 Close-up view from 80th to 100th seconds to show the behaviour of Fig. 5.58.

The RMS curves of d_3 , d_4 and d_3d_4 of pressure signal P_A is constant in expressing the changes in the values during leaking data compared to the non-leaking data which is relatively visible in Fig. 5.60.

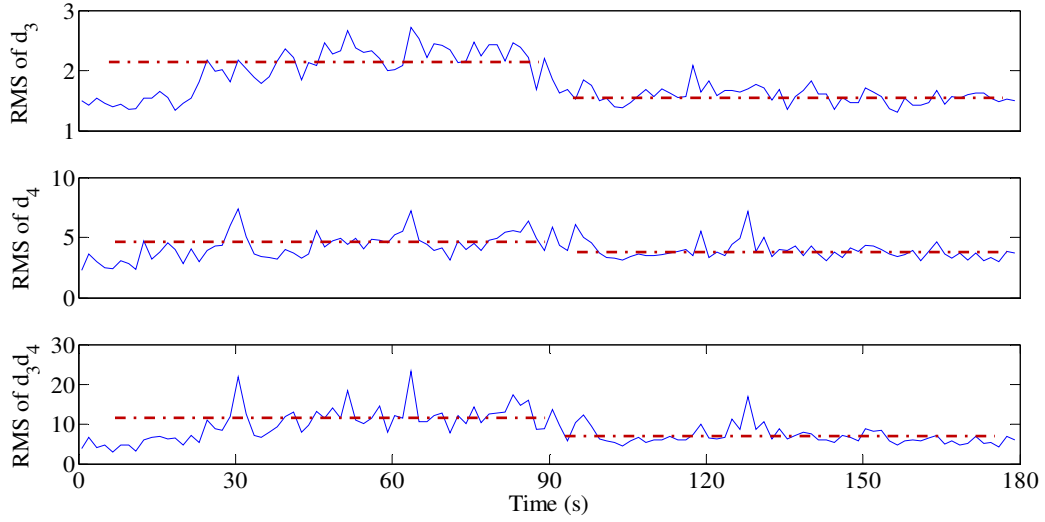


Fig. 5.60 RMS values of wavelet coefficient, d_3 , d_4 and d_3d_4 as shown in Fig. 5.58.

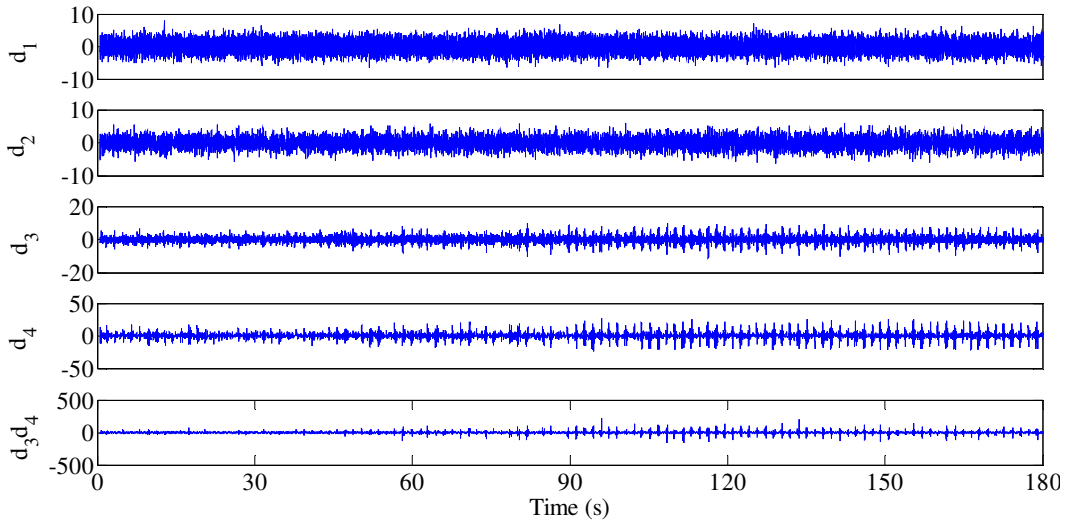


Fig. 5.61 Four-level detail wavelet coefficients of P_B pressure signal shown in Fig. 5.56.

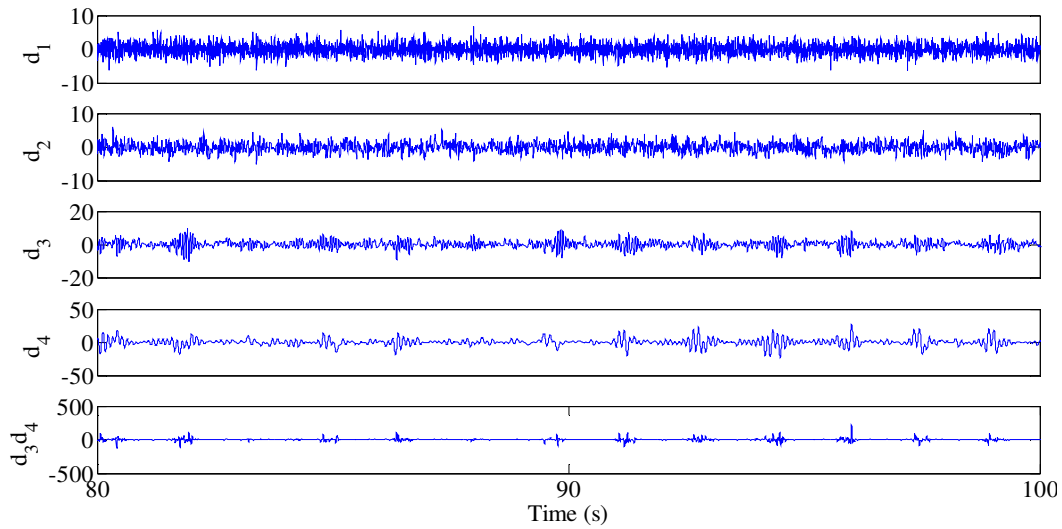


Fig. 5.62 Close-up view from 80th to 100th seconds to show the behaviour of Fig. 5.61.

The RMS curves of d_3 , d_4 and d_3d_4 of pressure signal P_B are consistent in expressing the changes in the values during leaking data when compared to the non-leaking data which is quite visible in Fig. 5.63.

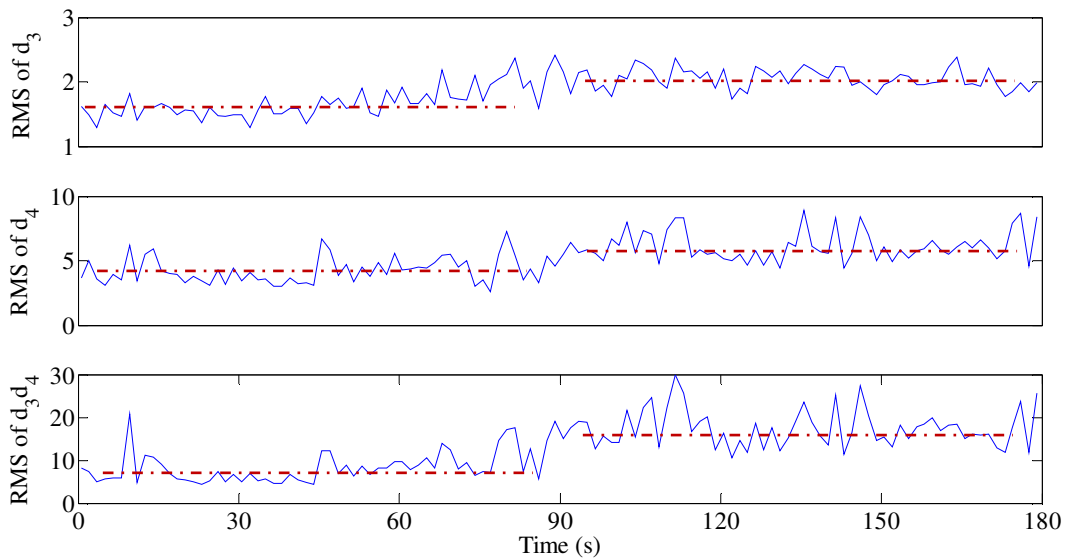


Fig. 5.63 RMS values of wavelet coefficient, d_3 , d_4 and d_3d_4 as shown in Fig. 5.61.

b) This test applies amplitude of 7 volts and a frequency of 4 rad/s as a sine wave input for the purpose of detecting an extra-small level internal leak as is shown in Fig. 5.64 and is elaborated by the close-up view in Fig. 5.65. Both graphs also present the angular velocity of the motor and displacement achieved by the piston. The pressures signals P_A and P_B obtained from both chambers of the cylinder are shown in Figs. 5.66 and 5.67.

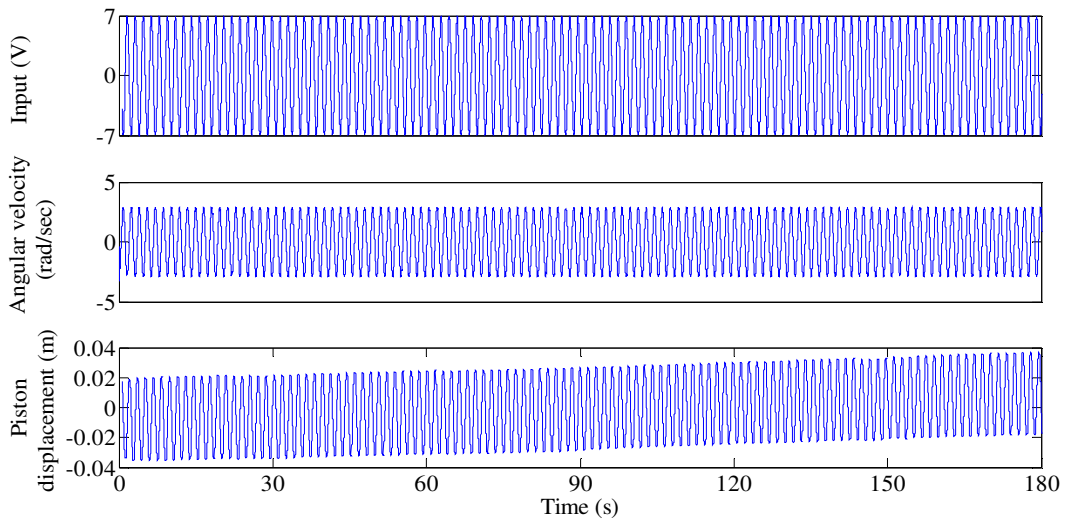


Fig. 5.64 Experimental input of $7\sin(4t)$ with angular velocity of motor and displacement of the piston.

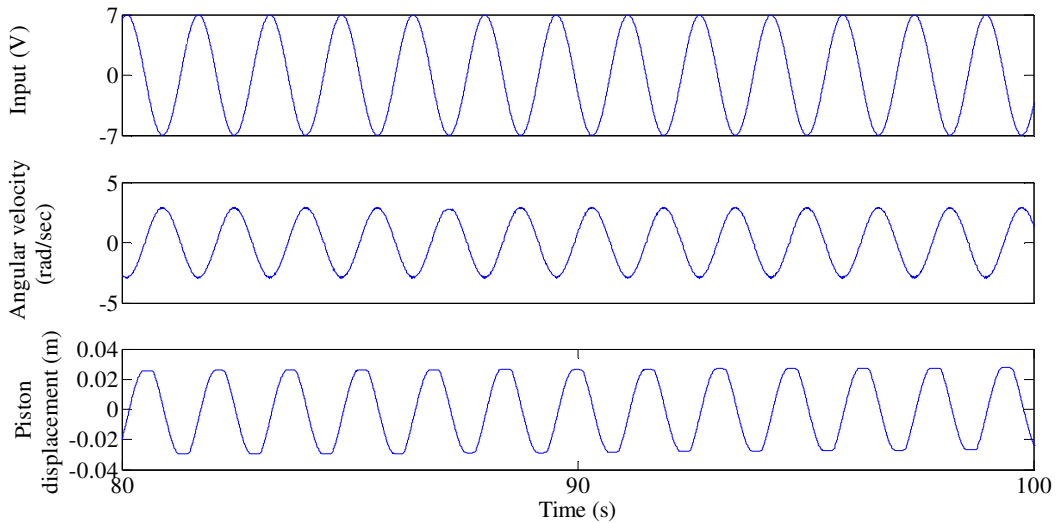


Fig. 5.65 Close-up view from 80th to 100th seconds to show the behaviour of Fig. 5.64.

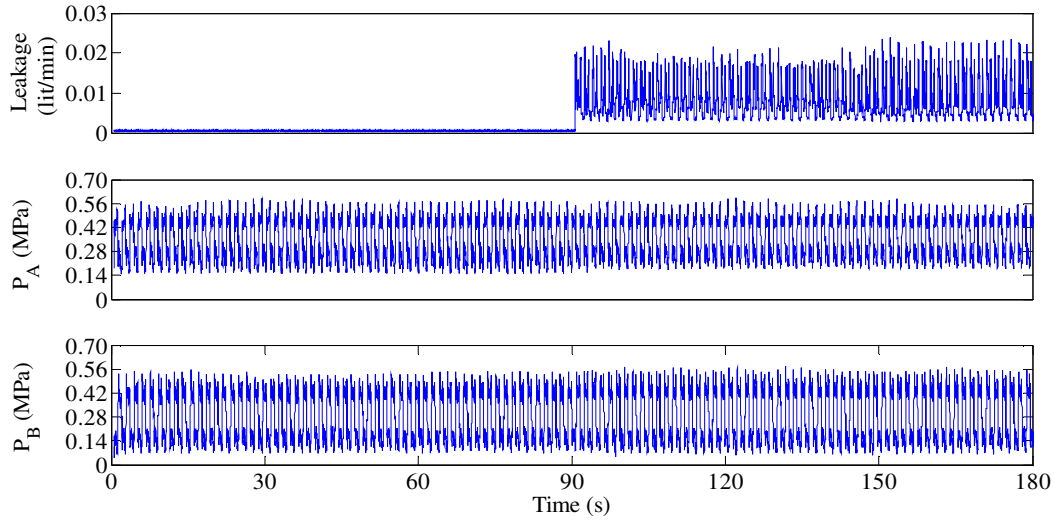


Fig. 5.66 Extra-Small level of internal leakage shown with the pressures as P_A and P_B at both sides of the cylinder.

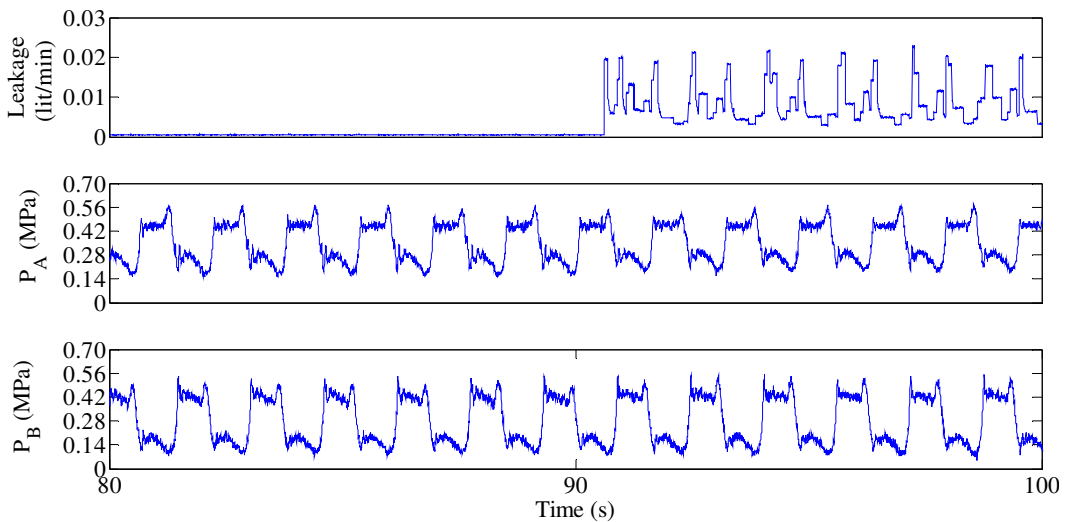


Fig. 5.67 Close-up view from 80th to 100th seconds to show the behaviour of Fig. 5.66.

In Figs. 5.68 and 5.71, the 3rd and 4th level of detail coefficient as d_3 and d_4 , along with amplified d_3d_4 , signify the leakage which is clearly indicated by the change in the plotted data. The close-up view from the 80th to 100th seconds of detail coefficients of P_A and P_B also help in observing the behaviour of the Wavelet transform during leakages which can be seen in Figs. 5.69 and 5.72.

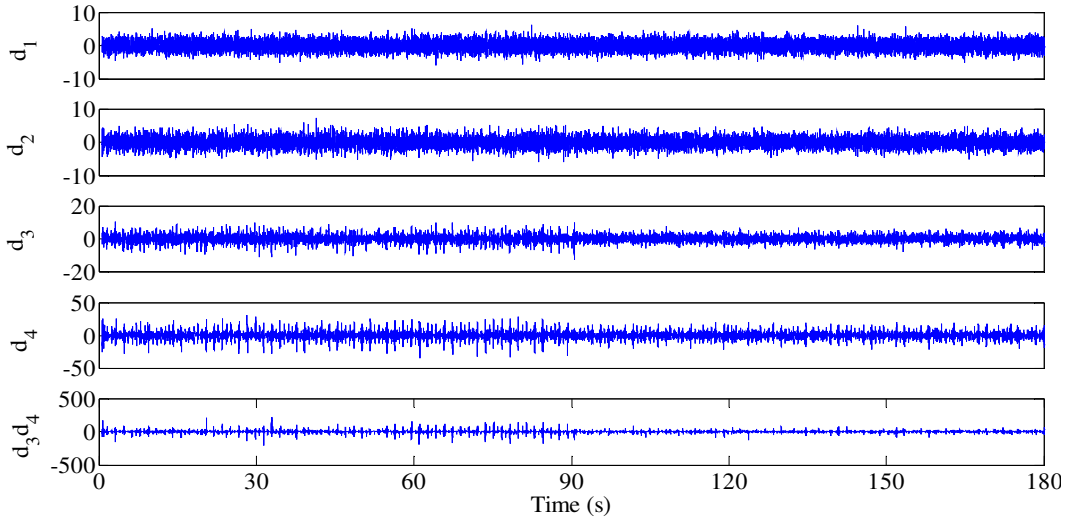


Fig. 5.68 Four-level detail wavelet coefficients of P_A pressure signal shown in Fig. 5.66.

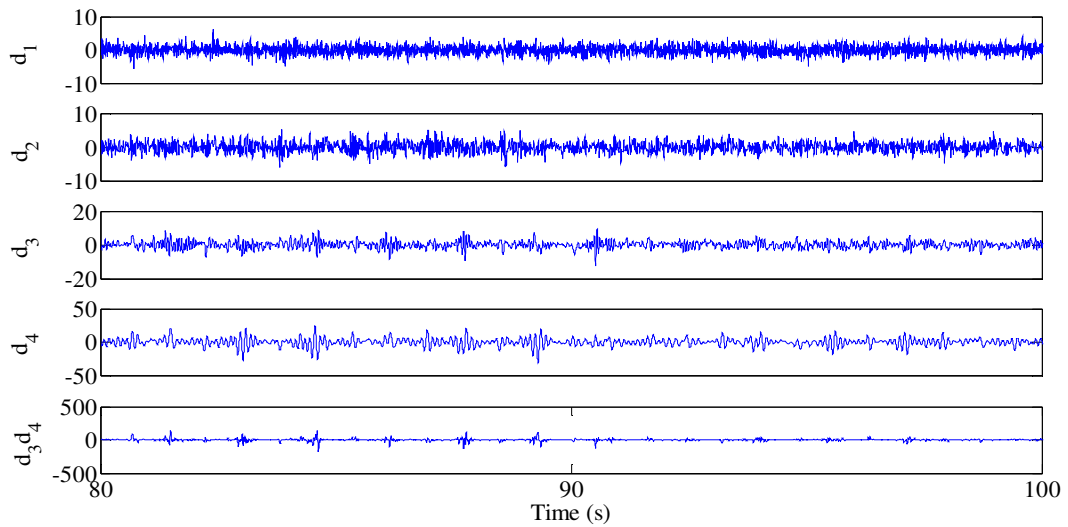


Fig. 5.69 Close-up view from 80th to 100th seconds to show the behaviour of Fig. 5.68.

The RMS curves of d_3 , d_4 and d_3d_4 of pressure signal P_A is standard in expressing the changes in the values during leaking data compared to the non-leaking data which is visible in Fig. 5.70.

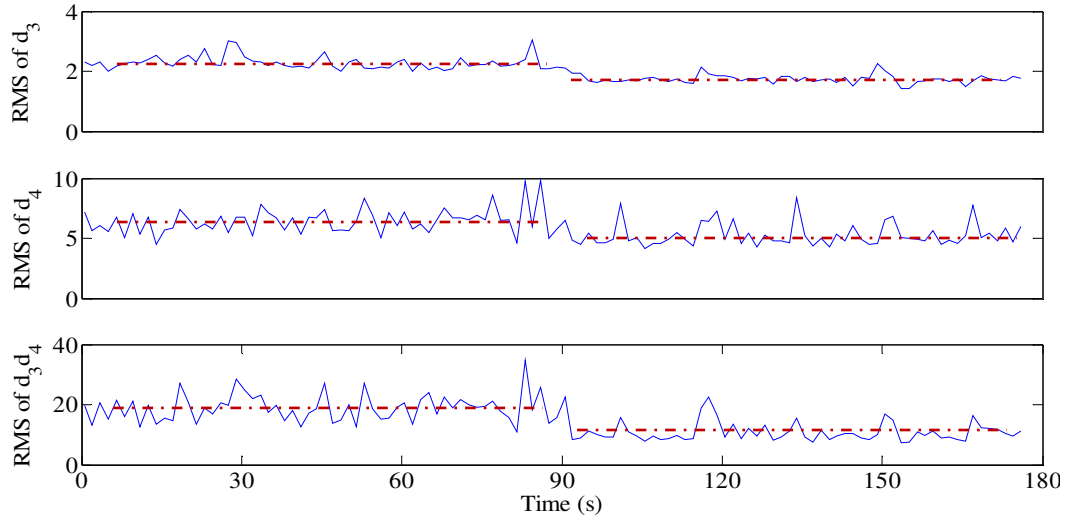


Fig. 5.70 RMS values of wavelet coefficient, d_3 , d_4 and d_3d_4 as shown in Fig. 5.68.

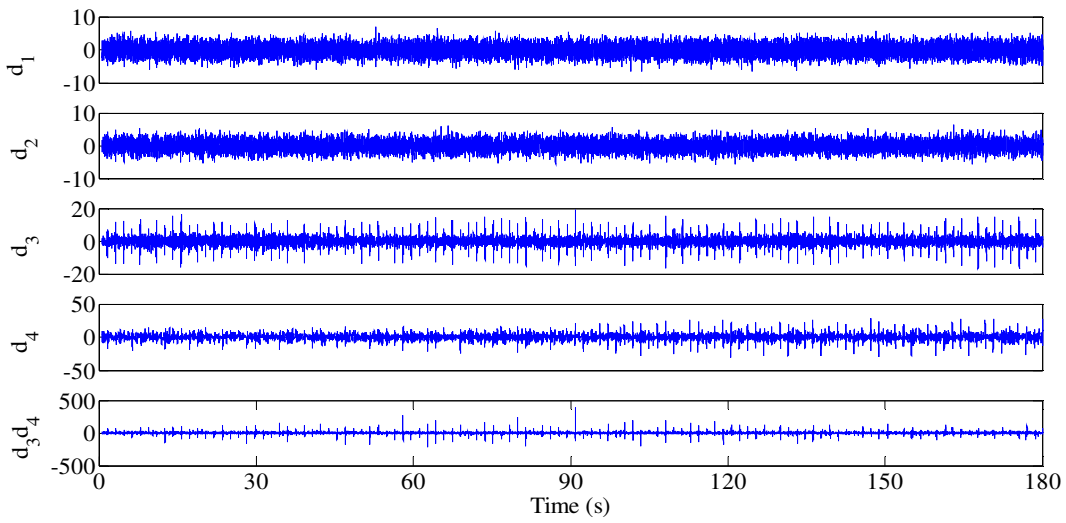


Fig. 5.71 Four-level detail wavelet coefficients of P_B pressure signal shown in Fig. 5.66.

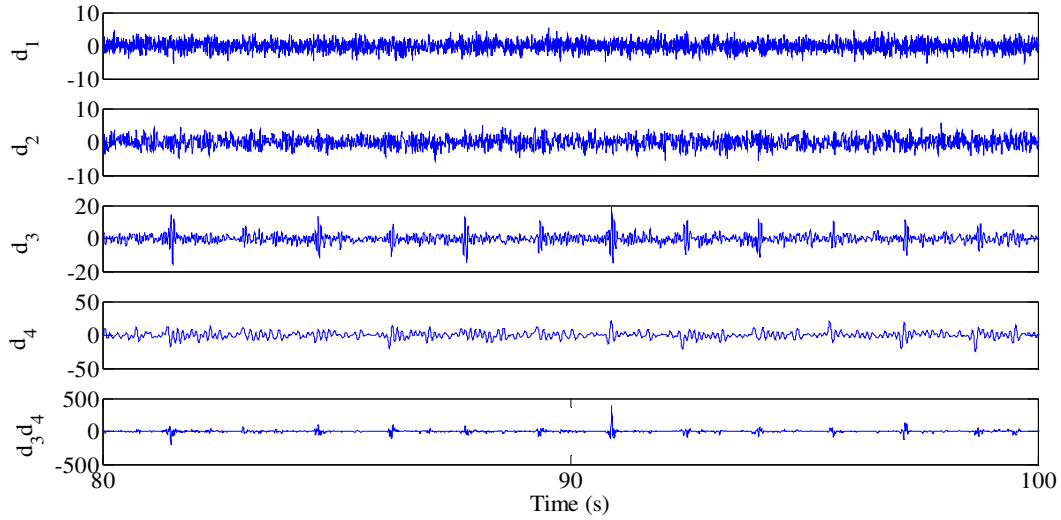


Fig. 5.72 Close-up view from 80th to 100th seconds to show the behaviour of Fig. 5.71.

The RMS curves of d_3 , d_4 and d_{3d_4} of pressure signal P_B is consistent in expressing the changes in the values during leaking data compared to non-leaking data, which is visible in Fig. 5.73.

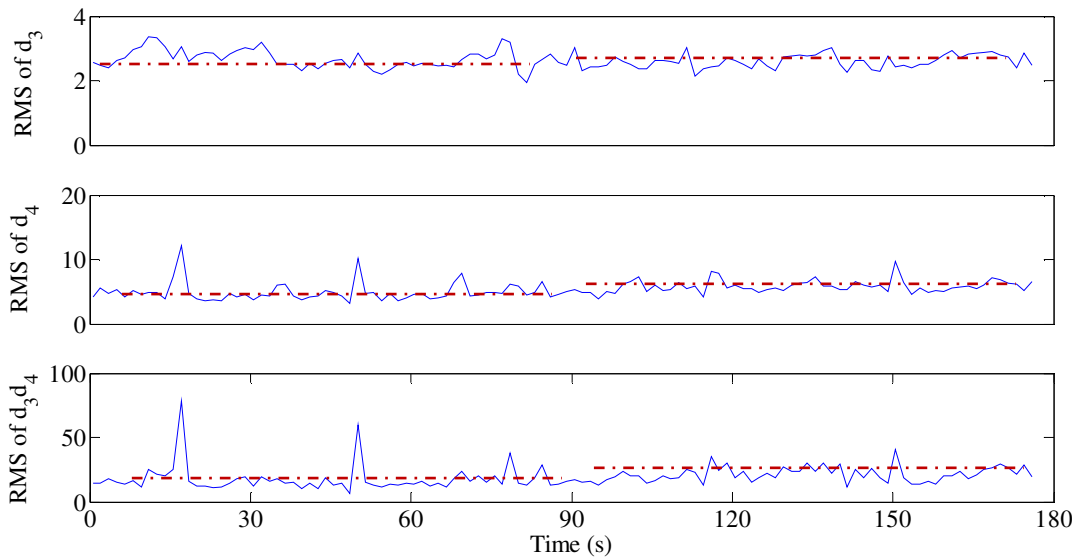


Fig. 5.73 RMS values of wavelet coefficient, d_3 , d_4 and d_{3d_4} as shown in Fig. 5.71.

c) The third experiment using extra-small internal leakage employs amplitude of 5 volts and a frequency of 2 rad/s as a sine wave input. As in the above experiments, the objective is to

identify extra-small level internal leakage, and fluctuations in pressure in pressures in chambers A and B of the cylinder. The results of these tests are shown in Figures 5.74 and 5.75 (close-up view).

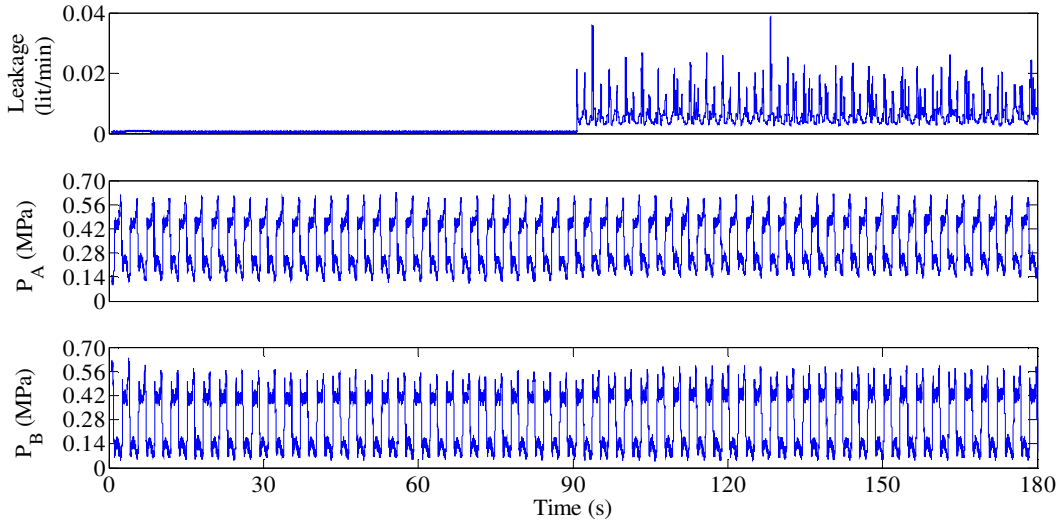


Fig. 5.74 Extra-small level of internal leakage shown with the pressures as P_A and P_B at both sides of the cylinder.

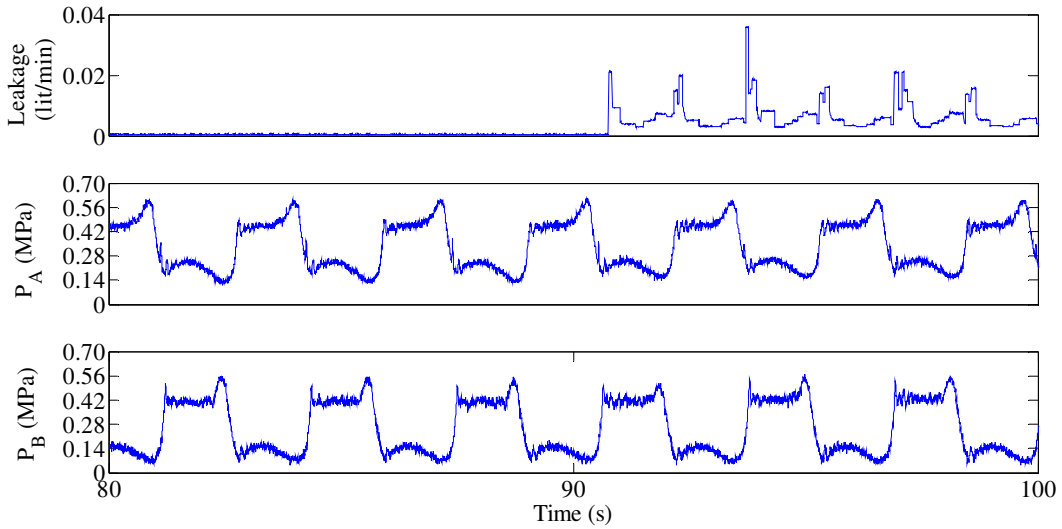


Fig. 5.75 Close-up view from 80th to 100th seconds to show the behaviour of Fig. 5.74.

In Figs. 5.76 and 5.79, the 3rd and 4th level of detail coefficient as d_3 and d_4 along with amplified d_3d_4 signify the leak through the change in the plotted data which is highly visible. The close-up view from the 80th to 100th seconds of the detail coefficients of P_A and P_B also help in observing the behaviour of the wavelet transform during leakages which can be seen in Figs. 5.77 and 5.80.

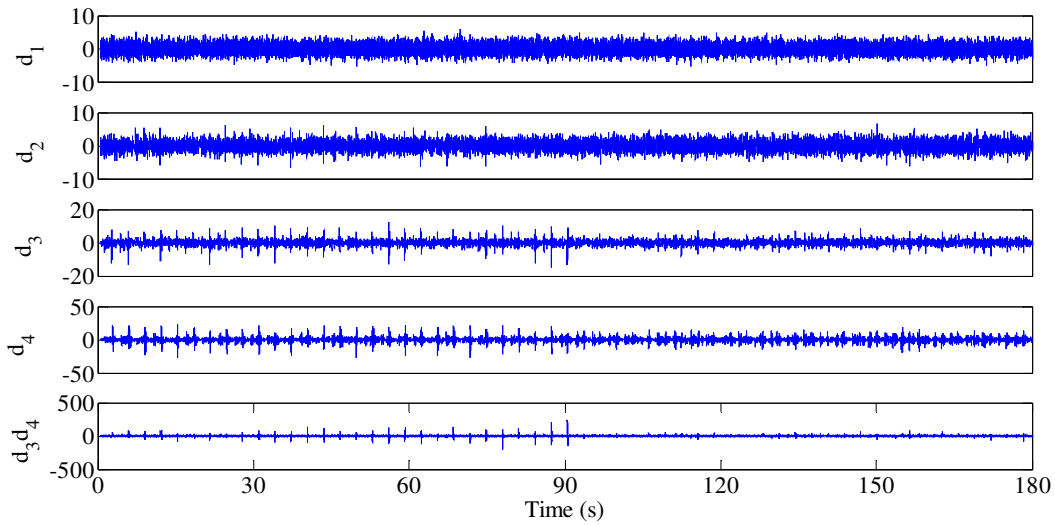


Fig. 5.76 Four-level detail wavelet coefficients of P_A pressure signal shown in Fig. 5.74.

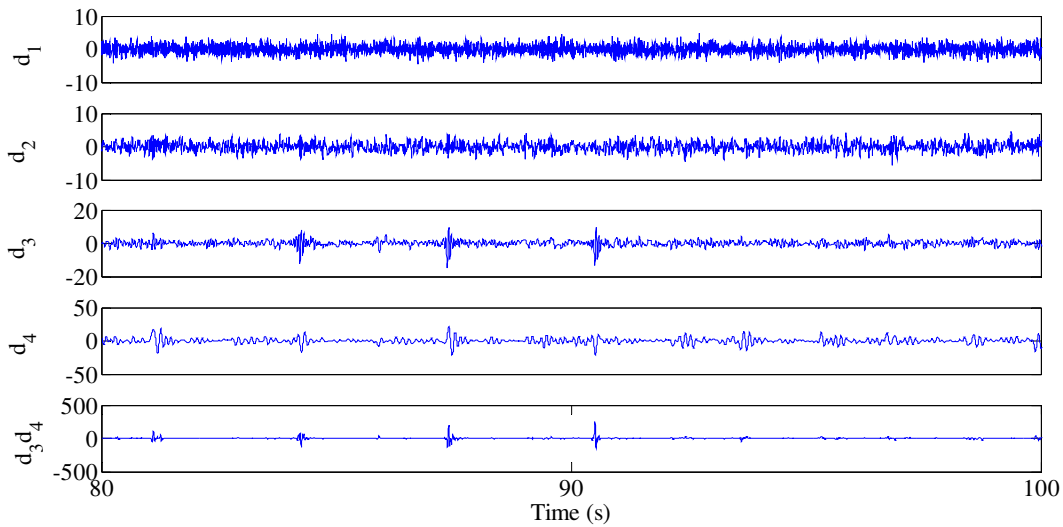


Fig. 5.77 Close-up view from 80th to 100th seconds to show the behaviour of Fig. 5.76.

The RMS curves of d_3 , d_4 and d_3d_4 of pressure signal P_A is habitual in expressing the changes in the values during leaking data when compared with the non-leaking data, This is evident in Fig. 5.78.

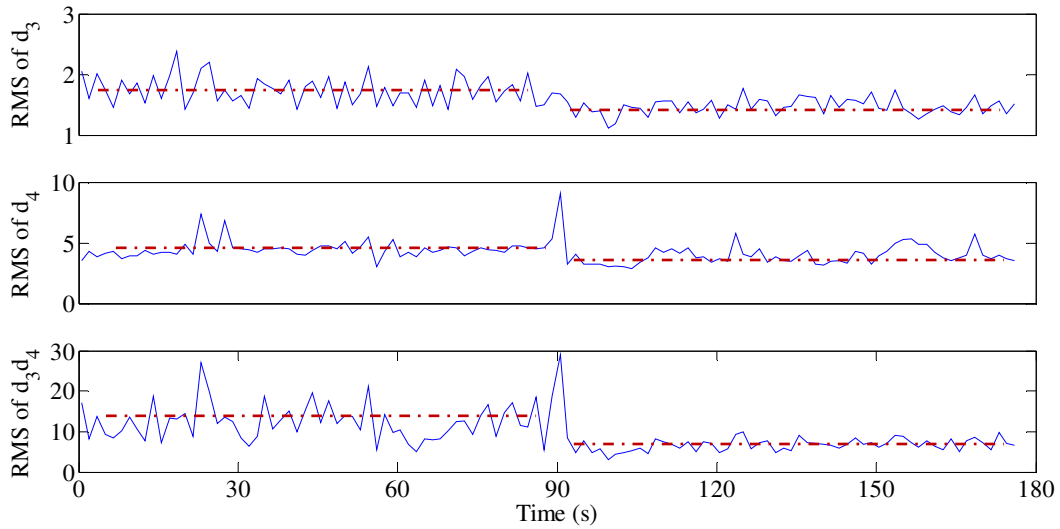


Fig. 5.78 RMS values of wavelet coefficient, d_3 , d_4 and d_3d_4 as shown in Fig. 5.76.

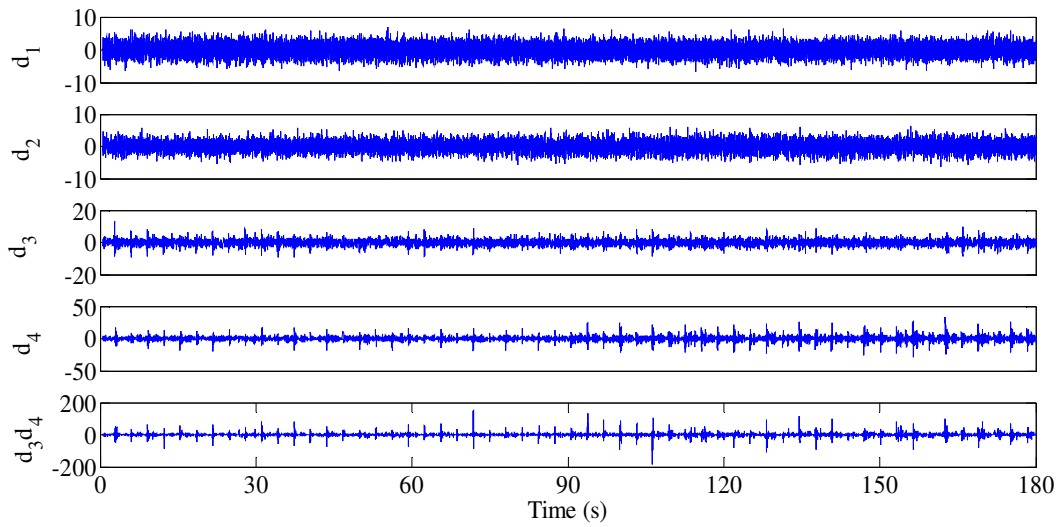


Fig. 5.79 Four-level detail wavelet coefficients of P_B pressure signal shown in Fig. 5.74.

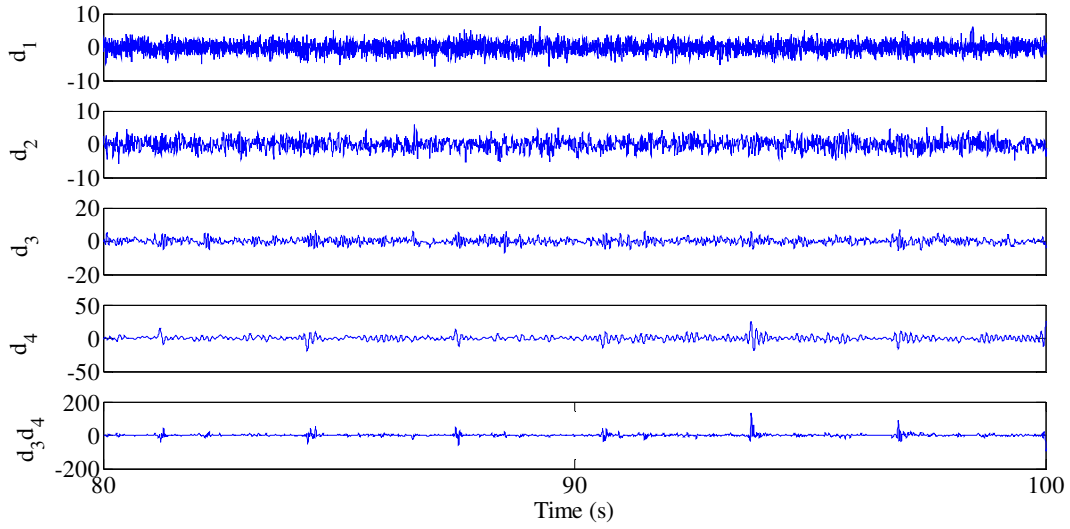


Fig. 5.80 Close-up view from 80th to 100th seconds to show the behaviour of Fig. 5.79.

The RMS curves of d_3 , d_4 and d_3d_4 of pressure signal P_B is traditional in expressing the changes in the values during leaking data as opposed to non-leaking data. This is somewhat visible in Fig. 5.81.

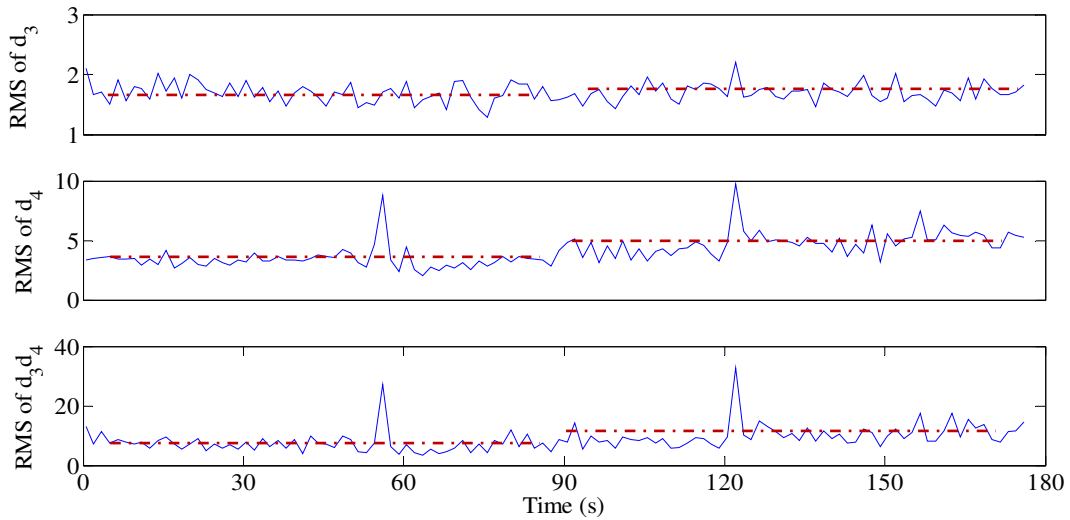


Fig. 5.81 RMS values of wavelet coefficient, d_3 , d_4 and d_3d_4 as shown in Fig. 5.79.

d) For the final experiment, the system is provided with higher amplitude (8 volts) and a frequency of 1 rad/s as an input for the sine wave in an attempt to observe extra-small levels of internal leakage and to acquire the internal pressures in chambers A and B of the cylinder. This is shown in Figs. 5.82 and 5.83 (close-up view).

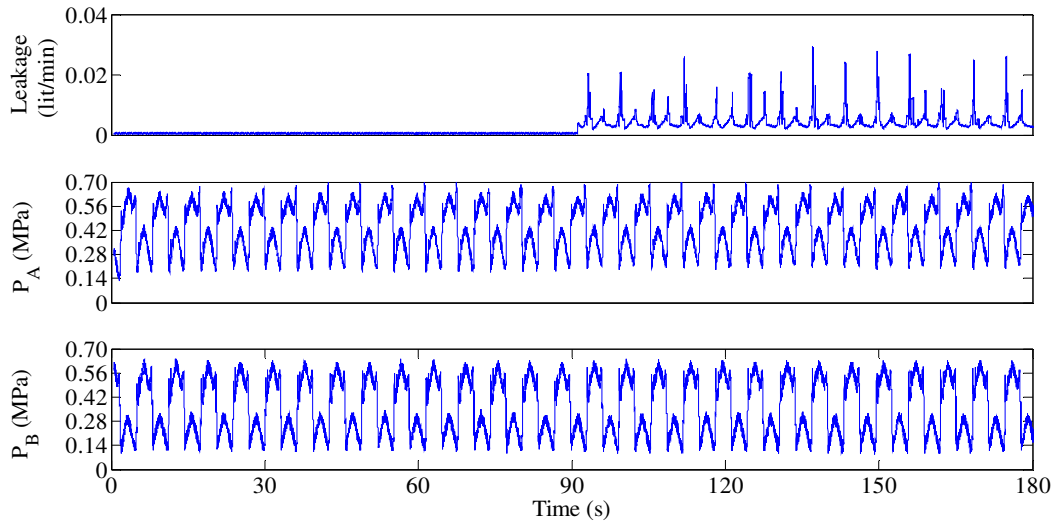


Fig. 5.82 Extra-small level of internal leakage shown with the pressures as P_A and P_B at both sides of the cylinder.

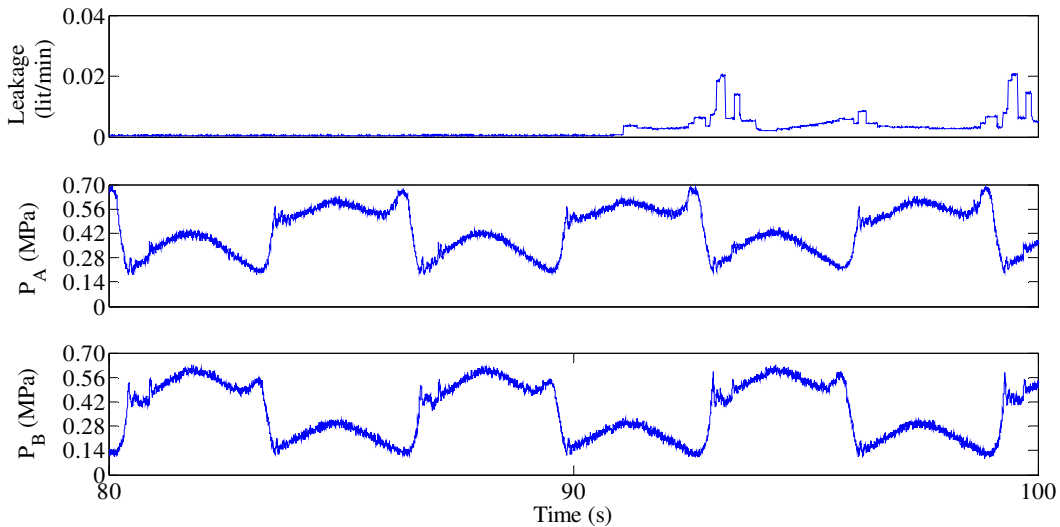


Fig. 5.83 Close-up view from 80th to 100th seconds to show the behaviour of Fig. 5.82.

In Figs. 5.84 and 5.87, the 3rd and 4th level of detail coefficient (labelled d_3 and d_4) along with amplified d_3d_4 signify the leak due which is clearly observable in the changes in the plotted data. The close-up view from the 80th to 100th seconds of the detail coefficients of P_A and P_B also help in studying the behaviour of the wavelet transform during leakages, which is presented in Figs. 5.85 and 5.88.

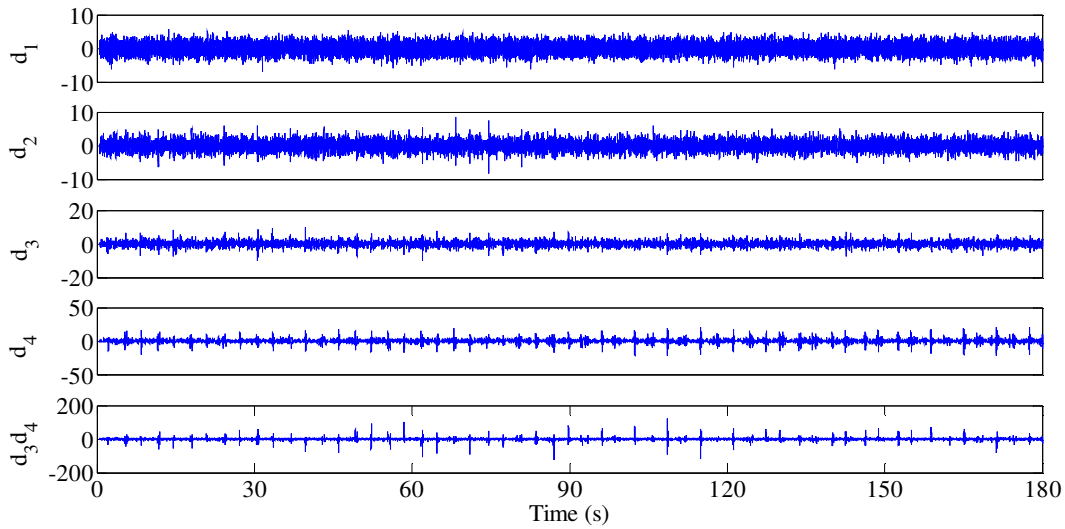


Fig. 5.84 Four-level detail wavelet coefficients of P_A pressure signal shown in Fig. 5.82.

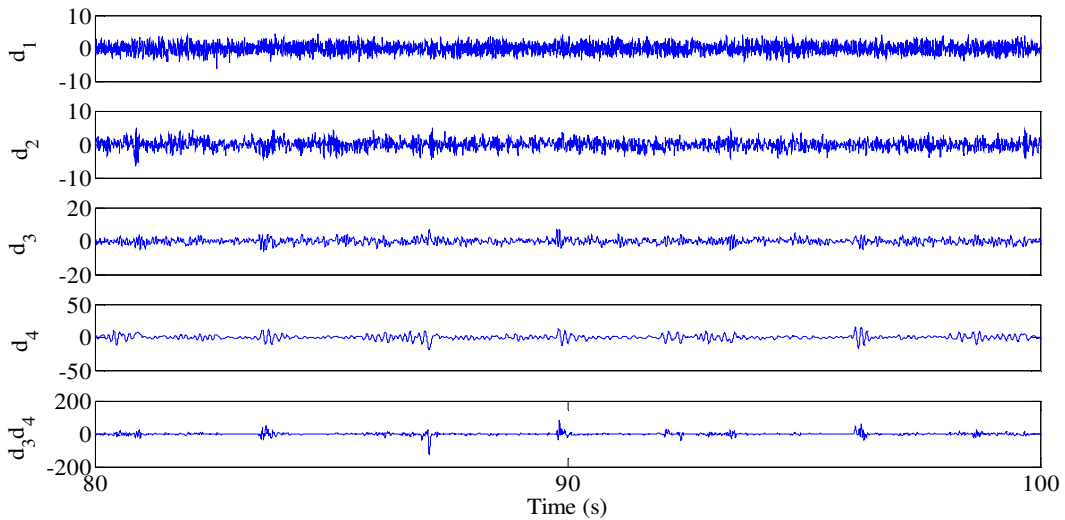


Fig. 5.85 Close-up view from 80th to 100th seconds to show the behaviour of Fig. 5.84.

The RMS curves of d_3 , d_4 and d_3d_4 of pressure signal P_A is conventional in expressing the changes in values during leaking data compared to non-leaking data which is evident in Fig. 5.86.

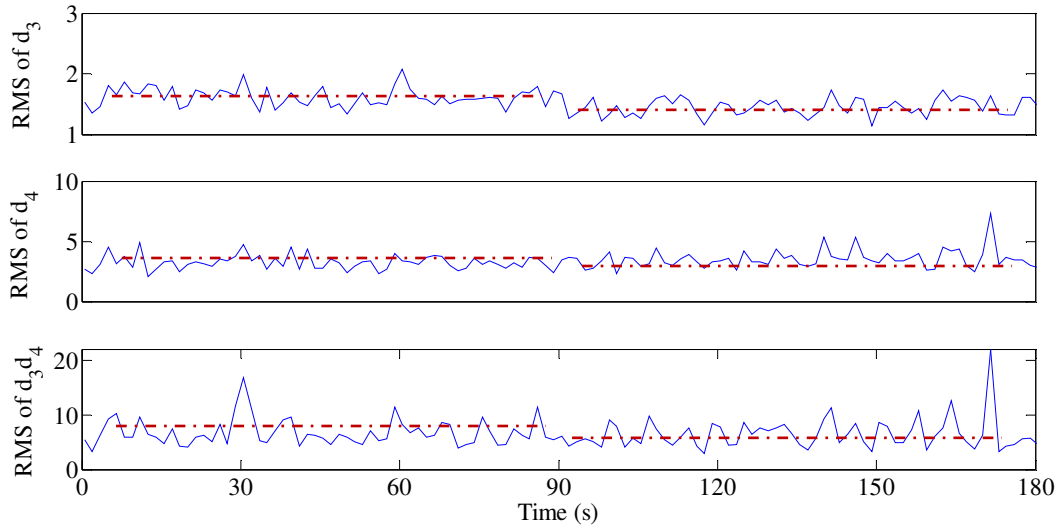


Fig. 5.86 RMS values of wavelet coefficient, d_3 , d_4 and d_3d_4 as shown in Fig. 5.84.

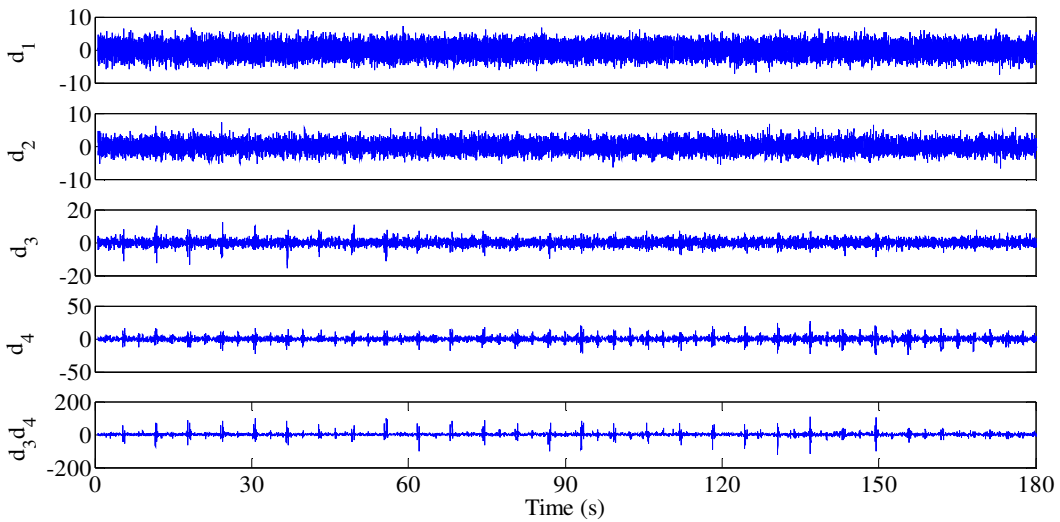


Fig. 5.87 Four-level detail wavelet coefficients of P_B pressure signal shown in Fig. 5.82.

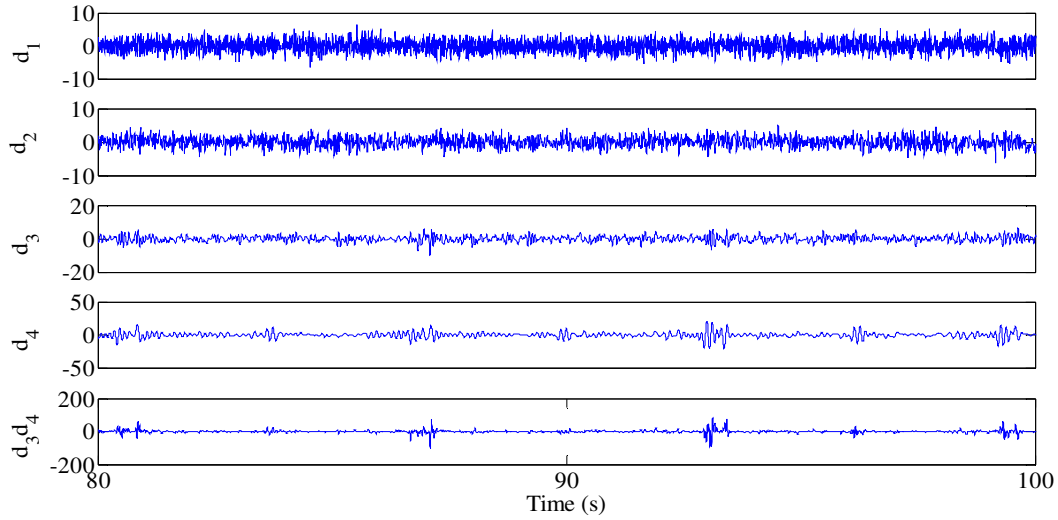


Fig. 5.88 Close-up view from 80th to 100th seconds to show the behaviour of Fig. 5.87.

The RMS curves of d_3 , d_4 and d_3d_4 of pressure signal P_B is conventional in expressing the changes in values during leaking data when contrasted to the non-leaking data as is suggested by Fig. 5.89.

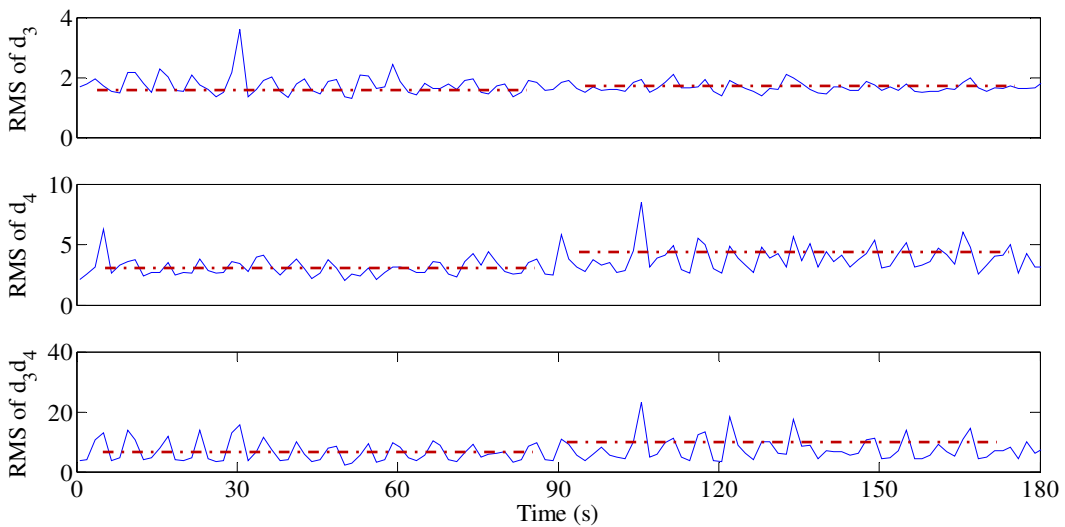


Fig. 5.89 RMS values of wavelet coefficient, d_3 , d_4 and d_3d_4 as shown in Fig. 5.87.

5.6 Evaluation of fault detection

The cases of large to extra-small level leaks presented in this chapter have been selected because they allow for the easy visualization of the effects of leakage on detail coefficients after the use of Wavelet transform. In total, 41 tests were conducted using various amplitudes and frequencies in sine wave input and leakage level. The mean value of leakage is derived from these varying levels. The entire data can be seen in Appendix A which shows the calculation of the RMS values of d_1 , d_2 , d_3 , d_4 and d_3d_4 for both sides of pressure chambers (P_A and P_B).

Furthermore, Fig. 5.90 depicts the difference in the RMS values of non-leaking and leaking data from pressure chamber P_A which shows the trend of decrease which is exactly similar as the calculation of RMS curves shown in all above various cases for pressure chamber P_A with a 100% success rate of fault detection with detail coefficient d_3 .

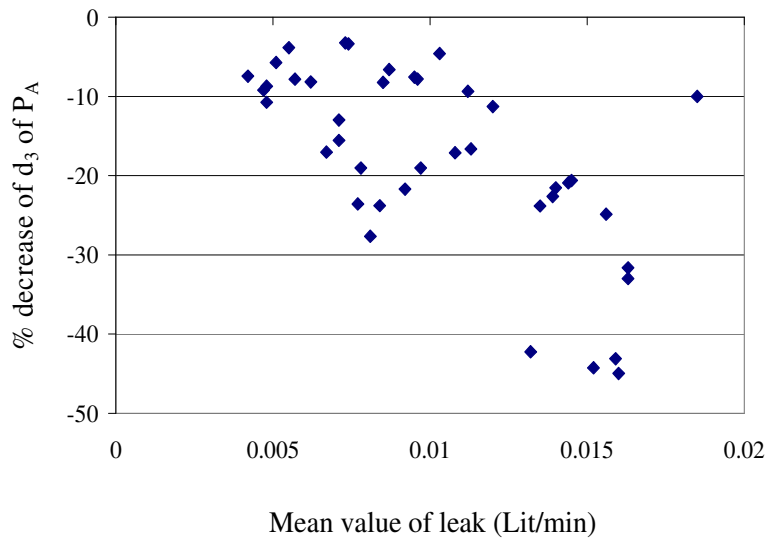


Fig. 5.90 Difference in non-leaking and leaking RMS values of d_3 on pressure chamber P_A with respect to mean values of leak.

Similarly, in Fig. 5.91 the points indicate a consistent downward trend with a fault detection success rate of 65% that is aided by detail coefficient d_4 on pressure chamber P_A .

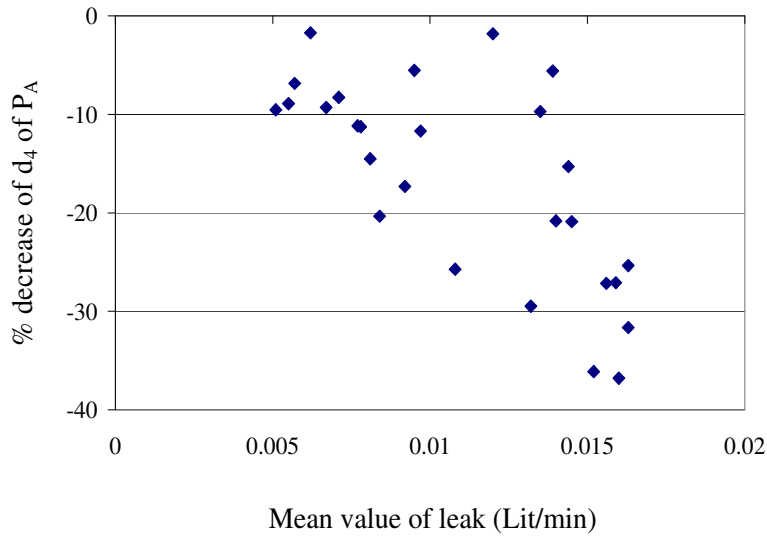


Fig. 5.91 Difference in non-leaking and leaking RMS values of d_4 on pressure chamber P_A with respect to mean values of leak.

Figure 5.92 depicts the difference in RMS values of amplified d_3 and d_4 which is shown as d_3d_4 . The amplification shows results with a fault detection success rate of 85% and exhibits consistent behaviour when the mean value of leak is increased.

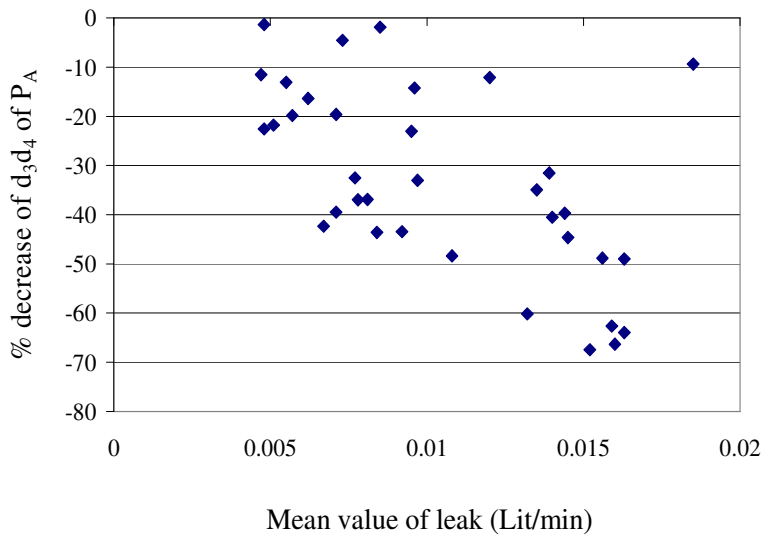


Fig. 5.92 Difference in non-leaking and leaking RMS values of d_3d_4 on pressure chamber P_A with respect to mean values of leak.

In case of P_B , the trend of the points in the plots has changed for all the cases shown in Appendix C. For P_A , the difference in the RMS values is depending on the points moving from higher to lower depending on the mean value of the leak; however, in the case of P_B the RMS values are positive in nature and trend upwards. This proves that there is an inverse relationship between the RMS values of the detail coefficients of both pressure chambers. Figure 5.93 depicts the difference in the RMS values of d_3 detail coefficient of pressure chamber P_B with an upward trend and achieving a success rate of 48% in detecting faults on the basis of d_3 which is similar to the RMS curves shown for P_B in all the cases described in above section. Figure 5.94 reflects the difference in the RMS values of d_4 with respect to non-leaking and leaking data on the same side of the cylinder with an upward trend and achieving a fault detection success rate of 76%.

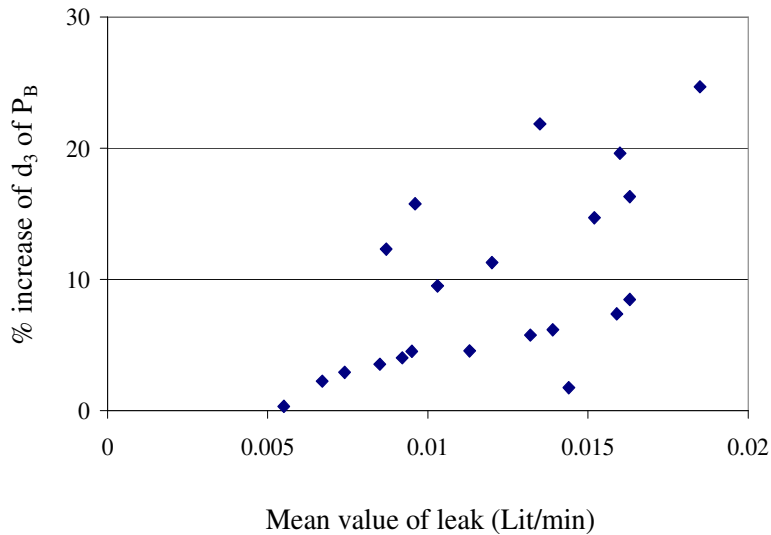


Fig. 5.93 Difference in non-leaking and leaking RMS values of d_3 on pressure chamber P_B with respect to mean values of leak.

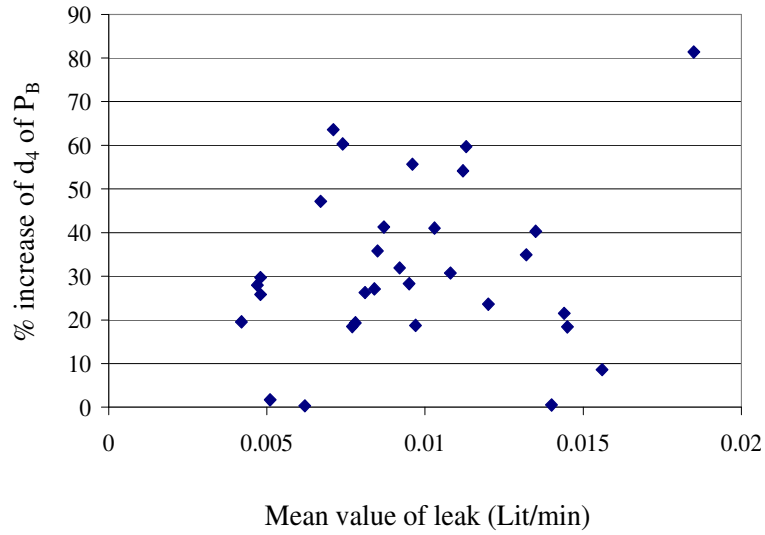


Fig. 5.94 Difference in non-leaking and leaking RMS values of d_4 on pressure chamber P_B with respect to mean values of leak.

The amplified version of d_3 and d_4 (d_3d_4) shows the higher success rate of 76% on pressure chamber P_B which is able to diagnose internal leakage with greater efficiency using Wavelet transform.

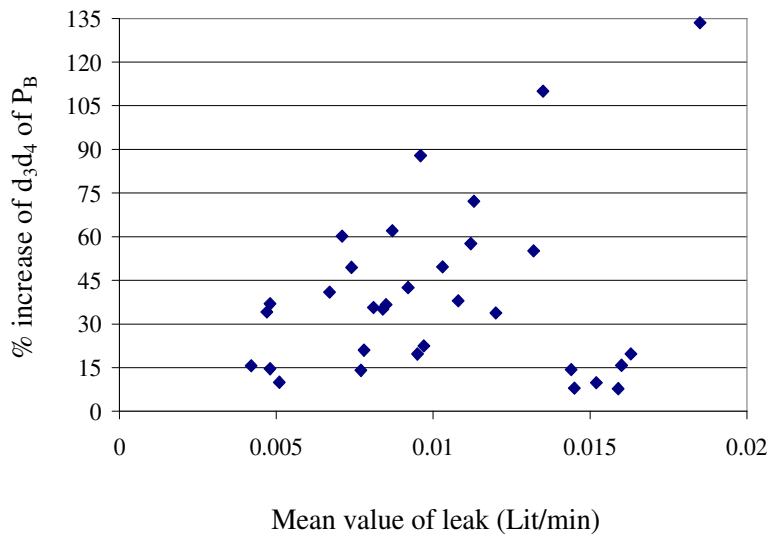


Fig. 5.95 Difference in non-leaking and leaking RMS values of d_3d_4 on pressure chamber P_B with respect to mean values of leak.

Table 5.1 reflects the success rate of internal leakage detection using differences in the RMS values of d_3 , d_4 and d_3d_4 detail coefficients for both pressure chambers as well as the cumulative success rates of both pressure signals. This is established on the basis of amplified detail coefficient d_3d_4 which is presented on the data sheets included in Appendix C. The difference of RMS percentage calculated in P_A of all non-leaking detail coefficient is lesser than leaking section and inversely on chamber P_B the RMS of non-leak detail coefficient is higher than leaking data.

Table 5.1 Comparison of success rate for fault detection on both sides of actuator.

Pressure chamber \ Detail Coefficient	P_A	P_B
d_3	100%	48%
d_4	64%	76%
d_3d_4	85%	76%
Cumulative success of d_3d_4 in both pressure chamber P_A and P_B	65%	

5.7 Summary

In the above experiments fault detection was conducted by analysing data that was obtained from the pressure sensors on both ends of the cylinder, which can be seen in Appendix C. The use of Wavelet transform proved to be highly useful in performing signal analyses aimed at detecting internal leakage data demonstrating a fault detection success rate of more than 80%. Furthermore, it provided experimental validation supporting the thesis that Discrete Wavelet Transform (DWT) is fully capable of detecting internal leakages ranging from the large to the extra-small.

The wavelet transform helped by calculating up to four levels the detail coefficients labelled as d_1 , d_2 , d_3 , d_4 along with the amplified result of d_3 and d_4 (labelled as d_3d_4) which was instrumental in detecting leakages. In addition, the behaviour of the RMS curves of sensitive detail coefficients (d_3 , d_4 and d_3d_4) helped in proving the effect of leakage during signal processing using Wavelet transform. It was consistently observed that the significant change in the signal occurred at the time the leakage began, and changes in the signal of detail coefficients were observed to be a reflection of the duration of the leak. Throughout this analysis of wavelet transform, db8 was used as mother wavelet for all experimental data. The leakage was categorized on four different levels: large leak, medium, small and extra-small. The internal leakage was shown with the help of a flowmeter installed on the internal leakage valve, and the smallest mean value of detected internal leakage was 0.0042litre/minute which was in the extra-small fault test case.

CHAPTER

6

CONCLUSIONS AND FUTURE WORK

6.1 Contribution of this thesis

In this study, an Electro Hydrostatic Actuation system was studied and tested using mathematical modeling and an experimental test rig. The EHA system was modeled mathematically using C++ for a non-linear model of EHA. The reason for the system's non-linearity was to allow for the use of orifices in both the mathematical model and also the experimental setup. The model was described with complete dynamic friction and motor equations which allowed for it to closely reflect the experimental performance of the test rig. This hydraulic system was equipped with a fixed displacement pump and a variable motor.

The performance of the system was confirmed by the results obtained from the simulation program written in visual studio C++ and the experimental test rig. The EHA test rig was equipped with a closed-loop around the motor which helped in controlling the velocity of the motor and the displacement of the piston in the open-loop system. The consistency of the data

produced by the mathematical model and the EHA system test rig confirmed the theoretical basis of this study. Moreover, the equations used to express the flow from orifices in simulation programming matched with the results of the real setup. The EHA system was tested under sine wave inputs with different amplitudes and frequencies to make the system work without the use of orifices as well as with the combination of orifices. The effect of orifices creates back pressure at both ends of the cylinder, especially when the system is provided with a higher value of amplitude.

In hydraulic cylinders, occurrence of internal leakage at the piston is very common and can arise as a result of an aging cylinder, dirt in the hydraulic oil, excessive load, or from wear and tear. Internal leakage in the cylinder can severely affect the performance of the actuation system in terms of piston displacement, reduced piston velocity and fluctuations in pressure measurements obtained from the ends of the cylinder. In order to gather the fault information created at piston, the experimental rig was examined for internal leakage created at the piston. Data related to the pressure measurements at the ends of cylinder was used for the purpose of fault detection. The methodology used for fault detection was related to signal processing with the help of Wavelet transform. Wavelets proved to be very useful in helping us to analyze the data and observe the changes in the signal at the time the fault was generated in the data collection. Different inputs were given to the EHA test rig to with a varying range of internal leakages beginning with a large leak and progressing to an extra-small leak. The reason for the continuous reduction in the leakage level was to examine and justify the performance of Wavelet analysis. Benefit of fault detection at early stage could help in the maintaining the performance of actuators.

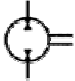



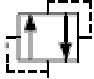




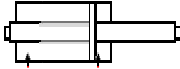
The EHA system was designed and constructed for the purpose of conducting research to understand the relationship between the behaviour of mathematical models of EHA systems, and an experimental test rig. Similar behaviour of simulation and experimental results validated the work performed. The effect of a non-linear system in the open-loop system was very good in the qualitative tracking of the displacement of the piston, and the angular velocity of the motor along with the pressures at the inlet/outlet of the pump and at the ends of the cylinder. Wavelet transform helped in detecting internal leakage by processing the pressure signals at the either end of the cylinder. As conclusion, Wavelet transform showed a success rate of better than 80% in detecting internal leakages with a minimum mean leak value of 0.0048 lit/min. The calculation of the RMS values of the detail coefficients obtained through the use of Wavelet transform on the pressure signal of the cylinder also proved the difference in the signals when non-leaking and leaking data were compared.

6.2 Future Work

There is much work left to be done on this highly industry-oriented topic. One such avenue would be to explore the effect of closing the loop across the displacement of the piston. This would require the use of an appropriate controller which would surely help in compensating for external disturbance. Another possible area of research would involve conducting internal and external leakage tests on closed loop system using online and offline methods to achieve greater effectiveness and efficiency with the help of a fault tolerant controller. A third potential avenue may be to see how a test rig will behave when there is extra load on the cylinder. The back force on the cylinder could be useful in determining the effectiveness of controllers designed for the displacement of the piston. Finally, it may be highly informative to compare valve-controlled

hydraulic systems and pump controlled EHA systems to observe the differences in efficiency and performance.

Appendix A: Details of the fittings applied in EHA

Name of Part	Symbol of Part	Description
Motor & Pump		Combined Hydraulic Pump and Motor
Check Valve		One directional free flow; blocked flow in other direction
Electric Motor		Variable RPM servo electric motor
Accumulator (Reservoir)		Oil Tank
Relief valve		Bi-directional relief valve
Shut off valve		Manual shut off valve
Filter		
Orifice		Variable throttle valve
Throttling valve with check valve		Free flow in one direction with restricted manual variable flow in other direction
Cylinder		Double rod cylinder

Appendix B: Steps to run the experimental test rig (EHA)

1. Establish a Simulink model using WinCon to send input signal.
2. Input signal is further sent to Quanser Data acquisition board which is connected to computer.
3. DAQ sends the voltage signal to the servo drive which is also connected to this board.
4. Servo drive sends the amplified voltage signal to the motor which is coupled with pump.
5. Combination of motor and pump allows the flow of hydraulic oil in the entire EHA test rig.
6. The pump is installed with two pressure sensors at inlet and outlet ports to monitor pressures.
7. Similarly, two pressure sensors are installed at the ends of actuator to record the pressure signals.
8. Hydraulic actuator is provided with a position encoder to measure the displacement of the piston.
9. All the pressure sensors and position encoder are also connected with data acquisition board which helps in gathering the data at each time interval with the help of WinCon.
10. User must make sure that all the pressure sensors are turned on during the operation of EHA and should be switched off if not required.
11. During the operation of EHA user must be careful from the motor and hydraulic cylinder.

Appendix C: Data sheet of RMS values of detail coefficients (d_1 , d_2 , d_3 , d_4 and d_3d_4) obtained on pressure chamber P_A and P_B of the actuator.

Mean value of leak	Input	Orifice size (closed)	Leakage level	RMS of P_A wavelet													
				d_1		d_2		d_3		d_4		d_3d_4					
				No Leak	Leak	No Leak	Leak	No Leak	d3 diff%	No Leak	Leak	d4 diff%	No Leak	Leak	d3d4 diff%		
0.0042	8sin(1t)	50%	extra-small	1.3651	1.3555	1.3436	1.3037	1.5757	1.4585	-7.43796409	3.1976	3.6659	14.64535902	6.5755	7.1309	8.446505969	
0.0047	8sin(1t)	25%	extra-small	1.239	1.3052	1.4547	1.3398	1.6095	1.4614	-9.20161549	3.3345	3.5556	6.630679262	7.7342	6.8412	-11.54611983	
0.0048	8sin(1t)	25%	extra-small	1.3018	1.3589	1.3786	1.2313	1.6835	1.5027	-10.7395307	3.4996	3.6742	4.989141616	9.0796	7.0297	-22.57698577	
0.0048	8sin(1t)	50%	extra-small	1.38	1.3368	1.3369	1.2806	1.6157	1.4751	-8.7021105	3.1901	3.5413	11.00905928	6.7596	6.6681	-1.353630392	
0.0051	7sin(4t)	75%	extra-small	1.3107	1.2615	1.7468	1.5241	2.0412	1.9245	-5.71722516	5.2417	4.7419	-9.535074499	13.6628	10.6827	-21.81178089	
0.0055	7sin(4t)	75%	extra-small	1.3713	1.2441	1.7556	1.4262	1.9761	1.9001	-3.84595921	5.0644	4.6129	-8.915172577	11.0903	9.6373	-13.10153918	
0.0057	5sin(2t)	75%	extra-small	1.363	1.2182	1.4436	1.2985	1.7096	1.5757	-7.8322414	2.9958	2.7908	-6.842913412	5.8248	4.6691	-19.84102458	
0.0062	5sin(2t)	75%	extra-small	1.3369	1.2224	1.4918	1.243	1.7098	1.5702	-8.16469762	3.05	2.9975	-1.721311475	6.0863	5.0901	-16.36790825	
0.0067	5sin(2t)	50%	extra-small	1.1397	1.1487	1.3772	1.3232	1.9304	1.6016	-17.0327393	4.3416	3.9378	-9.300718629	12.8527	7.4097	-42.3490784	
0.0071	5sin(2t)	50%	extra-small	1.2752	1.2117	1.2433	1.3491	1.7673	1.4925	-15.5491427	4.4175	4.0523	-8.267119411	11.852	7.1732	-39.47688154	
0.0071	3sin(4t)	75%	extra-small	1.0664	1.1533	1.4463	1.2119	1.9819	1.7249	-12.9673545	4.5216	4.6933	3.797328379	11.1792	8.9859	-19.61947188	
0.0073	3sin(4t)	75%	extra-small	1.1431	1.1162	1.4668	1.2957	2.0551	1.9883	-3.2504501	5.3578	5.3995	0.778304528	12.783	12.2013	-4.550574982	
0.0074	8sin(1t)	zero	small	1.317	1.2477	1.3612	1.4039	1.7666	1.7071	-3.36805162	3.5993	4.7215	31.17828467	9.7797	9.9691	1.936664724	
0.0077	7sin(4t)	50%	extra-small	1.3409	1.339	1.5923	1.3514	2.3792	1.8179	-23.5919636	6.1514	5.465	-11.15843548	17.3962	11.7344	-32.54618825	
0.0078	7sin(4t)	50%	extra-small	1.3435	1.3316	1.564	1.3301	2.2693	1.8371	-19.0455206	5.9073	5.2424	-11.25556515	17.4728	11.0142	-36.96373792	
0.0081	7sin(4t)	25%	extra-small	1.2237	1.2682	1.5178	1.3306	2.2258	1.6101	-27.6619642	6.4233	5.4919	-14.50033472	17.5234	11.0563	-36.9055092	
0.0084	7sin(4t)	25%	extra-small	1.1878	1.1816	1.3907	1.2541	2.2952	1.7491	-23.793133	6.6651	5.31	-20.33127785	19.0737	10.7566	-43.60506876	
0.0085	5sin(2t)	25%	extra-small	1.1508	1.1184	1.2535	1.1564	1.6419	1.5069	-8.22218169	3.3969	3.5262	3.806411728	5.9801	5.8676	-1.881239444	
0.0087	5sin(2t)	25%	extra-small	1.1208	1.1286	1.1782	1.1997	1.7055	1.5928	-6.60803283	3.8987	4.3035	10.38294816	7.5998	8.1462	7.189662886	
0.0092	7sin(4t)	zero	extra-small	1.1889	1.1917	1.3938	1.277	2.2511	1.7628	-21.6916174	5.8449	4.8325	-17.32108334	16.5452	9.3553	-43.45610812	

0.0095	8sin(1t)	zero	medium	1.2471	1.2284	1.4021	1.3222	1.9906	1.8398	-7.57560534	5.5399	5.2336	-5.528980668	15.7051	12.0851	-23.04983731
0.0096	8sin(1t)	zero	small	1.3829	1.2653	1.3115	1.3588	1.9272	1.7768	-7.80406807	5.7001	6.3198	10.87173909	16.9743	14.556	-14.24683198
0.0097	5sin(2t)	zero	extra-small	1.1096	1.1414	1.2639	1.2277	1.7837	1.4439	-19.0502887	4.3433	3.8355	-11.69157093	8.5452	5.7233	-33.02321771
0.0103	8sin(1t)	zero	Large	1.348	1.2812	1.3487	1.413	1.8007	1.7179	-4.59821180	4.6313	5.2718	13.8298102	11.858	12.992	9.563164109
0.0108	7sin(4t)	zero	small	1.2803	1.2252	1.4607	1.4186	2.1122	1.7504	-17.1290597	6.3473	4.7149	-25.71802184	17.0532	8.7991	-48.40205944
0.0112	3sin(4t)	50%	extra-small	1.0395	1.0413	1.4177	1.2602	2.5939	2.3509	-9.36813292	6.518	8.8593	35.92052777	19.2341	27.2322	41.58291784
0.0113	3sin(4t)	50%	extra-small	1.0353	1.044	1.4257	1.2978	2.9187	2.4331	-16.6375441	7.8675	9.2773	17.91928821	26.6063	29.4968	10.86396831
0.012	5sin(2t)	zero	small	1.1714	1.1466	1.352	1.2754	1.8093	1.605	-11.2916597	4.9048	4.8161	-1.808432556	9.6823	8.5093	-12.11489006
0.0132	3sin(4t)	25%	extra-small	1.0914	1.1308	1.4748	1.2504	2.8375	1.6387	-42.2484581	5.8195	4.1044	-29.47160409	21.5964	8.6027	-60.16604619
0.0135	3sin(4t)	25%	extra-small	1.1851	1.1537	1.157	1.1943	2.0723	1.5783	-23.8382473	4.0851	3.6888	-9.701108908	9.8752	6.4242	-34.94612767
0.0139	5sin(2t)	zero	Large	1.274	1.3023	1.2426	1.1658	1.8266	1.4131	-22.6376875	4.532	4.2783	-5.597969991	11.7191	8.0242	-31.52887167
0.014	3sin(4t)	zero	extra-small	1.1449	1.0613	1.3513	1.2937	2.7639	2.1683	-21.549260	7.2689	5.756	-20.81332801	25.3746	15.0898	-40.53187045
0.0144	7sin(4t)	zero	medium	1.346	1.3557	1.3083	1.2847	2.0556	1.6257	-20.9136018	6.5141	5.5178	-15.29451498	16.646	10.0342	-39.72005287
0.0145	7sin(4t)	zero	Large	1.3343	1.3513	1.3314	1.2945	2.1728	1.7247	-20.6231590	6.8596	5.4267	-20.88897312	18.0296	9.9781	-44.6571194
0.0152	3sin(4t)	zero	small	1.068	1.0502	1.3007	1.2264	3.005	1.6748	-44.2662229	6.2312	3.9812	-36.10861471	23.5039	7.6431	-67.48156689
0.0156	7sin(4t)	zero	medium	1.2512	1.2991	1.3848	1.3242	2.2114	1.6613	-24.8756443	6.8994	5.026	-27.15308578	17.0816	8.7395	-48.83676002
0.0159	3sin(4t)	zero	medium	1.0742	1.0861	1.2753	1.252	2.4858	1.4139	-43.1209268	5.0547	3.6854	-27.08963935	16.4258	6.134	-62.65630898
0.016	3sin(4t)	zero	medium	1.0965	1.0704	1.3173	1.2371	2.757	1.5169	-44.9800507	5.8293	3.685	-36.78486268	19.1781	6.4593	-66.31939556
0.0163	3sin(4t)	zero	Large	1.2278	1.2189	1.1092	1.0535	1.8329	1.253	-31.6383872	3.5613	2.6587	-25.34467751	7.4215	3.7845	-49.00626558
0.0163	5sin(2t)	zero	medium	1.1754	1.1589	1.2919	1.2412	2.4051	1.6115	-32.996549	6.8897	4.7093	-31.64724153	24.9759	8.9978	-63.974071
0.0185	5sin(2t)	zero	medium	1.2303	1.1704	1.3886	1.2896	1.8945	1.7049	-10.0079176	4.6993	4.7569	1.225714468	11.1522	10.1033	-9.40531913

When RMS values of leak goes down the success rate is as follows:

100%

65%

85%

Mean value of leak	Input	Orifice size (closed)	Leakage level	RMS of P _B wavelet												
				d ₁		d ₂		d ₃		d ₄			d ₃ d ₄			
				No Leak	Leak	No Leak	Leak	No Leak	Leak	d ₃ diff%	No Leak	Leak	d ₄ diff%	No Leak	Leak	d ₃ d ₄ diff%
0.0042	8sin(1t)	50%	extra-small	1.6815	1.6523	1.5161	1.5155	1.7302	1.7052	-1.44492	3.1948	3.8193	19.54739	6.8714	7.9476	15.66201938
0.0047	8sin(1t)	25%	extra-small	1.4983	1.599	1.7786	1.6362	1.7276	1.6922	-2.049085	2.7085	3.4664	27.98228	5.3731	7.2049	34.09205114
0.0048	8sin(1t)	25%	extra-small	1.5794	1.7132	1.6752	1.4574	1.6623	1.6527	-0.577513	2.5051	3.2496	29.71937	4.7761	6.5396	36.92343125
0.0048	8sin(1t)	50%	extra-small	1.709	1.6597	1.4627	1.5075	1.7593	1.6955	-3.626442	3.1748	3.9954	25.8473	7.1654	8.2157	14.65793954
0.0051	7sin(4t)	75%	extra-small	1.6555	1.6909	1.7591	1.829	2.6617	2.5123	-5.612954	7.0034	7.1209	1.677757	22.1848	24.4008	9.988821175
0.0055	7sin(4t)	75%	extra-small	1.6203	1.6362	1.8595	1.7	2.4916	2.5	0.337133	6.8856	6.7432	-2.068084	19.5033	19.2099	-1.5043608
0.0057	5sin(2t)	75%	extra-small	1.4991	1.533	1.6445	1.7339	2.0589	1.927	-6.406333	3.296	3.1396	-4.745145	6.7036	6.1396	-8.41338982
0.0062	5sin(2t)	75%	extra-small	1.522	1.52077	1.6444	1.5644	2.0375	1.9097	-6.272393	3.2399	3.2511	0.34569	6.6125	6.3179	-4.455198488
0.0067	5sin(2t)	50%	extra-small	1.4137	1.415	1.6643	1.6369	1.9314	1.9749	2.252252	3.161	4.6516	47.15596	7.5547	10.6451	40.90698506
0.0071	5sin(2t)	50%	extra-small	1.6169	1.4857	1.4329	1.6458	1.7244	1.7162	-0.475528	3.1829	5.2064	63.5741	7.0536	11.302	60.23023704
0.0071	3sin(4t)	75%	extra-small	1.3552	1.5423	1.636	1.5695	2.0576	1.862	-9.506221	5.2838	5.2489	-0.660509	11.7558	11.3119	-3.776008438
0.0073	3sin(4t)	75%	extra-small	1.4407	1.4462	1.6921	1.6737	1.9975	1.8844	-5.662078	5.6412	5.268	-6.615613	13.9538	10.4913	-24.81402915
0.0074	8sin(1t)	zero	small	1.6015	1.473	1.616	1.6927	1.8232	1.8766	2.928916	2.901	4.6509	60.32058	7.3422	10.9729	49.4497562
0.0077	7sin(4t)	50%	extra-small	1.661	1.6881	1.578	1.5026	3.1012	2.8617	-7.722817	5.554	6.5803	18.47857	22.8331	26.0425	14.05591006
0.0078	7sin(4t)	50%	extra-small	1.6784	1.6849	1.5229	1.5158	2.8833	2.7864	-3.360732	5.9272	7.0739	19.3464	23.7141	28.6925	20.99341742
0.0081	7sin(4t)	25%	extra-small	1.4735	1.5966	1.7638	1.6369	2.448	2.3889	-2.414216	4.3785	5.5283	26.26013	14.0635	19.0785	35.65968642
0.0084	7sin(4t)	25%	extra-small	1.4086	1.4249	1.5006	1.4673	2.6926	2.6657	-0.999034	4.5419	5.7736	27.11861	15.3698	20.7752	35.16896772
0.0085	5sin(2t)	25%	extra-small	1.4095	1.3696	1.5357	1.4271	1.857	1.9228	3.543349	3.4096	4.6296	35.78132	7.4485	10.1768	36.62885145
0.0087	5sin(2t)	25%	extra-small	1.3752	1.3788	1.3808	1.4857	1.7375	1.9514	12.31079	3.5665	5.0391	41.28978	7.3041	11.8393	62.09115428
0.0092	7sin(4t)	zero	extra-small	1.4368	1.4307	1.5633	1.5224	2.6375	2.7441	4.041706	4.3974	5.8012	31.92341	14.907	21.2486	42.54108808
0.0095	8sin(1t)	zero	medium	1.4675	1.4276	1.6847	1.5745	2.046	2.1387	4.530792	4.0996	5.2594	28.29056	12.1899	14.5872	19.6662811
0.0096	8sin(1t)	zero	small	1.6717	1.5022	1.5076	1.6591	1.716	1.9865	15.7634	3.8327	5.9663	55.66833	7.9316	14.8987	87.83978012
0.0097	5sin(2t)	zero	extra-small	1.353	1.3991	1.5279	1.5376	1.9723	1.904	-3.462962	4.1359	4.9108	18.73595	8.8639	10.8536	22.44722977
0.0103	8sin(1t)	zero	Large	1.6362	1.4885	1.5851	1.7331	1.7449	1.9108	9.507708	3.7062	5.2277	41.05283	9.782	14.6387	49.64935596

0.0108	7sin(4t)	zero	small	1.5298	1.4291	1.7017	1.6918	2.5521	2.5488	-0.129305	4.4355	5.7992	30.74512	15.1883	20.9634	38.02334692
0.0112	3sin(4t)	50%	extra-small	1.3074	1.3251	1.5459	1.5471	2.3544	2.3535	-0.038226	5.1601	7.9557	54.17724	14.9161	23.5125	57.63168657
0.0113	3sin(4t)	50%	extra-small	1.304	1.317	1.4786	1.5621	2.2901	2.3947	4.567486	5.0478	8.0624	59.72107	13.9955	24.0973	72.17891465
0.012	5sin(2t)	zero	small	1.4612	1.3887	1.6532	1.5947	1.7172	1.9112	11.29746	4.6136	5.7034	23.62147	9.1453	12.2397	33.83595945
0.0132	3sin(4t)	25%	extra-small	1.385	1.4564	1.7444	1.6028	1.9506	2.0631	5.767456	4.5159	6.0925	34.9122	10.9526	16.9959	55.17685298
0.0135	3sin(4t)	25%	extra-small	1.5658	1.5041	1.364	1.5209	1.7122	2.0865	21.86076	4.1679	5.8485	40.32246	8.0744	16.9594	110.039136
0.0139	5sin(2t)	zero	Large	1.5878	1.6227	1.4722	1.3347	1.4712	1.562	6.171833	4.5408	4.3604	-3.972868	8.6194	8.2842	-3.88890178
0.014	3sin(4t)	zero	extra-small	1.4891	1.3374	1.5901	1.6028	2.5694	2.3296	-9.332918	6.6792	6.7139	0.519523	22.5157	21.1878	-5.89766252
0.0144	7sin(4t)	zero	medium	1.6391	1.6484	1.485	1.4647	2.0894	2.1262	1.761271	5.0837	6.1775	21.51583	14.5679	16.6538	14.31846732
0.0145	7sin(4t)	zero	Large	1.6362	1.6428	1.4746	1.4637	2.2487	2.1207	-5.692178	5.2737	6.2445	18.40833	15.885	17.1554	7.997481901
0.0152	3sin(4t)	zero	small	1.3433	1.3152	1.559	1.5881	2.3214	2.6628	14.70664	6.4481	6.2574	-2.957460	19.6559	21.5892	9.835723625
0.0156	7sin(4t)	zero	medium	1.4832	1.579	1.6529	1.5478	2.4288	2.2545	-7.176383	6.0482	6.5696	8.620747	19.4309	18.8105	-3.192852621
0.0159	3sin(4t)	zero	medium	1.362	1.3644	1.6147	1.664	2.1454	2.3037	7.378577	6.3196	5.8199	-7.907146	17.7459	19.1262	7.778134668
0.016	3sin(4t)	zero	medium	1.3777	1.359	1.619	1.5862	2.1598	2.5836	19.62219	6.3865	6.0853	-4.716198	19.1379	22.1658	15.82148512
0.0163	3sin(4t)	zero	Large	1.6144	1.6057	1.317	1.2898	1.5242	1.773	16.32332	5.0172	4.96	-1.140078	10.111	12.108	19.75076649
0.0163	5sin(2t)	zero	medium	1.3644	1.362	1.5095	1.4468	1.6933	1.8369	8.480482	6.4098	5.7455	-10.36381	13.0434	12.2188	-6.321971265
0.0185	5sin(2t)	zero	medium	1.4294	1.314	1.5352	1.4309	1.4514	1.8096	24.67962	2.9352	5.3239	81.38117	4.819	11.2546	133.5463789

When RMS values of leak goes up the success rate is as follows:

48%

76%

76%

References

1. Antonino-Davin J. A., Riera-Guasp M., Pineda-Sanchez M., and Perez, "A Critical Comparison between DWT and Hilbert-Huang-Based Methods for the Diagnosis of Rotor Bar Failures in Induction Machines", *IEEE Trans. on Industry Applications*, vol. 45, pp. 1794-1803, 2009.
2. Azlan N Z, "Modeling and Control of Electrohydraulic Robot Manipulator", ME Thesis, Universiti Teknologi Malaysia, 2006.
3. Burrus C. S., Gopinath R. A., and Guo, H., "Introduction to Wavelets and Wavelet Transforms", Prentice Hall, 1998.
4. Chinniah Y A, "Fault Detection in the Electrohydraulic Actuator Using Extended Kalman Filter", PhD Thesis, University of Saskatchewan, 2004.
5. Cusido J., Romeral L., Ortega J. A., Rosero J. A., and Garcia, E. A, "Fault Detection in Induction Machines Using Power Spectral Density in Wavelet Decomposition", *IEEE Trans. on Industrial Electronics*, vol. 55, No. 2, pp. 633-643, 2008.
6. Daubechies I., "Ten Lectures on Wavelets Montpelier", Capital City Press, 1992.
7. Donoho D. L., "Unconditional Bases are Optimal Bases for Data Compression and For Statistical Estimation", *Applied and Computational Harmonic Analysis*, vol. 1, pp. 100-115, 1993.
8. Gao Y., Zhang Q., and Kong X., "Wavelet Based Pressure Analysis for Hydraulic Pump Health Diagnosis", *Trans. ASAE*, vol. 46, pp. 969-976, 2003.
9. Gao Y., Zhang Q., and Kong X., "Comparison of Hydraulic Pump Fault Diagnosis Methods: Wavelet vs. Spectral Analysis", *Proceedings, ASME International Mechanical Engineering Congress and Exposition*, pp. 73-78, 2005.
10. Gao B., Fu, Y-L, and Z-C, "Research on dual-variable integrated electro-hydrostatic actuator", *Chinese Journal of Aeronautics*, vol. 19, No. 1, pp. 77-82, 2006.
11. Gao Q., Duan C., Fan H., and Meng Q., "Rotating Machine Fault Diagnosis Using Empirical Mode Decomposition", *Mechanical Systems and Signal Processing*, vol. 22, pp. 1072-1081, 2008.
12. Goharrizi A. Y., "Leakage Detection in Hydraulic Actuators based on Wavelet Transform", PhD Thesis, University of Manitoba, 2011.
13. Goharrizi A.Y. and Sepehri N., "A Wavelet-Based Approach to Internal Seal Damage Diagnosis in Hydraulic Actuators," *IEEE Transactions on Industrial Electronics* , vol. 57, No. 5, pp. 1755-1763, 2010.

14. Habibi S. and Goldenburg A., "Design of a New High Performance Electrohydraulic Actuator", IEEE/ASME Transactions on Mechatronics, vol. 5, No. 2, 2000.
15. He L., "Dynamical Adaptive Backstepping-Sliding Mode Control of Pneumatic Actuator", MSc Thesis, University of Manitoba, 2010.
16. Heney P., "F-35 Fighter Incorporates EHA", Hydraulics and Pneumatic: The International Magazine of Fluid Power and Motion Control Systems, Penton Publication, USA, vol. 55, No. 12, pp. 16, 2002.
17. Kang K., Pachter M., Houppis C.H., and Rasmussen S., "Modeling and Control of an Electro-Hydrostatic Actuator", Aerospace and Electronics Conference, vol. 1, pp. 22-26, 1995.
18. Khan H., Abou S., and Sepehri N., "Fault Detection in Electro-Hydraulic Servo-Positioning Systems Using Sequential Test of Wald", Proceedings, Canadian Conference on Electrical and Computer Engineering, pp. 1628-1633, 2002.
19. Li J., Fu Y., Wang Z., and Zhang G., "Research on Fast Response and High Accuracy Control of an Airborne Electro Hydrostatic Actuation System", Intelligent Mechatronics and Automation, pp. 428- 432, 2004.
20. Lischinsky P., "Canudas-de-Wit C., and Morel G., "Friction Compensation for an Industrial Hydraulic Robot", IEEE Control System Magazine, vol. 19, pp. 25-32, 1999.
21. Loutridis S. J., "Damage Detection in Gear Systems Using Empirical Mode Decomposition", Engineering Structures, vol. 26, pp. 1833-1841, 2004.
22. Merritt H., "Hydraulic Control Systems", John Wiley & Sons, 1967.
23. Proakis J. G. and Manolakis D. G., "Digital Signal Processing", 4th Ed. Prentice Hall, 2007.
24. Rongjie K., Zongxia J., Shuai W., Yaoxing S., and Mare J-C, "The Nonlinear Accuracy Model of Electro-Hydrostatic Actuator", IEEE Conference on Robotics, Automation and Mechatronics, pp. 107-111, 2008.
25. Sampson E B, "Fuzzy Control of the Electro Hydraulic Actuator", MSc Thesis, University of Saskatchewan, 2005.
26. Skormin V. A., Apone J., and Dunphy J. J., "Online Diagnostics of a Self-contained Flight Actuator", IEEE Trans. on Aerospace and Electronic Systems, vol. 30, pp. 186-196, 1994.
27. Skormin V. A. and Apone J., "Online Diagnostics of a Variable Displacement Pump of a Flight Actuation System", Proc. of the IEEE National Aerospace and Electronics Conference, vol. 1, pp. 503-510, 1995.

28. The Mathworks, "Wavelet Toolbox User's Guide", The Mathworks Inc., Natick, Massachusetts, USA, 2005.
29. Thomas A., "The Application of the wavelet transform to the processing of aeromagnetic data", Ph.D. Thesis, University of Western Australia, 2000.
30. Williamson C., and Ivantysynova M., "Stability and Motion Control of Inertial Loads with Displacement Controlled Hydraulic Actuators", Proceedings of the 6th FPNI PhD Symposium, West Lafayette, USA, pp 499–514, 2010.
31. Yu D., "Fault Diagnosis for a Hydraulic Drive System Using Parameter Estimation Method", Control Engineering Practice, vol. 5, pp. 1283-1291, 1997.
32. Zafarifar B., "Micro-Codable Discrete Wavelet Transform", Master Thesis, Delft University of Technology, Netherland, 2002.
33. Zavarehi M. K., Lawrence P. D., and Sassani F., "Nonlinear Modeling and Validation of Solenoid Controlled Pilot-Operated Servovalves", IEEE/ASME Tran. Mechatronics, vol. 4, pp. 324-334, 1999.
34. Zhang J. Q. and Yan Y., "A Wavelet-Based Approach to Abrupt Fault Detection and Diagnosis of Sensors", IEEE Trans. on Instrumentation and Measurement, vol. 50, pp. 1389-1396, 2001.
35. Zhang Y. M. and Jiang J., "Active Fault-Tolerant Control System against Partial Actuator Failures", IEEE Proc. of Control Theory Application, vol. 149, pp. 95-104, 2002.
36. Zhou R., Lin T. Han J., and Yan D., "Fault Diagnosis of Airplane Hydraulic Pump", Proceeding of the 4th World Congress on Intelligent Control and Automation, vol. 4, pp. 3150-3152, 2002.